Nonlinear terahertz spectroscopy of electronic and vibrational responses in condensed matter systems

by

Harold Young Hwang

B.S. Chemical Engineering, Cornell University (2005)

Submitted to the Department of Chemistry

in partial fulfillment of the requirements for the degree of

Doctor of Philosophy

at the

MASSACHUSETTS INSTITUTE OF TECHNOLOGY

June 2012

Author .....

Department of Chemistry

May 16, 2012

Certified by .....

Keith A. Nelson

Professor

Thesis Supervisor

Accepted by .....

Robert W. Field

Chairman, Department Committee on Graduate Students

This doctoral thesis has been examined by a committee of the Department of Chemistry as follows:

Professor Robert W. Field.....
Chairperson

Professor Keith A. Nelson .....
Thesis Supervisor

Professor Andrei Tokmakoff .....

Professor Moungi G. Bawendi .....

Nonlinear terahertz spectroscopy of electronic and vibrational responses in condensed matter systems

by

Harold Young Hwang

Submitted to the Department of Chemistry
on May 16, 2012, in partial fulfillment of the
requirements for the degree of
Doctor of Philosophy

Abstract

In this work, I describe experiments utilizing high-field terahertz (THz) pulses to initiate nonlinear responses in several classes of materials. We have developed several methods for interrogating the nonlinear THz response of materials including collinear and noncollinear THz-pump/THz-probe spectroscopy, and THz-pump/optical probe spectroscopies including THz Kerr effect spectroscopy. We have observed nonlinear free-carrier absorption, occurring through the saturation of free-carrier mobility in bulk semiconductors. We have demonstrated that highly energetic electrons in the conduction band can generate electron-hole pairs in indium antimonide, and have elucidated the dynamics of the carrier generation process. We have observed nonlinear conductivity responses in graphene, showing that a strong THz pulse can heat the electron distribution leading to saturable absorption in the THz range. We have demonstrated THz-induced optical anisotropy in simple liquids, allowing for the measurement of subsequent orientational dynamics. We have driven nonlinear vibrational dynamics in ferroelectrics, demonstrating that the strong anharmonicity of lattice vibrational modes can induce an anisotropic optical response. We have begun to study nonlinear vibrational responses in molecular crystals, which is of importance in mode coupling and energy transfer processes in the THz range. Finally, we have driven nonlinear metamaterial responses in gallium arsenide and vanadium dioxide. In GaAs, we have shown that metamaterial properties may be tuned by an intense THz field if the substrate material (GaAs) is changed by the incident THz pulse, and we have demonstrated carrier multiplication locally in the metamaterial split ring resonator gaps where substantial electric field enhancement occurs. In VO_2, we have shown that THz radiation can drive an insulator-to-metal phase transition, opening up new possibilities in the control of the states of matter with THz fields. This work has demonstrated only a few of the capabilities made possible by the interaction of intense THz radiation with matter, and provides a general framework to open up new research in a nascent field.

Thesis Supervisor: Keith A. Nelson
Title: Professor of Chemistry

Acknowledgements

My graduate work at MIT would not have been a success without my many interactions with fellow colleagues here at MIT and throughout the scientific community. I am particularly indebted to my thesis advisor, Prof. Keith Nelson, whose constant enthusiasm and inquisitive nature have helped drive the research described in this work. I have learned innumerable lessons from him in how to go about curiosity-driven research, and will take that with me wherever I end up. He has kept me in check with a healthy dose of scientific skepticism for which I am grateful, constantly pushing me to think more critically about the scientific questions we are trying to address. I am also indebted to Prof. Andrei Tokmakoff, from whom I learned a great deal about spectroscopy and with whom I have had several interesting conversations about the possibilities of nonlinear spectroscopy.

My fellow colleagues in the Nelson group have been an invaluable resource to draw from. My initial interactions with Team THz have greatly shaped my scientific growth throughout my years here at MIT. Prof. Janos Hebling has provided guidance and wisdom in understanding nonlinear optical principles, and THz propagation. Dr. Matthias Hoffmann was a wonderful mentor and teacher, patiently instilling his years of experience and knowledge. I am still grateful for our continued interaction, including a small stint at his recent appointment at DESY in Hamburg, Germany, before he moved on to SLAC. Dr. Ka-Lo Yeh was an enthusiastic and strongly-willed coworker whose energetic work ethic helped create a good working environment in the lab.

The great group dynamic in the lab has helped me learn and appreciate both the scientific and non-scientific aspects of graduate school. My fellow incoming classmates, Kit Werley, Johanna Wolfson, and Jeremey Johnson have been great resources for support and kindness throughout the years.

Team THz as it exists today—Nate Brandt, Sharly Fleischer, Brad Perkins, Xibin Zhou, Jian Lu, and Hsiang-Yu Yang—have been instrumental in understanding not only how and why we do our work, but also in enjoying my work and having a good time while doing it. Nate has been instrumental in getting the project to its current state. His hard work and dedication to our research was a motivating force in our work together. I will have fond memories of our late nights at LCLS, sleeping in the parking lot and returning to our hotel long after breakfast had ended. Sharly has been a wonderful scientific resource and has added much fun and games to our lab environment. I will remember our Christmas song for many years to come. Brad has been a great coworker always ready to discuss anything that has been on my mind and I highly regard our conversations together. Xibin has been great to work and learn from, with an inquisitive nature that has really stimulated my own understanding of many physical and

chemical phenomena. Jian and Hsiang-Yu are both new to Team THz, and I look forward to seeing what new and interesting directions they will take the project.

My other fellow Nelson group members have also been an important scientific resource and have also provided me with countless laughs and support including Dylan Arias, Patrick Wen, Kara Manke, Steph Teo, Ben Ofori-Okai, David Veysset, Alex Maznev, Felix Hofmann, Jeff Eliason, Sam Teitelbaum, Colby Steiner, and Yongbao Sun.

I would like to thank past Nelson group members, Darius Torchinsky, Eric Statz, Kathy Stone, Christoph Kleiber, and Taeho Shin for their patient teachings and words of wisdom. I am particularly indebted to Darius for his amazing teaching abilities that I take to heart to this day as he continues to explain complex concepts to me in understandable language. I wish him all the best in his future endeavors, and look forward to my continuing interactions with him in the future.

I also have past and present Tokmakoff group members to thank for guiding my understanding of nonlinear spectroscopy including Krupa Ramasesha, Sean Roberts, Ziad Ganim, Josh Lessing, Kevin Jones, and Poul Petersen. In particular, Sean Roberts and Ziad Ganim have had critical roles in my understanding of nonlinear spectroscopy, and no one could have filled in the position of partner in crime for our many investigations into drunken discussions about our projects, science in general, and discovering that there is a world out there that is not based solely on science.

Much of the work in this thesis would not be possible without the strong collaborators we have had the opportunity to work with. Samples in Chapter 6 were fabricated by Jing Kong's group at MIT by Hootan Farhat and Allen Hsu. Samples in Chapter 8 were provided to us by Jean Toulouse and Yehudit Garcia. The results in Chapter 9 were obtained in collaboration with Rick Averitt's group at Boston University. Mengkun Liu was instrumental in not only providing some of the experimental vision for the projects, but also keeping our collaboration alive as we struggled early on to make any sort of progress. Our work together has been enjoyable and I have learned a great deal as a result of our interaction together. Most all my understanding of correlated materials stems from his patient teachings. Our ability to synthesize new ideas together has really helped us make this collaboration a success. Kebin Fan has led the fabrication of all the samples in Chapter 9 and has been instrumental in understanding the GaAs data. I have yet to hear him say 'no' to any fabrication request, and it has been a source of inspiration for me. Aaron Sternbach is an undergraduate in Rick's group who has performed many of the simulations in Chapter 9. I am indebted to his hard work and can-do attitude. Jingdi Zhang is a graduate student that I would like to thank for his help in understanding correlated materials and multiferroics. I look forward to working with all our BU collaborators in the future as the opportunity presents itself.

Furthermore, I would like to thank our collaborators at Stanford University for our couple weeks of experiments at the LCLS. Aaron Lindenberg's group was a pleasure to work with, and Dan Daranciang in particular was a great team member to get our experiments working through the wee hours of the night/morning, as the lack of sleep was painful, yet somehow enjoyable at the same time. It was an exciting couple weeks of hard work to say the least.

I would also like to thank the rest of our collaborators, throughout the years for offering new insights into new systems unknown to me, including: theorists Warren Perger, and Tim Korter, giving me new insights into first principles calculations of low energy vibrations in molecular crystal systems, Darrel Schlom and his student Alex Melville for introducing me to the world of europium oxide and all the rich physics it has to offer, Dan Hooks for his patient and enthusiastic attitude for providing us with the right samples we need to study energetic materials, Hou Tong Chen and Nathaniel Grady for our work together studying nonlinear THz effects in YBCO, and finally Chang-Beom Eom and his post-docs Seung Hyub Baek and Kwang-Hwan Cho for proving samples and guidance in our PMT-PT and ferroelectric switching work that is currently underway.

I would also like to thank my girlfriend, Jennifer Scherer, for her constant support and encouragement. It has made the past year a happy and joyful one.

Most of all, I am thankful for my family and friends—my parents Yun Chong and Young Sook Hwang, and my sisters Nancy and Diana Hwang in particular—whose support and love throughout my life have enabled my pursuit of knowledge, and have also encouraged and fostered it.

Harold Hwang

May 30, 2012

Dedicated to 엄마 and 아빠.

Their love and support throughout my life have made this thesis possible.

Contents

“Think left and think right and think low and think high.

Oh, the thinks you can think up if only you try!”

—Dr. Seuss

Chapter 1

Introduction

The terahertz (THz = 10^{12} Hz) region of the electromagnetic spectrum corresponds to the frequency range of ν = 0.1-10 THz (λ = 3000-30 μm, 1 THz = 1 ps = 10^{-12} s = 33 cm^{-1} = 4 meV = 300 μm). Light at these frequencies lies in between microwave and infrared frequencies. As a result, technologies in this range have been limited since it is in the upper limit of what is possible with electronics and the lower limit of what is possible with optics.

At microwave frequencies, state-of-the-art electronics can now respond on the tens to hundreds of picoseconds timescale, pushing ever farther into the THz range [1, 2]. Optical methods of generating and detecting THz radiation have advanced significantly as well. Though phenomena in this range have long been observed in Fourier-transform infrared spectroscopy [3], research at the lower frequency limits of the THz region (0.1-5 THz) had not come into the popularity it sees today until the development of coherent broadband THz sources in the 1980s from David Auston's research at Bell Laboratories [4-7].

David Auston's work had demonstrated some of the first broadband THz sources, including sources based on phonon-polaritons in $LiTaO_3$, and photoconductive (or Auston) switches. His work pioneered both free-space and polaritonic THz generation and detection platforms. Auston switches and all-optical methods of measuring THz pulses allow for the determination of the full phase and amplitude of the THz electric field. This direct measurement is not possible in other regions of the spectrum where heterodyning is necessary to back out the phase and amplitude of a given light pulse. Auston had also demonstrated one of the first THz time-resolved experiments studying free-carrier absorption in photo-excited GaAs on a picosecond timescale [8].

Including free-carrier absorption, a wide variety of physical phenomena occur at THz energies. As a result, THz spectroscopy has garnered widespread interest as a tool to understand such processes. For example, free carriers in semiconductors can strongly absorb THz radiation and there is a peak in the absorption spectrum of free carriers in doped semiconductors in the THz range [9]. The hydrogen-like impurity states in semiconductors also lie in the THz range along with intersubband transitions in confined semiconductor nanostructures [9, 10]. In molecular systems, rotations and collective vibrations may also occur at THz frequencies. In the solid state, THz frequencies correspond to the energy scales of phonons, magnons—various quasiparticle entities arising from lattice, spin, and electronic degrees of freedom [7, 11-15]. The superconducting gap spans THz energies in many superconducting materials [16, 17] and the continuous conductivity background in several classes of conductors (metal conductors, Mott insulators, magneto-resistive systems, etc) [18, 19] goes through the THz range.

The wealth of systems with both specific and non-specific responses in the THz range has opened up a wealth of research in chemistry and physics. Specifically, the dynamic THz responses of materials following ultrafast optical excitation have been found to provide useful insights in understanding the various systems listed above. Their studies have motivated time-resolved THz spectroscopy, including nonlinear optical-pump/THz-probe spectroscopy [8, 18, 20]. However, studies using a THz field instead of an optical field to initiate a nonlinear change in a material response have been largely limited by technological capabilities.

Until recently, the only ultrafast (femto- to pico-seconds) THz sources available with enough power to generate nonlinear responses were free-electron lasers (FELs). At longer (nano- to micro-second) timescales, with intense THz lasers (often molecular lasers and FELs), several groups have demonstrated THz saturable absorption, dynamical carrier generation via impact ionization, the Poole-Frenkel effect, and classical nonlinear optical phenomena such as second harmonic generation (SHG) [21]. Recent advances in high power ultrafast THz generation [22, 23] have enabled observation of the dynamics of the above processes at the relevant fundamental timescales, and have opened up new possibilities due to the wealth of phenomena at THz energies.

In the low THz range (0.1-3 THz), there have been several demonstrations of nonlinearities in bulk and confined semiconductor structures, nonlinear vibrational absorption, molecular orientation and alignment among other things [21, 24-28]. In the multi-THz range (>10 THz) sometimes classified as long-wavelength IR, nonresonant and resonant effects in semiconductors and superconductors have been observed as well [29, 30].

An alternative to free-space nonlinear THz spectroscopy has been developed in this work using metamaterials. Metamaterials are subwavelength structures engineered to have particular electromagnetic responses [31-33]. Due to the scale invariance of electromagnetism, metamaterials can be designed for any part of the electromagnetic spectrum. The strong response of metamaterials to their environment and their ability to greatly enhance (by orders of magnitude) THz field strengths [34] makes them ideally suited to the study of nonlinear effects in many systems. Experiments involving the interaction of THz material responses with THz metamaterial responses will be discussed later in this work.

In this work, I will present several experiments that have revealed novel responses under THz excitation, probed in a variety of frequency ranges. First, I will discuss THz generation schemes and spectroscopies that have enabled the observation of THz-induced nonlinear phenomena. Then I will present work utilizing our techniques to study electronic nonlinearities, vibrational nonlinearities, and finally, systems where both nonlinear electronic and vibrational responses may be strongly coupled.

This work will demonstrate only some of the scientific capabilities that nonlinear THz spectroscopy has allowed access to. Though still in its infancy, I believe studying nonlinear interactions in the THz range will continue to advance our fundamental understanding of several classes of systems of both basic scientific and practical significance.

References

[1] W. R. Deal. "Solid-state amplifiers for terahertz electronics." *in Microwave Symposium Digest (MTT), 2010 IEEE MTT-S International*,(2010).

[2] L. A. Samoska. "An Overview of Solid-State Integrated Circuit Amplifiers in the Submillimeter-Wave and THz Regime." *Terahertz Science and Technology, IEEE Transactions on*, **1**, 9 (2011).

[3] P. L. Richards. "High-Resolution Fourier Transform Spectroscopy in the Far-Infrared." *J. Opt. Soc. Am.*, **54**, 1474 (1964).

[4] D. H. Auston. "Picosecond optoelectronic switching and gating in silicon." *Applied Physics Letters*, **26**, 101 (1975).

[5] D. H. Auston and K. P. Cheung. "Coherent time-domain far-infrared spectroscopy." *J. Opt. Soc. Am. B*, **2**, 606 (1985).

[6] D. H. Auston, K. P. Cheung, J. A. Valdmanis and D. A. Kleinman. "Cherenkov Radiation from Femtosecond Optical Pulses in Electro-Optic Media." *Physical Review Letters*, **53**, 1555 (1984).

[7] K. P. Cheung and D. H. Auston. "Excitation of Coherent Phonon Polaritons with Femtosecond Optical Pulses." *Physical Review Letters*, **55**, 2152 (1985).

[8] M. C. Nuss, D. H. Auston and F. Capasso. "Direct Subpicosecond Measurement of Carrier Mobility of Photoexcited Electrons in Gallium Arsenide." *Physical Review Letters*, **58**, 2355 (1987).

[9] P. Y. Yu and M. Cardona. **Fundamentals of Semiconductors: Physics and Materials Properties**. (Berlin Heidelberg: Springer) (2010).

[10] C. Luo, K. Reimann, M. Woerner and T. Elsaesser. "Nonlinear terahertz spectroscopy of semiconductor nanostructures." *Applied Physics A: Materials Science & Processing*, **78**, 435 (2004).

[11] M. Schall, M. Walther and P. Uhd Jepsen. "Fundamental and second-order phonon processes in CdTe and ZnTe." *Physical Review B*, **64**, 094301 (2001).

[12] T. Kampfrath, A. Sell, G. Klatt, A. Pashkin, S. Mahrlein, T. Dekorsy, M. Wolf, M. Fiebig, A. Leitenstorfer and R. Huber. "Coherent terahertz control of antiferromagnetic spin waves." *Nat Photon*, **5**, 31 (2011).

[13] N. S. Stoyanov, D. W. Ward, T. Feurer and K. A. Nelson. "Terahertz polariton propagation in patterned materials." *Nat Mater*, **1**, 95 (2002).

[14] M. Wagner, M. Teich, M. Helm and D. Stehr. "Temperature dependence of the intraexcitonic AC Stark effect in semiconductor quantum wells." *Applied Physics Letters*, **100**, 051109 (2012).

[15] P. Gaal, W. Kuehn, K. Reimann, M. Woerner, T. Elsaesser and R. Hey. "Internal motions of a quasiparticle governing its ultrafast nonlinear response." *Nature*, **450**, 1210 (2007).

[16] M. Beck, M. Klammer, S. Lang, P. Leiderer, V. V. Kabanov, G. N. Gol'tsman and J. Demsar. "Energy-Gap Dynamics of Superconducting NbN Thin Films Studied by Time-Resolved Terahertz Spectroscopy." *Physical Review Letters*, **107**, 177007 (2011).

[17] H. J. Choi, D. Roundy, H. Sun, M. L. Cohen and S. G. Louie. "The origin of the anomalous superconducting properties of MgB_2." *Nature*, **418**, 758 (2002).

[18] M. K. Liu, B. Pardo, J. Zhang, M. M. Qazilbash, S. J. Yun, Z. Fei, J.-H. Shin, H.-T. Kim, D. N. Basov and R. D. Averitt. "Photoinduced Phase Transitions by Time-Resolved Far-Infrared Spectroscopy in V_2O_3." *Physical Review Letters*, **107**, 066403 (2011).

[19] A. Pashkin, C. Kübler, H. Ehrke, R. Lopez, A. Halabica, R. F. Haglund, Jr., R. Huber and A. Leitenstorfer. "Ultrafast insulator-metal phase transition in VO_2 studied by multiterahertz spectroscopy." *Physical Review B*, **83**, 195120 (2011).

[20] M. C. Beard, G. M. Turner and C. A. Schmuttenmaer. "Transient photoconductivity in GaAs as measured by time-resolved terahertz spectroscopy." *Physical Review B*, **62**, 15764 (2000).

[21] S. D. Ganichev and W. Prettl. **Intense Terahertz Excitation of Semiconductors**. (USA: Oxford University Press) (2006).

[22] K. L. Yeh, M. C. Hoffmann, J. Hebling and K. A. Nelson. "Generation of 10 μJ ultrashort terahertz pulses by optical rectification." *Applied Physics Letters*, **90**, 171121 (2007).

[23] H. Hirori, A. Doi, F. Blanchard and K. Tanaka. "Single-cycle terahertz pulses with amplitudes exceeding 1 MV/cm generated by optical rectification in $LiNbO_3$." *Applied Physics Letters*, **98**, 091106 (2011).

[24] S. Fleischer, Y. Zhou, R. W. Field and K. A. Nelson. "Molecular Orientation and Alignment by Intense Single-Cycle THz Pulses." *Physical Review Letters*, **107**, 163603 (2011).

[25] J. Hebling, M. C. Hoffmann, H. Y. Hwang, K.-L. Yeh and K. A. Nelson. "Observation of nonequilibrium carrier distribution in Ge, Si, and GaAs by terahertz pump–terahertz probe measurements." *Physical Review B*, **81**, 035201 (2010).

[26] M. C. Hoffmann, J. Hebling, H. Y. Hwang, K.-L. Yeh and K. A. Nelson. "THz-pump/THz-probe spectroscopy of semiconductors at high field strengths [Invited]." *J. Opt. Soc. Am. B*, **26**, A29 (2009).

[27] M. C. Hoffmann, J. Hebling, H. Y. Hwang, K.-L. Yeh and K. A. Nelson. "Impact ionization in InSb probed by terahertz pump—terahertz probe spectroscopy." *Physical Review B*, **79**, 161201 (2009).

[28] M. Jewariya, M. Nagai and K. Tanaka. "Ladder Climbing on the Anharmonic Intermolecular Potential in an Amino Acid Microcrystal via an Intense Monocycle Terahertz Pulse." *Physical Review Letters*, **105**, 203003 (2010).

[29] W. Kuehn, K. Reimann, M. Woerner and T. Elsaesser. "Phase-resolved two-dimensional spectroscopy based on collinear n-wave mixing in the ultrafast time domain." *The Journal of Chemical Physics*, **130**, 164503 (2009).

[30] A. Pashkin, M. Porer, M. Beyer, K. W. Kim, A. Dubroka, C. Bernhard, X. Yao, Y. Dagan, R. Hackl, A. Erb, J. Demsar, R. Huber and A. Leitenstorfer. "Femtosecond Response of Quasiparticles and Phonons in Superconducting $YBa_2Cu_3O_{7-\delta}$ Studied by Wideband Terahertz Spectroscopy." *Physical Review Letters*, **105**, 067001 (2010).

[31] H. Tao, L. R. Chieffo, M. A. Brenckle, S. M. Siebert, M. Liu, A. C. Strikwerda, K. Fan, D. L. Kaplan, X. Zhang, R. D. Averitt and F. G. Omenetto. "Metamaterials on Paper as a Sensing Platform." *Advanced Materials*, **23**, 3197 (2011).

[32] H. Tao, A. C. Strikwerda, K. Fan, W. J. Padilla, X. Zhang and R. D. Averitt. "Reconfigurable Terahertz Metamaterials." *Physical Review Letters*, **103**, 147401 (2009).

[33] H.-T. Chen, W. J. Padilla, J. M. O. Zide, A. C. Gossard, A. J. Taylor and R. D. Averitt. "Active terahertz metamaterial devices." *Nature*, **444**, 597 (2006).

[34] C. A. Werley, K. Fan, A. C. Strikwerda, S. M. Teo, X. Zhang, R. D. Averitt and K. A. Nelson. "Time-resolved imaging of near-fields in THz antennas and direct quantitative measurement of field enhancements." *Opt. Express*, **20**, 8551 (2012).

Chapter 2

THz Generation and Detection

The field of nonlinear optics has enabled spectroscopies in several portions of the electromagnetic spectrum. Nonlinear spectroscopies in the mid-IR to the ultraviolet (UV) make use of pulses generated through nonlinear optical processes—from parametric amplification [1-3] to high harmonic generation [4, 5]. The first demonstrations of nonlinear optics followed shortly after the invention of the laser—which provided the high intensities of light required to drive nonlinear optical processes—in the form of second harmonic generation [6]. The first demonstrations of optical rectification followed soon thereafter [7], forming the basis for broadband THz generation. In this chapter, I will discuss nonlinear optical methods for generating THz radiation, which have been incorporated in nonlinear THz spectroscopic methodologies described later in this work. Then I will describe ultrafast methods for THz detection in a related process—electro-optic sampling—which allows for the measurement of the full amplitude and phase of a THz pulse.

2.1 Optical Rectification

Nonlinear optical processes may be described perturbatively through an expansion of the polarization, *P*, of a material in the light-matter interaction [8]

$$P(t) = \chi^{(1)}E(t) + \chi^{(2)}E^2(t) + \chi^{(3)}E^3(t) + \cdots \qquad (1)$$

where $\chi^{(n)}$ is the susceptibility, and *E(t)* is the electric field. $\chi^{(1)}$ forms the linear response term for the polarization, which dominates the expansion at low light intensity. At high intensities, the higher order terms of the expansion become significant. Perturbative optical nonlinearities may be accounted for by considering the dependence of the polarization on the field. For example, in second order processes ($\chi^{(2)}$), the polarization scales as the square of the incident electric field.

Both second harmonic generation (SHG) and optical rectification are second order nonlinear optical processes. Whereas SHG can be described as a process where two interactions between the incident light field and matter give $\chi^{(2)}(2\omega_0 : \omega_0 + \omega_0)$—two fields at a frequency ω_0 yield one field at twice the frequency $2\omega_0$—optical rectification is a process where two interactions between the incident light field and matter give $\chi^{(2)}(0 : \omega_0 - \omega_0)$—two fields at a frequency ω_0 yield one field at 'zero' frequency. In the far-field, since the emitted light must integrate to zero as a result of Maxwell's equations, optical rectification with ultrashort optical pulses gives rise to ultrashort pulses with bandwidths in the THz range.

Whereas SHG is a special case of sum frequency generation, optical rectification is a special case of difference frequency generation. As a result, THz generation by optical rectification may be thought of as a process where different frequencies within the bandwidth

of the optical generation pulse mix, forming light at the difference frequency. As such, typical bandwidths of ultrashort THz pulses generated by optical rectification are limited by the generation pulse bandwidth. However, the bandwidth of ultrashort THz pulses is often limited by the material response of the generation crystal, where strong lattice phonon absorptions tend to give bandwidths less than the transform-limited bandwidth.

Several materials have proved useful for optical rectification, resulting in generation of light pulses with bandwidths throughout the THz region of the spectrum. In this section, I will describe THz generation in the nonlinear crystals zinc telluride (ZnTe) and lithium niobate ($LiNbO_3$, LN).

2.1.1 Collinearly Phase-Matched THz Generation in Zinc Telluride

Conventional THz time domain spectroscopy makes use of relatively weak THz pulses generated in either ZnTe, or photoconductive (Auston) switches. In this section, I will focus on THz generation by optical rectification in ZnTe.

ZnTe has been used for THz generation due to its nonlinear properties and the fact that simple, collinear THz-optical phase matching can be achieved in fairly thick crystals. The second order nonlinear polarization for optical rectification is described by

$$P^{(2)} = \chi^{(2)} E E^* \qquad (2)$$

The subsequent radiated field is related to the second order polarization by a second derivative [9]. Since femtosecond pulses can typically be described with Gaussian envelope functions, the resulting emitted THz electric field from optical rectification is the so-called Mexican hat function (second derivative of a Gaussian).

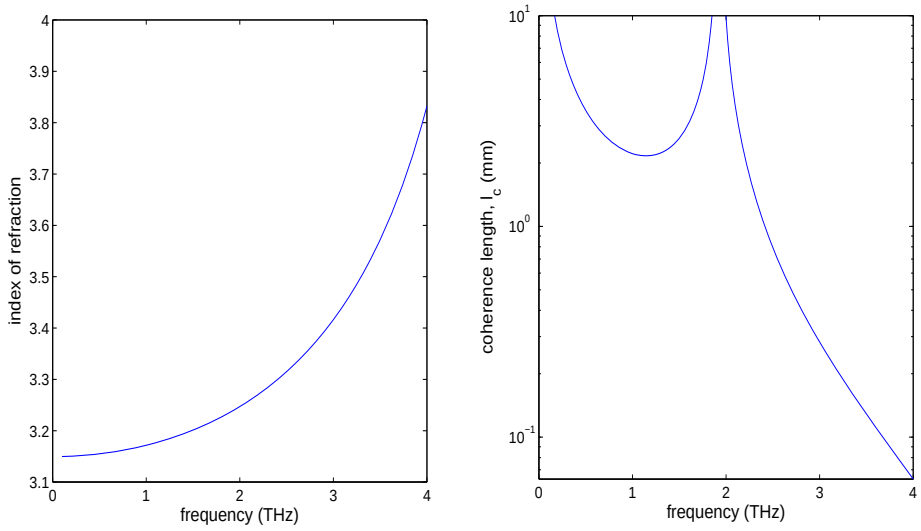

Figure 1: THz index of refraction and coherence length in ZnTe. **(a)** THz index of refraction from 0-4 THz. There is significant dispersion over the range due to a strong 4 THz phonon mode in ZnTe. **(b)** Coherence length calculation where the phase matching is determined by the difference between the group index of the optical generation pulse at 800 nm and the THz index. For 1 mm thick ZnTe crystals, effective phase matching occurs up to about 2.5 THz.

As discussed above, ultrashort THz pulses generated by optical rectification are typically limited by the material response. For the broad bandwidth that can be achieved with femtosecond pulses, it can be difficult to phase match the entire available THz bandwidth. This is due to strong phonon absorptions in the nonlinear crystal, which introduces significant dispersion near phonon resonances, and which lie in the THz range. A coherence length calculation (figure Figure 1) in ZnTe shows that it is difficult to generate THz frequencies above about 3 THz in crystals as thick as 1 mm [10]

$$l_c = \frac{\pi c}{\omega_{THz}\left|n_{opt} - \lambda_{opt}\frac{dn_{opt}(\lambda_{opt})}{d\lambda} - n_{THz}(\omega)\right|} \qquad (3)$$

where l_c is the coherence length, $n_{opt} - \lambda_{opt}\frac{dn_{opt}(\lambda_{opt})}{d\lambda}$ is the optical group index ($n_{opt} - \lambda_{opt}\frac{dn_{opt}(\lambda_{opt})}{d\lambda} = 2.85 + 0.48 = 3.34$ at 800 nm since the group velocity of the optical pulse, and not its phase, needs to travel with the phase of the generated THz pulse), and $n_{THz} = \sqrt{(289.27 - \frac{6\omega_{THz}^2}{4\pi^2})/(29.16 - \frac{\omega_{THz}^2}{4\pi^2})}$ [10] is the THz index of refraction.

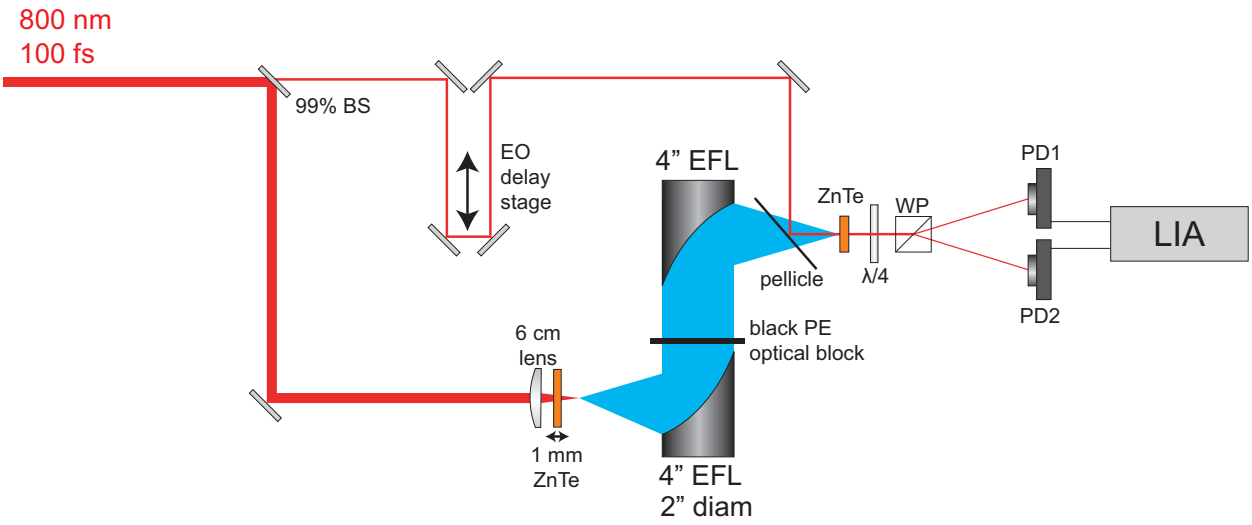

Figure 2: ZnTe THz generation and electro-optic THz detection setup. A femtosecond 800 nm optical pulse generates THz pulses by optical rectification in ZnTe. The optical beam is filtered from the generated THz pulse with an opaque piece of black polyethylene, and an electro-optic sampling pulse is split off early to detect the THz pulse at a focus in an electro-optic crystal. In this case, the electro-optic crystal is ZnTe as well.

The experimental setup for THz generation by optical rectification in ZnTe is illustrated in figure 2. Collinearly phase matched THz generation results in a straightforward experimental setup, where a femtosecond optical pulse pumps a nonlinear THz generation crystal. After the femtosecond pulse exits the nonlinear generation crystal, the optical pump is blocked and the emitted THz field is directed onto an electro-optic sampling crystal for detection.

The details of electro-optic sampling will be discussed later in this chapter. Figure 3 illustrates the results from a typical ZnTe generation scheme in a 1 mm thick crystal. The spectrum extends to about 2.5 THz. The dips in the spectrum correspond to rotational modes of water vapor in the air over the THz beam path.

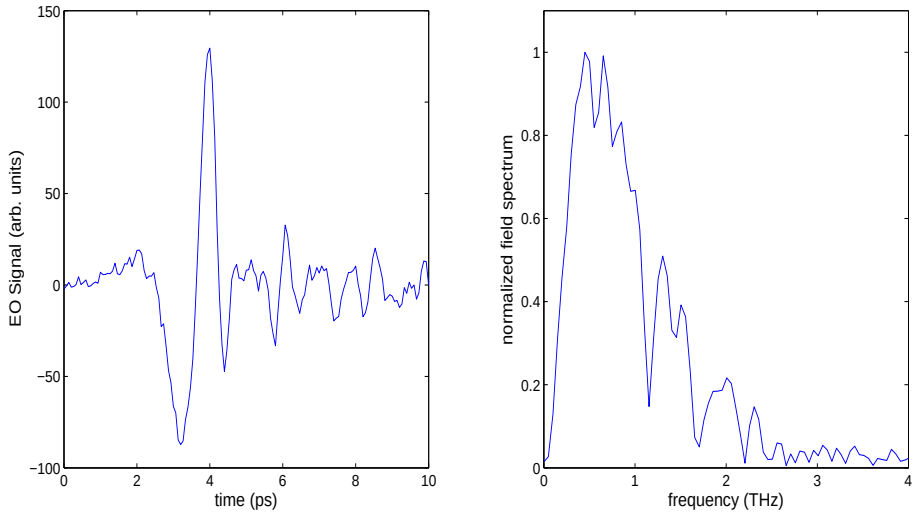

Figure 3: THz electric field generated in a 1 mm thick ZnTe crystal measured by electro-optic sampling. **(left)** The THz electric field in the time domain from generation in ZnTe. The oscillations after the THz pulse are from the free-induction decay (FID) of water vapor rotations in the air. **(right)** The Fourier-transform amplitude spectrum of the THz pulse. The dips in the spectrum correspond to the water rotational modes. The spectrum extends to about 2.5 THz.

THz generation in ZnTe is a straightforward method due to the collinear phase matching considerations, yielding pulses up to about 2.5 THz limited ultimately by the phase-matching of the optical pump and generated THz fields (due to the material response of the ZnTe generation crystal). However, pulses generated with this method cannot provide large fields (> 100 kV/cm) unless large-area crystals are utilized [11, 12], since multiphoton absorption leads to a saturation of the generation efficiency at higher pump fluences [13]. For efficient high-field THz generation, we must use crystals that can generate THz radiation more efficiently. This

requires a novel phase matching scheme in the nonlinear crystal, lithium niobate (LN), which has a larger second-order nonlinear coefficient for optical rectification.

2.1.2 Noncollinearly Phase-Matched THz Generation in Lithium Niobate: Tilted Pulse Front Generation

The breakthrough that has enabled nonlinear THz spectroscopies has been high-field THz generation in lithium niobate [14, 15]. LN has a much larger nonlinear optical coefficient for optical rectification. However, there is a fundamental problem with generating THz pulses in lithium niobate due to the large mismatch between the phase velocity of the generated THz pulse and the group velocity of the optical pump pulse [14, 16, 17]. This is analogous to an acoustic wave front propagating from a body moving faster than the speed of sound. Since the optical generation pulse propagates faster than the generated THz pulse (figure 4), the generated THz pulse travels at an angle with respect to the propagation vector of the optical pulse, just as an acoustic wavefront propagates at an angle with respect to a body moving faster than the speed of sound. This is called Cherenkov radiation, and this limits the phase, or velocity, matching in optical rectification in LN. To overcome this limitation, velocity matching of the THz and optical pulses have been achieved with tilted pulse front (TPF) excitation.

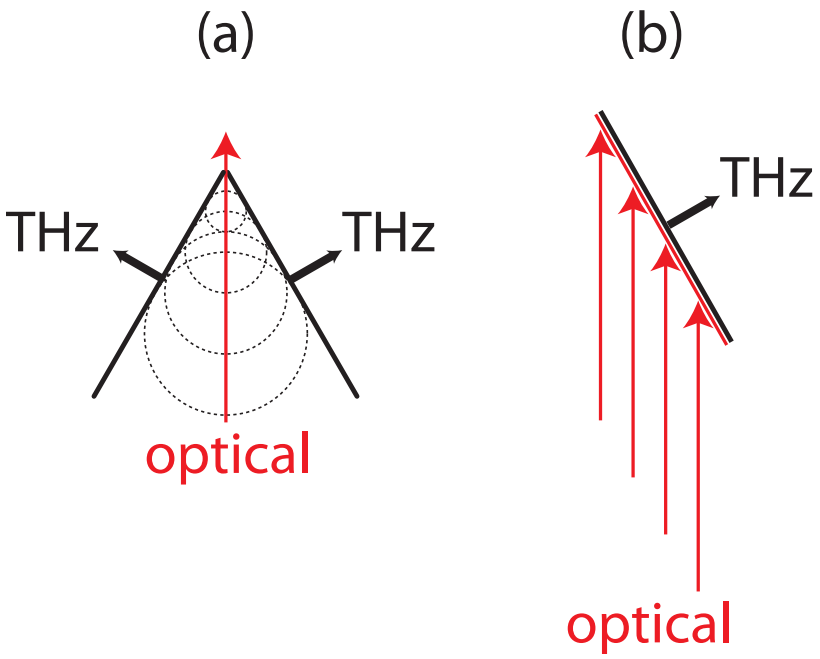

Figure 4: Cherenkov radiation from optical rectification in LN. **(a)** When an optical pulse propagates (vertical axis) through lithium niobate, the velocity mismatch between the optical pump pulse and the generated THz pulse causes the THz pulse to propagate at an angle with respect to the optical pulse. **(b)** With tilted pulse front excitation, half of the Cherenkov cone is velocity matched with the optical by tilting the intensity front of the optical pulse with a grating.

For TPF, the optical intensity front is tilted with a grating and subsequently imaged onto a lithium niobate prism, such that one half of the generated Cherenkov cone co-propagates with the optical pulse (figure 4b). As a result, the generated THz radiation is coherently summed as it propagates in the prism. An in-depth description of the generation process is given in [18]. The TPF generation scheme is illustrated in figure 5.

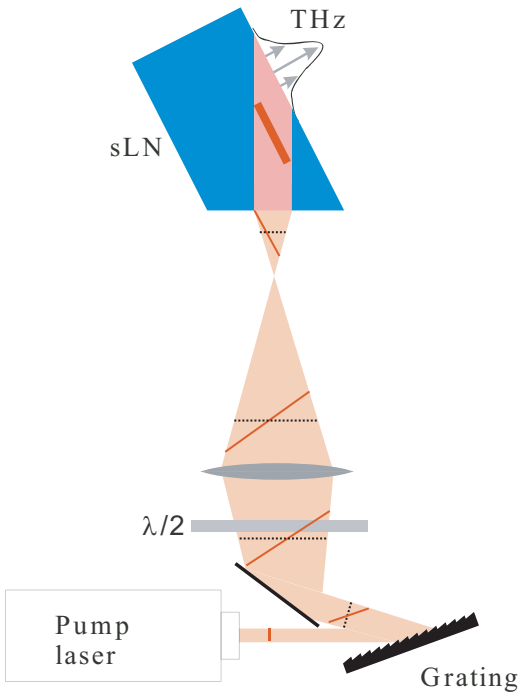

Figure 5: Tilted pulse front THz generation scheme. The intensity front is tilted by a grating. The tilted angle is fine-tuned with a single lens. The one lens image temporally focuses the femtosecond pulse as well as tunes the tilt angle in space to achieve noncollinear velocity matching of the optical and generated THz pulses in the LN prism. The red lines in the width of the beam are cartoon indications of the tilt of the intensity front of the optical pulse throughout the setup.

With TPF excitation, THz generation efficiencies have been demonstrated to be about 0.1% in energy, and THz pulse energies as high as 40 μJ with a 40 mJ 800 nm pump at 10 Hz repetition rate have been achieved. For the nonlinear measurements described in this work, 1.5-7.5 μJ THz pulses have generated with 5-7.5 mJ 800 nm pump pulses at 1 kHz repetition rate with pulse durations of 35 and 100 fs. Figure 6 is a plot of a typical THz pulse generated by TPF excitation along with its bandwidth. The bandwidth is similar to that with optical rectification in 1 mm thick ZnTe.

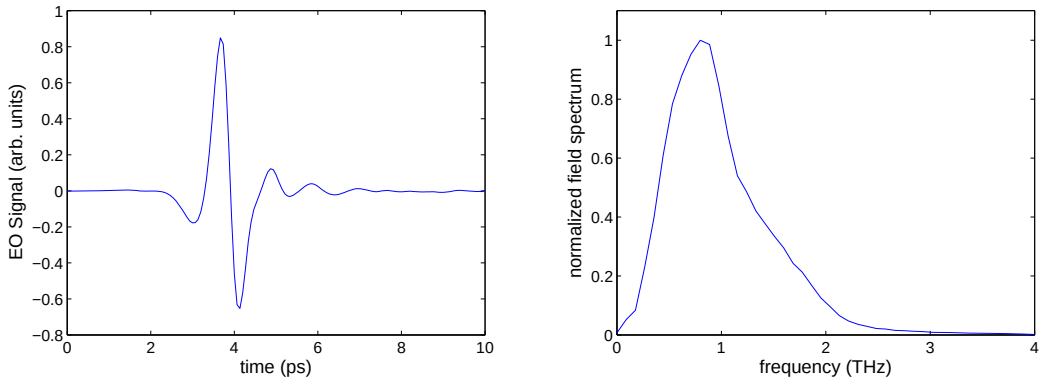

Figure 6: THz electric field obtained from tilted pulse front excitation in LN. (left) The time-domain THz electric field. (right) The Fourier-transform amplitude spectrum. The spectrum extends to about 2.5 THz in this case.

2.2 Broadband THz Generation in a Two-Color Plasma

Optical rectification schemes for THz generation have been found to be quite useful for bandwidths up to a few THz. However, all optical rectification methods are ultimately limited by the material response, where phonon dispersion and absorption limit the bandwidth of the generated THz pulses. Most efficient nonlinear optical crystals exhibit strong responses above a few THz. However, recent breakthroughs in THz generation from a plasma in air have opened up the THz spectrum through to the mid-IR [19-22]. Many studies have aided in the development of ultrabroadband THz sources from an air plasma [23-26]. With this method, there are no strong absorptions that limit the spectral bandwidth, since the generation scheme relies on tunnel ionization where liberated electrons are accelerated in the laser field. With this method, a femtosecond laser pulse is mixed with its second harmonic to introduce an asymmetry in the pumping electric field which subsequently generates a local nonlinear current in the plasma that radiates an ultrashort THz pulse. Though large peak electric fields (> 100

kV/cm) have been measured with this method, the extreme broad bandwidth of the radiated field results in relatively weak spectral brightness at a given frequency.

The generation scheme is illustrated in figure 7. An 800 nm femtosecond optical pulse is passed through a barium borate (BBO) crystal to generate the second harmonic at 400 nm. The copropagating fundamental and second harmonic are focused in air to form a plasma, where the pulse fluence is above the ionization threshold of air. Imaging the plasma focus onto an electro-optic crystal allows for the measurement of the emitted THz field by electro-optic sampling. With electro-optic sampling, the detected bandwidth is limited by the gate pulse duration (discussed in the next section) and the material response. Typically, the material response is the main limiting factor for measurement of the detection bandwidth.

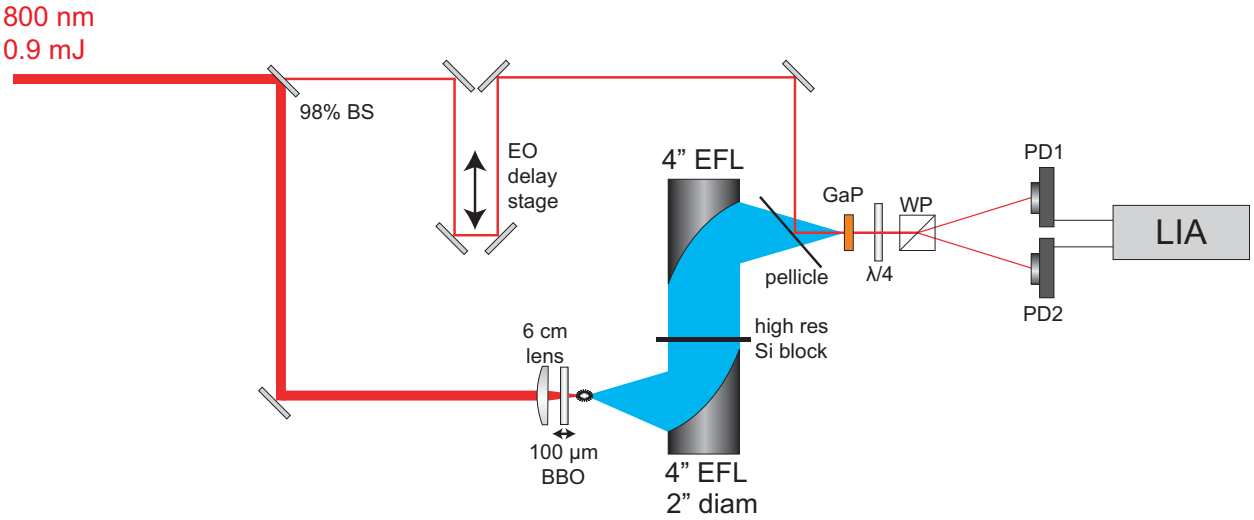

Figure 7: Two-color plasma generation setup. A femtosecond (100 or 35 fs) 800 nm, 0.9 mJ pulse is passed through a BBO crystal to generate the second harmonic. The fundamental and second harmonic are focused in air to form a two-color plasma, which radiates an ultrabroadband THz pulse. The optical light is filtered from the THz pulse with a high-resistivity silicon wafer, and the transmitted THz pulse is measured with electro-optic detection in GaP.

More recent studies have used the air plasma to subsequently measure the THz pulse as well [27, 28]. In this case, since the plasma response is frequency-independent for the relevant frequency range, the coherent detection of the generated ultrabroadband THz pulse is limited by the gate pulse duration only.

Figure 8 is a typical THz pulse generated by a two-color plasma in air, measured with gallium phosphide (GaP) as the electro-optic crystal. The detection bandwidth is limited by the GaP which exhibits a strong phonon absorption near 8 THz [26]. If ZnTe is used as the electro-optic detection crystal instead, the detection bandwidth is limited to below 4 THz (ZnTe has a strong 4 THz phonon mode). This generation and detection scheme can be used in a non-degenerate THz pump-probe setup where modulations of higher lying THz spectral responses can be probed following excitation with a strong THz pulse generated in LN using the tilted pulse front.

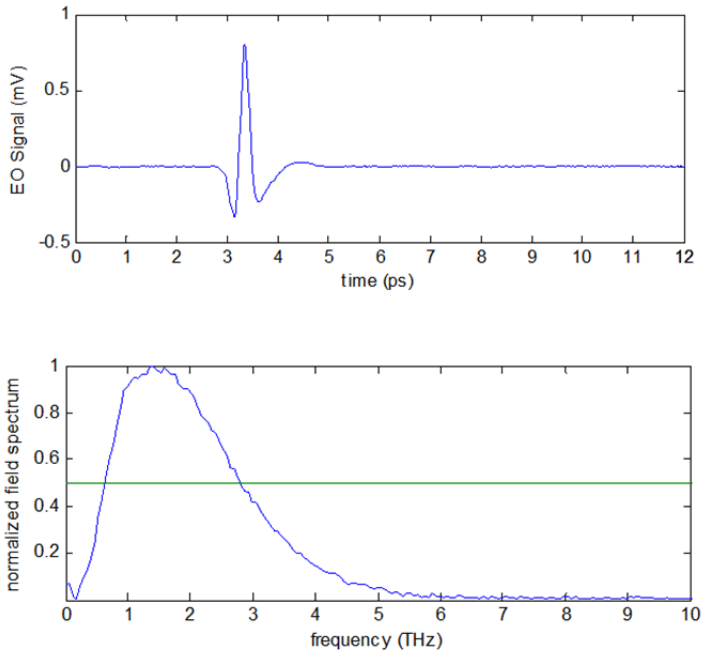

Figure 8: THz pulse generated by a two-color plasma. The pulse was measured with electro-optic sampling in GaP. The bandwidth extends to about 6 THz.

2.3 Electro-optic Sampling

We have discussed several methods for generating ultrashort THz pulses by a variety of methods. In this section, I will discuss the detection of ultrashort THz pulses by electro-optic sampling. A unique feature of THz spectroscopy is the measurement of the full amplitude and phase of the THz pulse. We can achieve this with electro-optic sampling, which relies on the linear Pockels effect where the polarization of an optical pulse may be modulated by the THz pulse. In the Pockels effect [8], a DC field can modulate the polarization of an optical pulse. Since the generated THz pulse is much longer in time than the optical generation pulse (figure 9), we can use the femtosecond optical pulse to gate the THz pulse in time. The THz electric field is averaged over the duration of the optical gate pulse (figure 9). At sufficiently low THz electric fields, the polarization modulation is linearly proportional to the THz electric field in zinc blend crystals [29, 30]

$$\frac{\Delta I}{I} = \lim_{\Delta I \to 0} sin\left(\frac{\omega n^3 E_{THz} r_{41} L}{c}\right) = \frac{\omega n^3 E_{THz} r_{41} L}{c} \qquad (4)$$

where $\Delta I/I$ is the difference in intensity of the two photodiodes in figures 2 & 7 normalized to their sum, ω is the optical angular frequency, *n* is the refractive index of the electro-optic crystal at the optical frequency, E_{THz} is the THz electric field, r_{41} is the electro-optic tensor element used for <110> oriented zinc blend crystals, *L* is the thickness of the electro-optic crystal, and *c* is the speed of light in vacuum. For simplicity, small $\Delta I/I$ is preferred such that linearity can be assumed. We can easily stay in the linear regime with attenuators in the THz beam path when the THz electric field is large. The above equation has been derived

considering zinc blend electro-optic crystals when the THz and optical gate pulse are co- or cross-polarized [29, 30].

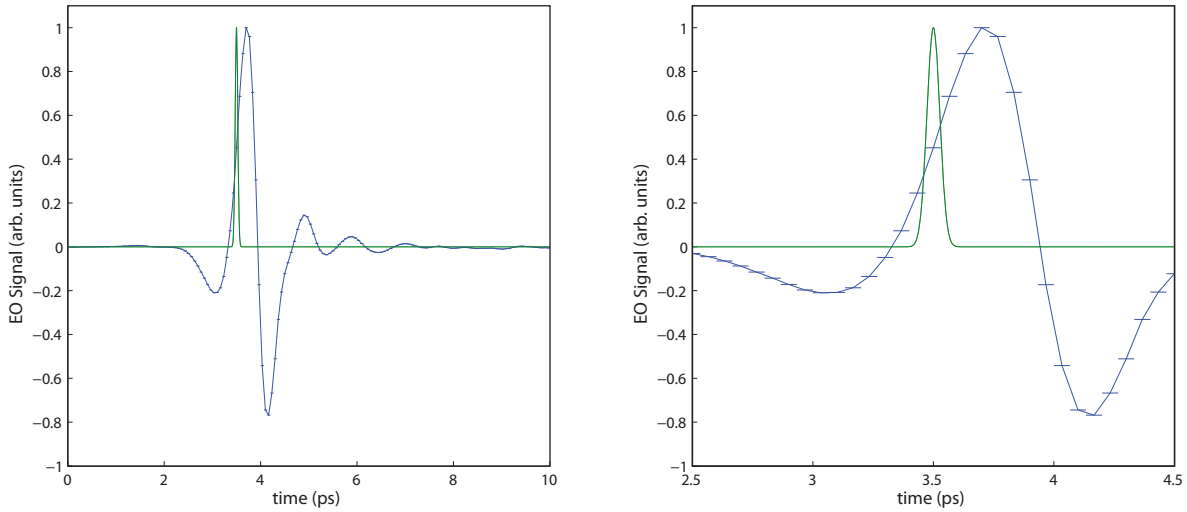

Figure 9: Electro-optic sampling measurement of the THz electric field generated by TPF. The THz pulse is depicted in blue, and the optical gate pulse is a Gaussian with duration ~70 fs (green). The electro-optic effect may be thought of as a quasi-DC electric field averaged over the duration of the gate for each THz-optical gate delay time. The THz electric field can be mapped out by variably delaying the optical gate with respect to the THz pulse.

By spatially overlapping a THz field with an optical gate (figure 2 & 7) at a recombination optic—in this case a pellicle beam splitter that is transparent to the THz and partially reflecting to the optical—and by variably delaying the optical gate pulse with respect to the THz pulse, we can measure the temporal profile of the THz electric field. The polarization rotation is measured by a balanced detection system [29, 30] where the rotated optical gate pulse is passed through a quarter waveplate—such that the pulse is elliptically polarized, instead of circularly polarized without any polarization modulation—and then a Wollaston prism is used to separate out the different polarizations. Each polarization is detected with a photodiode, and the difference

signal is the balanced polarization modulation. Since the THz pulse is optically gated, the inherent limit in the detection bandwidth corresponds to the pulse width of the optical gate. Typically, for optical rectification in nonlinear crystals, the material response supports a bandwidth smaller than the bandwidth of the optical gating pulse.

2.3.1 Optical Gate Duration Effects in Electro-optic Sampling

The optical gate duration may affect the measurement of a THz pulse if the duration of the gate is comparable to one lobe of the THz pulse. We can think of this effect as a simple convolution of the THz electric field with the optical gating pulse: $E_{THz}^{measured} = E_{THz} \otimes E_{gate}$ (figure 10). Since the THz detection bandwidth is typically limited by the electro-optic crystal response, a longer gate pulse yields a lower measured peak THz electric field.

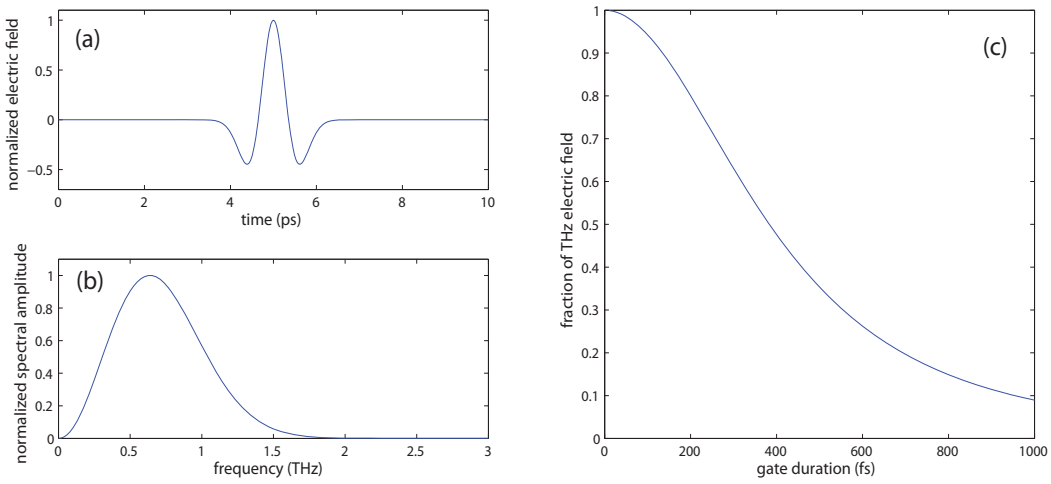

Figure 10: Effect of optical gate pulse duration on electro-optic sampling peak field. **(a)** An idealized THz pulse (second derivative of a Gaussian). **(b)** Amplitude spectrum of the THz pulse in (a). **(c)** Fraction of the peak electric field after convolution of the THz pulse with a Gaussian optical gate pulse. The duration of the optical gate is on the horizontal axis. The vertical axis is the fraction of the THz peak field strength given after convolution with the optical gate pulse.

Assuming a linear response in the electro-optic detection, and since the optimal pulse duration for the highest generation efficiency may not be transform-limited, this may affect the quantitative measurement of peak THz electric fields (a small portion of the optical generation pulse is typically split off to use for electro-optic sampling). For example, if the gate pulse is 200 fs and the THz pulse in figure 10a is being measured with electro-optic sampling, the measured peak electric field will be 80% of the actual electric field (the measured field by electro-optic sampling with a delta function gate pulse). A solution to this problem is to use shorter pulses for electro-optic detection with compressed pulses from the oscillator seed for the laser amplifier [31].

2.4 Conclusions

Several advances in THz generation have opened up new spectroscopic capabilities in the THz range. In particular, nonlinear THz spectroscopy has been made possible by the generation of high-field THz pulses in LN with TPF. We are interested in the dynamic responses initiated by strong THz electric fields, and as a result, we can incorporate the different THz generation schemes to design nonlinear THz spectrometers with probes throughout the THz to mid-IR and optical ranges. These spectroscopies will be discussed in more detail in chapter 4.

References

[1] D. Brida, C. Manzoni, G. Cirmi, M. Marangoni, S. De Silvestri and G. Cerullo. "Generation of broadband mid-infrared pulsesfrom an optical parametric amplifier." *Opt. Express*, **15**, 15035 (2007).

[2] C. J. Fecko, J. J. Loparo and A. Tokmakoff. "Generation of 45 femtosecond pulses at 3 µm with a $KNbO_3$ optical parametric amplifier." *Optics Communications*, **241**, 521 (2004).

[3] G. Schweitzer, L. Xu, B. Craig and F. C. DeSchryver. "A double OPA femtosecond laser system for transient absorption spectroscopy." *Optics Communications*, **142**, 283 (1997).

[4] P. B. Corkum and F. Krausz. "Attosecond science." *Nat Phys*, **3**, 381 (2007).

[5] T. Brabec and F. Krausz. "Intense few-cycle laser fields: Frontiers of nonlinear optics." *Reviews of Modern Physics*, **72**, 545 (2000).

[6] P. A. Franken, A. E. Hill, C. W. Peters and G. Weinreich. "Generation of Optical Harmonics." *Physical Review Letters*, **7**, 118 (1961).

[7] M. Bass, P. A. Franken, J. F. Ward and G. Weinreich. "Optical Rectification." *Physical Review Letters*, **9**, 446 (1962).

[8] R. W. Boyd. **Nonlinear Optics**. (San Diego, USA: Elsevier Science) (2003).

[9] I. Wilke and S. Sengupta. "Nonlinear optical techniques for terahertz pulse generation and detection - optical rectification and electrooptic sampling." *in* Terahertz Spectroscopy: Principles and Applications. edited by S. L. Dexheimer (CRC Press 2007).

[10] A. Nahata, A. S. Weling and T. F. Heinz. "A wideband coherent terahertz spectroscopy system using optical rectification and electro-optic sampling." *Applied Physics Letters*, **69**, 2321 (1996).

[11] T. Löffler, T. Hahn, M. Thomson, F. Jacob and H. Roskos. "Large-area electro-optic ZnTe terahertz emitters." *Opt. Express*, **13**, 5353 (2005).

[12] F. Blanchard, L. Razzari, H. C. Bandulet, G. Sharma, R. Morandotti, J. C. Kieffer, T. Ozaki, M. Reid, H. F. Tiedje, H. K. Haugen and F. A. Hegmann. "Generation of 1.5 μJ single-cycle terahertz pulses by optical rectification from a large aperture ZnTe crystal." *Opt. Express*, **15**, 13212 (2007).

[13] M. C. Hoffmann, K.-L. Yeh, J. Hebling and K. A. Nelson. "Efficient terahertz generation by optical rectification at 1035 nm." *Opt. Express*, **15**, 11706 (2007).

[14] K. L. Yeh, M. C. Hoffmann, J. Hebling and K. A. Nelson. "Generation of 10 μJ ultrashort terahertz pulses by optical rectification." *Applied Physics Letters*, **90**, 171121 (2007).

[15] H. Hirori, A. Doi, F. Blanchard and K. Tanaka. "Single-cycle terahertz pulses with amplitudes exceeding 1 MV/cm generated by optical rectification in $LiNbO_3$." *Applied Physics Letters*, **98**, 091106 (2011).

[16] D. H. Auston, K. P. Cheung, J. A. Valdmanis and D. A. Kleinman. "Cherenkov Radiation from Femtosecond Optical Pulses in Electro-Optic Media." *Physical Review Letters*, **53**, 1555 (1984).

[17] J. Hebling, G. Almasi, I. Kozma and J. Kuhl. "Velocity matching by pulse front tilting for large area THz-pulse generation." *Opt. Express*, **10**, 1161 (2002).

[18] K.-L. Yeh. "The generation of high field terahertz radiation and its application in terahertz nonlinear spectroscopy." (*PhD*) Department of Chemistry, Massachusetts Institute of Technology: Cambridge, MA (2009).

[19] K. Y. Kim, A. J. Taylor, J. H. Glownia and RodriguezG. "Coherent control of terahertz supercontinuum generation in ultrafast laser-gas interactions." *Nat Photon*, **2**, 605 (2008).

[20] M. D. Thomson, V. Blank and H. G. Roskos. "Terahertz white-light pulsesfrom an air plasma photo-inducedby incommensurate two-color opticalfields." *Opt. Express*, **18**, 23173 (2010).

[21] P. B. Petersen and A. Tokmakoff. "Source for ultrafast continuum infrared and terahertz radiation." *Opt. Lett.*, **35**, 1962 (2010).

[22] T. Fuji and T. Suzuki. "Generation of sub-two-cycle mid-infrared pulses by four-wave mixing through filamentation in air." *Opt. Lett.*, **32**, 3330 (2007).

[23] D. J. Cook and R. M. Hochstrasser. "Intense terahertz pulses by four-wave rectification in air." *Opt. Lett.*, **25**, 1210 (2000).

[24] M. Kress, T. Löffler, S. Eden, M. Thomson and H. G. Roskos. "Terahertz-pulse generation by photoionization of airwith laser pulses composed of both fundamental and second-harmonicwaves." *Opt. Lett.*, **29**, 1120 (2004).

[25] X. Xie, J. Dai and X. C. Zhang. "Coherent Control of THz Wave Generation in Ambient Air." *Physical Review Letters*, **96**, 075005 (2006).

[26] T. Bartel, P. Gaal, K. Reimann, M. Woerner and T. Elsaesser. "Generation of single-cycle THz transients with high electric-field amplitudes." *Opt. Lett.*, **30**, 2805 (2005).

[27] J. Dai, X. Xie and X. C. Zhang. "Detection of Broadband Terahertz Waves with a Laser-Induced Plasma in Gases." *Physical Review Letters*, **97**, 103903 (2006).

[28] N. Karpowicz, J. Dai, X. Lu, Y. Chen, M. Yamaguchi, H. Zhao, X. C. Zhang, L. Zhang, C. Zhang, M. Price-Gallagher, C. Fletcher, O. Mamer, A. Lesimple and K. Johnson. "Coherent heterodyne time-domain spectrometry covering the entire ``terahertz gap''." *Applied Physics Letters*, **92**, 011131 (2008).

[29] P. C. M. Planken, H.-K. Nienhuys, H. J. Bakker and T. Wenckebach. "Measurement and calculation of the orientation dependence of terahertz pulse detection in ZnTe." *J. Opt. Soc. Am. B*, **18**, 313 (2001).

[30] N. C. J. van der Valk, T. Wenckebach and P. C. M. Planken. "Full mathematical description of electro-optic detection in optically isotropic crystals." *J. Opt. Soc. Am. B*, **21**, 622 (2004).

[31] K. Reimann, R. P. Smith, A. M. Weiner, T. Elsaesser and M. Woerner. "Direct field-resolved detection of terahertz transients with amplitudes of megavolts per centimeter." *Opt. Lett.*, **28**, 471 (2003).

Chapter 3

Data Analysis

In the previous chapter I discussed methods for generating and detecting ultrafast THz pulses. When interrogating samples with THz radiation, we need a way to take the measured information (the THz electric field) and turn it into something useful. Since we measure the amplitude and phase of a THz electric field, we can extract useful physical quantities. Typically, these are the complex index, which by arithmetic manipulation is related to the complex dielectric function or complex conductivity. I will focus on the extraction of the complex index for a transmission measurement with an air reference. Then I will briefly describe how to extract the same parameters on thin film samples. Finally, I will describe how to fit our THz dynamic measurements to various decay functions.

3.1 Extracting Complex Material Parameters in Transmission Experiments

For THz transmission experiments, we measure the THz electric field after it passes through a sample and then compare the transmitted THz field to a reference field, which is typically that of the same pulse that has passed through only air. Comparing the frequency dependent responses after Fourier transformation allows us to extract the complex index.

3.1.1 THz Transmission

We measure the THz electric field in our experiments. The frequency dependence of the transmission through a sample can easily be obtained by Fourier transformation of the reference THz electric field $E_{ref}(t)$ and the THz field transmitted through a sample $E_{sam}(t)$ by the following expression

$$T_E(\omega) = \frac{\left|\int_{-\infty}^{\infty} E_{sam}(t)e^{-i\omega t}dt\right|}{\left|\int_{-\infty}^{\infty} E_{ref}(t)e^{-i\omega t}dt\right|} \qquad (1)$$

where $T_E(\omega)$ is the field transmission, and $\left|\int_{-\infty}^{\infty} E(t)e^{-i\omega t}dt\right|$ is the amplitude of the Fourier transform of the reference or sample field. The power transmission $T_P(\omega)$ is simply given by the square of the field transmission

$$T_P(\omega) = [T_E(\omega)]^2 = \frac{\left|\int_{-\infty}^{\infty} E_{sam}(t)e^{-i\omega t}dt\right|^2}{\left|\int_{-\infty}^{\infty} E_{ref}(t)e^{-i\omega t}dt\right|^2} \qquad (2)$$

This may in turn be related to the absorbance $A(\omega)$ by

$$A(\omega) = -\ln(T_P(\omega)) \qquad (3)$$

In some experiments, we are interested in averaging transmission effects over the entire spectrum, which we call the integrated transmission $\langle T \rangle$

$$\langle T \rangle = \frac{\int_{-\infty}^{\infty} E_{sam}^2(t)dt}{\int_{-\infty}^{\infty} E_{ref}^2(t)dt} \qquad (4)$$

which can be related to an averaged absorption over the bandwidth (α_{eff}) by:

$$\alpha_{eff} = -\frac{1}{d} ln\left(\frac{(\langle n \rangle - 1)^2}{(\langle n \rangle + 1)^2} \cdot \langle T \rangle\right) \qquad (5)$$

where *d* is the thickness of the sample and $\langle n \rangle$ is the average index over the bandwidth given by the time delay of the main pulse through the sample $\langle n \rangle = \frac{c \cdot \tau_{delay}}{d}$, where *c* is the speed of light in vacuum and τ_{delay} is the delay of the pulse compared to that of the reference THz electric field. The factor before the averaged transmission comes from the Fresnel equations for reflection losses. For experiments where air is not the reference, the 1 in equation 5 is replaced by the refractive index of the reference material.

3.1.2 Complex Index of Refraction and the Absorption Coefficient

The derivation for the extraction of the complex index from experimental determination of a THz electric field passing through a sample is taken largely from [1]. The transmission calculated above only takes advantage of the amplitude of the Fourier transform of the THz electric fields. However, we can also make use of the phase of the Fourier transform to extract the full complex index of refraction of the sample material

$$\hat{n} = n + i\kappa \qquad (6)$$

where *n* is the real index of refraction and *κ* is the extinction coefficient. If a plane wave $E(z,t) = E_0 e^{i(kz-\omega t)}$ is travelling through a medium with complex index $\hat{n}$, with $k = \frac{n\omega}{c} = (n + i\kappa)\frac{\omega}{c}$, the intensity is given by

$$I \propto EE^* = E_0^2 e^{\frac{izn\omega}{c} - z\kappa\omega/c - i\omega t)} e^{\frac{-izn\omega}{c} - \frac{z\kappa\omega}{c} + i\omega t)} = E_0^2 e^{-\frac{2\kappa\omega z}{c}} \qquad (7)$$

κ is related to the Beer's Law ($I(z) = I_o e^{-\alpha z}$) absorption coefficient, α, by

$$\alpha = \frac{2\kappa\omega}{c} \qquad (8)$$

In order to extract the complex index from the THz transmission, let's look more closely at the equation governing propagation of a plane wave through a material with complex index $\hat{n}$.

$$E(z,t) = E_0 e^{i(kz-\omega t)} = E_0 e^{i\left[(n+i\kappa)\frac{\omega}{c}z - \omega t\right]} = E_0 e^{-\kappa\frac{\omega}{c}z + in\frac{\omega}{c}z - i\omega t} \qquad (9)$$

Separating the time-dependent term ($E_0(t) = E_0 e^{-i\omega t}$), we get

$$E(z,t) = E_0(t) e^{-\kappa\frac{\omega}{c}z + in\frac{\omega}{c}z} \qquad (10)$$

We are interested in the frequency-dependent complex index for a sample of thickness *d*, so after Fourier transformation in the time domain and propagation for a thickness *z = d* through a sample, we get

$$E(\omega) = E_0(\omega) e^{-\kappa(\omega)\frac{\omega}{c}d + in(\omega)\frac{\omega}{c}d} \qquad (11)$$

Just as in calculating the effective absorption in equation 5, we need to account for Fresnel reflection losses at the front and back sides of our sample. The transmission coefficient for the electric field going from a medium of refractive index n_1, to a medium of refractive index n_2 at normal incidence is

$$T = \frac{2n_1}{n_1 + n_2} \qquad (12)$$

For a given sample, there is a reflection off the front surface (n_1 to n_2, i.e. air to sample) and the back surface (n_2 to n_1—sample to air), $T = \frac{2n_1}{n_1+n_2} \cdot \frac{2n_2}{n_1+n_2}$, where n_1 = 1 for air yields

$$T = \frac{4n_{sam}(\omega)}{(n_{sam}(\omega) + 1)^2} \qquad (13)$$

We can multiply the Fresnel loss term by equation 11 to obtain the THz electric field after it has passed through the sample

$$E_{sam}(\omega) = E_0(\omega)\left(\frac{4n_{sam}(\omega)}{(n_{sam}(\omega)+1)^2}\right)e^{-\kappa(\omega)\frac{\omega}{c}d+in(\omega)\frac{\omega}{c}d} \qquad (14)$$

We consider a reference THz electric field, E_{ref}, that only travels through air

$$E_{ref} = E_0(\omega)e^{i\frac{\omega}{c}d} \qquad (15)$$

which experiences no Fresnel reflection loss and which does not absorb or disperse the THz electric field. We can now express the complex transmission as a ratio of the sample and reference fields, as in the case when only considering the amplitude of the Fourier transformed THz electric fields (equation 1)

$$\frac{E_{sam}(\omega)}{E_{ref}(\omega)} = \left(\frac{4n_{sam}(\omega)}{(n_{sam}(\omega)+1)^2}\right)e^{-\kappa_{sam}(\omega)\frac{\omega}{c}d+i[n_{sam}(\omega)-1]\frac{\omega}{c}d} = Ae^{i\phi} \qquad (15)$$

The real (dispersive) part of the complex index can be extracted from the phase term, $\phi = [n_{sam}(\omega)-1]\frac{\omega}{c}d$

$$n_{sam}(\omega) = \frac{c\phi}{\omega d} + 1 \qquad (16)$$

The imaginary (absorptive) part of the complex index can be extracted from the amplitude term, $A = \left(\frac{4n_{sam}(\omega)}{(n_{sam}(\omega)+1)^2}\right)e^{-\kappa_{sam}(\omega)\frac{\omega}{c}d}$

$$\kappa_{sam}(\omega) = -\frac{c}{\omega d}ln\left[A\left(\frac{(n_{sam}(\omega)+1)^2}{4n_{sam}(\omega)}\right)\right] \qquad (17)$$

which is related to the absorption coefficient, α, by equation 8

$$\alpha = -\frac{2}{d}ln\left[A\left(\frac{(n_{sam}(\omega)+1)^2}{4n_{sam}(\omega)}\right)\right] \qquad (18)$$

We have formulated a method to extract the complex index of refraction from THz electric field measurements. It is worth mentioning that the real (n) and imaginary (κ) parts of the complex index of refraction are related fundamentally through the Kramers-Kronig relationship [1-3]

$$n(\omega) = 1 + \frac{1}{\pi}\int_{-\infty}^{\infty} \frac{\kappa(\omega')}{\omega' - \omega} d\omega' \qquad (19)$$

$$\kappa(\omega) = -\frac{1}{\pi}\int_{-\infty}^{\infty} \frac{n(\omega') - 1}{\omega' - \omega} d\omega' \qquad (20)$$

This reflects the fact that if one part of the complex index is determined across a wide frequency range, the other part can be derived accordingly.

One practical consideration that must be taken into account when extracting the complex index from experimental measurements is the unwrapping of the phase in the Fourier transform of the THz electric fields. For a strongly dispersive sample, the resolution in the frequency domain must be fine enough to ensure that no adjacent discrete frequency points change by more than a factor of 2π. This may be easily averted by sufficient zero-padding of experimental data in the time domain prior to Fourier transformation.

3.1.3 Complex Dielectric and Conductivity

The extraction of the complex index of refraction from experimentally determined THz electric fields is straightforward. However, it may be of interest at times to extract related quantities, such as the complex dielectric function or the complex conductivity. These follow from simple arithmetic expressions. The complex dielectric function may be calculated from the complex index by [4-6]

$$\hat{\epsilon} = \epsilon_1 + i\epsilon_2 = \hat{n}^2 = n^2 - \kappa^2 + 2in\kappa \qquad (21)$$

So it follows that the real and imaginary parts of the complex dielectric function are

$$\epsilon_1 = n^2 - \kappa^2 \qquad (22)$$

$$\epsilon_2 = 2n\kappa \qquad (23)$$

We can do a similar manipulation to find the complex conductivity [4]

$$\hat{\sigma} = \sigma_1 - i\sigma_2 = -i\omega\hat{\epsilon} = -i\omega(\epsilon_1 + i\epsilon_2) = \omega\epsilon_2 - i\omega\epsilon_1 \qquad (24)$$

so it follows that the real and imaginary parts of the conductivity are

$$\sigma_1 = \omega\epsilon_2 = 2n\kappa\omega\epsilon_0 \qquad (25)$$

$$\sigma_2 = \omega\epsilon_1 = \omega(n^2 + \kappa^2)\epsilon_0 \qquad (26)$$

3.1.4 Extracting Complex Material Parameters in Thin-Film Transmission

We are often interested in the properties of thin films. We can extract thin film quantities in transmission measurements as well. In the limit of high conductivity we can extract the complex conductivity with the Tinkham formula [4, 5, 7, 8]

$$\hat{\sigma}(\omega) = \left((1 + n_s)\frac{t_f}{t_s} - n_s - 1\right)\frac{1}{Z_0 d} \qquad (27)$$

where n_s is the substrate refractive index, t_f and t_s are the complex transmission coefficients ($t = E_t(\omega)/E_i(\omega)$, the complex ratio of the transmitted and incident THz electric fields) of the film + substrate and substrate respectively, Z_0 is the vacuum impedance, and d is the thickness of the film. For poorly conducting thin films, the complex material properties may be extracted using the previous expressions detailed above using the small film thickness value of the film. However, this may lead to large errors since the film thickness values are typically quite small.

3.2 Fitting to a Convolution

We perform several experiments interrogating the dynamics of THz pump-induced changes. Often, the changes decay on the timescale of the THz-pump pulse itself. On this timescale, it is important to take into account the duration of the pump pulse when extracting decay constants. Often, the effect depends on the intensity of the THz pulse ($I_{THz} \propto E_{THz}^2$). For these measurements, we deconvolve the duration of the pulse from the subsequent dynamics by performing an iterative least squares fit of the signal, *S*, to the experimentally measured square of the THz-pump field and a decay function, *D*

$$S_{fit} = E_{THz}^2(t) \otimes D(t) \qquad (28)$$

where *D* can be any decay or rise function. For single exponential decays, we use

$$D = \Theta(t) A e^{-\frac{t}{\tau}} \qquad (29)$$

for biexponential decays, we use

$$D = \Theta(t) \left(A e^{-\frac{t}{\tau_1}} + B e^{-\frac{t}{\tau_2}} \right) \qquad (30)$$

for exponentially rising signal, we use

$$D = \Theta(t) A \left(1 - e^{-\frac{t}{\tau}} \right) \qquad (31)$$

for exponentially rising signal with a subsequent exponential decay, we use

$$D = \Theta(t) \left[A \left(1 - e^{-\frac{t}{\tau_1}} \right) + B e^{-\frac{t}{\tau_2}} \right] \qquad (32)$$

where *Θ(t)* is the Heaviside step function, *A*, and *B* are scaling factors, and τ, τ_1, and τ_2 are decay constants.

3.3 Conclusions

We have discussed the extraction of relevant physical quantities from measurements of THz electric fields in thick samples and thin films. These data extraction techniques will be used throughout this work to describe nonlinear THz spectroscopies in several classes of systems.

References

[1] B. M. Fischer. "Broadband THz time-domain spectroscopy of biomolecules: A comprehensive study of the dielectric properties of biomaterials in the far-infrared." (*PhD*) Fakultat fur Mathematik und Physik, Albert-Ludwigs-Universitat Freiburg im Breisgau: Freiburg, Germany (2005).

[2] R. D. L. Kronig. "On the theory of dispersion of x-rays." *J. Opt. Soc. Am.*, **12**, 547 (1926).

[3] H. A. Kramers. "La diffusion de la lumiere par les atoms." *Atti Cong. Intern. Fisica, (Transactions of Volta Centenary Congress) Como*, **2**, 545 (1927).

[4] C.-W. Chen, Y.-C. Lin, C.-H. Chang, P. Yu, J.-M. Shieh and C.-L. Pan. "Frequency-Dependent Complex Conductivities and Dielectric Responses of Indium Tin Oxide Thin Films From the Visible to the Far-Infrared." *Quantum Electronics, IEEE Journal of*, **46**, 1746 (2010).

[5] J. J. Tu, C. C. Homes and M. Strongin. "Optical Properties of Ultrathin Films: Evidence for a Dielectric Anomaly at the Insulator-to-Metal Transition." *Physical Review Letters*, **90**, 017402 (2003).

[6] D. Nakamura, Y. Imai, A. Maeda and I. Tsukada. "Superconducting Fluctuation Investigated by THz Conductivity of $La_{2-x}Sr_x$$CuO_4$ Thin Films." *Journal of the Physical Society of Japan*, **81**, 044709

[7] M. Tinkham. "Energy Gap Interpretation of Experiments on Infrared Transmission through Superconducting Films." *Physical Review*, **104**, 845 (1956).

[8] R. A. Kaindl, M. A. Carnahan, J. Orenstein, D. S. Chemla, H. M. Christen, H.-Y. Zhai, M. Paranthaman and D. H. Lowndes. "Far-Infrared Optical Conductivity Gap in Superconducting MgB_2 Films." *Physical Review Letters*, **88**, 027003 (2001).

Chapter 4

Methods

The development of high-field THz sources capable of driving nonlinear material responses [1, 2] has led to the development of spectroscopies making use of such sources. Several nonlinear THz spectroscopic methodologies have been developed in our lab, analogous to spectroscopies in other, more established wavelength regimes. These spectroscopic methods include: nonlinear transmission spectroscopy [3-5], collinear and noncollinear THz-pump/THz-probe spectroscopy [3-5], THz-pump/optical probe spectroscopy—including THz Kerr effect spectroscopy [6] where the polarization of the optical probe is measured—and THz field induced second harmonic generation (TFISH) [7, 8]. In most of these spectroscopies, we are interested in initiating a change in a material with a THz pulse and then measuring the system response due to the strong excitation. These techniques can interrogate several types of effects ranging from resonant to nonresonant effects, and perturbative to non-perturbative effects. In this chapter, I will describe the experimental methodologies outlined above in detail.

4.1 Nonlinear THz Transmission Spectroscopy

Using the microjoule THz pulses from our tilted pulse front generation scheme, we can measure high-field effects in materials with nonlinear transmission spectroscopy (figure 1) [3-5].

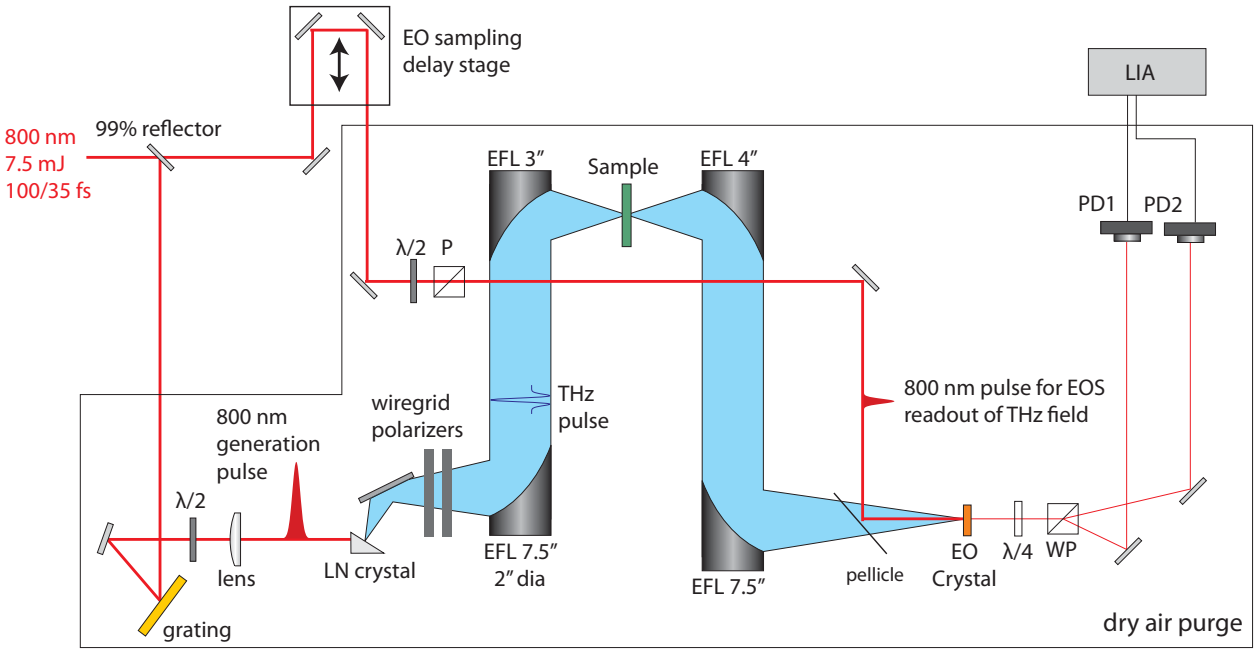

Figure 1: Nonlinear THz transmission setup. The output of an amplified laser system is split into two arms with a 99% beam splitter. The 99% reflection is used to generate high-field THz pulses while the 1% transmitted arm is used for electro-optic detection of the THz electric field. A pair of wiregrid polarizers is used to variably attenuate the THz pulses in order to measure field-dependent effects.

The output of the lithium niobate generation crystal is imaged onto a sample using a flat mirror to redirect the beam to a more convenient direction and a pair of off-axis parabolas as the focusing optics. A second pair of off-axis parabolas images the THz pulse at the sample onto an electro-optic sampling crystal. A time-delayed optical readout pulse is used to gate the THz field in time, and the THz electric field coming out of the sample is measured by changing the

relative delay of the THz and optical pulses. A pair of wiregrid polarizers at the output of the generation crystal is used to variably attenuate the THz pulse. Frequency-dependent transmission and integrated transmission may be determined by comparison to a reference material—often dry air.

4.2 THz-Pump/THz-Probe Spectroscopy

When we see significant nonlinear transmission in a material, we are often interested in the dynamics of the THz-induced change. To measure the dynamics we can use one THz pulse to induce a change, and then a second time-delayed THz pulse to probe the changes as a function of delay time after the initial THz excitation. These are THz-pump/THz-probe spectroscopies. We have developed two classes of these measurements: collinear and noncollinear [3-5].

4.2.1 Collinear THz-Pump/THz-Probe Spectroscopy

For collinear THz-pump/THz-probe measurements, we generate two THz pulses that are time-delayed with respect to one another with the same generation crystal. We do this by splitting the optical generation pulse into two arms that are recombined on the tilted pulse front grating at a shallow angle. The relative time delay is achieved by an optical delay line as shown in figure 2. With the tilted pulse front technique, the grating is imaged onto the lithium niobate generation crystal to achieve noncollinear velocity matching in the generation medium. Since the two optical generation pulses are recombined on the same spot on the grating, they are imaged with approximately the same tilt in their intensity fronts, yielding two time-delayed THz pulses. The THz pulses are steered to a sample and finally to an electro-optic detection crystal

with the same four parabolic mirror setup described for the THz nonlinear transmission measurements. The THz pulses are detected with electro-optic sampling using an optical readout pulse that is split off earlier in the setup. Typically, large pump-induced changes are observed by chopping the probe arm of the optical generation pulses and measuring the signal with a lock-in amplifier at the chopping frequency. For sensitive detection of the pump-induced changes, where small changes in the probe are expected, we can perform differential chopping, where both the pump and probe generation arms are chopped to separate out the pump-induced changes in the probe. This is discussed in more detail later in this chapter.

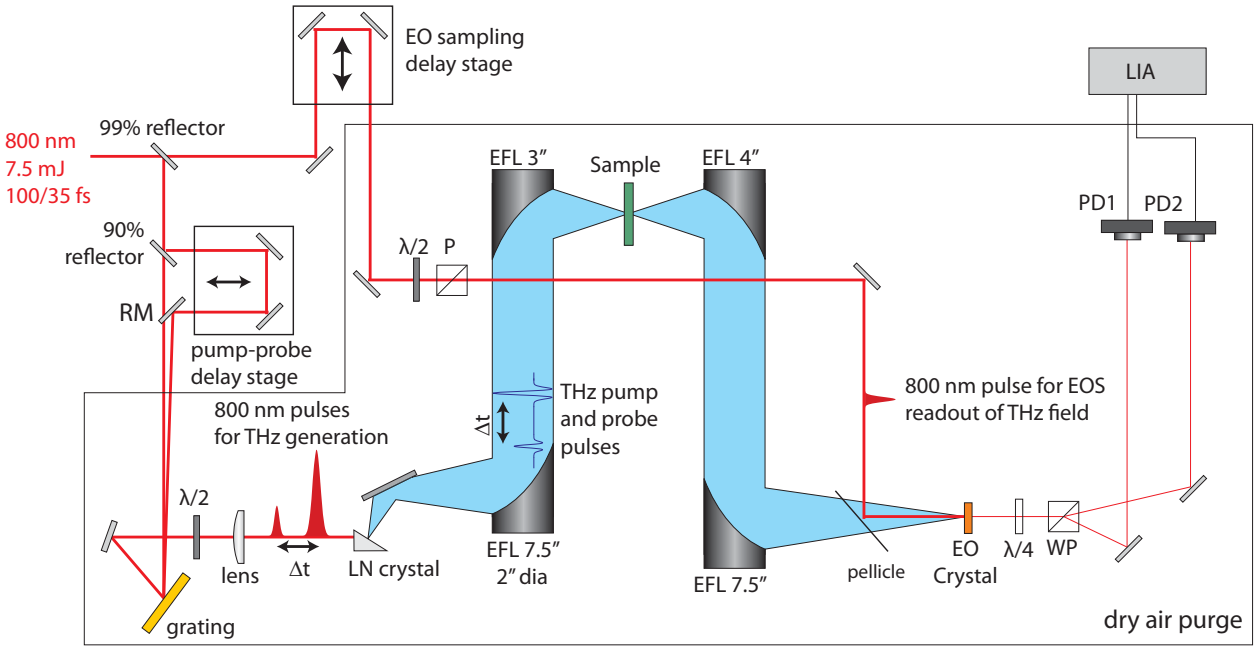

Figure 2: Collinear THz-pump/THz-probe setup. The 800 nm THz generation pulse is split into a pump and a probe arm that will generation the THz-pump and THz-probe pulses respectively. An optical delay stage delays the pump with respect to the probe, yielding variably time-delayed THz pulses from a common lithium niobate generation crystal. A small portion of the optical beam is split off for electro-optic measurement of the THz electric fields. Pump, probe, and both pump and probe contributions may be observed with different chopping schemes.

Using a common generation crystal to generate two time-delayed THz pulses presents a problem in this technique because when the two optical generation arms overlap in time, highly nonlinear mixing of the optical and THz pulses occurs in the generation crystal. This obscures the dynamics near the pump probe overlap time (time-zero). As such, we may only observe dynamics longer than about twice the THz pulse duration, or when the two generated THz pulses are sufficiently separated in time. However, for samples with low dispersion, low absorption, and large nonlinearity, we may overcome this limitation by observing dynamics initiated by the round-trip reflection of the pump pulse in the material (figure 3). Another solution to the problem, when the sample exhibits high dispersion, large absorption, or weak nonlinear response, is to go to a noncollinear geometry.

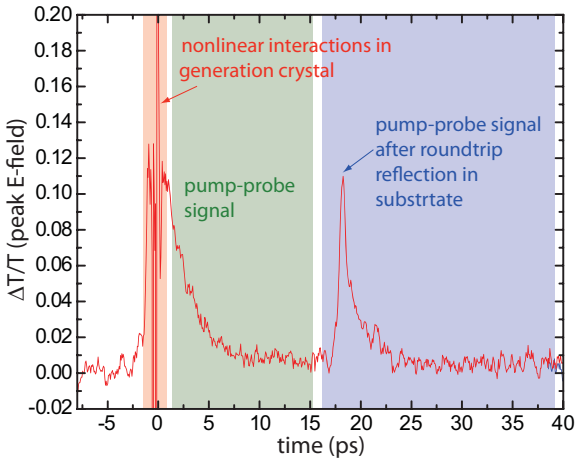

Figure 3: Illustration of nonlinear effects near time zero in a collinear THz-pump/THz-probe experiment, and of THz-pump/THz-probe signal from a low dispersion/low absorption substrate material after round-trip reflection of the THz pump in the substrate. THz-pump/THz-probe peakscan data is shown for graphene on a fused silica substrate. The nonlinear effects in the generation crystal are shown in red. The pump-probe signal after sufficient temporal separation of THz pump and THz probe pulses is shown in green. Pump-probe signal initiated after a round-trip of the THz pump pulse in the fused silica substrate is shown in blue. Since the optical generation pulses are separated in time by 20 picoseconds in the blue region, early time dynamics are not obfuscated by nonlinear interactions of the pump and probe pulses in the generation crystal.

For THz-pump/THz-probe experiments, full frequency-resolved information may be obtained by measuring the full THz probe field with electro-optic detection. The full probe field is measured for each delay time between the THz pump and the THz probe such that the time-dependent evolution of the probe transmission can be determined from Fourier transformation of the probe pulse.

Another method to measure dynamics in our pump-probe setup is to sit on the peak of the probe THz electric field at the appropriate electro-optic sampling delay and measure its evolution as a function of THz-pump/THz-probe delay time. We call this a pump-probe peak-scan measurement. Pump-probe peak scans work best for samples with flat responses in the THz range such that there is a minimal frequency-dependence to the response in the sample material.

4.2.2 Noncollinear THz-Pump/THz-Probe Spectroscopy

For noncollinear THz-pump/THz-probe measurements, two separate generation schemes are used. As shown in figure 4, THz pump pulses are generated by tilted pulse front generation in lithium niobate, and the THz probe arm is generated by a variably time-delayed optical pulse by one of several different generation mechanisms. Any collinearly phase-matched generation scheme can be used ranging from optical rectification in ZnTe [9], two-color plasma generation [10], to optical rectification in GaSe [11-15]. The THz pump and THz probe pulses are collimated using two separate parabolic mirrors. Each pulse is directed onto a common large parabolic mirror focusing each beam to the same spot where we place a sample. A second large parabolic

mirror collimates each arm and then a second pair of parabolic mirrors individually focuses each arm to an electro-optic crystal such that the electric field of either arm can be measured independent of the other. Similar chopping schemes used for the collinear pump-probe setup are also used in the noncollinear measurements.

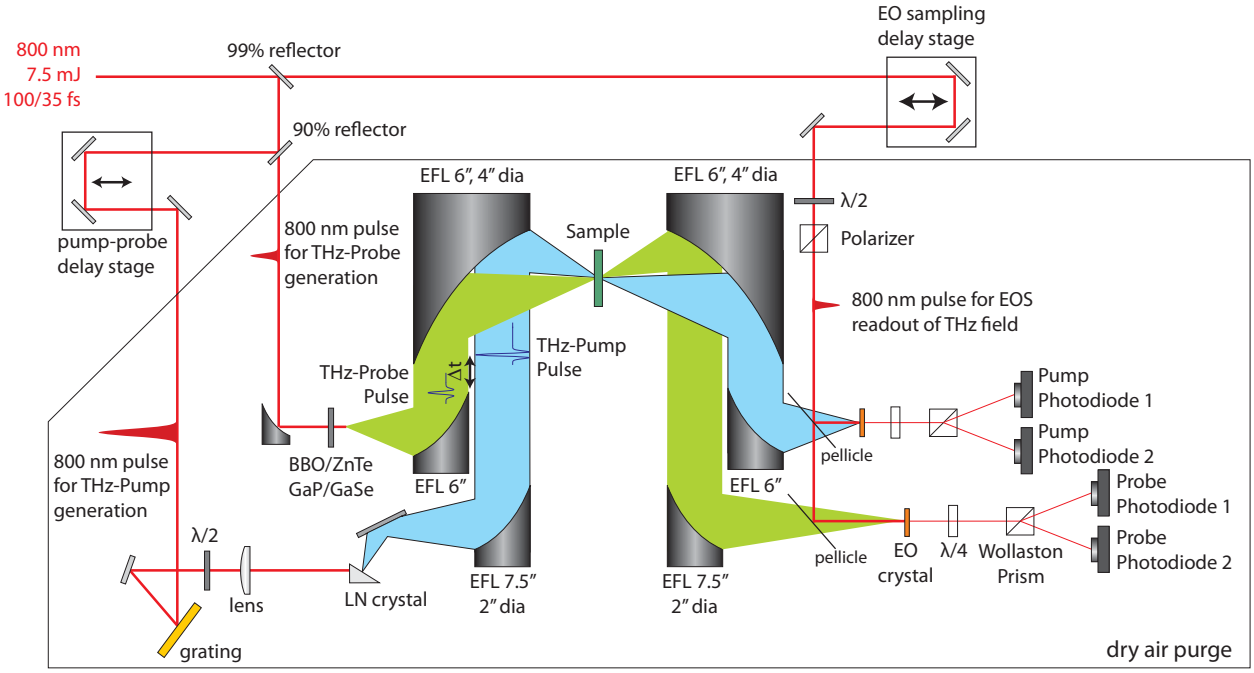

Figure 4: Noncollinear THz-pump/THz-probe setup. An 800 nm amplified optical pulse is split into three arms. Two arms are used for the generation of the THz pump and THz probe pulses. The third arm is used for electro-optic sampling of the THz electric fields. The THz pump pulse is generated by tilted pulse front excitation in lithium niobate, and directed onto a sample with a pair of off-axis parabolic mirrors. The THz probe pulse is generated by one of a variety of collinearly phase-matched methods including optical rectification in ZnTe, GaP, or GaSe, or broadband generation by two-color mixing in a laser-induced plasma. The THz probe pulse is directed onto the sample with a pair of off-axis parabolic mirrors. The THz pump and THz probe arms are separated spatially since different generation schemes are used. However, they are focused to the same spot on the sample since both beams hit a common large diameter off-axis parabolic mirror immediately before the sample (any parallel beams hitting a parabola will focus to the same spot). For clarity, the THz pump and THz probe pulses are shown horizontally displaced. They are vertically displaced in the actual setup. The electric field of either the THz pump or THz probe pulse is measured independently with electro-optic sampling. For higher frequency THz to IR probe frequencies, other probe detection schemes may be used.

The variety of probe generation schemes gives flexibility in the different effects that may be probed. This technique provides a versatile platform for probing spectroscopic changes from the single to several THz range. It can also be modified to enable probing in the mid-IR (~3-10 micron), where the coupling between collective and local vibrational motions can be observed.

4.3 THz-Pump/Optical-Probe Spectroscopy

THz-pump/optical-probe spectroscopies are also useful in studying a variety of systems where the THz-induced nonlinearity can change the response in the optical regime. Simple experiments can be performed in collinear or noncollinear geometries in both reflection and transmission (figure 5). Furthermore, THz-induced optical anisotropy can be readily observed with a setup similar to electro-optic sampling of THz transients. That is to say, we can probe polarization dynamics with THz Kerr effect spectroscopy [6].

4.3.1 THz Kerr Effect Spectroscopy

A THz electric field can be used to induce optical anisotropy in a material either resonantly (coupling through a dipole) or nonresonantly (coupling through the polarizability) with THz Kerr effect spectroscopy. This is analogous to optical Kerr effect spectroscopy where an optical pulse is used to induce an anisotropy in the polarization of a material. In either case, we can sensitively measure the induced anisotropy by analyzing the polarization of a time-delayed optical probe pulse. The setup is shown in figures 5c and 5d. The optical probe is overlapped with the THz pump pulse in space and variably delayed time and then the polarization rotation

is measured with either crossed polarizers, or with a quarter waveplate and polarizing beam splitter.

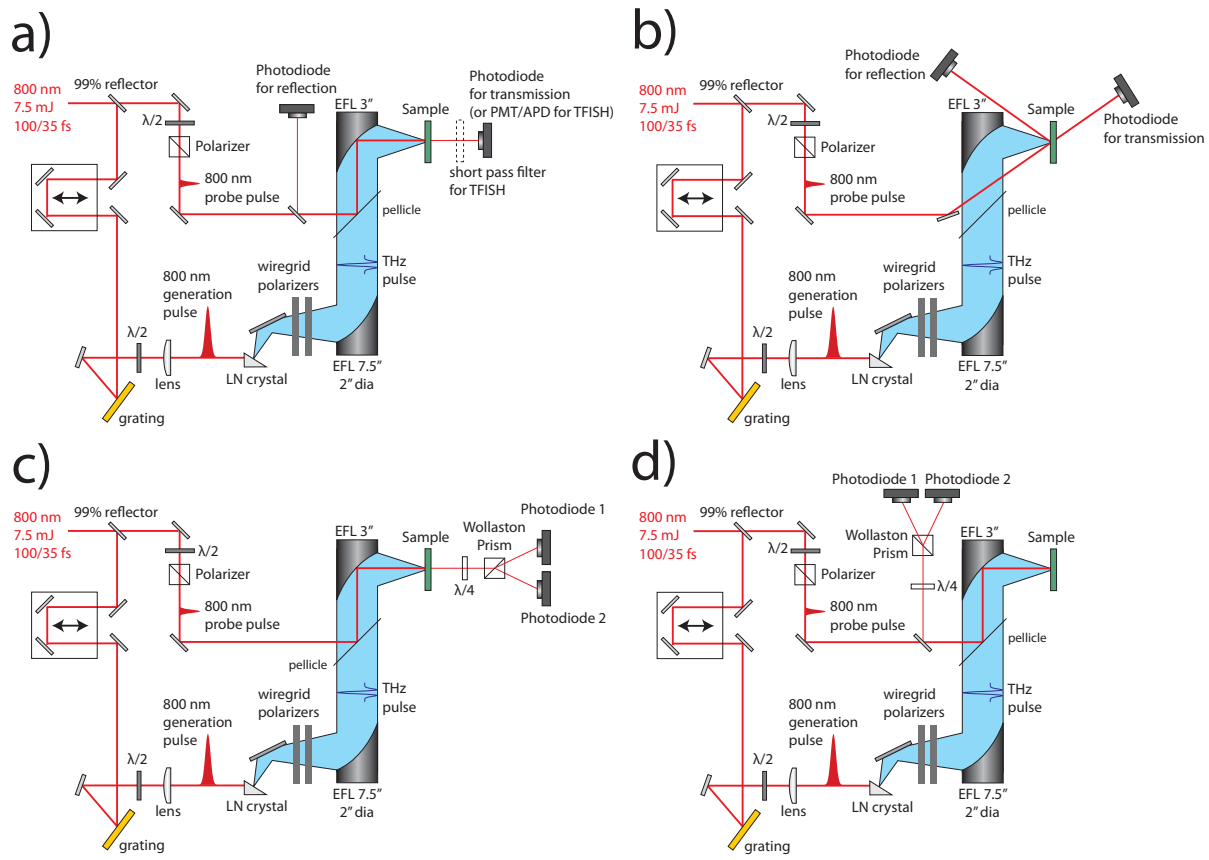

Figure 5: THz-pump/optical-probe schemes. In all setups, a polarizer in the probe arm can set the relative polarization angle between the THz pump and optical probe. A pair of wiregrid polarizers is used in the THz pump arm to variably attenuate the THz field for determination of the field-dependence of the measured effects. (a) THz-pump/optical-probe in either retroreflecting geometry or transmission. For TFISH measurements, the photodiode is replaced with a photomultiplier tube (PMT) or avalanche photodiode (APD) and a short-pass filter to block the fundamental from hitting the detector. (b) noncollinear geometry where the optical probe is at an angle with respect to the THz pump field. (c) THz Kerr effect setup in transmission for dynamic polarization experiments. A quarter waveplate and polarizing beam splitter (Wollaston prism) are used to heterodyne the measurement. They also allow for balanced detection. Both heterodyning of the signal and balanced detection increase the signal-to-noise ratio of the measurements [16]. Note that the input polarization of the optical probe may be turned to 45 degrees with respect to the THz pulse, and then the waveplate and Wollaston prism may be replaced with a second polarizer set to 90 degrees with respect to the first polarizer with a single photodiode to measure polarization dynamics as well. (d) THz Kerr effect setup in retroreflecting geometry.

4.3.2 THz Field Induced Second Harmonic Spectroscopy (TFISH)

Another way to probe THz-induced responses is with THz-induced second harmonic generation (TFISH) [7, 8]. Here, a THz pulse is used to break the symmetry of a material such that the second harmonic of an optical probe pulse can be generated. Since even-order nonlinear processes are allowed only in noncentrosymmetric materials, TFISH measurements on centrosymmetric materials provide a way to observe THz-induced distortions in symmetry. The setup is similar to a THz-pump/optical-probe setup, except that the fundamental of the optical pulse is filtered out (figure 5a). The induced second harmonic signal tends to be very weak, so sensitive detection devices are needed such as photomultiplier tubes or avalanche photodiodes.

4.4 Differential Chopping

All of the time-resolved spectroscopic techniques described in this chapter involve several pulses of light. In particular, the THz-pump/THz-probe methods require sensitive detection of potentially small changes in the THz probe pulse to observe any nonlinear response. For large THz-induced nonlinear responses, changes in the THz probe pulse are easily detected by chopping the probe arm of the experiment. This is atypical of pump-probe experiments in the optical and IR regimes, where pump-induced modulations of the probe are measured by chopping the pump arm of the experiment. For smaller changes in the probe field, it can be useful to isolate the nonlinear component of the signal with differential chopping [17, 18]. This

allows us to subtract out the linear responses of the pump and the probe such that only the pump-induced nonlinearity remains in the electro-optic signal (figure 6).

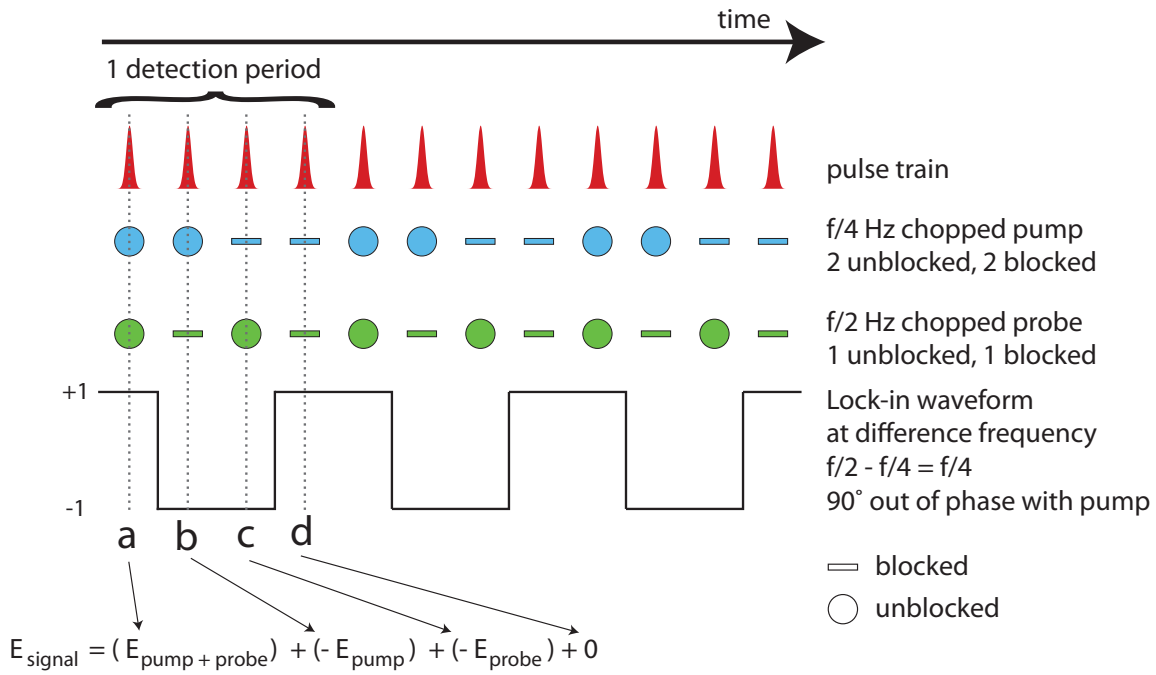

Figure 6: Time schematic of differential chopping. The pump/probe pulses are separated in time by much smaller increments than adjacent pulses in the pulse train, so only the pulse train is illustrated (red). The pump arm (blue) of the experiment is chopped at a quarter of the laser repetition rate (f/4) such that 2 pulses are unblocked, and 2 pulses are blocked for each period. The probe arm (green) is chopped at half the laser repetition rate (f/2) such that 1 pulse is unblocked and 1 pulse is blocked for each period. The lock-in waveform is shown as a square wave (black) at the difference frequency (f/2 - f/4 = f/4). However, for differential chopping to work, the proper phase for the lock-in waveform must be chosen. Here it is 90 degrees out of phase with the pump. The result is that over one detection period, (a) the response from both the pump and probe going through the sample is detected, (b) the response from only the pump is subtracted away, (c) the response from only the probe is subtracted away, and (d) the effect of both the pump and probe being blocked is zero, leaving only the pump-induced change in the probe remaining. A f/2-f/4 scheme is shown for clarity. However, in the experiments described in this work, a f/4 - f/6 = f/12 was used to take into account the fact that the lock-in amplifier applies a sine wave and not a square wave for the lock-in waveform. Using a data acquisition card, we can instead apply a square wave and we can detect the signal at f/4.

For our experiments we would like to measure the induced change in the probe due to the pump. In experiments in the collinear geometry, the pump response is always present at the detection crystal at any moderate time delay. In experiments in the noncollinear geometry, some of the pump light may be scattered in the probe arm of the experiment. In either case, we would like to minimize the signal at the electro-optic sampling crystal due to the THz pump field. Another way to portray this is:

$$E_{signal} = E_{pump+probe} - E_{pump} - E_{probe}$$

where the pump-induced changes in electric field are expressed by E_{signal}, the superposition of the pump and probe fields is $E_{pump+probe}$, the pump field is E_{pump}, and the probe field is E_{probe}. Differential chopping allows one to isolate E_{signal} by locking-in at the difference frequency at the proper lock-in phase. When the phase is properly chosen, the detection scheme is as follows. $E_{pump+probe}$ is the electric field when both the pump and the probe are unblocked—they both go through the sample ('a' in figure 6). In this case, the nonlinear transmission of the pump and the nonlinear response of the probe are both present. E_{pump} is the transmission of the pump field without the probe ('b' in figure 6). Any nonlinearities in the pump transmission are subtracted out by judicious choice of the lock-in phase. E_{probe} is the transmission of the probe field without the pump ('c' in figure 6). Since the probe field should be too weak to induce any nonlinearities, this is just the linear response of the sample to the probe field. This is subtracted from the sum as well (since the amplitude of the lock-in waveform is -1 at this part of the detection period). The last portion of the signal is zero ('d' in figure 6) since both the pump and probe are blocked, and this contributes nothing to the differential signal. With the proper phase the desired signal is isolated.

4.6 Conclusions

The rest of this work will describe the uses of these experimental setups to study nonlinear THz responses in a wide variety of systems. The development of these methodologies has enabled the study of physical and chemical properties including electronic transport phenomena in solid state materials, nonlinear lattice responses related to phase transitions, and energy relaxation.

4.7 References

[1] K. L. Yeh, M. C. Hoffmann, J. Hebling and K. A. Nelson. "Generation of 10 μJ ultrashort terahertz pulses by optical rectification." *Applied Physics Letters*, **90**, 171121 (2007).

[2] H. Hirori, A. Doi, F. Blanchard and K. Tanaka. "Single-cycle terahertz pulses with amplitudes exceeding 1 MV/cm generated by optical rectification in $LiNbO_3$." *Applied Physics Letters*, **98**, 091106 (2011).

[3] J. Hebling, M. C. Hoffmann, H. Y. Hwang, K.-L. Yeh and K. A. Nelson. "Observation of nonequilibrium carrier distribution in Ge, Si, and GaAs by terahertz pump–terahertz probe measurements." *Physical Review B*, **81**, 035201 (2010).

[4] M. C. Hoffmann, J. Hebling, H. Y. Hwang, K.-L. Yeh and K. A. Nelson. "THz-pump/THz-probe spectroscopy of semiconductors at high field strengths [Invited]." *J. Opt. Soc. Am. B*, **26**, A29 (2009).

[5] M. C. Hoffmann, J. Hebling, H. Y. Hwang, K.-L. Yeh and K. A. Nelson. "Impact ionization in InSb probed by terahertz pump—terahertz probe spectroscopy." *Physical Review B*, **79**, 161201 (2009).

[6] M. C. Hoffmann, N. C. Brandt, H. Y. Hwang, K.-L. Yeh and K. A. Nelson. "Terahertz Kerr effect." *Applied Physics Letters*, **95**, 231105 (2009).

[7] D. J. Cook, J. X. Chen, E. A. Morlino and R. M. Hochstrasser. "Terahertz-field-induced second-harmonic generation measurements of liquid dynamics." *Chemical Physics Letters*, **309**, 221 (1999).

[8] J. Chen, P. Han and X. C. Zhang. "Terahertz-field-induced second-harmonic generation in a beta barium borate crystal and its application in terahertz detection." *Applied Physics Letters*, **95**, 011118 (2009).

[9] A. Rice, Y. Jin, X. F. Ma, X. C. Zhang, D. Bliss, J. Larkin and M. Alexander. "Terahertz optical rectification from <110> zinc-blende crystals." *Applied Physics Letters*, **64**, 1324 (1994).

[10] H. G. Roskos, M. D. Thomson, M. Kreß and T. Löffler. "Broadband THz emission from gas plasmas induced by femtosecond optical pulses: From fundamentals to applications." *Laser & Photonics Reviews*, **1**, 349 (2007).

[11] R. A. Kaindl, F. Eickemeyer, M. Woerner and T. Elsaesser. "Broadband phase-matched difference frequency mixing of femtosecond pulses in GaSe: Experiment and theory." *Applied Physics Letters*, **75**, 1060 (1999).

[12] K. Reimann, R. P. Smith, A. M. Weiner, T. Elsaesser and M. Woerner. "Direct field-resolved detection of terahertz transients with amplitudes of megavolts per centimeter." *Opt. Lett.*, **28**, 471 (2003).

[13] R. Huber, A. Brodschelm, F. Tauser and A. Leitenstorfer. "Generation and field-resolved detection of femtosecond electromagnetic pulses tunable up to 41 THz." *Applied Physics Letters*, **76**, 3191 (2000).

[14] A. Sell, A. Leitenstorfer and R. Huber. "Phase-locked generation and field-resolved detection of widely tunable terahertz pulses with amplitudes exceeding 100 MV/cm." *Opt. Lett.*, **33**, 2767 (2008).

[15] A. Sell, R. Scheu, A. Leitenstorfer and R. Huber. "Field-resolved detection of phase-locked infrared transients from a compact Er:fiber system tunable between 55 and 107 THz." *Applied Physics Letters*, **93**, 251107 (2008).

[16] C. A. Werley, S. M. Teo and K. A. Nelson. "Pulsed laser noise analysis and pump-probe signal detection with a data acquisition card." *Review of Scientific Instruments*, **82**, 123108 (2011).

[17] P. Gaal, W. Kuehn, K. Reimann, M. Woerner, T. Elsaesser and R. Hey. "Internal motions of a quasiparticle governing its ultrafast nonlinear response." *Nature*, **450**, 1210 (2007).

[18] W. Kuehn, K. Reimann, M. Woerner and T. Elsaesser. "Phase-resolved two-dimensional spectroscopy based on collinear n-wave mixing in the ultrafast time domain." *The Journal of Chemical Physics*, **130**, 164503 (2009).

Chapter 5

Electronic THz Nonlinearities in Semiconductors

The study of hot carrier effects plays a central role in the advancement of semiconductor science. Properties of hot carriers are influenced by both the carrier-carrier interactions and carrier-lattice interactions. Information about these scattering processes, which determine high-field transport phenomena in semiconductors, is highly valuable because they constitute the basis of many ultrafast electronic and optoelectronic devices. With the advent of ultrafast lasers, the dynamics of hot carrier effects have been studied intensively on the picosecond and femtosecond time scales. In a typical experiment, new carriers are generated by an optical pump beam with a photon energy, ε_{ph}, above the bandgap, ε_g, of the semiconductor. The newly generated electrons and holes share the excess energy ε_{ph}-ε_g in a ratio inversely proportional to their effective masses and subsequently undergo cooling processes mediated by carrier–carrier and carrier–phonon scattering. The dynamics of these cooling processes can then be monitored

by short probe pulses of appropriate wavelength. This technique has successfully been applied to a large range of semiconductors and semiconductor nanostructures, and a substantial amount of basic information has been collected in this way [1].

With photo excitation, an equal number of electrons and holes are created. Hence, most ultrafast optical studies are performed in the presence of a plasma containing both types of carriers. Experimental observations can be complicated by the dynamics that involve both electrons and holes. When properties such as the coupling to the phonons and carrier–carrier scattering are different for the two components and the density of carriers is time-dependent, a direct interpretation of the experimental data is further hindered. Near-IR pump/THz probe experiments also suffer from this shortcoming [2-4].

In this chapter, I discuss results from nonlinear THz transmission and THz-pump/THz-probe measurements used to monitor the intervalley and intravalley dynamics of extremely hot free electrons in bulk semiconductors (gallium arsenide [GaAs], germanium [Ge], and silicon [Si]) and the generation of new carriers by impact ionization in InSb. In our experiments, we achieved THz electric field strengths of up to 150 kV/cm at the semiconductor surface. Fields of this magnitude and correspondingly hot electrons are present inside different fast semiconductor devices such as Gunn diodes and avalanche photodiodes.

Electron heating by the THz pulse and strong intervalley scattering cause a large fraction of the electrons to scatter out from the initial lowest energy conduction band valley into side valleys. Based on a rough estimate, electrons can reach an average energy on the order of 1 eV. Since free-carrier absorption is proportional to carrier concentration and carrier mobility, and because different conduction band valleys usually have significantly different mobilities from

each other, the change in the distribution of electrons amongst the different valleys causes a change in THz absorption. This behavior has been observed with nanosecond transmission experiments with field strengths up to 10 kV/cm [5]. In the experiments here, we have the additional capability to monitor the change in THz absorption using a variably delayed single-cycle THz pulse, enabling us to resolve the carrier dynamics on the picosecond time scale.

5.1 Experimental Technique

The experimental setup shown in figure 1 was used to elucidate the dynamics of hot carriers in doped semiconductors. We generated single-cycle THz pulses by optical rectification of pulses from a femtosecond laser using the tilted-pulse-front method [6]. This technique uses a tilted intensity front of a femtosecond laser pulse to achieve velocity matching between the phonon-polaritons inside lithium niobate and the femtosecond laser light [7]. The tilted pulse front enables the use of high optical pulse energy to build up large THz field amplitudes while averting unwanted nonlinear optical effects. THz pulse energies greater than 10 μJ can be achieved using this method [8]. Because the angle of the pulse front tilt can be arbitrarily chosen, the method can also be adapted for other materials and wavelengths [9].

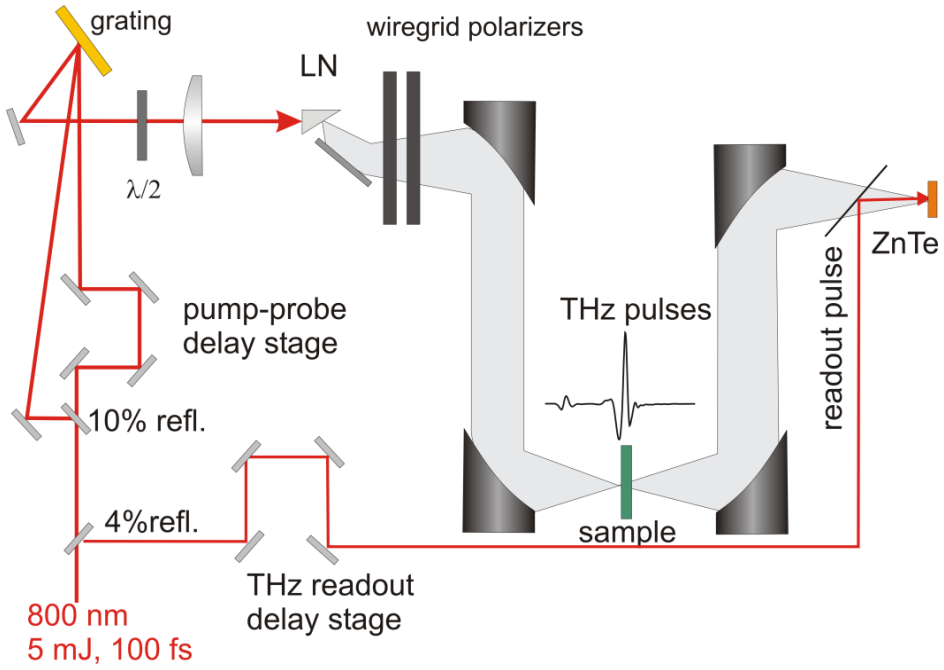

Figure 1: Schematic illustration of the experimental setup. Collinear THz pulses are generated by tilted pulse front excitation in LiNbO3 (LN) and detected electro-optically. This is discussed in detail in chapter 4.

For our experiments a regeneratively amplified titanium sapphire laser system with 6 mJ pulse energy and 100 fs pulse duration at a repetition rate of 1 kHz was used. The optical beam was split using a 10:90 beamsplitter into two parts that were recombined under a small angle at the same spot on the grating. The 10% part was passed through a chopper wheel (not shown in figure) and was used to generate the THz probe. The 90% part was variably delayed and was used to generate the THz pump pulse. The single-cycle THz pulses were focused onto the sample using a 90-degree off-axis parabolic mirror pair with 190 and 75 mm focal lengths. The ratio of focal lengths allows us to reduce the beam diameter at the sample to about 1 mm. Another off-axis parabolic mirror pair with focal lengths of 100 and 190 mm was used to image the sample plane onto the ZnTe detector crystal for electro-optic sampling of the THz field using balanced detection and a lock-in amplifier [10]. Because larger than 2π phase shifts are

routinely observed with thicker ZnTe crystals, we used a ZnTe compound detector with an active layer of 0.1 mm and a total thickness of 1.1 mm to ensure the linearity of the detected signal and to eliminate THz pulse reflections [11] within the crystal. Selective chopping of the probe beam provided excellent suppression of the pump pulse. Spectral analysis of our THz pump-probe results was conducted in the 0.2 to 1.6 THz range where the spectral amplitude was sufficiently high. A pair of wiregrid polarizers was used to attenuate the THz pulses for intensity-dependent studies. We measured the THz fields *E(t)* that reached the ZnTe crystal with and without the sample in the beam path and calculated the effective absorption coefficient

$$\alpha_{eff} = -\frac{1}{d} ln\left(T^2 \cdot \frac{\int_0^{t_{max}} E_{sam}^2(t)dt}{\int_0^{t_{max}} E_{ref}^2(t)dt} \right) \quad (1)$$

where *d* is the sample thickness, t_{max} is the time window of the measurement, and *T* is a factor accounting for reflection losses at the sample surfaces. The quantity α_{eff} is equivalent to the energy absorption coefficient averaged over our bandwidth. Referencing the recorded data against the electric field measured without the sample enables us to compensate nonlinear effects within the LN generation crystal to a large degree. Only in a time interval of ±1 ps around the overlap time of the pump and probe does the data become unreliable.

The same setup can be reconfigured for intensity-dependent transmission studies by simply blocking the optical pulse used to generate the THz probe beam, chopping the portion used to create the THz pump, and changing the angle between the first and second THz wiregrid polarizers to vary the intensity of the THz pump pulse.

5.2 Hot Electron Dynamics in GaAs, Ge, and Si

5.2.1 Saturation of Free-Carrier Absorption in n-Type GaAs

Free-carrier absorption is readily observed in bulk doped semiconductors in the THz range, where there is often a peak in the absorption spectrum [2, 12]. The free-carrier absorption coefficient (α_c) in semiconductors can be described approximately using the Drude model [13]:

$$\alpha_c(\omega) = \frac{\varepsilon_b \omega_p^2 \gamma}{nc(\omega^2 + \gamma^2)} = \frac{e^2 N_c \gamma}{\varepsilon_0 ncm^*(\omega^2 + \gamma^2)} = \frac{eN_c \gamma^2 \mu}{\varepsilon_0 nc(\omega^2 + \gamma^2)} \qquad (2)$$

where ε_0 is the permittivity of free space, ε_b is the relative permittivity of the semiconductor in the absence of free carriers, ω_p is the plasma frequency screened by ε_b, γ is the momentum relaxation rate, n is the real part of the refractive index, c is the speed of light in vacuum, N_c is the free carrier concentration, m^* and e are the effective mass and electric charge of the free carrier and $\mu = e/(m^*\gamma)$ is the carrier mobility. Note the overall magnitude of the free-carrier absorption coefficient, α_c, is proportional to the free-carrier concentration and the mobility, and inversely proportional to the effective mass. Linear THz-TDS measurements of n-type GaAs revealed the Drude behavior of GaAs that is dependent on both the doping concentration and mobility of the sample.

In order to investigate free-carrier absorption in strong THz fields, nonlinear THz transmission measurements were performed on a 450 μm thick, n-type GaAs wafer with a carrier concentration of 8 x 10^{15} cm^{-3} at 300 K. THz pulse energies and peak fields of up to 2 μJ and 150 kV/cm, respectively, were used. Figure 2a illustrates the averaged THz absorption (obtained by calculating α_{eff} in equation 1 from experimental data) between 0.35 and 1.5 THz

for a range of peak fields. At THz fields smaller than 10 kV/cm, the absorption approaches the values obtained in linear THz transmission experiments conducted using a spectrometer with photoconductive switches. Starting at peak fields of 30 kV/cm, we observe a drastic drop in the absorption coefficient. At fields larger than 100 kV/cm, the saturation effect appears to level off slightly. Figure 2b shows the corresponding absorption spectra for various selected field strengths above 50 kV/cm. Even though the overall spectrum does not change in shape, the absorption drops uniformly over a broad frequency range.

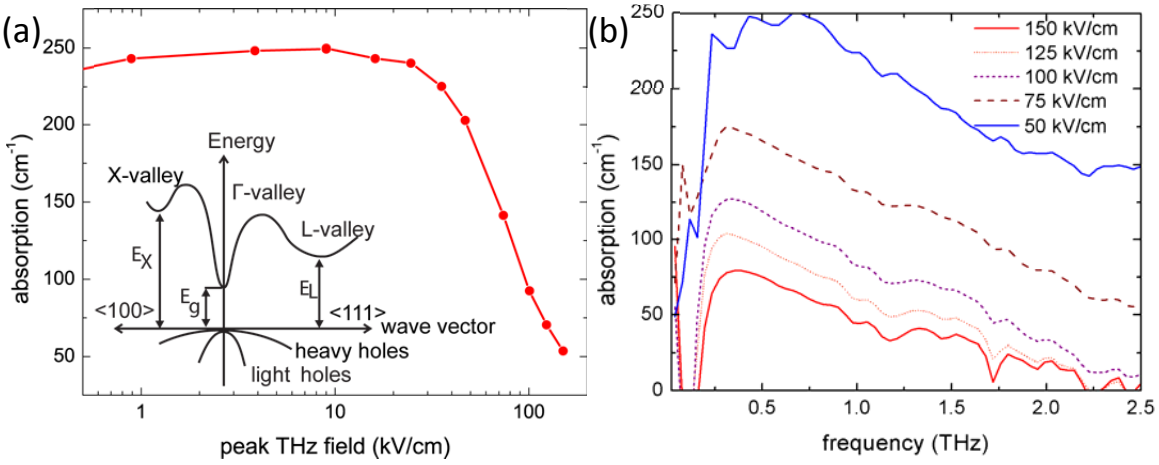

Figure 2: **(a)** Average THz absorption in n-type GaAs for peak fields between 1 and 150 kV/cm. The inset shows the simplified band structure of GaAs. **(b)** Frequency-resolved absorption spectra at selected field strengths.

The decrease in absorption can be explained qualitatively by the change of carrier mobility due to the acceleration of the free electrons in the conduction band by the electric field of the THz pulse. Taking into account energy relaxation during the 1 ps pump pulse duration, we estimate the average carrier energy just after the pump pulse to be in the 0.5–1.3 eV range, exceeding the energy necessary for carriers to cross into the side valleys. These

values are consistent with Monte-Carlo simulations that show that electrons can reach ballistic velocities of up to 108 cm/s within 30 fs in external electric fields [14]. The ballistic acceleration competes with phonon scattering processes after 30 fs, leading to an average heating of the electron gas on a time scale faster than the THz pulse duration of 1 ps.

Electrons with these high energies can scatter into satellite valleys (L and X) of the conduction band, which have an energy separation from the bottom of the zone center (Γ-valley) of 0.29 eV and 0.48 eV, respectively. The effective mass at the zone center is $0.063m_0$ leading to high mobility and high THz absorption. The effective mass in the side valleys is much higher ($0.85m_0$), resulting in much smaller mobility.

In addition to the difference in mobilities among the initial and side valleys, nonparabolicity of the valleys can also result in a decrease in mobility and a concomitant decrease in THz absorption that accompanies the increase in carrier kinetic energy within a single valley. Energy-dependent effective mass and nonparabolicity parameters reported for GaAs [14] indicate that adding 0.3 eV of kinetic energy to electrons in the lowest-energy valleys reduces their THz absorption by 2/3.

5.2.2 Time-Resolved Absorption Measurements of Hot-Carrier Relaxation in GaAs

With simple intensity-dependent transmission measurements we are unable to observe relaxation of the excited carriers back into the Γ valley after the strong heating of the electron gas by the THz pulse. This cooling process, which includes distinct intervalley and intravalley relaxation processes, can only be observed via time-resolved measurements.

Figure 3a shows the time-resolved absorption upon THz excitation of the n-type GaAs sample. The equilibrium frequency-averaged absorption of 125 cm^{-1} drops below 30 cm^{-1} immediately after the arrival of the THz pump pulse. The drop in absorption occurs on the same timescale as the time resolution provided by our pulses. A complete recovery of the absorption is reached after 7 ps. An exponential fit of the absorption (solid curve in Figure 3a) yields a carrier relaxation time of τ_r = 1.9 ps. In the spectrally resolved data (shown in Figure 3b), we observe that the equilibrium Drude form of the spectrum is fully restored by about 5 ps. Similar to the field-dependent nonlinear transmission measurements shown in Figure 2a, the time-resolved absorption spectra in our pump-probe measurements can be fit to a simple Drude model. Keeping the carrier concentration at the constant value obtained from Hall measurements by the manufacturer, we can extract an averaged effective mass. The result of the time evolution of this quantity for different pump strengths is shown in Figure 4. At high field strengths the average effective mass exceeds a value of $0.3m_0$ suggesting that a sizeable fraction of the carriers is scattered into the side valleys with higher effective mass. As the pump intensity is decreased, the average effective mass decreases as well. At the lowest intensity (the data at 7% of the maximum intensity in figure 4) the magnitude of the time-dependent response goes to zero, which is consistent with the nonlinear transmission measurements presented in figure 2. Qualitatively we also infer a rise in the momentum scattering time from the slightly longer relaxation time observed at high pump field strengths, although the data quality does not allow us to make quantitative conclusions.

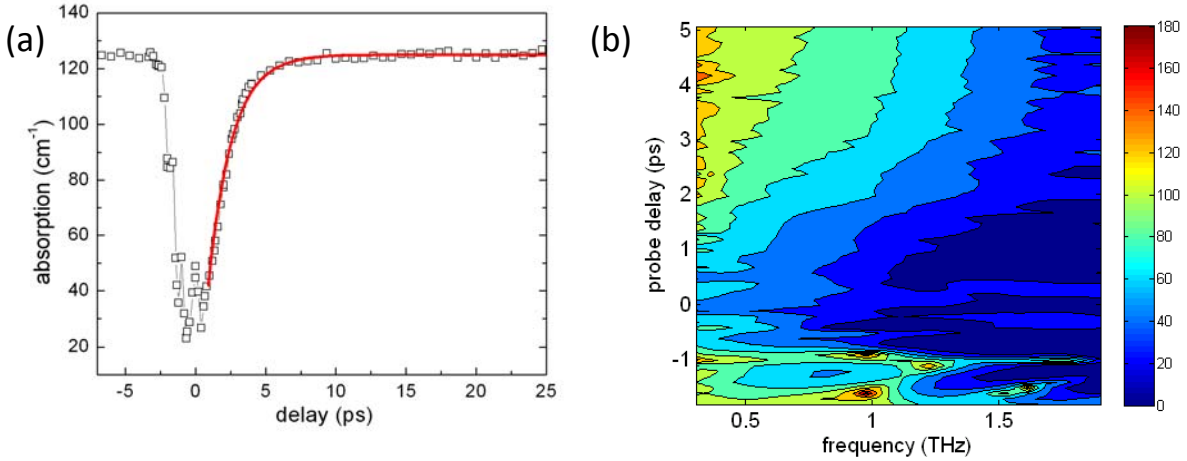

Figure 3: (a) Recovery of the frequency-integrated absorption as a function of THz probe delay after the arrival of a strong THz-pump pulse at t=0. **(b)** Frequency dependent absorption coefficient (cm^{-1}) as a function of probe delay times, revealing the relaxation of the excited carriers back to their equilibrium Drude-like behavior 5 ps after the arrival of the pump pulse.

From our data, we infer that the relaxation time from the L-valley is much larger than the scattering time into it, and we account for this by considering the difference in the number of final states for both processes. Additionally, repeated scattering from the upper Γ-state to the L-valley make the L-valley's relaxation time appear longer. A detailed discussion of intervalley scattering in GaAs is presented in section 5.2.5 in relation to experiments on germanium and silicon.

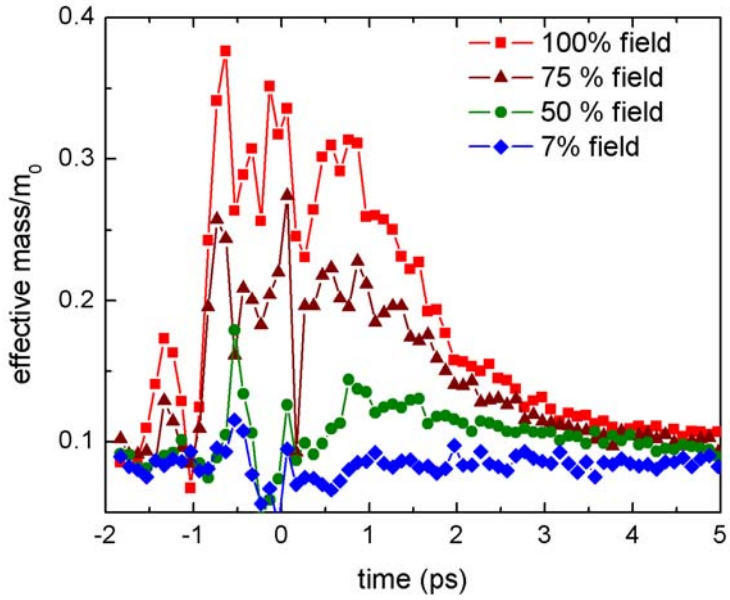

Figure 4: Average effective mass, relative to the electron mass, obtained from Drude fits to the absorption spectra for different pump field strengths.

5.2.3 Saturation of Free-Carrier Absorption in n-Type Ge

We have also studied nonlinear free-carrier absorption in n-type germanium (Ge). Results of nonlinear transmission measurements in a ⟨111⟩ oriented sample are shown in Figure 5. The 6-mm-thick sample contained phosphorus impurities [15], identified by THz time domain spectroscopy (THz-TDS) [16] using low THz fields at 10 K, making the sample n-type with a free-electron concentration of n = 5 (± 2) x 10^{14} cm^{-3} at room temperature. THz pulse energies and peak intensities reached 2 μJ and 150 MW/cm2, respectively. At THz pulse energies larger than 0.2 μJ, we observe strong saturation of the free-carrier absorption (Figure 5b). The absorption spectra at different field strengths, obtained by Fourier transformation of the THz field profiles, are shown in the inset of Figure 5a. At the maximum field strength, the absorption spectrum is strongly saturated over the frequency range between 0.2 and 1.8 THz. At low THz fields

corresponding to pulse energies below 10 nJ, the shape of the absorption spectrum approaches the familiar Drude model shape observed in low-intensity THz-TDS measurements at room temperature (dotted line in Figure 5a). An unexpected behavior is apparent in the absorption spectra at intermediate pulse energy (100 nJ). In this case the absorption is still substantially saturated at low frequencies but at frequencies above 1.0 THz the absorption is increased relative to the low-intensity values. This behavior was not observed in similar intensity-dependent transmission measurements in GaAs or Si, although these materials also showed strong saturation of free-carrier absorption at high THz pulse energy.

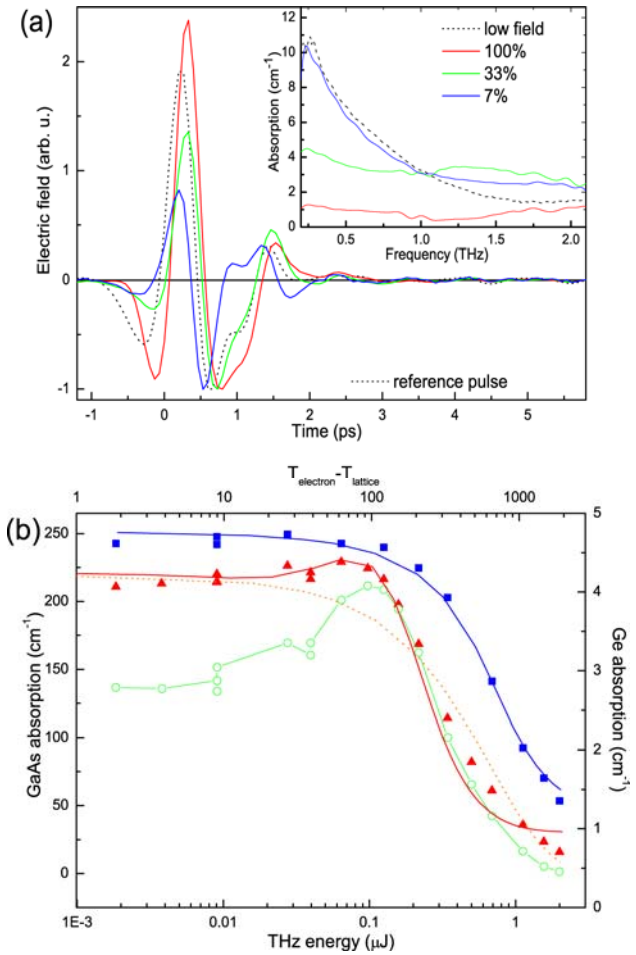

Figure 5. (a) Incident (dotted black) and transmitted THz pulse field profiles for 6 mm thick germanium at 100%, 33% and 7% of the maximum THz field strength. The temporal profiles are

normalized to the second negative peaks. The inset shows the corresponding absorption spectra and the low-field (dashed) absorption spectrum measured with 9 orders of magnitude lower THz pulse energies. (b) Frequency-integrated THz absorption versus THz pulse energy for GaAs (squares) and Ge (triangles), at room temperature. Also shown is the Ge absorption integrated in the 1.0-1.3 THz range (open circles) which highlights the increase in absorption at intermediate THz field levels. The solid and dotted curves are results of model calculations.

Figure 5b shows spectrally integrated absorption data from intensity-dependent transmission measurements for Ge and n-type ⟨100⟩ oriented GaAs [17] (carrier concentration N_c = 8 x 10^{15} cm^{-3}, thickness 0.4 mm) in which the incident THz pulse energy was varied by three orders of magnitude. At intermediate THz pulse energies (100 nJ) the spectrally integrated absorption in Ge is greater than in the unperturbed sample by up to 10% and up to 30% when integrated only in a frequency range between 1.0 and 1.3 THz. In contrast, the absorption in GaAs decreases monotonically with increasing THz pulse energy. This unusual behavior of Ge was not observed in earlier absorption saturation measurements [5] conducted with narrowband 40 ns duration pulses at 606 GHz frequency.

5.2.4 Time-Resolved Absorption Measurements of Hot-Carrier Relaxation in Ge: Comparison to GaAs and Si

To examine the dynamics of the electronic responses, THz-pump/THz-probe measurements were performed as described above. Figure 6 displays THz probe field profiles after transmission through the Ge sample for 1, 3, and 5 ps delay between the pump and the probe pulses. The corresponding absorption spectra are plotted in the inset. For short probe delays the absorption spectra of Ge (and not of GaAs and Si) are significantly different from a Drude-type free-carrier spectrum. At low frequency the absorption shows a narrow peak and at higher frequency the absorption is flat. For intermediate delays this flat part increases with increasing

negative slope and the narrow peak becomes less pronounced. For long delays, the spectrum develops into a Drude-type form. The absorption measured at long delays is somewhat larger than the linear absorption because the probe pulse, though much weaker than the pump, still induces some nonlinear absorption as shown in Figure 5b. Contrary to Ge, GaAs and Si showed strong saturation at all frequencies measured, exhibited Drude-type spectra at all delay times, and recovered, but did not exceed, the original absorption strength over all frequencies at long times. The saturation and time-dependent recovery of the spectrally integrated absorption is shown in Figure 7 for Ge, GaAs, and n-type ⟨100⟩ oriented Si (0.45 mm, N_c = 5 x 10^{14} cm^{-3}).

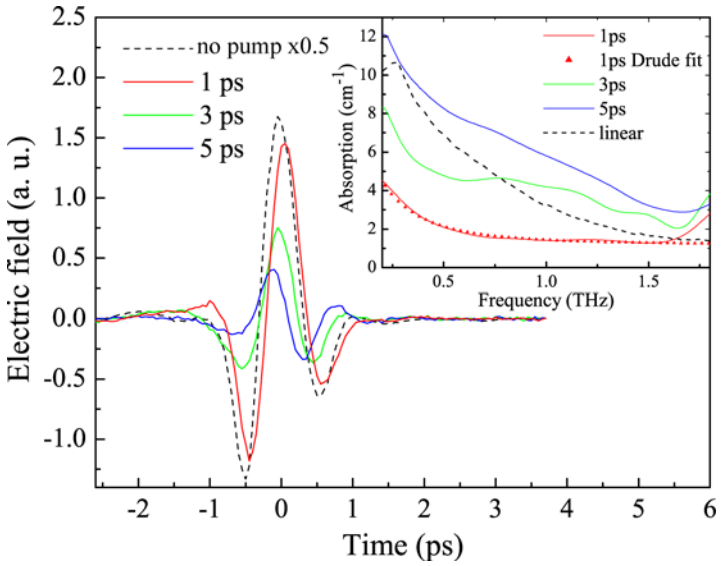

Figure 6. The incident (dotted black, scaled by a factor of 0.5) and transmitted THz probe field profiles for 6 mm thick germanium measured with the THz-pump/THz-probe setup for 1, 3, and 5 ps probe delays, respectively. The electric fields are measured in arbitrary units but the scale for the different transmitted traces is the same. The inset shows the corresponding absorption spectra, the linear absorption spectrum (dotted black), and a fit to the sum of two Drude-type components at 1 ps (red triangles).

5.2.5 Intervalley Carrier Scattering

The observed saturation and subsequent recovery of the free-carrier absorption can be explained qualitatively in terms of electron scattering amongst different valleys. The inset of Figure 7a shows the simplified conduction-band structure for Ge. The L valley has the lowest energy and it is initially populated. In GaAs, the conduction band structure has different relative values for the Γ, L, and X valleys. The Γ valley has the lowest energy and is occupied initially before the arrival of the THz pulse. For Si, the X(Δ) valley has the lowest energy.

A simple estimate based on the amount of absorbed THz energy and the number of carriers in the illuminated volume indicates that the average energy deposited per free carrier at the highest pump pulse intensity was 2.1 eV in GaAs and 0.9 eV in Ge, providing access to side valleys [13] at higher energies: the L (0.31 eV) and X (0.52 eV) valleys in GaAs and the Γ (0.14 eV) and X (0.19 eV) valleys in Ge. The energized electrons may be scattered into the side valleys during the THz pump pulse because the intervalley scattering time is typically on the subpicosecond time scale [18]. Since the mobility in the X valley of Ge is nearly five times smaller than in the initial L valley, scattering into the X valley decreases the free-carrier absorption according to equation 2. In the L and X valleys of GaAs the effective mass is about three and six times larger, respectively, than in the initial valley [19]. Assuming comparable scattering rates in the different valleys, this means correspondingly lower mobilities in the L and X valleys. Therefore scattering into these side valleys results in a decrease in the THz absorption. Besides the mobility differences of the initial and side valleys, the nonparabolicity of the valleys can also result in a decrease in mobility and THz absorption with increasing carrier kinetic energy within a single valley.

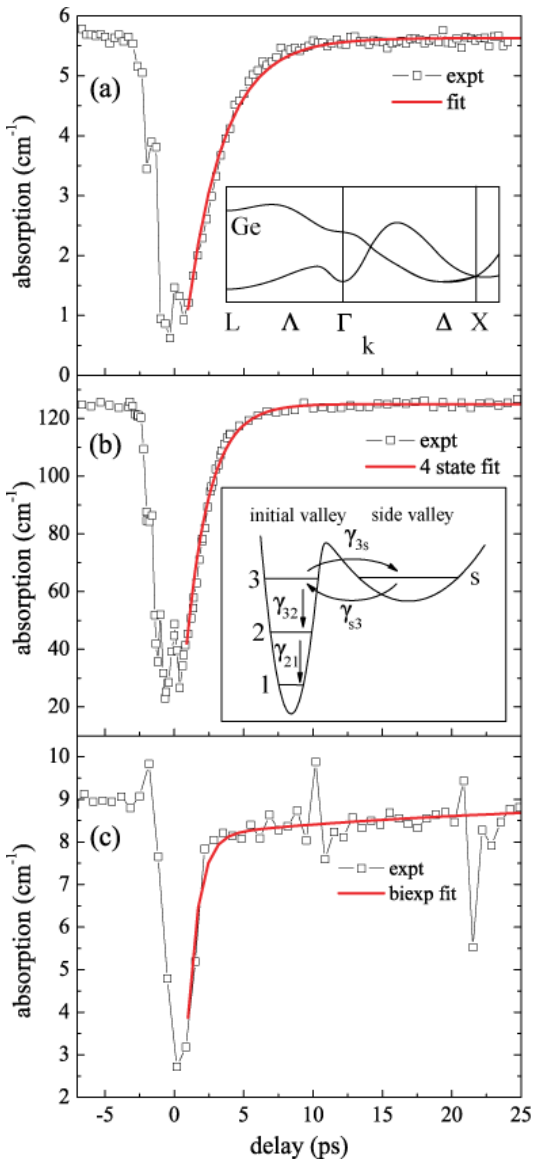

Figure 7. Spectrally averaged THz probe pulse absorption versus delay for (a) Ge, (b) GaAs, and (c) Si. The insets show (a) schematic illustrations of the conduction band structure for Ge and (b) the states and transfer rates of a simplified rate equation model.

After the THz pump pulse leaves the sample, the electrons scatter among the initial and side valleys, the average electron energy decreases (losing energy to the lattice) [20], and the absorption recovers. A three-level rate equation model for the populations of states in the initial and side valleys in GaAs (neglecting the high-lying X valley) was successfully

demonstrated earlier [20] to simulate optical-pump/THz-probe experiments [4]. The inset of Figure 7b shows an extension of this model to four states to take into account the nonparabolicity of the initial valley. From the populations $n_i(t)$ obtained for the different states *i* in the model, the overall absorption coefficient was calculated as $\alpha(t) \propto \sum_i \mu_i n_i(t)$, where μ_i is the mobility of state *i*. For GaAs, using this simple model and the previously reported intervalley scattering rates [20] γ_{s3} = 2 ps^{-1} and γ_{3s} = 20 ps^{-1} and intravalley relaxation rate [14] γ_{32} = 20 ps^{-1} yielded a good but not perfect fit to the measured spectrally averaged time-dependent absorption, shown in Figure 7b, with the best-fit parameter value γ_{32} = 9 ps^{-1}. A rate equation model of this sort, however, is inadequate to describe the dynamics of highly excited free carriers in detail. Monte Carlo simulations taking into account the full band structure [19] can provide more reliable results. In the absence of such calculations, we fit the spectrally integrated absorption recovery dynamics to single or multiple exponential decays in order to obtain approximate time scales for overall energy relaxation of the hot carriers in the different samples. For GaAs and Ge we obtained good fits (see Figure 7) with single-exponential decay times τ_r = 1.9 and 2.7 ps, respectively. For Si, a biexponential decay was necessary, with distinct time constants τ_{r1} = 0.8 ps and τ_{r2} = 24 ps. Since in Si, there is only one rather high-lying (L) side valley (about 0.8 eV above the bottom of the conduction band) that is accessible energetically, the fast decay may reflect the rate of relaxation out of this valley and the slow decay the cooling of the electrons in the initial nonparabolic [19] X valley.

Our most striking results are from Ge, where we observed increased (rather than decreased) absorption at intermediate THz pulse energy (Figure 5b) and non-Drude-type transient absorption spectra for short probe delay times (Figure 6 inset). Compared to GaAs and

Si, Ge is unique in that it has an intermediate-energy Γ valley whose mobility is higher rather than lower than that of the initially occupied (L) valley. Although the population of the Γ valley is usually neglected for static cases [21] since the density of states (DOS) is 50 and 150 times lower than in the initial (L) and the highest lying (X) valleys, respectively, its dynamical effects are strongly evident in our pump-probe and nonlinear transmission measurements. As we will discuss, both unusual observations can be explained assuming significantly larger Γ valley population than that expected from the DOS and a thermalized electron energy distribution among the valleys.

The non-Drude transient absorption spectra may arise from different Drude-type spectra associated with the different valleys, one component corresponding to a narrow absorption band from the Γ valley and another component corresponding to an extremely broad absorption band from the other low-mobility valleys. As shown in the inset of Figure 6, a good fit to the observed absorption spectrum at 1 ps probe delay is possible assuming that 2.4% of the conduction-band electrons are in the Γ valley and the momentum relaxation time is ~3 times longer (1.4 ps^{-1}) than in the L valley. The Γ valley population calculated from the DOS and thermalized electron energy distribution is only 0.5% (five-fold smaller) assuming parabolic bands and about 0.02% (120-fold smaller) taking the nonparabolicity of the L valley into account.

We used a simple model to estimate the carrier absorption saturation as a function of THz pulse energy, assuming that the overall absorption was the sum of absorption by electrons in the different valleys and accounting for the nonparabolicity of the lowest valley only. The

energy dependent distributions of electrons in the three valleys were calculated from the DOS $g_i(E) \propto (m_i^*)^{3/2}$ and the Fermi-Dirac distribution $F_i(E)$, and the absorption was calculated as

$$\alpha \propto \sum_i \int g_i(E) F_i(E) \mu_i(E) dE \qquad (3)$$

where in the lowest valley only, m_i^* and μ_i were treated as functions of E.

For GaAs this simple model resulted in monotonically decreasing THz absorption as a function of THz pulse energy (or electron temperature), with a good fit to the measured data (Figure 5b) assuming an electron temperature of 2200 K upon irradiation by a 2 μJ THz pump pulse. As indicated by the dotted curve in Figure 5b, the result of a similar calculation for Ge also shows monotonically decreasing absorption with increasing THz pulse energy, without the maximum in absorption seen experimentally at intermediate THz pump pulse energies. However, a good fit is obtained with the same momentum relaxation rate found above, γ = 1.4 ps^{-1}, for the Γ valley, with the population in the Γ valley 50 times higher than its expected thermalized population and with an electron temperature of 11000 K at 2 μJ THz pump pulse energy, i.e., five times higher than the electron temperature in GaAs. Of course, comparable electron temperatures are expected for a given THz pulse energy in GaAs and Ge at the input faces of the samples. However, the electron temperature at the output face is eight times larger for Ge than for GaAs because far less of the THz pump pulse is absorbed in the Ge sample than in the GaAs sample. As a result, the average electron temperature throughout the sample is significantly larger in Ge than in GaAs. The electron temperature in Ge corresponds to an average electron energy of 0.95 eV. When accounting for 20–30% energy dissipation to the

lattice during the pump pulse [18], this corresponds to a total absorbed energy of 1.2 eV, comparing favorably to the estimate of 0.9 eV mentioned above.

Like the non-Drude transient absorption spectrum in Ge, the increased absorption in Ge at moderate THz pulse energies can be accounted for by the high mobility of the Γ valley but only assuming a substantially higher transient population in that valley than determined by DOS considerations. This extra population might be caused by direct acceleration of the electrons by the THz field (without phonon scattering), which is possible since the THz pulse duration is comparable to the electron-phonon scattering time. A strong increase in THz absorption was also observed in InSb by high intensity THz transmission [22] and THz-pump/THz-probe [23] measurements and this effect was explained by the impact ionization process (this will be discussed later in this chapter). Although Ge has a band gap and impact ionization threshold [19] more than three times larger than InSb, the field of the THz pulses with the highest energy should be enough to achieve electron energies larger than the band gap, in the absence of significant energy relaxation during the pulse. Hence, from a purely energetic point of view we cannot rule out impact ionization as the cause of a small absorption increase at intermediate energy. However, this explanation is unlikely for two reasons. First, increased absorption from impact ionization in InSb was observed to occur after the THz pulse [23] but not during it. Second, the largest effect of impact ionization should be expected at the highest THz energies and not at intermediate energies.

5.2.6 Saturable Absorption and Dynamics in GaAs, Ge, and Si: Conclusions

We have investigated the differences of intervalley and intravalley dynamics of hot free electrons in bulk semiconductors in the absence of band-to-band excitation by time-resolved and frequency-resolved THz-pump/THz-probe measurements. We have observed unique effects in bulk Ge that we attribute to a significantly higher than thermalized population of the Γ valley of the conduction band whose mobility is higher than that of the lowest-energy valley. The behavior is simpler in Si and GaAs, whose side valleys have lower mobilities than their initially populated valleys. Although the empirical Drude model should not be adequate for the highly excited electron distributions that we generate, the qualitative features of our data are reproduced. More quantitative insight can be achieved by Monte Carlo simulations [19] taking into account the contributions of different scattering mechanisms and the full band structure which are beyond the scope of this work. Experimentally, direct observation of the intervalley and intravalley dynamics might be achieved by following pulsed THz excitation with infrared probe pulses, in order to monitor absorption or stimulated emission from individual conduction-band valleys.

5.3 THz-Induced Impact Ionization in InSb

Indium antimonide (InSb) is a model system for the study of hot-electron dynamics due to its low band gap of 170 meV at room temperature [24, 25] and the fact that it has the highest electron mobility and saturation velocity among all known semiconductors. The wealth of nonequilibrium transport phenomena that have been observed in this material [1, 26, 27] is of special interest due to the large nonparabolicity of the conduction band [28] which results in

negative differential mobility at comparatively low dc voltages and strong interactions of hot carriers with the LO phonon mode. Some of these properties are exploited for use in a few types of technologies. The small bandgap in InSb makes it well suited for applications in infrared sensors covering the wavelength range from 1 μm to 5 μm [29]. The high mobility of InSb enables fabrication of transistors with extremely high switching speeds [30]. However, further technological applications are complicated by the low threshold for impact ionization. As a result, the elucidation of carrier dynamics on the ultrashort timescale is of great technological as well as fundamental interest.

Impact ionization by electric fields is a well known effect in InSb [1]. In bulk InSb, impact ionization is usually observed at relatively low dc fields of several hundred V/cm and occurs when the electron has acquired enough energy from the driving field to exceed the ionization threshold [31], usually on the order of the band gap. The balance between the acceleration of carriers in an applied external field on one hand and the dissipation of energy by collisions with phonons [32] on the other hand plays a crucial role. Recently, high-intensity THz sources have made it possible to investigate impact ionization by purely optical methods. Intensity-dependent THz transmission measurements with 40 ns long pulses [33, 34] and more recently Z-scan measurement with single-cycle pulses [22] have been performed. In the latter case the THz pulse duration was as short as the characteristic electron momentum relaxation time $\tau \approx$ 1–10 ps.

In this section, I will discuss experimental observations of carrier generation in InSb at 80 and 200 K due to impact ionization induced by below-bandgap infrared (IR) radiation on the picosecond time scale, where $\omega\tau \approx 1$. Near single-cycle pulses with field strengths up to 100

kV/cm and a duration of 1 ps were used. The rise time of the THz pulses was less than the electron momentum relaxation time of τ = 2.5 ps in InSb at 77 K. This leads to highly accelerated carriers that can cause carrier multiplication through impact ionization [17]. THz radiation can also be used as a very sensitive probe to directly monitor free-carrier behavior in semiconductors [35]. Because of the small bandgap, undoped InSb has a high intrinsic carrier concentration of 2 x 10^{16} cm^{-3} at room temperature. Even at 200 K the absorption still exceeds 200 cm^{-1} at frequencies below 1 THz. At temperatures of 80 K, the intrinsic carrier concentration is on the order of 10^9 cm^{-3}, and the remaining carrier concentration is dominated by impurities. The combination of sub-bandgap direct excitation of doped semiconductors and time-resolved spectroscopy provides an excellent tool for observing carrier dynamics [17, 36].

5.3.1 Experimental Setup

The experimental setup shown in Figure 1 was used for collinear THz-pump/THz-probe measurements. Spectral analysis of our THz-pump/THz-probe results was conducted in the 0.2–1.6 THz range where the spectral amplitude was sufficiently high. A pair of wire-grid polarizers was used to attenuate the THz pulses for intensity-dependent studies. The samples were an n-type Te doped and a nominally undoped InSb wafer, each 450 µm thick, with carrier concentrations at 77 K of 2.0 x 10^{15} cm^{-3} and 2.0 – 4.9 x 10^{14} cm^{-3} respectively. The mobility at 77K as specified by the manufacturer was 2.5 x 10^5 $cm^2/V{\cdot}s$ and 0.5 x 10^6 $cm^2/V{\cdot}s$ for the undoped sample. The THz fields were polarized parallel to the (100) axes of the crystals. We measured the THz fields *E(t)* that reached the ZnTe crystal with and without the sample in the beam path from which we calculated the effective absorption coefficient (equation 1).

5.3.2 THz-Induced Impact Ionization Dynamics in InSb

Figure 8 shows time-resolved absorption traces for the doped sample at 80 and 200 K covering a probe delay range of up to 30 ps. At both temperatures, the absorption increases after THz excitation and reaches a plateau after 30 ps with a total increase in absorption of 80–90 cm^{-1}. This rise is caused by the generation of new carriers through impact ionization. Unique to the measurement at 200 K is an initial dip in the absorption immediately after THz excitation. The drop in absorption in this case is caused by a decrease in the mobility of the hot electrons as a result of both the strong nonparabolicity of the Γ valley in the conduction band of InSb [37] and scattering of the hot electrons into side valleys [5, 36, 38]. No such initial decrease is observed at 80 K. The difference in the early-time absorption behavior is due to the opposing effects of impact ionization and carrier heating, both caused by the THz pump pulse. Electron heating leads to a decrease in mobility due to the strong nonparabolicity in the conduction band of InSb [37] and scattering into side valleys with lower mobility [36], similar to the case of GaAs discussed in the previous section. The carrier mobility μ directly influences the absorption coefficient α which is described approximately by the Drude model and parametrized by the plasma frequency $\omega_p = (Ne^2/\epsilon_0\epsilon_\infty m^*)^{1/2}$ and the momentum scattering rate γ in equation 2. In the low-frequency limit ($\omega \ll \gamma$) the absorption α is directly proportional to the carrier mobility $\mu = e/\gamma m^*$. Due to the small band gap of InSb, the intrinsic carrier concentration at 200 K is much higher than that at 80 K. The effect of absorption saturation is thus much stronger at 200 K. After 4 ps, the additional absorption caused by the newly generated carriers exceeds the saturation effect, the magnitude of which is also diminishing as a result of the

cooling of the hot carriers, thereby leading to the delayed rise observed in the overall absorption.

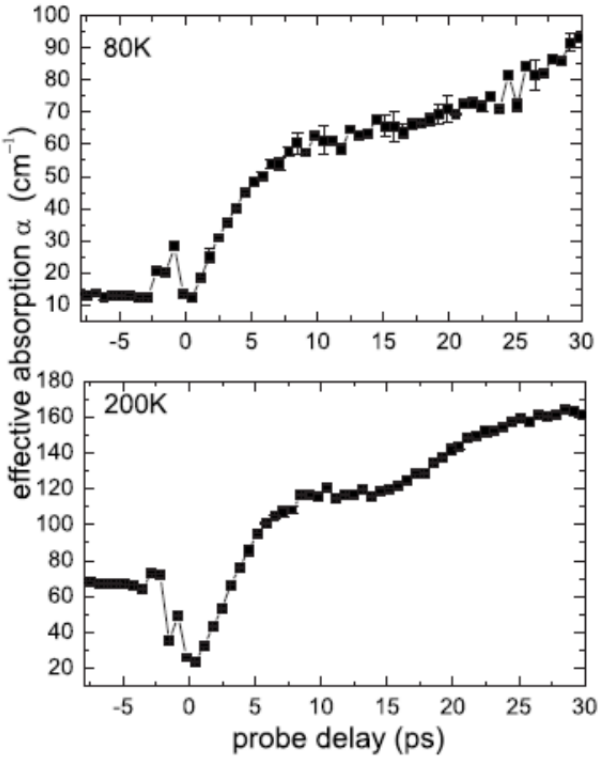

Figure 8: THz-pump/THz-probe time-resolved absorption data, spectrally averaged over the 0.2-1.6 THz range, from doped InSb (N_c = 2.0 x 10^{15} cm^{-3}) at 80 K and 200 K. The deviation starting at 12 ps is due to reheating caused by the THz pulse reflection within the sample.

Comparison between the equilibrium absorption of InSb at 80 K and the value measured 30 ps after intense THz excitation shows an eightfold increase, indicating a similar increase in carrier concentration from 2 x 10^{15} cm^{-3} to 1.6 x 10^{16} cm^{-3} (the absorption is proportional to the carrier density, see equation 2). The same analysis cannot be applied reliably at 200 K due to the very large intrinsic carrier absorption, which overwhelms the dynamic range of our spectrometer system. The absorption at high carrier concentrations (such as those at 200 K)

takes away all of the spectral density from the low end of our experimental THz bandwidth (where the absorption is the strongest) such that the measured effective absorption is lower than what would be indicated by the actual carrier concentration in the sample. This leads to an apparent saturation of the frequency-averaged absorption shown in Figure 8b. Some signal at $t < 0$ appears in Figure 8a because of the nonlinear interaction in the LN crystal between the THz-pump and -probe fields, the optical pulses that generate them, as well as nonlinear interactions in the sample.

We employed a simple system of rate equations, displayed below, to model the dynamics of impact ionization in the first 30 ps, assuming quadratic scaling (as proposed by Keldysh) [39] of the impact ionization probability above the threshold energy $\varepsilon_{th} \approx \varepsilon_g$,

$$\frac{dN}{dt} = C(\varepsilon(t) - \varepsilon_{th})^2 \cdot N(t) \cdot \Theta(\varepsilon(t) - \varepsilon_{th}) \qquad (4)$$

$$\frac{d\varepsilon}{dt} = -C(\varepsilon(t) - \varepsilon_{th})^2 \cdot \varepsilon_{th} \cdot \Theta(\varepsilon(t) - \varepsilon_{th}) - \frac{\varepsilon}{\tau_\varepsilon} \qquad (5)$$

In this model $N(t)$ is the electron concentration, $\varepsilon(t)$ is the average carrier energy, and $\Theta(t)$ is the Heaviside step function. We used a numerical value of $C = 7 \times 10^{50}$ $J^{-2}s^{-1}$ obtained from by Devreese et. al. [40]. The energy relaxation time τ_e was assumed to be time and energy independent.

A numerical solution, taking into account the reflection at the sample interface, is shown in Figure 9. The effect of absorption saturation due to carrier heating [36] was accounted for approximately by assuming $\alpha_{eff} \propto N(t)[\varepsilon_0 - \varepsilon(t)]/\varepsilon_0$ where ε_0 is the average carrier energy immediately after excitation. From this fit we obtained a phenomenological

relaxation time τ_e = 7 ps, much longer than the 1.3–2.0 ps calculated for the energy relaxation time in the dc limit by Kobayashi [41].

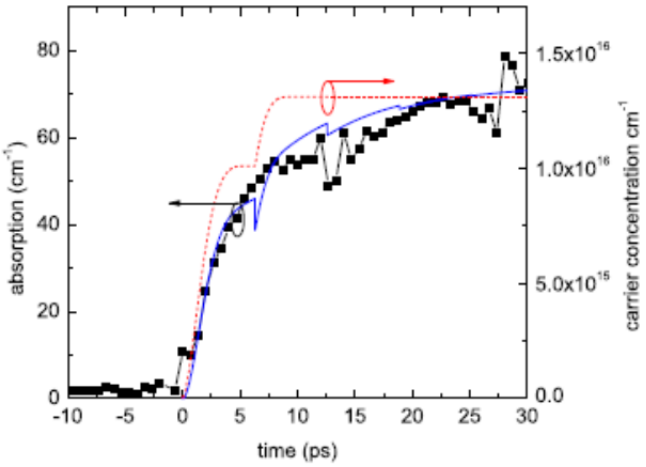

Figure 9: Experimental data for the undoped sample at 80 K (squares) and simulation results for the carrier concentration (dashed) and absorption (solid line) based on quadratic scaling of impact ionization rate with carrier energy. Parameters used were: $N(t = 0) = 5 \times 10^{13}$ cm^{-3}, energy relaxation time τ_e = 7 ps and $\varepsilon_0 = \varepsilon(t = 0) = 1.3\ eV$.

5.3.3 Intensity Dependence of Impact Ionization in InSb

Intensity-dependent experimental results similar to the one shown in Figure 10 indicate no observable absorption increase for single-cycle THz pulses with peak electric fields lower than 75 kV/cm. The intensity dependence of impact ionization by 40 ns far-infrared pulses has been observed by Ganichev [33] using photoconductive measurements. In this case, the electron concentration change $\Delta n/n_0$ by impact ionization could be modeled using the Fokker–Planck equation, leading to a dependence on the applied electric field E given by

$$\frac{\Delta n}{n_0} = A \exp\left(-{E_0^2}/{E^2}\right) \qquad (6)$$

where A is a proportionality constant.

To check the validity of equation 6 in the regime of very short pulses with high energy, we performed a series of intensity-dependent pump-probe measurements with the probe delay held constant at 35 ps after the arrival of pump. Figure 10b shows the intensity-dependent spectrally averaged THz absorption for the doped InSb at 80 K. We observe saturation of new carrier generation at high pump fluences. The solid curve shows a fit to the experimental data using equation 6 with parameter values A = 14.5 and E_0 = 104 kV/cm. The parameter E_0 is a characteristic field that gives electrons enough energy to create an electron–hole pair. While the fit gives adequate agreement with equation 6, the critical field E_0 is roughly 2 orders of magnitude higher than that observed in [33] for 40 ns THz laser pulses. This discrepancy can only be understood when taking into account the fundamentally nonequilibrium carrier heating induced by the single-cycle THz pulse as opposed to the quasi-CW AC field case in previous experiments.

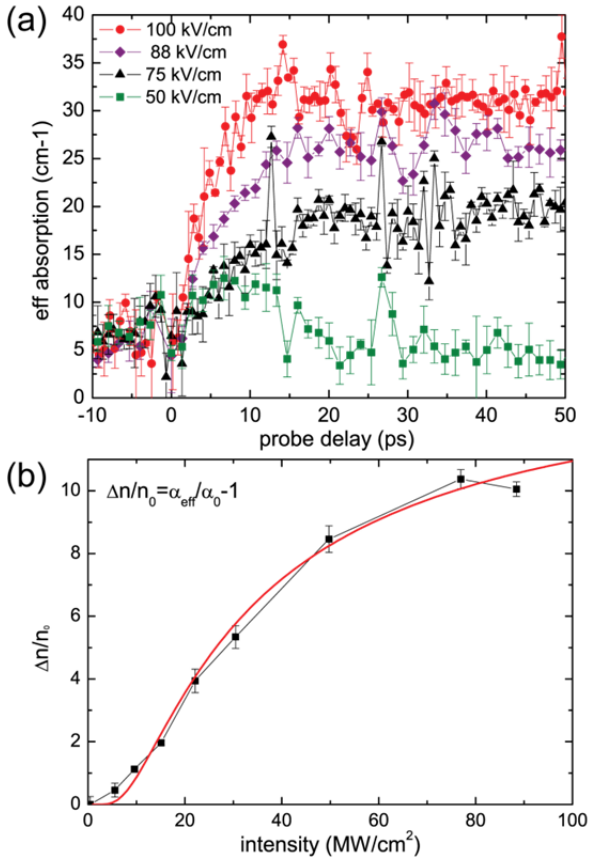

Figure 10: (a) Time-resolved averaged absorption (0.2–1.6 THz) in undoped InSb at 80 K for various fields. (b) Intensity-dependent average absorption for the doped sample 35 ps after the THz excitation, the solid line is a fit to Eq. (2).

DC measurements have shown an exponential increase in the carrier-generation rate [42] in the 250–500 V/cm range and the rate saturated above 800 V/cm at a value as low as 0.007 ps^{-1}. In our opinion, ionization of shallow impurities, instead of band-to-band impact ionization, is responsible for this behavior. For a drift velocity of 4 x 10^7 cm/s in fields above 500 V/cm [43] and the dependence of the avalanche multiplication on the electric field [44], we are able to extrapolate a rate of 18 ps^{-1} for a static field strength of 48 kV/cm. The corresponding single-cycle generation rate of 18 ps^{-1} was obtained from the best fit of Figure 9, in which a peak electric field of 100 kV/cm was used. Consequently, we observed that the peak field

required for impact ionization by the single-cycle THz-pulse excitation is a factor of 2 larger than in the static field case. This difference can be attributed to the significantly shorter peak pulse duration compared to the momentum relaxation time in InSb and the fact that in equations 4 and 5 we followed the average carrier energy and not an energy distribution.

5.3.4 Electron-Lattice Interaction in InSb

In order to elucidate the lattice dynamics further, we performed a series of intensity-dependent pump-probe measurements with a fixed probe delay. Figure 11 shows the absorption spectra obtained with different pump intensities at a probe delay of 35 ps for the doped and undoped samples at 80K. At frequencies below 0.6 THz, we observe the expected Drude-type contribution from free-carrier absorption which is more pronounced at higher pump fluence. In addition, we observe a distinct absorption peak at 1.2 THz in the undoped sample and a weak feature that indicates a similar peak in the doped sample.

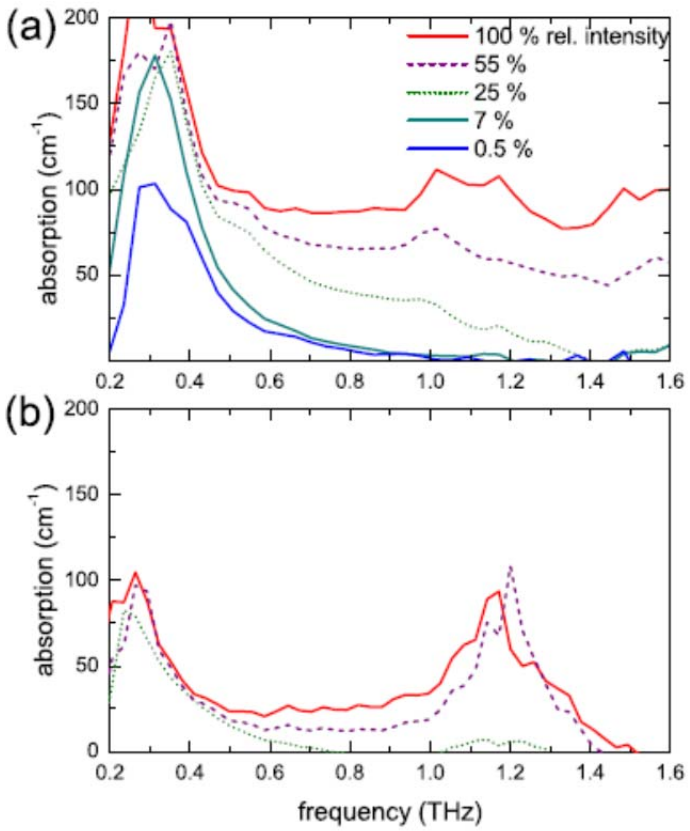

Figure 11: THz absorption spectra at various pump intensities measured at a probe delay time of 35 ps for the (a) doped sample and (b) undoped sample at 80K.

Figure 12 illustrates the appearance of this peak for pump-probe delay times up to 7 ps in the doped sample at 200 K. The evolution of the low-frequency Drude behavior is clearly separated from the phonon-mediated peak at 1.2 THz.

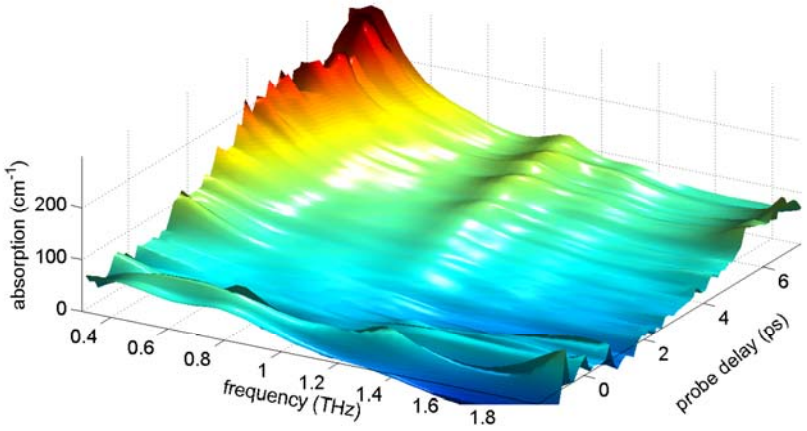

Figure 12: Frequency dependent absorption coefficient of doped InSb for probe delays up to 7 ps at a temperature of 200 K.

The amplitude—but not the frequency—of the peak is highly intensity dependent and appears to approach its asymptotic value just above 50% of the maximum intensity. The behavior of this peak suggests that its origin is lattice vibrational rather than electronic. Polar optical phonon scattering is well known as the dominant energy-loss mechanism for hot electrons in InSb [45]. The main channel of energy loss is through the emission of LO phonons with a frequency of 5.94 THz. These phonons decay into acoustic modes through anharmonic coupling and through the second-order electric moment of the lattice [46].

A series of sum and difference phonon peaks between 1 and 10 THz has been observed and assigned in the far-infrared spectrum of InSb [47]. At very low THz fields, produced by a photoconductive antenna, we also were able to observe some of these weak absorption peaks in the undoped sample. The assignments reported [47] indicate a 1.2 THz difference frequency between the LO and LA modes at the zone boundary. The drastic change in the absorption coefficient of the difference phonon peak is the result of large changes in phonon populations

due to energy transfer from the hot electrons generated by the THz-pump pulse. Monte Carlo simulations [48] have shown that substantial phonon population changes can occur even at comparatively low dc fields. The simulations calculate phonon population changes due to an applied step-function dc field. Phonon populations begin to change on the picosecond timescale after instantaneous switching of the applied dc field.

The temporal evolution of the electron-lattice interaction can be studied by separating the spectrally resolved pump-probe data into two different frequency bands: 0.2–0.6 and 1.0–1.2 THz. This is illustrated in Figure 13 where data from time-resolved measurements at full THz intensity and at half the full intensity are shown for the doped sample. For the low-frequency band, the rise in absorption is almost identical at the two intensities, while the contribution from the absorption between 1.0 to 1.2 THz is reduced considerably when the THz intensity is halved. The higher-frequency portion of the absorption spectrum is clearly more sensitive to the intensity of the THz-pump pulse, as illustrated in Figure 11b. In addition, at the lower intensity there is a delay of approximately 10 ps before the rise of the absorption signal. This delay was reproduced qualitatively for all measurements at intermediate THz-pump levels. We do not have a complete understanding of the intensity dependence of the delay, but we note that the delay is on the order of the LO phonon decay time in InSb [46] suggesting that it arises from LO phonon decay into LA phonons. The large fluctuations observed at 12 and 24 ps are due to THz-pump pulse reflections in the sample that are overlapped in the electro-optic crystal with the THz probe pulse.

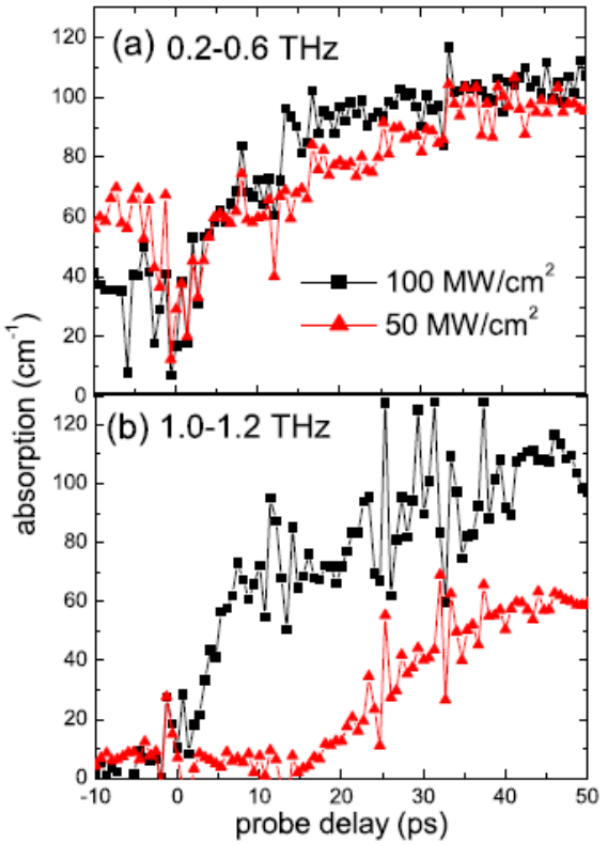

Figure 13: Time-resolved spectrally averaged absorption for the doped sample at 80 K with 100% pump intensity (black squares) and 50% pump intensity (red triangles). Spectrally averaged absorption is shown in the range **(a)** 0.2-0.6 THz, and **(b)** 1.0-1.2 THz.

5.3.5 Impact Ionization in InSb: Conclusions

The presently developed THz-pump/THz-probe technique permits sensitive monitoring of carrier dynamics in semiconductors on the picosecond timescale. In InSb, we observed the dynamics of carrier generation by impact ionization, yielding up to a sevenfold increase in carrier density following intense THz excitation. Our ability to spectrally analyze the time-resolved signal allowed us to detect distinct features that we attribute decay of electronic energy into LO and LA modes, giving rise to a difference phonon absorption in our signal. Monte Carlo simulations are needed for a more in-depth understanding of the interplay

between hot electrons and lattice, taking into account effects such as impact ionization, intervalley- and polar-optical phonon scattering processes, and changes in phonon population. Experimentally, a broader probe bandwidth exceeding 2 THz will enable us to monitor the phonon dynamics directly. Additional effects of the THz fields themselves, including the possibility of THz-induced band-to-band tunneling [49] that could produce new carriers directly, also warrant further analysis.

References

[1] C. L. Dick, Jr. and B. Ancker-Johnson. "Nonequilibrium Carrier Phenomena in n-Type InSb." *Physical Review B*, **5**, 526 (1972).

[2] M. van Exter and D. Grischkowsky. "Carrier dynamics of electrons and holes in moderately doped silicon." *Physical Review B*, **41**, 12140 (1990).

[3] S. E. Ralph, Y. Chen, J. Woodall and D. McInturff. "Subpicosecond photoconductivity of $In_{0.53}Ga_{0.47}As$: Intervalley scattering rates observed via THz spectroscopy." *Physical Review B*, **54**, 5568 (1996).

[4] M. C. Nuss, D. H. Auston and F. Capasso. "Direct Subpicosecond Measurement of Carrier Mobility of Photoexcited Electrons in Gallium Arsenide." *Physical Review Letters*, **58**, 2355 (1987).

[5] A. Mayer and F. Keilmann. "Far-infrared nonlinear optics. II. $\chi^{(3)}$ contributions from the dynamics of free carriers in semiconductors." *Physical Review B*, **33**, 6962 (1986).

[6] J. Hebling, G. Almasi, I. Kozma and J. Kuhl. "Velocity matching by pulse front tilting for large area THz-pulse generation." *Opt. Express*, **10**, 1161 (2002).

[7] T. Feurer, N. S. Stoyanov, D. W. Ward, J. C. Vaughan, E. R. Statz and K. A. Nelson. "Terahertz Polaritonics." *Annual Review of Materials Research*, **37**, 317 (2007).

[8] K. L. Yeh, M. C. Hoffmann, J. Hebling and K. A. Nelson. "Generation of 10 μJ ultrashort terahertz pulses by optical rectification." *Applied Physics Letters*, **90**, 171121 (2007).

[9] M. C. Hoffmann, K.-L. Yeh, J. Hebling and K. A. Nelson. "Efficient terahertz generation by optical rectification at 1035 nm." *Opt. Express*, **15**, 11706 (2007).

[10] Q. Wu and X. C. Zhang. "Free-space electro-optic sampling of terahertz beams." *Applied Physics Letters*, **67**, 3523 (1995).

[11] D. Turchinovich and J. I. Dijkhuis. "Performance of combined 〈100〉 – 〈110〉 ZnTe crystals in an amplified THz time-domain spectrometer." *Optics Communications*, **270**, 96 (2007).

[12] P. G. Huggard, J. A. Cluff, G. P. Moore, C. J. Shaw, S. R. Andrews, S. R. Keiding, E. H. Linfield and D. A. Ritchie. "Drude conductivity of highly doped GaAs at terahertz frequencies." *Journal of Applied Physics*, **87**, 2382 (2000).

[13] P. Y. Yu and M. Cardona. **Fundamentals of Semiconductors: Physics and Materials Properties**. (Berlin Heidelberg: Springer) (2010).

[14] H. Shichijo and K. Hess. "Band-structure-dependent transport and impact ionization in GaAs." *Physical Review B*, **23**, 4197 (1981).

[15] J. H. Reuszer and P. Fisher. "An Optical Determination of the Ground-State Splittings of Group V Impurities in Germanium." *Physical Review*, **135**, A1125 (1964).

[16] M. Schall, H. Helm and S. R. Keiding. "Far Infrared Properties of Electro-Optic Crystals Measured by THz Time-Domain Spectroscopy." *International Journal of Infrared and Millimeter Waves*, **20**, 595 (1999).

[17] M. C. Hoffmann, J. Hebling, H. Y. Hwang, K.-L. Yeh and K. A. Nelson. "THz-pump/THz-probe spectroscopy of semiconductors at high field strengths [Invited]." *J. Opt. Soc. Am. B*, **26**, A29 (2009).

[18] B. R. Nag. *in* Semiconductors probed by ultrafast laser spectroscopy Vol. 1. edited by R. R. Alfano (Academic Press 1984).

[19] M. V. Fischetti. "Monte Carlo simulation of transport in technologically significant semiconductors of the diamond and zinc-blende structures. I. Homogeneous transport." *Electron Devices, IEEE Transactions on*, **38**, 634 (1991).

[20] C. J. Stanton and D. W. Bailey. "Rate equations for the study of femtosecond intervalley scattering in compound semiconductors." *Physical Review B*, **45**, 8369 (1992).

[21] A. Urbanowicz, R. Adomavičius, A. Krotkus and V. L. Malevich. "Electron dynamics in Ge crystals studied by terahertz emission from photoexcited surfaces." *Semiconductor Science and Technology*, **20**, 1010 (2005).

[22] H. Wen, M. Wiczer and A. M. Lindenberg. "Ultrafast electron cascades in semiconductors driven by intense femtosecond terahertz pulses." *Physical Review B*, **78**, 125203 (2008).

[23] M. C. Hoffmann, J. Hebling, H. Y. Hwang, K.-L. Yeh and K. A. Nelson. "Impact ionization in InSb probed by terahertz pump—terahertz probe spectroscopy." *Physical Review B*, **79**, 161201 (2009).

[24] D. G. Avery, D. W. Goodwin, W. D. Lawson and T. S. Moss. "Optical and Photo-Electrical Properties of Indium Antimonide." *Proceedings of the Physical Society. Section B*, **67**, 761 (1954).

[25] C. L. Littler and D. G. Seiler. "Temperature dependence of the energy gap of InSb using nonlinear optical techniques." *Applied Physics Letters*, **46**, 986 (1985).

[26] S. Ašmontas, J. Požela, L. Subačius and G. Valušis. "Electron gas heating and cooling effects by microwave electric fields in compensated InSb." *Solid-State Electronics*, **31**, 701 (1988).

[27] R. D. Larrabee and W. A. Hicinbothem, Jr. "Current oscillations and microwave emission in indium antimonide." *Electron Devices, IEEE Transactions on*, **13**, 121 (1966).

[28] E. O. Kane. "Band structure of indium antimonide." *Journal of Physics and Chemistry of Solids*, **1**, 249 (1957).

[29] D. G. Avery, D. W. Goodwin and A. E. R. Miss. "New infra-red detectors using indium antimonide." *Journal of Scientific Instruments*, **34**, 394 (1957).

[30] T. Ashley, A. R. Barnes, L. Buckle, S. Datta, A. B. Dean, M. T. Emery, M. Fearn, D. G. Hayes, K. P. Hilton, R. Jefferies, T. Martin, K. J. Nash, T. J. Phillips, W. A. Tang, P. J. Wilding and R. Chau. "Novel InSb-based quantum well transistors for ultra-high speed, low power logic applications." *in Solid-State and Integrated Circuits Technology, 2004. Proceedings. 7th International Conference on*,Beijing, China (2004).

[31] W. Shockley. "Problems related to p-n junctions in silicon." *Solid-State Electronics*, **2**, 35 (1961).

[32] S. D. Ganichev and W. Prettl. **Intense Terahertz Excitation of Semiconductors**. (USA: Oxford University Press) (2006).

[33] S. D. Ganichev, A. P. Dmitriev, S. A. Emel'yanov, Y. V. Terent'ev, I. D. Yaroshetskii and I. N. Yassievich. "Impact ionization in semiconductors under the influence of the electric field of an optical wave." *JETP*, **63**, 256 (1985).

[34] S. D. Ganichev, J. Diener and W. Prettl. "Nonlinear far-infrared absorption in InSb due to light impact ionization." *Applied Physics Letters*, **64**, 1977 (1994).

[35] M. C. Beard, G. M. Turner and C. A. Schmuttenmaer. "Transient photoconductivity in GaAs as measured by time-resolved terahertz spectroscopy." *Physical Review B*, **62**, 15764 (2000).

[36] J. Hebling, M. C. Hoffmann, H. Y. Hwang, K.-L. Yeh and K. A. Nelson. "Observation of nonequilibrium carrier distribution in Ge, Si, and GaAs by terahertz pump–terahertz probe measurements." *Physical Review B*, **81**, 035201 (2010).

[37] X. M. Weng and X. L. Lei. "Hot Electron High-Frequency Mobility in Wide- and Narrow-Gap Semiconductors." *physica status solidi (b)*, **187**, 579 (1995).

[38] E. Constant. "Non-steady-state carrier transport in semiconductors in perspective with submicrometer devices." *in* Hot-Electron Transport in Semiconductors. edited by L. Reggiani (Springer Berlin Heidelberg 1985).

[39] L. V. Keldysh. "Concerning theory of impact ionization in semiconductors." *JETP*, **21**, 1135 (1965).

[40] J. T. Devreese, R. G. Welzenis and R. P. Evrard. "Impact ionisation probability in InSb." *Applied Physics A: Materials Science & Processing*, **29**, 125 (1982).

[41] T. Kobayashi. "Detailed calculation of energy relaxation time of hot electrons in InSb." *Journal of Applied Physics*, **48**, 3154 (1977).

[42] A. Krotkus and Z. Dobrovolskis. **Electrical conductivity of narrow-gap semiconductors**. (Mokslas, Vilnus: (1988).

[43] R. Asauskas, Z. Dobrovolskis and A. Krotkus. "Maximum drift velocity of electrons in indium antimonide at 77 degrees Kelvin." *Soviet Physics Semiconductors*, **14**, 1377 (1980).

[44] V. V. Gavrushko, O. V. Kosogov and V. D. Lebedeva. "Avalanche multiplication in diffused P-N junctions in InSb." *Soviet Physics Semiconductors*, **12**, 1398 (1978).

[45] E. M. Conwell. "High field transport in semiconductors." *in* Solid State Physics, Supplement 9. edited by F. Seitz, D. Turnbull and H. Ehrenreich (Academic Press 1967).

[46] D. K. Ferry. "Decay of polar-optical phonons in semiconductors." *Physical Review B*, **9**, 4277 (1974).

[47] E. S. Koteles, W. R. Datars and G. Dolling. "Far-infrared phonon absorption in InSb." *Physical Review B*, **9**, 572 (1974).

[48] R. Brazis and R. Raguotis. "Electron and phonon dynamics in indium antimonide crystals." *Optical and Quantum Electronics*, **40**, 249 (2008).

[49] E. O. Kane. "Zener tunneling in semiconductors." *Journal of Physics and Chemistry of Solids*, **12**, 181 (1960).

Chapter 6

Nonlinear Conductivity in Graphene

The discovery of single-layer graphene has generated intense fundamental scientific and applications-based interest over the past several years. The characteristic linear electronic dispersion of the material gives rise to massless Dirac fermions which have a constant Fermi velocity [1]. As a result, graphene exhibits unique carrier transport properties that are of interest in electronics and optics applications. Advances in large-area graphene fabrication by chemical vapor deposition [2] have shown promise for the development of practical graphene electronic and optical devices [3, 4].

The dc to THz-frequency conductivity of graphene can be large compared to the conductivity at higher frequencies (mid-IR to visible) [5, 6], and several theoretical investigations have predicted extraordinary effects from both electronic and electromagnetic stimuli, including nonlinear frequency conversion and nonlinear conductivity effects due to the strong interaction of low-frequency light with graphene [7-12]. Ultrafast studies of

photoexcited carriers in graphene with visible to near-IR pumping and visible to THz probing have revealed various aspects of inter and intra-band conductivity dynamics [5, 13-15]. However, excitation in the visible to near-IR range is relatively inefficient since the absorption at these frequencies is weak [6]. Furthermore, the creation of electron-hole pairs in graphene with optical excitation leads to complicated relaxation dynamics related to electron-hole recombination.

Tabletop generation of THz pulses with microjoule energies and field amplitudes of hundreds of kV/cm [16] has enabled nonlinear electronic spectroscopy of conventional semiconductors [17-19], demonstrating that they can be suitable for applications like ultrafast THz saturable absorbers [20]. Recent theoretical and experimental work has also demonstrated that graphene is a good saturable absorber in the near-IR to visible range [3, 4]. Here we present nonlinear THz transmission results that demonstrate THz-induced transparency in graphene, and we study the dynamics of the nonlinear response with time-resolved THz-pump/THz-probe measurements.

6.1 Experimental Setup

The experimental setup is shown in Figure 1. High-field THz pulses were generated by optical rectification with tilted pulse front (TPF) excitation in lithium niobate (LN), giving pulse energies in excess of 3 μJ at 1 kHz repetition rate [16, 21, 22]. THz pulses were collimated and focused onto the sample with a pair of off-axis parabolic mirrors, and the transmitted THz light was imaged onto a ZnTe electro-optic sampling crystal for detection. The maximum THz energy at the sample was 1.5 μJ and the spot size was 1 mm, giving a maximum fluence of 190 $\mu J/cm^2$.

THz fluence-dependent transmission measurements were performed by varying the THz pulse transmission through a pair of polarizers prior to the sample. The time-dependent THz field profile after passing through the sample $E_{sam}(t)$ or with the sample removed $E_{ref}(t)$ was measured by electro-optic sampling with a variably delayed 800-nm readout pulse. Fourier transformation of the field profiles yielded the THz spectra $E_{sam}(\omega)$ and $E_{ref}(\omega)$.

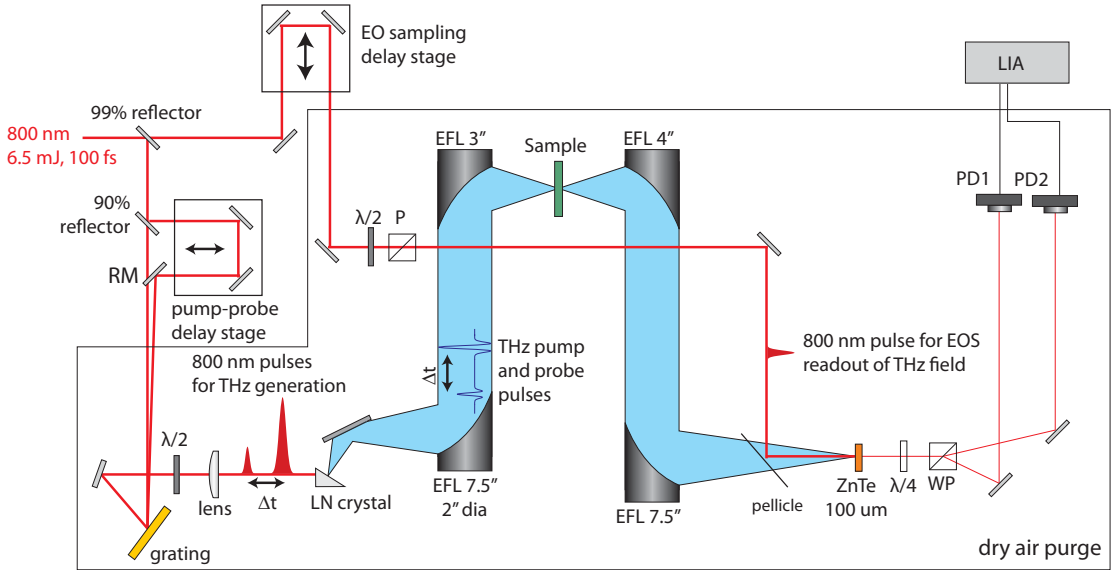

Figure 1. Experimental setup for both THz transmission and THz-pump THz-probe spectroscopy. In transmission experiments, the optical pulse that generates the THz probe pulse is blocked. The transmitted THz field is overlapped with a variably delayed 800-nm readout pulse in a ZnTe electro-optic sampling (EOS) crystal, and the THz-induced depolarization of the readout pulse reveals the time-dependent THz field profile. EOS – electro-optic sampling, RM – recombination mirror, EFL – effective focal length, LN – lithium niobate, P – polarizer, WP – Wollaston prism, PD – photodiode, λ/2 – half waveplate, λ/4 – quarter waveplate, LIA – lock-in amplifier.

THz-pump/THz-probe measurements were performed in a collinear geometry by splitting the optical pulse used for THz generation into pump and probe pulses with an adjustable time delay between them and then recombining them in a common LN crystal [17-

19]. The transmitted THz fields were measured by electro-optic sampling in ZnTe [23, 24]. For the time-resolved measurements, the peak amplitude in the transmitted THz probe field profile is reported as a function of THz pump-probe delay.

Graphene samples were grown on a copper substrate by chemical vapor deposition [2] and transferred to either fused silica or high resistivity silicon substrates. The graphene covered roughly half of the substrate area, which allowed us to record reference and sample scans with a common substrate. Hall effect measurements on several device sizes indicate a sheet hole concentration of about 5.5 x 10^{12} cm^{-2} for either fused silica or silicon substrate samples. Based on a linear density of states and a Fermi-Dirac thermal distribution, the Fermi energy was $E_f \approx$ -270 meV [25]. All measurements were performed on graphene grown by chemical vapor deposition (CVD) on copper and transferred to fused silica or silicon substrates at room temperature. Samples were fabricated by Hootan Farhat and Allen Hsu in Prof. Jing Kong's group at MIT.

6.2 THz Saturable Absorption in CVD Graphene

Figure 2a shows the spectrally resolved THz field transmission intensity $T = |E_{sam}(\omega)|/|E_{ref}(\omega)|$ for various THz field strengths as a function of frequency, indicating induced transparency with increasing fluence. This can be attributed to a decrease in carrier mobility as THz excitation redistributes carrier energies within the conduction band [7, 8]. In this case, the largest effect comes from redistribution of holes since the sample is strongly hole-doped.

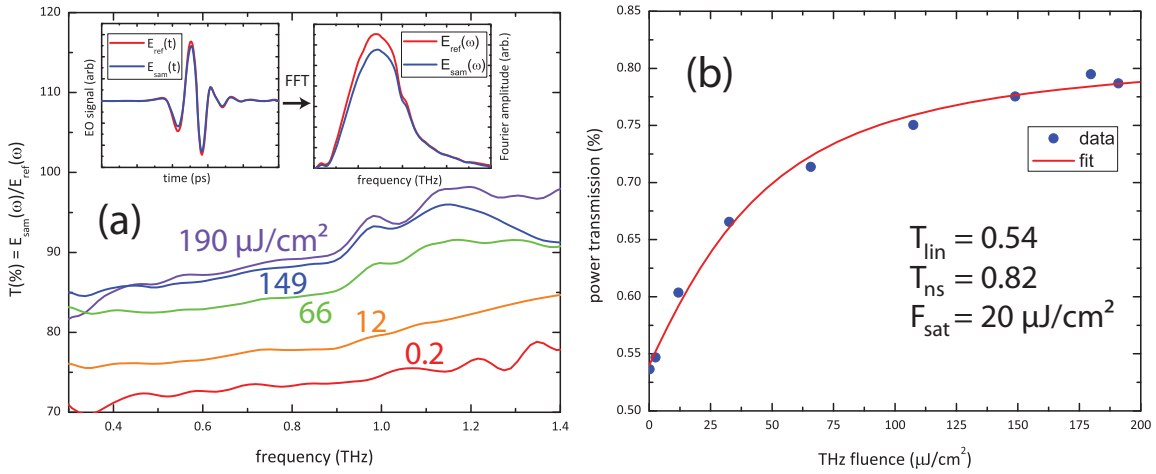

Figure 2. (a) THz field percent transmission at different pump fluences. The transmission increases as THz field strength increases. (b) THz power transmission integrated over the entire THz pulse versus THz fluence. Experiment (dots) and fit to saturable transmission function (line).

Figure 2b shows the power transmission of the entire THz pulse, $\int E_{sam}^2(t)dt \,/\, \int E_{ref}^2(t)dt$, plotted versus THz fluence. The inset of figure 2a shows representative THz time and frequency profiles measured in the experiment. The average power transmission went from 54% at low fluence to 79% at the highest THz fluence. (The peak field transmission max(E_{sam})/max(E_{ref})—goes from 74% to 87% for the steady state transmission) The power transmission was fit to a saturable power transmission function [20]:

$$T(F_p) = T_{ns}\frac{ln\left[1+\frac{T_{lin}}{T_{ns}}(e^{F_p/F_{sat}}-1)\right]}{F_p/F_{sat}} \quad (1)$$

where T_{lin} and T_{ns} are linear and nonsaturable power transmission coefficients, F_p is the THz fluence, and F_{sat} is the saturation fluence. From our fit, we found T_{lin} = 0.54, T_{ns} = 0.82, and F_{sat} = 20 μJ/cm^2.

6.3 Modified Drude-Type Conductivity in Graphene

At first glance, the strong induced transparency that we measure is in contrast to expectations from simple heating in a Drude-like treatment of the frequency-dependent intraband conductivity σ in graphene [5, 13-15]:

$$\frac{\sigma_{intra}(\omega)}{\sigma_Q} = \frac{8k_BT}{\pi\hbar}\ln\left(e^{\frac{-E_F}{2k_BT}} + e^{\frac{E_F}{2k_BT}}\right)\frac{1}{\omega^2\tau + 1/\tau} \quad (2)$$

where σ_Q is the universal dc quantum conductivity, T is temperature, E_F is the Fermi energy, and τ is the momentum scattering time. Here the electron and hole responses are symmetric, such that electron- or hole-doped graphene should exhibit the same conductivity. Hole-doped graphene at our carrier sheet densities should only exhibit an intraband response since the calculated Fermi energy far exceeds the photon energies of our THz pulses. As a result, we ignore the interband contribution to the conductivity. The conductivity can be related to the transmission T by:

$$\mathrm{T}(\omega) = \frac{1}{\left|1 + \frac{Z_0\sigma(\omega)}{n_s + 1}\right|^2} \quad (3)$$

where Z_0 is the vacuum impedance and n_s is the substrate refractive index.

Under this treatment, it is assumed that the pump pulse creates a distribution of hot carriers that thermalize in a short time compared to the experimental time resolution (~100 fs). The hot carrier distribution induces a decrease in transmission (i.e. increased absorption) based on equation 2 for the intraband conductivity. However, our experiments show a strong induced transparency and not induced absorption.

Theoretical treatments of graphene under a dc bias or ac excitation at THz frequencies [7, 8] have predicted a very strong decrease in carrier mobility and consequently a decrease in conductivity at even modest dc and THz field strengths (~1 kV/cm). These studies take into account damping due to electron-impurity and both electron-acoustic phonon and electron-optic phonon scattering at typical carrier densities (N = 0.5-1.5 x 10^{12} cm^{-2}). By separating the mobility into impurity, acoustic phonon, and optic phonon contributions at various lattice temperatures it is possible to assess which scattering mechanisms dominate in the conductivity. At low lattice temperatures, impurity scattering dominates. At moderate temperatures (T ~ 300 K), acoustic phonon scattering becomes significant, and finally at still higher temperatures (T > 700 K) optic phonon scattering becomes significant. For the nonlinear conductivity response, similar arguments explain the decrease in conductivity with increasing field strength since the relative change in electron temperature versus lattice temperature decreases with increasing lattice temperature and increasing field strength. As the acoustic and optical phonon modes are more populated at higher lattice temperatures, energy dissipation occurs more efficiently, limiting the electron drift velocity v_d and thus the conductivity since $v_d = \mu E$ and $\sigma = Ne\mu$ (at high hole concentration assuming electron and hole mobilities are roughly equal) where μ is mobility, E is applied electric field, N is the number density of carriers, and e is the charge of an electron.

Indeed, increasing the scattering rate in the Drude-like conductivity (equation 2) leads to induced transparency in the transmission. Taking into account that the induced absorption from heated carriers is weak according to the Drude-like treatment of the conductivity, and that faster scattering rates lead to strong induced transparency, fits of the power transmission

(figure 2b) to the Drude-like conductivity give τ = 140 fs at the lowest fluence and τ = 38 fs at the highest fluence. This indicates a large change in momentum scattering rate as a function of pump fluence.

Though empirically similar, it is worth noting that THz-induced transparency in graphene is quite different from that in conventional semiconductors. In conventional semiconductors, the mobility is determined by the average effective mass in a given part of the conduction band, where heating a distribution of electrons in the conduction band leads to inter and intravalley scattering into lower mobility regions of the conduction band. This is different in the case of graphene, where the linear dispersion implies zero effective mass for a large range of energies, and therefore where hotter distributions of electrons or holes do not experience a different effective mass. Furthermore, there is a symmetry between holes and electrons in graphene arising from the symmetric linear electronic dispersion. At high THz pump fluences, the interactions giving rise to the induced transparency or reduced mobility occur through scattering processes from impurities, and phonon scattering as discussed above. In conventional semiconductors, the scattering processes are thought to mainly contribute to the relaxation of energetic carriers after excitation.

This raises a question about the nature of the light-matter interaction in graphene: how does the THz pulse heat the distribution of carriers? Since the linear dispersion prohibits a classical acceleration of the electrons in the THz field (carriers have a constant Fermi velocity), a different mechanism must govern how carriers gain energy in graphene. This points to Coulomb processes—impact ionization and Auger recombination—as heating and cooling mechanisms in

graphene along with the impurity- and phonon-assisted effects described above [26, 27]. However, calculations of this nature are out of the scope of this work.

6.4 THz Saturable Absorption Dynamics in CVD Graphene

Time-resolved THz-pump/THz-probe measurements were performed in a collinear geometry as has been described in previous work [17-19] by directing two variably delayed optical pulses into the lithium niobate nonlinear crystal to generate a strong THz pump pulse and a weak THz probe pulse. In time-resolved THz pump-probe measurements, the signal at t = 0 was not reliable because this corresponded to the two optical pulses that generated the THz pump and probe pulses overlapping inside the LN crystal where they could interact nonlinearly, influencing the THz generation process (figure 3). However, there was a significant back-reflection of the THz pump pulse from the substrate-air interface (~35% and 55% reflection of the THz field per interface in fused silica and silicon respectively), and the reflected THz pump pulse was sufficiently intense to produce a significant change in probe pulse transmission. Our signal from each sample therefore consists of two temporally separated components: a signal that starts at t = 0, which is only reliable at time delays greater than the THz pulse duration of about 1 ps, and another signal that starts when the THz pump-probe delay time matches the THz round-trip time t_{RT} (roughly 20 ps) inside the sample. Since the second signal component permits reliable measurement of the sample response at short probe delay times relative to t_{RT}, we used this component for our analysis. In principle the signal could be influenced by sample responses from the first pass of the THz pump pulse through the graphene layer at t = 0 as well as the second pass at $t = t_{RT}$, but the sample response does not appear to persist for nearly that

long. The time-dependent data shown in figure 4 are the second signals in figure 3, with the time axes rescaled to set $t = 0$ as the arrival time of the reflected THz pump pulse. These signals allow us to examine the sample responses with time-coincident THz pump (after reflection) and probe pulses that were not generated at the same time in the LN crystal, avoiding signal contributions from unwanted nonlinear optical effects of overlapping optical pulses in the LN. At three round trip reflections (around 40 ps after time zero) in the substrate material, the normalized signals look identical. Thus although the signals at 20 and 40 ps are smaller than that at time zero—due to the Fresnel losses at each interface for each round trip of the pump in the substrate—the dynamics of the change remain the same. As a result, in the fluence regime from the first to the third round trip reflection of the pump in the substrate, there does not appear to be a fluence dependence in the dynamics.

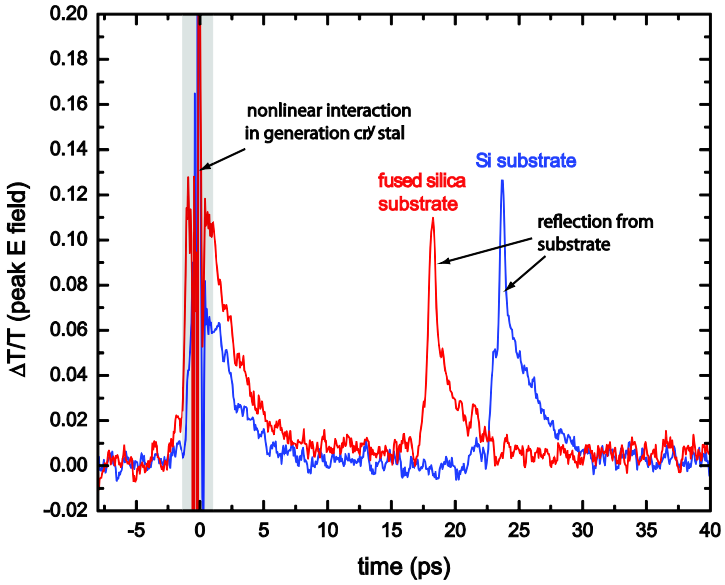

Figure 3. THz-pump/THz-probe peak field scans for graphene on fused silica (red) and silicon (blue). The EOS delay was set so that the optical readout pulse was temporally overlapped with the peak of the transmitted THz probe pulse, and the THz pump-probe time interval was varied. The large signals at time zero may have contributions from the nonlinear interaction of the optical pump pulses that were temporally overlapped in the THz generation crystal. The second

signals are due to reflections of the THz pump pulse in the sample substrates; the time delays are consistent with the THz refractive indices in fused silica and silicon. The second signals are reproduced in Fig. 4.

The results, shown in figure 4, reveal recovery of graphene absorption with a dynamical component that is faster than the time resolution given by the THz pulse and a slower component that can be fit to an exponential decay with τ_r = 1.7 ps for graphene on fused silica and τ_r = 2.9 ps for graphene on silicon. The difference in decay times may be attributed to different interactions of the graphene layer with the two substrates. The peak change in $\Delta T/T$ reaches 12% and 14%, corresponding to absolute transmission of the THz probe pulse of 92% and 96% (85% and 92% in peak intensity transmission), in the fused silica and silicon substrates respectively. This is in good agreement with the maximum power transmission obtained from a fit to the saturable power transmission function (equation 1 where T_{ns} = 0.82) above.

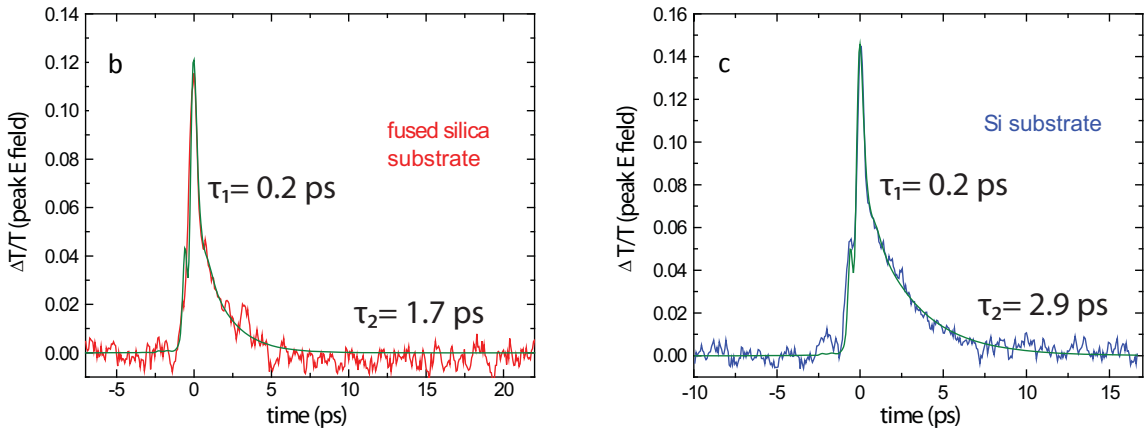

Figure 4. (a) and (b) THz-pump/THz-probe data from graphene. The zero of time corresponds to the arrival of the THz pulse in the graphene after an internal reflection at the substrate-air interface. The data were fit to a convolution of the square of the THz pump field with a biexponential decay.

6.5 Conclusions

We observed strong THz-induced transparency in CVD-grown graphene. We believe the effect is due to redistribution of holes by the THz pulse, which suppresses the carrier mobility through enhanced scattering processes at higher carrier energies. Time-resolved THz-pump/THz-probe spectroscopy indicated carrier cooling on a picosecond timescale, which is consistent with similar studies done with optical pump pulses [5, 13-15]. Our result suggests that graphene may be suitable for use as an ultrafast THz saturable absorber. Further study is needed to fully explain the phenomena observed in our experiments including a more detailed theoretical treatment of scattering processes in graphene to fit our experimental conditions, and temperature-dependent studies to investigate the effect of lattice temperature on such scattering processes.

References

[1] A. K. Geim and K. S. Novoselov. "The rise of graphene." *Nat Mater*, **6**, 183 (2007).

[2] X. Li, W. Cai, J. An, S. Kim, J. Nah, D. Yang, R. Piner, A. Velamakanni, I. Jung, E. Tutuc, S. K. Banerjee, L. Colombo and R. S. Ruoff. "Large-Area Synthesis of High-Quality and Uniform Graphene Films on Copper Foils." *Science*, **324**, 1312 (2009).

[3] G. Xing, H. Guo, X. Zhang, T. C. Sum and C. H. A. Huan. "The Physics of ultrafast saturable absorption in graphene." *Opt. Express*, **18**, 4564 (2010).

[4] Q. Bao, H. Zhang, Y. Wang, Z. Ni, Y. Yan, Z. X. Shen, K. P. Loh and D. Y. Tang. "Atomic-Layer Graphene as a Saturable Absorber for Ultrafast Pulsed Lasers." *Advanced Functional Materials*, **19**, 3077 (2009).

[5] H. Choi, F. Borondics, D. A. Siegel, S. Y. Zhou, M. C. Martin, A. Lanzara and R. A. Kaindl. "Broadband electromagnetic response and ultrafast dynamics of few-layer epitaxial graphene." *Applied Physics Letters*, **94**, 172102 (2009).

[6] K. F. Mak, M. Y. Sfeir, Y. Wu, C. H. Lui, J. A. Misewich and T. F. Heinz. "Measurement of the Optical Conductivity of Graphene." *Physical Review Letters*, **101**, 196405 (2008).

[7] W. S. Bao, S. Y. Liu, X. L. Lei and C. M. Wang. "Nonlinear dc transport in graphene." *Journal of Physics: Condensed Matter*, **21**, 305302 (2009).

[8] W. S. Bao, S. Y. Liu and X. L. Lei. "Hot-electron transport in graphene driven by intense terahertz fields." *Physics Letters A*, **374**, 1266 (2010).

[9] S. Mikhailov, A. "Non-linear electromagnetic response of graphene." *EPL*, **79**, 27002 (2007).

[10] S. A. Mikhailov and K. Ziegler. "Nonlinear electromagnetic response of graphene: frequency multiplication and the self-consistent-field effects." *Journal of Physics: Condensed Matter*, **20**, 384204 (2008).

[11] S. A. Mikhailov. "Non-linear graphene optics for terahertz applications." *Microelectronics Journal*, **40**, 712 (2009).

[12] A. R. Wright, X. G. Xu, J. C. Cao and C. Zhang. "Strong nonlinear optical response of graphene in the terahertz regime." *Applied Physics Letters*, **95**, 072101 (2009).

[13] J. M. Dawlaty, S. Shivaraman, J. Strait, P. George, M. Chandrashekhar, F. Rana, M. G. Spencer, D. Veksler and Y. Chen. "Measurement of the optical absorption spectra of epitaxial graphene from terahertz to visible." *Applied Physics Letters*, **93**, 131905 (2008).

[14] P. A. George, J. Strait, J. Dawlaty, S. Shivaraman, M. Chandrashekhar, F. Rana and M. G. Spencer. "Ultrafast Optical-Pump Terahertz-Probe Spectroscopy of the Carrier Relaxation and Recombination Dynamics in Epitaxial Graphene." *Nano Letters*, **8**, 4248 (2008).

[15] J. Lee, K. M. Dani, A. Mohite, R. Sharma, A. Taylor and R. P. Prasankumar. "Probing Intraband Conductivity Dynamics in Graphene." *in International Conference on Ultrafast Phenomena*,Snowmass Village, CO USA (2010).

[16] K. L. Yeh, M. C. Hoffmann, J. Hebling and K. A. Nelson. "Generation of 10 μJ ultrashort terahertz pulses by optical rectification." *Applied Physics Letters*, **90**, 171121 (2007).

[17] M. C. Hoffmann, J. Hebling, H. Y. Hwang, K.-L. Yeh and K. A. Nelson. "THz-pump/THz-probe spectroscopy of semiconductors at high field strengths [Invited]." *J. Opt. Soc. Am. B*, **26**, A29 (2009).

[18] M. C. Hoffmann, J. Hebling, H. Y. Hwang, K.-L. Yeh and K. A. Nelson. "Impact ionization in InSb probed by terahertz pump—terahertz probe spectroscopy." *Physical Review B*, **79**, 161201 (2009).

[19] J. Hebling, M. C. Hoffmann, H. Y. Hwang, K.-L. Yeh and K. A. Nelson. "Observation of nonequilibrium carrier distribution in Ge, Si, and GaAs by terahertz pump–terahertz probe measurements." *Physical Review B*, **81**, 035201 (2010).

[20] M. C. Hoffmann and D. Turchinovich. "Semiconductor saturable absorbers for ultrafast terahertz signals." *Applied Physics Letters*, **96**, 151110 (2010).

[21] T. Feurer, N. S. Stoyanov, D. W. Ward, J. C. Vaughan, E. R. Statz and K. A. Nelson. "Terahertz Polaritonics." *Annual Review of Materials Research*, **37**, 317 (2007).

[22] J. Hebling, G. Almasi, I. Kozma and J. Kuhl. "Velocity matching by pulse front tilting for large area THz-pulse generation." *Opt. Express*, **10**, 1161 (2002).

[23] P. C. M. Planken, H.-K. Nienhuys, H. J. Bakker and T. Wenckebach. "Measurement and calculation of the orientation dependence of terahertz pulse detection in ZnTe." *J. Opt. Soc. Am. B*, **18**, 313 (2001).

[24] N. C. J. van der Valk, T. Wenckebach and P. C. M. Planken. "Full mathematical description of electro-optic detection in optically isotropic crystals." *J. Opt. Soc. Am. B*, **21**, 622 (2004).

[25] T. Fang, A. Konar, H. Xing and D. Jena. "Carrier statistics and quantum capacitance of graphene sheets and ribbons." *Applied Physics Letters*, **91**, 092109 (2007).

[26] F. Rana. "Electron-hole generation and recombination rates for Coulomb scattering in graphene." *Physical Review B*, **76**, 155431 (2007).

[27] T. Winzer, A. Knorr and E. Malic. "Carrier Multiplication in Graphene." *Nano Letters*, **10**, 4839 (2010).

Chapter 7

THz Kerr Effect in Liquids

The Kerr effect is a change *Δn* in the optical refractive index, which is exhibits quadratic dependence on an externally applied electric field. In the dc limit, this is usually expressed as $\Delta n = K\lambda E^2$ with the Kerr constant *K* and the vacuum wavelength λ. At optical frequencies, an intensity-dependent modulation of the refractive index $\Delta n = n_2^I I(t)$ is observed, resulting in well-known nonlinear optical effects like self-focusing (Kerr lensing), self-phase modulation, and birefringence that is usually measured through the depolarization of a separate, weak optical beam in what is conventionally designated as the optical Kerr effect (OKE). The optical Kerr effect [1-4] can be observed in isotropic materials, including liquids and gases, that do not possess a second-order contribution $\chi^{(2)}$ to the polarization that leads to a linear dependence on the electric field (Pockels effect). Using ultrashort laser pulses, information about the dynamical responses of liquids on femtosecond time scales can be obtained [5-7]. In addition to

orientational degrees of freedom, molecular vibrations excited through impulsive stimulated Raman scattering may be observed.

Here we present results in which the refractive index at optical frequencies is perturbed not by optical pulses but single-cycle terahertz pulses. Processes in the terahertz frequency range correspond to timescales on the order of molecular relaxation constants in liquids and glasses, but until recently the terahertz field strengths have been too small to induce observable higher-order nonlinear effects. Due to the phase-stability of terahertz generation processes, a femtosecond optical pulse that is used to produce a terahertz pulse can be used to time-resolve individual cycles of the terahertz field, and we anticipate that the optical pulse can also be used to time-resolve a Kerr response to individual cycles of the terahertz field. This is in contrast to all-optical Kerr experiments where only the Kerr response to the intensity envelope of the optical excitation pulse can be observed. Z-scan measurements [8] of ZnTe during terahertz generation by an optical pulse [9] suggested significant terahertz-induced Kerr index change, but conventional OKE and mixed optical/terahertz effects, as well as cascaded $\chi^{(2)}$ effects (present in the noncentrosymmetric crystals), were also present. Here we present results in centrosymmetric media with only terahertz excitation to demonstrate unambiguously and generally the terahertz Kerr effect.

7.1 Experimental Setup

The experimental setup is shown in figure 1 and described in chapter 4. Single-cycle terahertz pulses with energies exceeding 1.5 μJ were generated by the tilted pulse front technique [10-12]. This method uses noncollinear velocity matching to enhance optical rectification in lithium

niobate through tilting of the intensity front of a femtosecond laser pulse with a grating. The generated field was collimated and focused onto the sample where the terahertz intensity exceeded 50 MW/cm^2. An Infrasil cuvette that is relatively transparent in the far-infrared, with a path length of L = 5 mm, was used for liquid samples. CS_2, benzene and CCl_4 have low absorption in the terahertz range, so a 5 mm sample length did not significantly diminish the terahertz pulse.

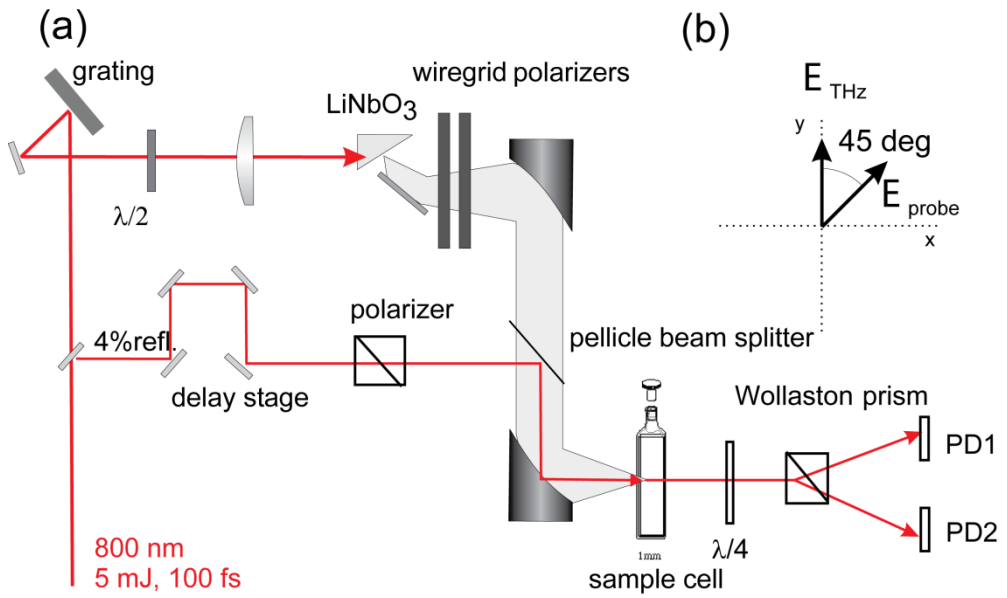

Figure 1: (a) Experimental setup. Terahertz radiation was generated by the tilted pulse front method and focused onto the sample in a 5 mm quartz cell. Light pulses with 800 nm wavelength and 100 fs duration were used to probe the sample, and their induced depolarization was analyzed. (b) The probe polarization at the sample was 45° with respect to the terahertz polarization.

A weak 800 nm probe beam was passed collinearly through the sample at a polarization of 45° with respect to the terahertz polarization. A combination of a quarter-wave plate and a Wollaston prism was used to analyze the change in refractive index. Two balanced photodiodes and a lock-in amplifier were used to record pump-probe data. In order to assess the field

strength and temporal shape of the terahertz field at the sample position, electro-optic sampling [13] with a 0.1 mm ZnTe crystal was used.

Since in our experiment the terahertz excitation pulse and the optical probe pulse travel through the sample together over a long distance (5 mm), it is important to have good velocity matching. The time-domain signal is optimal if the phase velocity of the terahertz pulse causing the birefringence and the group velocity of the optical pulse probing it are identical. In this case the optical pulse envelope remains fixed at the same part of the terahertz wave cycle as the two pulses propagate through the thick sample. The matching of the optical (group) refractive index and the terahertz refractive index in our samples allows us to use long path lengths, thus enhancing measurement sensitivity to small refractive index changes.

7.2 THz Kerr Effect in CS_2, CH_2I_2, Benzene, CCl_4, and Chloroform

Figure 2a shows results of terahertz-pump/optical-probe scans for CS_2, CH_2I_2, benzene, CCl_4, and chloroform, normalized to unity. The overall signal levels in the different samples reflect the differences in electronic and molecular polarizabilities. CS_2, CH_2I_2, and benzene have the strongest signals, which show slow decays due to the orientational contributions to their polarizabilities [5, 14] as will be discussed in more detail below. The observed signal from CCl_4 is substantially weaker and has no orientational component because of the molecular symmetry. $CHCl_3$ should show orientational signal but the level is apparently too low to detect above noise in our current measurements. Surprisingly, nitrobenzene which has a value of 5.8 x 10^{-20} m^2V^{-2} for $\chi^{(3)}$ at optical frequencies [15], roughly twice that of CS_2, yielded no measurable signal. This was also the case for tetrahydrofuran (THF), which is known to have a very low polarizability.

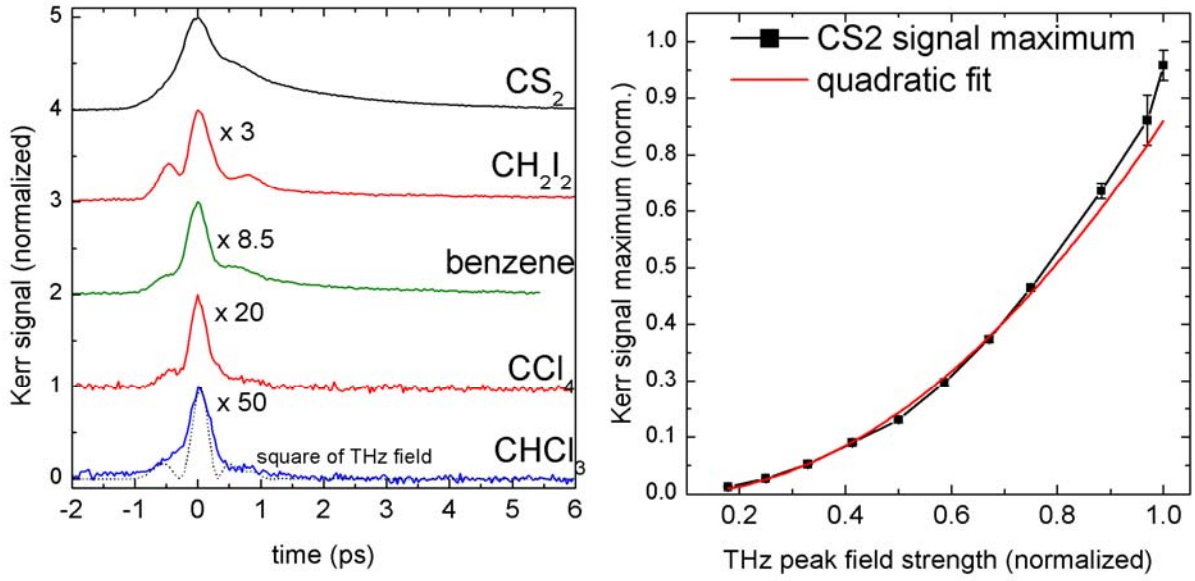

Figure 2: (a) Terahertz Kerr signals obtained from five different liquids. The dotted line indicates the square of the electric field measured by electro-optic sampling with ZnTe. (b) The magnitude of the Kerr signal (shown for CS_2) scales quadratically with the applied terahertz field.

The magnitudes of the observed Kerr signals scale quadratically with the terahertz field amplitude (figure 2b) as expected for a $\chi^{(3)}$ process. From the observed magnitude of the Kerr signal, i.e., from the difference signal $\Delta I/I$ in our balanced detection system, the phase retardation $\Delta\phi$ of the probe pulse of frequency ω accumulated while traversing the sample cell with length L can be calculated and the change in refractive index Δn caused by the terahertz field can be deduced from the expressions

$$\frac{\Delta I}{I} = sin\Delta\phi = sin\frac{\Delta n\omega L}{c} = sin\frac{(n_x - n_y)\omega L}{c} \qquad (1)$$

At the maximum terahertz pump strength we obtain $\Delta I/I$ of 2.7 x 10^{-3}, corresponding to an index change of Δn = 4.3 x 10^{-6}, in the case of CS_2. For a terahertz electric field of 150 kV/cm we obtain a Kerr constant K of 2.4 x 10^{-14} m/V^2 which is close to the DC value for CS_2 of 2.8 x 10^{-14}

m/V^2 [16]. In all-optical Kerr measurements, the refractive index change for a weak probe of linearly polarized light at frequency ω' is connected to the nonlinear refractive index n_2 by

$$\Delta n(\omega') = 2n_2\langle E(\omega)E(\omega)\rangle \quad (2)$$

and related to the nonlinear susceptibility by $n_2 = \frac{3}{2n_0}\chi^{(3)}_{xxxx}(\omega';\omega',\omega,-\omega)$, where n_0 is the unperturbed refractive index. The angled brackets indicate a time average over the electric field cycles. The nonlinear refractive index can also be given in terms of intensity $\Delta n = n_2^I I$ where the relationship between the nonlinear coefficients is given by $n_2^I = n_2/(\varepsilon_0 n_0 c)$, where ε_0 is the vacuum permittivity. Table 1 summarizes our results for the observed peak refractive index change and the derived nonlinear constants for the five liquids.

Liquid	**Δn** **×10^{-6}**	***K*** **(10^{-14} m/V)**	**n_2^I** **(10^{-16} cm^2/W)**	**n_2^I [15]** **(10^{-16} cm^2/W)**	**$\chi^{(3)}$** **(10^{-20} m^2/V^2)**	**τ_0** **(ps)**
CS_2	4.3	2.4	440	332	2.08	1.7
Benzene	0.5	0.26	56	168	0.22	2.1
CCl_4	0.23	0.12	27	15	0.10	-
$CHCl_3$	0.086	0.045	10	30	0.04	-
CH_2I_2	1.4	0.75	140	147	0.70	13

Table 1: Refractive index change *Δn*, nonlinear refractive index n_2 in terms of intensity, nonlinear susceptibility $\chi^{(3)}(\omega_{THz},\omega_{THz},\omega_{opt})$, and rotational relaxation time constant τ_0 for the terahertz Kerr effect in various liquids. The measured terahertz pulse parameters used for the calculation are: duration 1 ps, beam diameter at focus 2 mm, energy 1.5 µJ. These correspond to a terahertz peak field of 150 kV/cm and peak intensity of 50 MW/cm^2. The fourth column contains reference values from [15].

Generally, our values for the nonlinear refractive index are on the same order of magnitude as values reported for all-optical measurements [15]. More quantitative comparison is difficult because in the available literature we found substantial variation in the reported values for n_2 and $\chi^{(3)}$ from OKE measurements.

7.3 Electronic and Nuclear Components of the Signal

The time-dependent polarization, *P*, can be expressed using a response function ***R(t)*** [17]

$$P_{ijkl}^{(3)}(t,\tau) = E_j^{pr}(t-\tau)\int_0^{\infty} d\tau' \boldsymbol{R}_{ijkl}^{(3)}(\tau')E_k^{pu^*}(t-\tau')E_l^{pu}(t-\tau') \qquad (3)$$

where τ is the delay between the pump and probe pulses E^{pu} and E^{pr}. The response function may be further separated into electronic and nuclear degrees of freedom $\boldsymbol{R}_{ijkl}^{(3)} = \boldsymbol{R}_{ijkl}^{(3)el} + \boldsymbol{R}_{ijkl}^{(3)nuc}$. For electronically nonresonant frequencies, the electronic response function is essentially instantaneous in time and contains no information about molecular dynamics. The second term contains the inter- and intramolecular contributions to the signal. For anisotropic molecules the main contribution to the nuclear term is from molecular orientational diffusion, which can be approximated to have an exponential decay with time constant τ_0. The induced difference Δn between the indices of refraction parallel and perpendicular to the terahertz field can then be written as

$$\Delta n(\tau) = n_2^e E^2(\tau) + \frac{n_2^o}{\tau_0}\int_{-\infty}^{t} E_{THz}^2(t)\cdot e^{-(t-\tau)/\tau_0}dt' \qquad (4)$$

where n_2^e contains the instantaneous the electronic contribution and n_2^o the orientational contribution to n_2. A fit of Eq. 4 to Δn(t) for CS_2 yields ratio n_2^o/n_2^e of about 0.4; subtraction of

the electronic contribution from the measured response yields the red trace in figure 3a which gives the purely molecular orientational contribution with orientational relaxation time τ_0 = 1.7 ps. In the case of diiodomethane (CH_2I_2), we observe a strong electronic contribution as well as a longer exponential contribution with a time constant of 13 ps (figure 3b). This relatively large value can be explained by the larger moment of inertia of the diiodomethane molecule. The exponential decay times that we measured are in reasonable agreement with reported values from all-optical Kerr effect measurements [14].

In CH_2I_2 and CCl_4, it can be seen that on the short time scale the nonlinear refractive index follows the square of the terahertz field. This is in contrast to all-optical Kerr measurements, where the birefringence change follows the envelope of the square of the electric field. CH_2I_2 and CCl_4 are favorable samples for this observation because in the former the electronic Kerr response, which is the part that follows the square of the pump field, is well separated temporally from the much slower orientational response, while in the latter there is no orientational response. A more extensive theoretical model of dynamic responses to terahertz fields [18] may enable spectroscopic exploitation of the fact that induced responses with well-defined polarities can be measured. So far we have not observed measurable optical birefringence in polar liquids although terahertz-induced second-order lattice vibrational responses were observed optically in ferroelectric crystals [19]. Therefore a strong molecular dipole does not necessarily facilitate the present class of measurement, and may hinder it through absorption of the terahertz pulse near the front of the sample. Other probing methods may enable detection of nonlinear terahertz pumping of molecular dipolar responses.

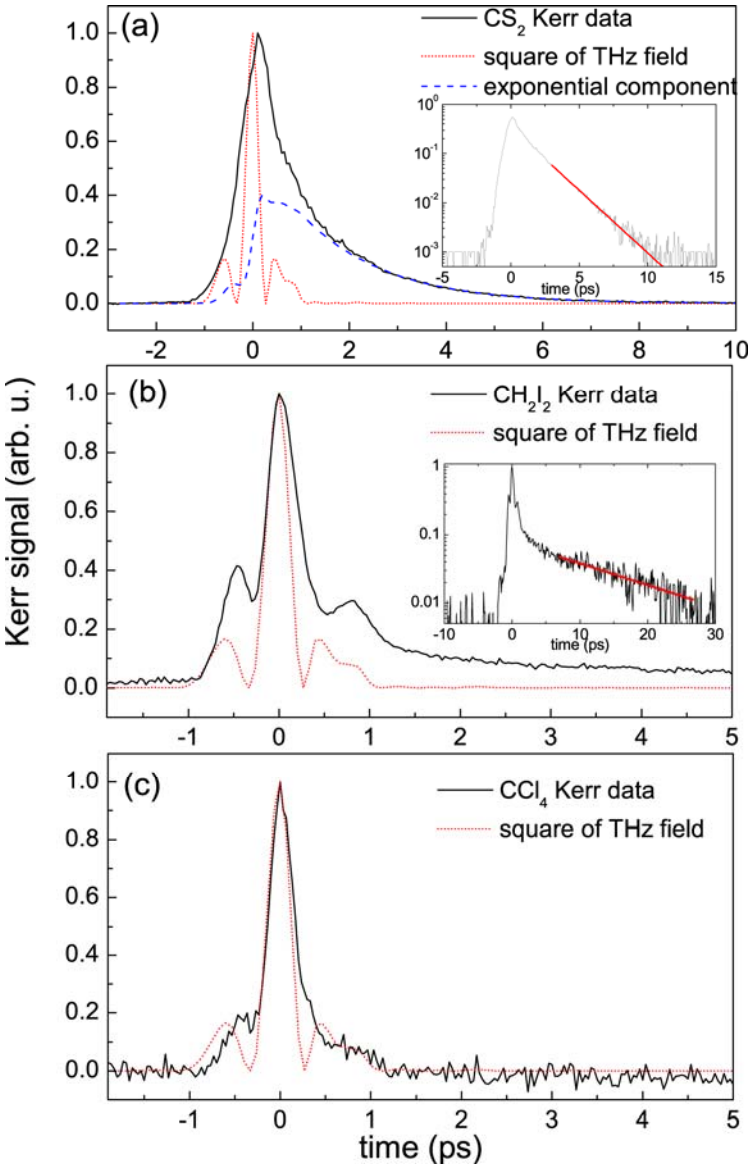

Figure 3: Terahertz Kerr signal in (a) CS_2, (b) CH_2I_2, and (c) CCl_4 (solid black lines). For comparison, the square of the terahertz electric field profile obtained from EO sampling is shown (dotted red lines). The dashed (blue) line in (a) is based on a fit to Eq. 4. The insets show data on a log scale together with exponential fits yielding decay constants of 1.7 ps in CS_2 and 13 ps in CH_2I_2.

7.4 Conclusions

We have observed terahertz-induced transient optical birefringence in liquids. The nonlinear refractive index n_2 is generally on the same order of magnitude as in all-optical measurements.

In materials with a small or slow contribution of molecular orientation such as CCl_4 and CH_2I_2, we are able to observe that the electronic part of the system response follows the square of the terahertz electric field. Therefore responses to each terahertz field polarity may be observed distinctly. This may enable novel spectroscopic measurements of responses with well-defined orientations in addition to alignments. The terahertz Kerr effect may reveal polarizability dynamics associated with electronic, vibrational, and structural responses in ordered and disordered solids as well as liquids.

References

[1] P. D. Maker, et al. "Intensity-Dependent Changes in the Refractive Index of Liquids." *Physical Review Letters*, **12**, 507 (1964).

[2] P. P. Ho and R. R. Alfano. "Optical Kerr effect in liquids." *Physical Review A*, **20**, 2170 (1979).

[3] K. Sala and M. C. Richardson. "Optical Kerr effect induced by ultrashort laser pulses." *Physical Review A*, **12**, 1036 (1975).

[4] C. J. Fecko, et al. "Isotropic and anisotropic Raman scattering from molecular liquids measured by spatially masked optical Kerr effect spectroscopy." *The Journal of Chemical Physics*, **117**, 1139 (2002).

[5] D. McMorrow, et al. "Femtosecond optical Kerr studies on the origin of the nonlinear responses in simple liquids." *Quantum Electronics, IEEE Journal of*, **24**, 443 (1988).

[6] Q. Zhong and J. T. Fourkas. "Optical Kerr Effect Spectroscopy of Simple Liquids." *The Journal of Physical Chemistry B*, **112**, 15529 (2008).

[7] N. A. Smith and S. R. Meech. "Optically-heterodyne-detected optical Kerr effect (OHD-OKE): Applications in condensed phase dynamics." *International Reviews in Physical Chemistry*, **21**, 75 (2002).

[8] Z-scan measurements are a form of nonlinear transmission measurements where a sample is moved along the propagation direction near a sample focus. The intensity changes predictably over the traversed distance under the assumption of Gaussian optics.

[9] W.-Q. He, et al. "Direct evidence of Kerr-like nonlinearity by femtosecond Z-scan technique." *Opt. Express*, **14**, 5476 (2006).

[10] K. L. Yeh, et al. "Generation of 10 μJ ultrashort terahertz pulses by optical rectification." *Applied Physics Letters*, **90**, 171121 (2007).

[11] T. Feurer, et al. "Terahertz Polaritonics." *Annual Review of Materials Research*, **37**, 317 (2007).

[12] J. Hebling, et al. "Velocity matching by pulse front tilting for large area THz-pulse generation." *Opt. Express*, **10**, 1161 (2002).

[13] C. Winnewisser, et al. "Electro-optic detection of THz radiation in $LiTaO_3$, $LiNbO_3$ and ZnTe." *Applied Physics Letters*, **70**, 3069 (1997).

[14] S. Ruhman, et al. "Nonrelaxational inertial motion in carbon disulfide liquid observed by femtosecond time-resolved impulsive stimulated scattering." *The Journal of Physical Chemistry*, **91**, 2237 (1987).

[15] R. L. Sutherland. **Handbook of Nonlinear Optics**. (New York: Dekker) (2003).

[16] A. Yariv and P. Yeh. **Optical waves in crystals**. (New York: Wiley) (1984).

[17] S. Mukamel. **Principles of nonlinear optical spectroscopy**. (New York: Oxford University Press) (1995).

[18] U. Haberle and G. Diezemann. "Dynamic Kerr effect responses in the terahertz range." *The Journal of Chemical Physics*, **122**, 184517 (2005).

[19] J. Hebling, et al. "High-Power THz Generation, THz Nonlinear Optics, and THz Nonlinear Spectroscopy." *Selected Topics in Quantum Electronics, IEEE Journal of*, **14**, 345 (2008).

Chapter 8

Nonlinear Responses in Ferroelectrics

Ferroelectric systems are of great scientific interest due to their strong nonlinear optical responses and unusually large dielectric constants. Whereas standard ferroelectrics exhibit macroscopic polar domains, there is a class of systems that blur the distinction between a polar ferroelectric phase and an isotropic paraelectric phase. These systems are the relaxor ferroelectrics, in which upon approaching the critical temperature T_c from above, ferroelectric nanodomains coexist with the isotropic paraelectric phase (figure 1) [1-3]. Above T_c, no polar domain exists in normal ferroelectrics but polar nanodomains persist well above the dynamic transition temperature of relaxors. Doping gives rise to dipolar defects, which transform the material into a relaxor. The impurities distort the highly polarizable host lattice, forming correlated polarization regions in the host lattice. At high impurity levels, the correlated regions overlap and the relaxor can enter into a long-range ordered ferroelectric state. It is also possible to form a dipole glass if the nanodomain orientations are frozen into place before they

begin to interact as the temperature is reduced and their correlation lengths increase [4]. In both conventional and relaxor ferroelectrics, the soft phonon mode whose coordinate corresponds to the collective motions of ions between their positions in the paraelectric and ferroelectric phases increases its dipole and shifts to lower frequency (i.e. softens) as the critical temperature is approached from above, and it typically lies in the THz range. In fact, the role of the soft mode in the ferroelectric phase transition may be exploited to control the ferroelectric polarization. This has been proposed theoretically by directly driving the soft mode with THz electric fields in lead titanate [5]. In these studies, the polarization of the driving field has been found to be an important factor in controlling the ferroelectric state. Polarization sensitive THz nonlinear spectroscopies can thus be important tools to study the onset of ferroelectricity in such systems.

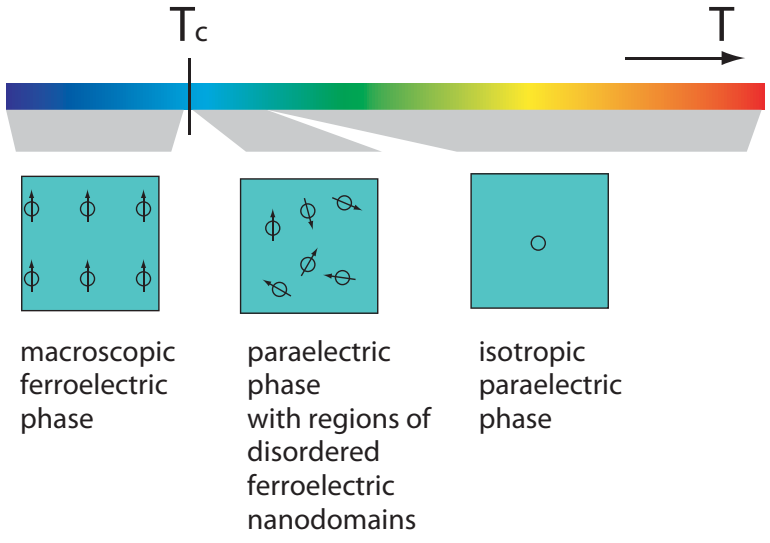

Figure 1: Relaxor ferroelectric schematic. At high temperatures, an isotropic paraelectric phase exists. As the ferroelectric transition temperature T_c is approached from above, disordered ferroelectric nanodomains coexist with the paraelectric phase. Finally, when below T_c, a macroscopic ferroelectric phase emerges.

Near T_c the dielectric function ε' can reach extremely high values, on the order of up to 10^5 at DC through microwave frequencies. Closely related to this are extremely high electrooptic effects which are among the highest in known materials [6] and hence of great interest for technological applications [7]. In the cubic phase above T_c, potassium tantalate niobate ($KTa_{1-x}Nb_xO_3$, KTN) has inversion symmetry and the lowest order electro-optic (EO) effect is the Kerr effect [6]. In the other phases, KTN is ferroelectric and the Pockels effect is observed since it does not have inversion symmetry [7].

Optical Kerr effect (OKE) spectroscopy has been used extensively to study a wide variety of materials [8-10]. OKE spectroscopy has proved useful for observation of vibrations coupled to molecular or material polarizabilities [10]. In the far-IR/THz regime, THz-induced Kerr effect measurements have been performed on liquids [11] showing a similar coupling to the polarizability (as discussed in the previous chapter). In this case, photon energies are not large enough to excite vibrational modes through Raman processes. However, THz fields may directly excite polar vibrational modes, as found in ferroelectric materials. In this chapter, I will discuss nonlinear THz measurements on the relaxor ferroelectrics (<100> cut) potassium tantalate/niobate $KTa_{1-x}Nb_xO_3$ (KTN, x = 0.018, T_c = 32 K) and $K_{1-y}Li_yTa_{1-x}Nb_xO_3$ (KLTN, x = 0.345, y = 0.01, T_c = 264 K).

8.1 Experimental Setup

The experimental setup is shown in Figure 2 (and has been described in chapters 4 and 7). Single-cycle THz pulses with energies exceeding 1.5 μJ were generated by the tilted pulse front technique [12-14]. The generated field was collimated and focused onto the sample where the

THz intensity exceeded 50 MW/cm^2 (> 250 kV/cm in field strength). Using a pair of wiregrid polarizers, the THz pump pulse could be variably attenuated, enabling intensity-dependent measurements. An ultrafast 100 fs 800 nm probe pulse was spatially overlapped with the THz pulse and the relative time delay was variably tuned. The polarization rotation of the optical probe pulse was measured in a balanced and heterodyned setup (similar to balanced detection for electro-optic sampling). Temperature-dependent measurements were performed in a closed-cycle liquid helium cryostat with TOPAS polymer windows.

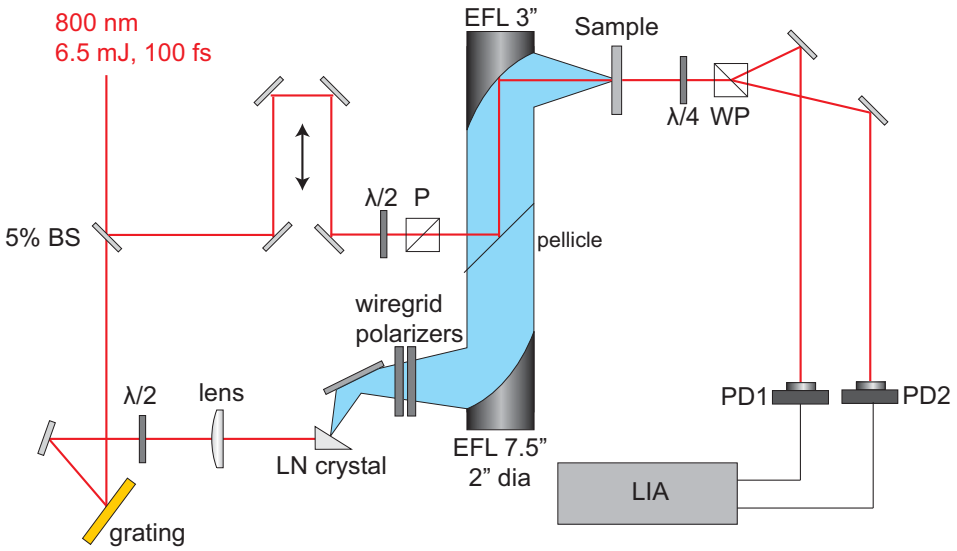

Figure 2: THz Kerr effect setup. THz pulses are generated using the tilted-pulse front technique and focused into a sample. Depolarization of a short 800 nm probe is detected with balanced photodiodes using lock-in techniques.

8.2 THz Kerr Effect in KTN

KTN is a relaxor ferroelectric material which is essentially a potassium tantalate ($KTaO_3$) crystal with niobium substitutions. The amount of niobium substitution tunes the ferroelectric phase

transition temperature T_c. The soft mode in KTN corresponds to the collective motion of the potassium and tantalum/niobium ions in the units cell out of phase with respect to the oxygen atoms (figure 3). The parent material, potassium tantalate, is a quantum paraelectric so it does not undergo a ferroelectric phase transition at a non-zero temperature [15]. Upon niobium substitution, the central cation in the unit cell experiences a displacement from the center and enables a stable ferroelectric phase above T = 0 K [2].

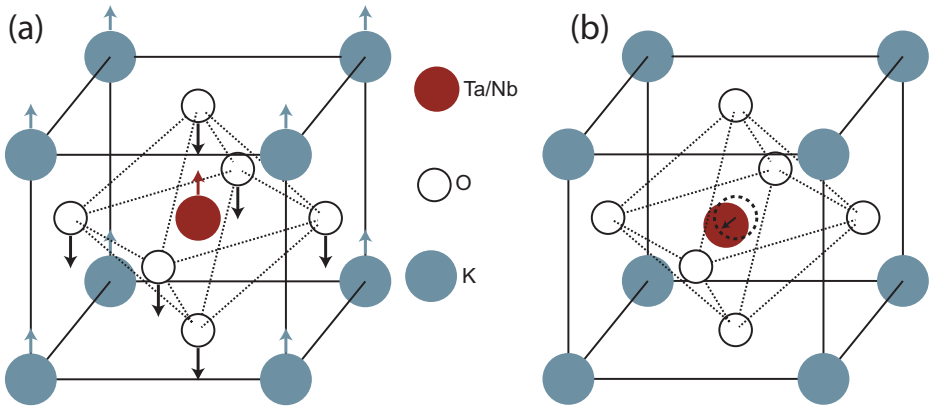

Figure 3: left) Ferroelectric soft mode in KTaO3. (right) Displacement of central cation in [111] direction upon doping with Nb.

Figure 4 shows THz Kerr effect data at room temperature in a 0.2 mm thick KTN crystal, fit to a single exponential convoluted with the square of the pump THz field. The decay constant from the fit was τ = 5.3 ps. Intensity-dependent THz Kerr effect measurements were performed (Figure 4a inset) confirming second-order dependence on the THz pump field.

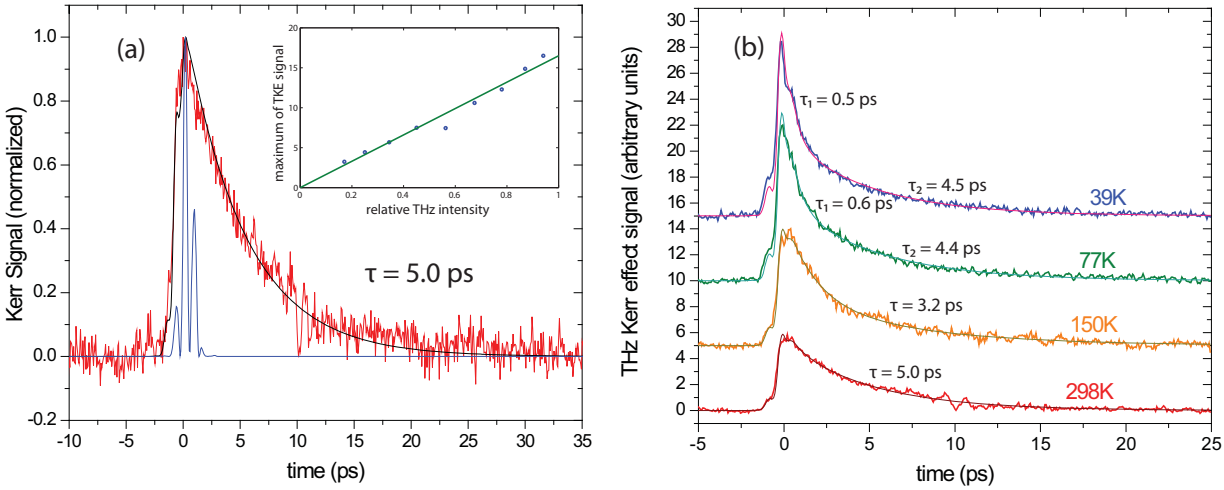

Figure 4: THz Kerr effect measurements on KTN. **(a)** THz Kerr effect in KTN at room temperature: experiment (red), fit (black), reference THz intensity (blue). **(inset)** Scaling of THz Kerr effect in KTN at room temperature as a function of relative THz intensity shows linear dependence confirming second order dependence on THz field. **(b)** Temperature dependence of the THz Kerr effect in KTN with fits to a convolution of the square of the THz pump field and a single exponential for high temperatures (150K and 298K) and a biexponential for low temperatures (39K and 77K). The faster time constant for low temperature measurements is much slower than the optical probe pulse duration and slower than the individual lobes of the square of the THz field.

8.2.1 Temperature Dependence

Temperature-dependent measurements were also performed to observe changes in the Kerr effect measurement as the Curie temperature was approached from above. The data were fit to either a single or biexponential decay convolved with the square of the pump THz pulse (Figure 4b). The THz Kerr effect signal increases as the temperature is decreased. The dynamics of the signal also change as a function of temperature. As temperature decreases, the time constant decreases as well, until the data no longer fit to a single exponential. At lower temperatures (below 80K) fits were performed with a biexponential function, since a single exponential did not yield a good fit. At low temperature, there is a fast contribution to the

signal (τ ≈ 0.5 ps) as well as a slower contribution (τ ≈ 5 ps) which is close to the decay constant at room temperature.

As in our THz Kerr effect measurements in simple liquids, we can calculate the induced change in refractive index *Δn* by the terahertz field

$$\frac{\Delta I}{I} = sin\Delta\phi = sin\frac{\Delta n\omega L}{c} = sin\frac{(n_x - n_y)\omega L}{c} \qquad (1)$$

where $\Delta I/I$ is the signal modulation measured in our balanced detection setup, $\Delta\phi$ is the phase retardation, ω is the probe pulse frequency, and *L* is the sample thickness (or in the case of poor phase matching, the coherence length). At room temperature with the maximum terahertz pump fluence, with a coherence length of L = 0.014 mm (at 0.7 THz, which is the peak of the incident THz spectrum, assuming the optical index is 2.5 and the THz index is 18) we obtain $\Delta I/I$ = 8.5 x 10^{-4}, yielding *Δn* = 7.7 x 10^{-6} in KTN. The refractive index change *Δn* ranges from about 8 x 10^{-6} at room temperature to 15 x 10^{-6} at 25 K (figure 5).

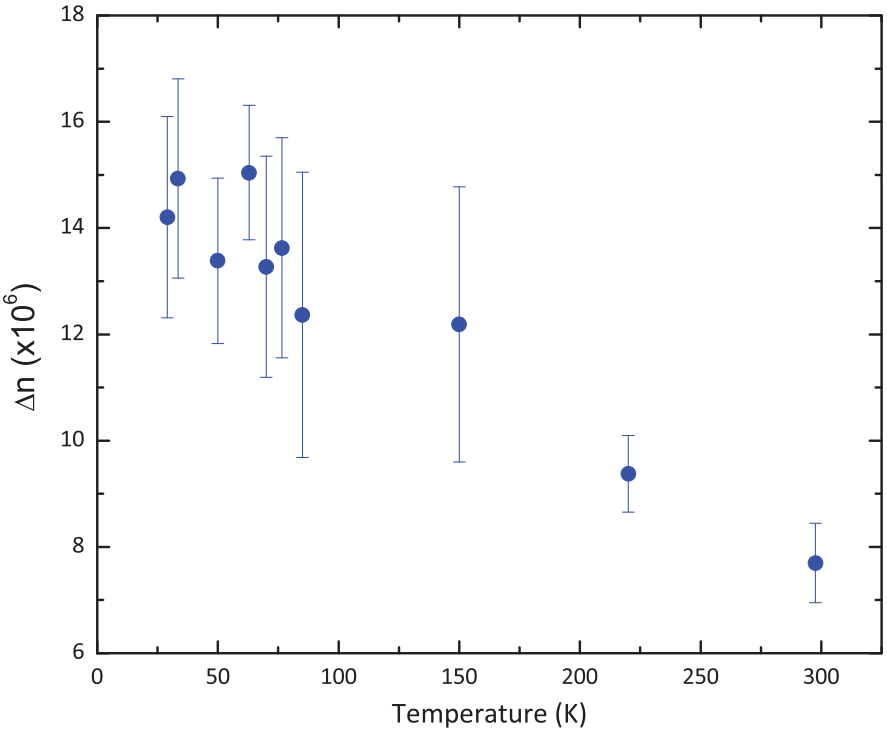

Figure 5: THz-induced change in refractive index Δn as a function of temperature. The induced change in refractive index changes by about a factor of 2 from room temperature to the phase transition temperature T_c.

To further elucidate the nonlinear THz dynamics in KTN, we performed linear THz time-domain measurements as a function of temperature. As the ferroelectric phase transition temperature is approached from above (T_c = 32 K), the soft mode in KTN redshifts and increases in magnitude. This is evident in the large decrease in THz transmission and increase in index (figure 6). The soft mode in KTN with 1.2% Nb doping goes from about 1.5 THz at 100 K to 0.3 THz at the phase transition temperature T_c = 25 K [16]. We could not measure the transmission below 100 K, indicating that the width of the soft phonon as well as its magnitude was large compared to our experimental bandwidth. For THz Kerr effect measurements, as the index increases, less of the THz pulse enters the crystal due to Fresnel reflection losses. However, as temperature is decreased, the magnitude of the THz Kerr effect signal increases, and we get a separation of timescales from single exponential decay dynamics to biexponential dynamics.

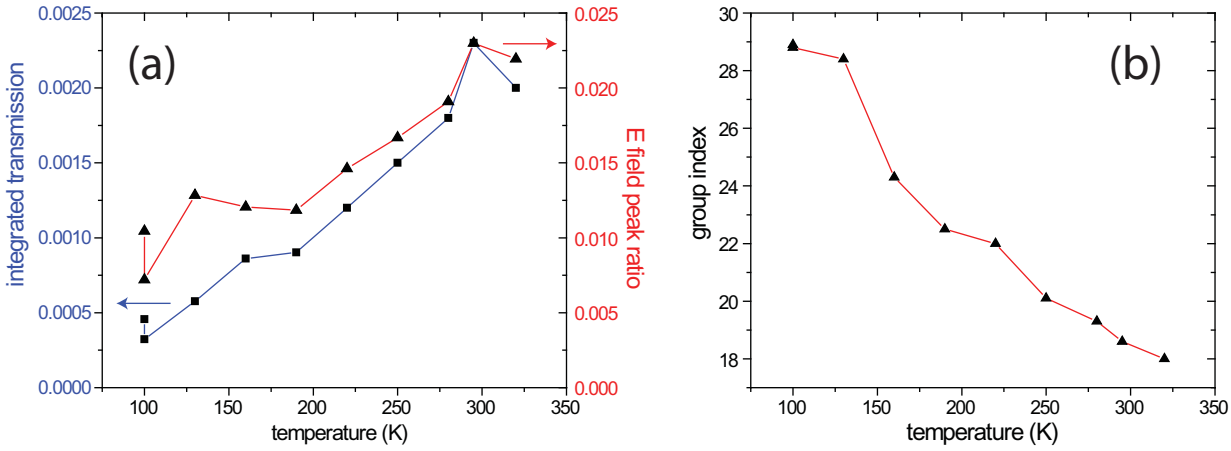

Figure 6: Temperature-dependent measurements on KTN with linear THz time-domain spectroscopy **(a)** Temperature dependence of KTN linear transmission measurements. The integrated transmission (blue) corresponds to the left axis. The ratio of the peak of the sample and reference THz electric fields (red) corresponds to the right axis. **(b)** Temperature dependence of KTN group index from linear THz transmission measurements. Note that both figures represent the respective lower bounds of the quantities shown since only the low frequencies from the pulse are transmitted, and all the high frequencies are absorbed (starting at about 0.7 THz).

8.2.2 The Origin of the Response

The large THz dielectric response in relaxor ferroelectrics makes phase-matched measurements on these materials difficult to realize. At room temperature in KTN, the THz index is ~18 whereas the optical (800 nm) index is ~2.5. Although previous studies on simple liquids have shown that the THz pump field can drive nonresonant electronic nonlinearities, we believe that this is not the dominant source of signal in KTN. All-optical Kerr effect measurements at several temperatures have shown that the electronic nonlinearity pumped by optical (800 nm) pulses is largely temperature independent down to the phase transition temperature (figure 7). If the KTN THz Kerr effect signal were induced by an instantaneous electronic response, the signal would be integrated over the propagation direction by the optical probe, yielding an

exponential decay in the signal as a function of pump-probe delay since the THz pulse would be absorbed as governed by Beer's law as it propagates into the crystal and the optical probe pulse would overlap with it deeper into the crystal at longer delays. In this case, the signal should decrease with decreasing temperature since more THz pump energy is reflected as the index increases, assuming the electronic response is temperature independent (confirmed in the all-optical Kerr effect measurements). In our case, we believe the long-lived signal arises from resonant dipole-mediated effects as opposed to nonresonant effects through the polarizability. Our temperature-dependent THz Kerr effect measurements show an increase in the magnitude of the Kerr effect as temperature is decreased—consistent with the increase in the soft mode dipole as the phase transition is approached. Though the phase matching in our experiment is poor, the dipole strength of the soft mode at all temperatures studied was very strong, minimizing the importance of phase matching since the interaction is strongest near the front face of the 0.2 mm crystal. As a result, we believe the THz Kerr effect signal in KTN occurs through a dipole-mediated response where the THz field resonantly pumps the soft vibrational mode.

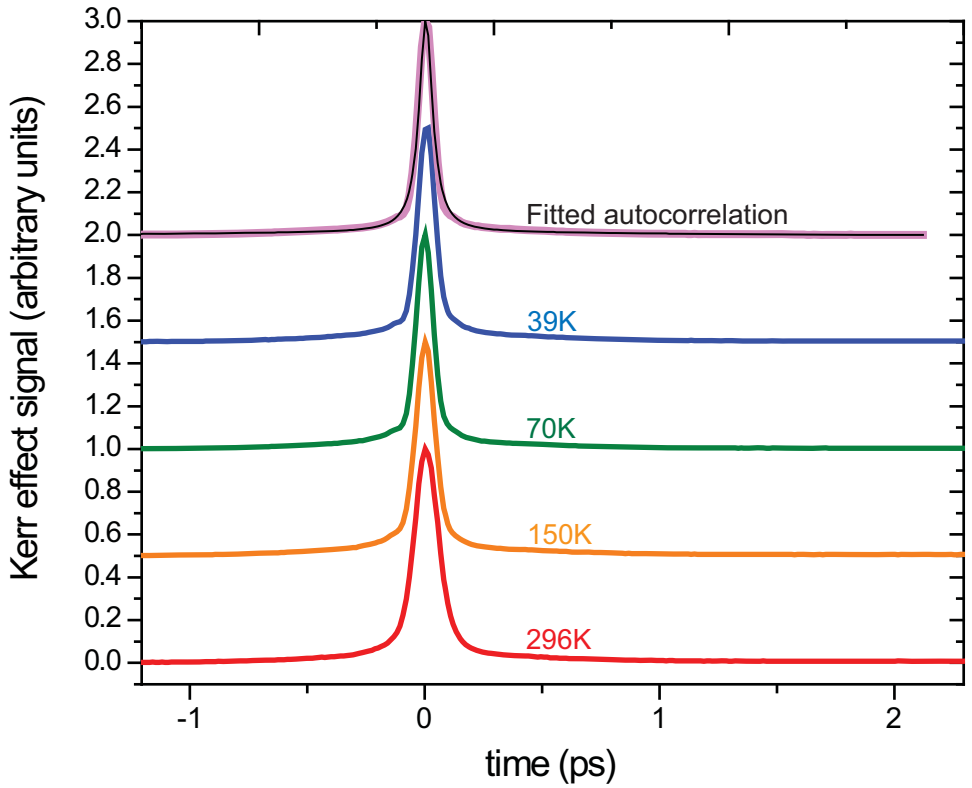

Figure 7: All-optical Kerr effect measurements on KTN at several temperatures. There is no temperature dependence of the all-optical response, indicating a minimal temperature dependence of the nonresonant electronic polarizability.

The second-order dependence of the Kerr signal level on the THz pump field strength suggests that the signal results from two THz dipole interactions. There are two main explanations for the origin of the signal: 1) the signal occurs through the creation of a non-equilibrium population induced by the THz pulse, or 2) the signal occurs through the creation of a 2-quantum coherence of the vibrational soft mode. If the 2-quantum coherence led to the birefringence response, we would expect that the signal would oscillate at twice the fundamental frequency as the system evolves through the coherence, instead of the monotonic decay we observe. Two-quantum rotational coherences induced in polar molecular gases by

strong THz pulses exhibit this feature in optical birefringence measurements [17]. This suggests that the signal comes from a non-equilibrium population distribution in the soft mode induced by the THz field. In this case, the non-equilibrium population of the soft mode changes the equilibrium bond distances in KTN. This leads to an induced anisotropy in the lattice. The population decay would then lead to the observed monotonically decreasing decay in the THz Kerr effect signal.

The separation of timescales at low temperature may be associated with the onset of ferroelectric nanodomains in the crystal. No other structural changes occur in KTN at the 1.8% Nb doping level. The crystal structure goes from the cubic paraelectric phase to the rhombohedral ferroelectric phase at T_c = 32 K [2]. The Burns temperature, the temperature at which ferroelectric nanodomains begin to form [18], occurs roughly 20 K above T_c in KTN for several Nb (1.2-15.7%) dopant concentrations [19, 20]. The macroscopic polarization response of a relaxor ferroelectric is tied to the formation of polar nanoregions (PNRs, or ferroelectric nanodomains), suggesting that the onset of the change in the dynamic response may be related to the formation of PNRs.

The observed effect suggests that experiments using only THz pulses, such as THz-pump/THz-probe, would be useful in further elucidating the nonlinear vibrational response. However, practical considerations make this measurement difficult to perform, since the transmission is very small (~0.2% in THz energy over our bandwidth at room temperature). One solution to this problem is to attach a crystal of intermediate index (between 1 and 18) before and after the KTN crystal to reduce Fresnel losses. However, the nonlinear response may be difficult to isolate since typical high-index materials are often other ferroelectrics that may

exhibit their own nonlinear responses. Nevertheless, other demonstrations of this method have been shown in previous work in the group. Another solution would be to go to even thinner crystals where we can reduce the overall absorption by making the path length shorter, though we would still lose a significant amount of THz light due to Fresnel losses.

8.3 THz Kerr Effect in KLTN

KLTN is a relaxor ferroelectric crystal similar to KTN in which some of the potassium ions are substituted with lithium ions. We have performed THz Kerr effect measurements on a 1.9 mm thick $K_{1-y}Li_yTa_{1-x}Nb_xO_3$ (KLTN, x = 0.345, y = 0.01, T_c = 264 K). THz Kerr effect measurements on KLTN showed a fast response (Figure 8) that could not be fit to a convolution with the THz intensity. However, in this case, the THz absorption is much stronger than in the case of KTN. This affects the shape of the Kerr effect signal. Assuming a strong lattice interaction with the THz pump pulse in KLTN as well, the lack of a long-lived response suggests fast lattice dynamics that cannot be resolved with our current setup. The signal is close to instantaneous with the square of the pump THz field. As temperature is increased, the lobe of the THz pulse occurring at longer time delays (~0.5 ps) grows in, suggesting less THz absorption at higher temperatures. This is consistent with the behavior of the soft mode, which blueshifts as the temperature is increased above T_c. Furthermore, there is some evidence that the dynamics begin to grow longer at higher temperatures—farther away from T_c, which is similar to what was observed in KTN.

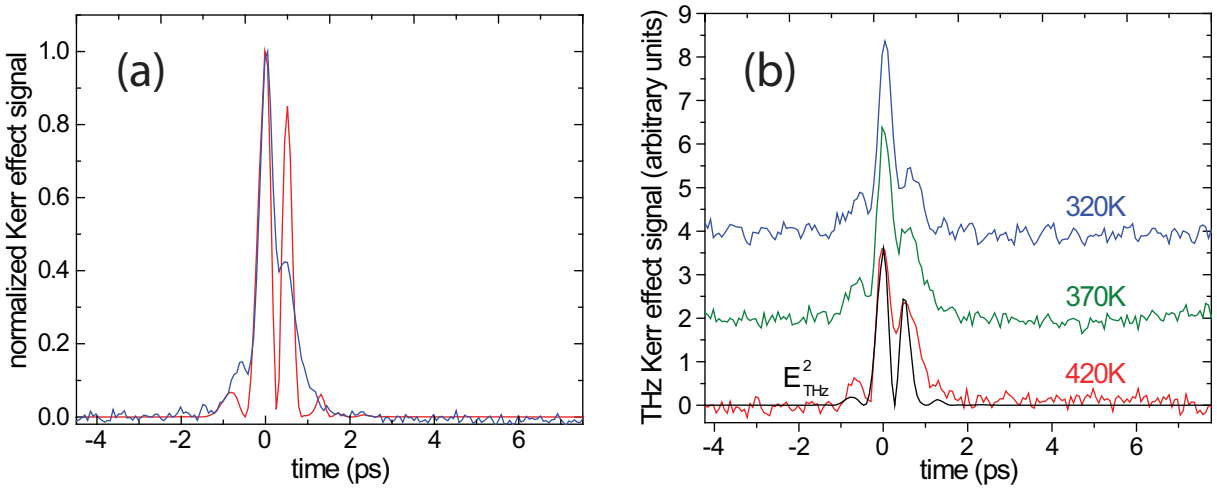

Figure 8: THz Kerr effect measurements on KLTN. **(a)** THz Kerr effect in KLTN at room temperature (blue) and the incident THz field (red). **(b)** Temperature dependence of THz Kerr effect in KLTN at several temperatures above T_c = 264 K. The square of the pump THz field is plotted in black.

8.4 Conclusions

We have performed THz Kerr effect measurements on the relaxor ferroelectrics KTN (1.8% Nb) and KLTN (1% Li, 34.5% Nb). The induced change in refractive index was on the order of 10^{-6} to 10^{-5}. KTN exhibits a long lived decay whereas KLTN shows a fast response that can follow the evolution of the THz intensity. The response in KTN is thought to arise from nonlinear pumping of the soft vibrational mode by the THz pump field. Due to the soft mode's very strong absorption and broad nature, nonlinear pumping of the soft mode is difficult to observe in nonlinear THz transmission spectroscopy. We have been able to observe a dynamic response from the lattice as the ferroelectric phase transition is approached from above, going through the temperature regime of ferroelectric nanodomain formation. The dynamics change from single exponential decay to biexponential decay going from high to low temperature near the Burns temperature, suggesting that the change in dynamics may be related to the formation of

ferroelectric nanodomains. The fast response in KLTN may be attributed to disorder in the lattice since it is highly doped with Nb ions. Further studies to model the index modulation from induced lattice asymmetry will help aid a better understanding of the effect of resonantly pumping the soft vibrational mode in relaxor ferroelectrics.

References

[1] G. A. Samara. "Glasslike Behavior and Novel Pressure Effects in $KTa_{1-x}Nb_xO_3$." *Physical Review Letters*, **53**, 298 (1984).

[2] G. A. Samara. "From Ferroelectric to Quantum Paraelectric: $KTa_{1-x}Nb_xO_3$ (KTN), A Model System." *AIP Conference Proceedings*, **706**, 176 (2004).

[3] G. A. Samara. "Ferroelectricity Revisited - Advances in Materials and Physics." *in* Solid State Physics: Advances in Research and Application. edited by H. Ehrenreich (Academic Press 2001).

[4] B. E. Vugmeister, P. DiAntonio and J. Toulouse. "Raman Study of Cluster Dynamics in Disordered Ferroelectrics." *Physical Review Letters*, **75**, 1646 (1995).

[5] T. Qi, Y.-H. Shin, K.-L. Yeh, K. A. Nelson and A. M. Rappe. "Collective Coherent Control: Synchronization of Polarization in Ferroelectric $PbTiO_3$ by Shaped THz Fields." *Physical Review Letters*, **102**, 247603 (2009).

[6] T. Itoh, M. Sasaura, S. Toyoda, K. Manabe, K. Nakamura and K. Fujiura. "High-Frequency Response of Electro-Optic Single Crystal $KTa_{1-x}Nb_xO_3$ in Paraelectric Phase." *in Conference on Lasers and Electro-Optics*,Baltimore, MD (2005).

[7] X. Wang, J. Wang, Y. Yu, H. Zhang and R. I. Boughton. "Growth of cubic $KTa_{1-x}Nb_xO_3$ crystal by Czochralski method." *Journal of Crystal Growth*, **293**, 398 (2006).

[8] G. Giraud, C. M. Gordon, I. R. Dunkin and K. Wynne. "The effects of anion and cation substitution on the ultrafast solvent dynamics of ionic liquids: A time-resolved optical Kerr-effect spectroscopic study." *The Journal of Chemical Physics*, **119**, 464 (2003).

[9] Q. Zhong and J. T. Fourkas. "Optical Kerr Effect Spectroscopy of Simple Liquids†." *The Journal of Physical Chemistry B*, **112**, 15529 (2008).

[10] C. J. Fecko, J. D. Eaves and A. Tokmakoff. "Isotropic and anisotropic Raman scattering from molecular liquids measured by spatially masked optical Kerr effect spectroscopy." *The Journal of Chemical Physics*, **117**, 1139 (2002).

[11] M. C. Hoffmann, N. C. Brandt, H. Y. Hwang, K.-L. Yeh and K. A. Nelson. "Terahertz Kerr effect." *Applied Physics Letters*, **95**, 231105 (2009).

[12] J. Hebling, G. Almasi, I. Kozma and J. Kuhl. "Velocity matching by pulse front tilting for large area THz-pulse generation." *Opt. Express*, **10**, 1161 (2002).

[13] M. C. Hoffmann, K.-L. Yeh, J. Hebling and K. A. Nelson. "Efficient terahertz generation by optical rectification at 1035 nm." *Opt. Express*, **15**, 11706 (2007).

[14] K. L. Yeh, M. C. Hoffmann, J. Hebling and K. A. Nelson. "Generation of 10 μJ ultrashort terahertz pulses by optical rectification." *Applied Physics Letters*, **90**, 171121 (2007).

[15] O. Svitelskiy and J. Toulouse. "Translational and rotational mode coupling in disordered ferroelectric $KTa_{1-x}Nb_xO_3$ studied by Raman spectroscopy." *Journal of Physics and Chemistry of Solids*, **64**, 665 (2003).

[16] L. Foussadier, M. D. Fontana and W. Kress. "Phonon dispersion curves in dilute KTN crystals." *Journal of Physics: Condensed Matter*, **8**, 1135 (1996).

[17] S. Fleischer, Y. Zhou, R. W. Field and K. A. Nelson. "Molecular Orientation and Alignment by Intense Single-Cycle THz Pulses." *Physical Review Letters*, **107**, 163603 (2011).

[18] G. Burns and F. H. Dacol. "Crystalline ferroelectrics with glassy polarization behavior." *Physical Review B*, **28**, 2527 (1983).

[19] L. A. Knauss, X. M. Wang and J. Toulouse. "Polarization-strain coupling in the mixed ferroelectric $KTa_{1-x}Nb_xO_3$." *Physical Review B*, **52**, 13261 (1995).

[20] J. Toulouse and R. K. Pattnaik. "Pretransitional condensation in mixed ferroelectrics." *Journal of Physics and Chemistry of Solids*, **57**, 1473 (1996).

Chapter 9

Metamaterial-Enhanced Nonlinear THz Spectroscopy

Metamaterials are engineered subwavelength structures that exhibit custom-tailored electromagnetic responses. For the THz range, metamaterials may by easily designed and fabricated with current micro-scale photolithography techniques. There has been much recent interest in the use of metamaterials to induce nonlinear responses in materials. In particular, it has recently been demonstrated that the antenna-like nature of certain THz metamaterial structures can enhance electric fields by over an order of magnitude [1]. It has been proposed to use such enhancements for second harmonic generation in ferroelectric crystals [2]. In this chapter, I will discuss several experiments that have demonstrated extraordinary nonlinearities with metamaterial-enhanced THz fields—nonlinear electronic effects in the semiconductor, gallium arsenide (GaAs), and a THz-induced insulator-to-metal phase transition (IMT) in vanadium dioxide (VO_2). The work in this chapter is a result of a collaboration with Mengkun

Liu, Kebin Fan, Aaron Sternbach, and others from the research groups of Prof. Richard Averitt and Prof. Xin Zhang at Boston University.

9.1 Nonlinear Metamaterials: Carrier Mobility Suppression and Impact Ionization in Gallium Arsenide

Nonlinear metamaterials is a rapidly developing field of fundamental interest with significant technological implications spanning from microwave through visible frequencies of light [3-8]. As with tunable and reconfigurable metamaterials [9, 10], nonlinear metamaterial responses depend highly on their physical structure and local environment. This is because the most significant nonlinearities take advantage of the local field enhancement within the active region of the subwavelength metamaterial elements which, in the case of split ring resonators, are the capacitive gaps. While the active volume of the enhanced gaps is small in comparison to the unit cell volume, the field enhancement can dominate volumetric effects leading to nonlinearities enhanced by two to four order of magnitude [7] in microwave studies.

Advances in nonlinear metamaterials coincide with the development of high-field terahertz sources capable of generating electric fields sufficient to induce nonlinear responses in conventional matter [11-15]. For example, in doped GaAs, velocity saturation and impact ionization have been observed [12, 15]. However, such effects require peak electric fields of over a hundred kV/cm. In this section, we will demonstrate that judicious incorporation of metamaterial elements with semiconductors enable significant enhancement of nonlinear electronic responses at reduced incident field strength compared to driving the same nonlinearities without metamaterials, due to the large field enhancements provided by

metamaterials [2, 16-18]. We will experimentally demonstrate different nonlinear responses in metamaterial split ring resonators on n-type GaAs and semi-insulating GaAs. We will show that with increasing incident THz electric field strengths, the metamaterial resonance can be enhanced or quenched as a result of a large change in the local conductivity of the capacitive gaps. Furthermore, we will demonstrate that around the resonance, the field-dependent nonlinearity provides a way to sweep the effective permittivity from negative to positive values. Finally, we will discuss damage to the GaAs due to the large localized THz fields in the metamaterial gaps.

9.1.1 Metamaterial Resonance Suppression on Moderate-Conductivity Substrates

To create nonlinear metamaterials, electric inductive-capacitive resonator (ELCR) arrays were fabricated by conventional microfabrication on a GaAs substrate. In figure 1a we show metamaterial structures on a 1.8-μm-thick doped GaAs film (carrier density n = 1 x 10^{16} cm^{-3}), which was grown on a semi-insulating GaAs (SI-GaAs) substrate using molecular-beam epitaxy (MBE). The ELCRs (figure 1a) consist of 200 nm thick Au with a 10 nm Cr adhesion layer. The ELCR dimension is l = 36 μm with a period of p = 50 μm. The capacitive gap has a width of g = 2.2 μm as shown in the inset of figure 1. The small gap width is crucial for the field enhancement as we will discuss in detail later. Low-field THz-TDS using ZnTe generated terahertz pulses was first employed to characterize the metamaterial response. In order to accurately extract the transmission response of the metamaterials, a bare n-type GaAs substrate was used as a reference. Figure 1b shows that the inductive-capacitice (LC) resonance

is at about 0.75 THz which is close to the peak frequency of THz pulses generated by tilted pulse front generation in $LiNbO_3$ [19].

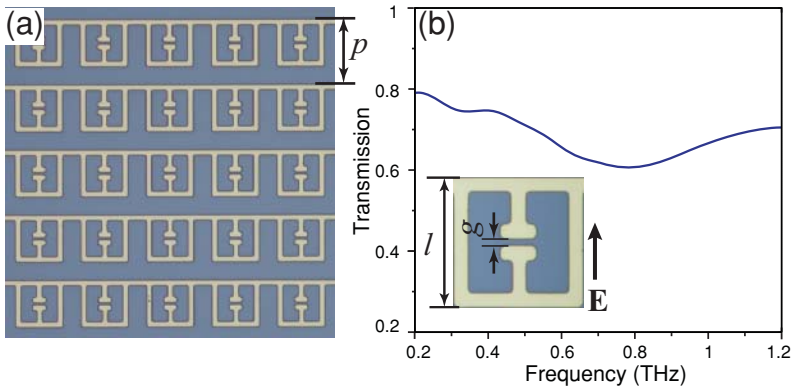

Figure 1. (a) Image of ELCR arrays on n-type GaAs substrate. The period, *p*, is 50 μm; the length of ring, *l*, is 36 μm; the gap is 2.2 μm. **(b)** Measured electric transmission of ELCRs on doped GaAs characterized by a ZnTe based THz-TDS.

High-field THz transmission experiments discussed later were conducted to address the nonlinear response of the n-doped GaAs. Tilted-pulse-front THz generation in a $LiNbO_3$ crystal renders a peak THz field strength of about 400 kV/cm in free space, with a 1 mm beam diameter at the focus. The field strength could be varied with a pair of wire grid polarizers in the THz beam path from 24 kV/cm to 400 kV/cm. The detailed experimental setup has been described elsewhere [11, 12, 20]. All experiments were performed at room temperature in a dry air environment at ambient pressure.

9.1.2 Recovery of Metamaterial Resonance with THz-Induced Carrier Mobility Saturation of a n-Doped GaAs Substrate

Figure 2a and b show the experimentally measured transmission of metamaterials as a function of frequency for various incident (peak) electric fields. With increasing field from 24 kV/cm to

400 kV/cm, two distinct nonlinear processes were observed. Under the lowest-field irradiation (24 kV/cm), the transmission response is close to the result shown in figure 1b. The weak LC resonance indicates a moderately conductive substrate, providing a path for electron flow, partially shorting the resonator gaps. As the incident field increases from 24 kV/cm to 160 kV/cm, the transmission at the metamaterial resonance (~0.73 THz) decreases significantly from 65% to about 30%, while the transmission away from resonance on the low frequency end increases notably (at 0.4 THz transmission goes from from 80% to over 90%). This global change of transmission over the entire spectrum indicates a global conductivity change in the entire n-GaAs film, which is comparable to other tunable metamaterial responses [21, 22]. This is indicative of THz saturable absorption by suppression of the carrier mobility (as discussed in Chapter 5). With further increase of the THz electric field, a different trend is shown in figure 2b. The on-resonance response starts to be quenched while the off-resonance transmission at lower frequencies (< 0.5 THz) remains almost unchanged. This on resonance transmission increment implies a local conductivity increase in the capacitive gaps of resonators.

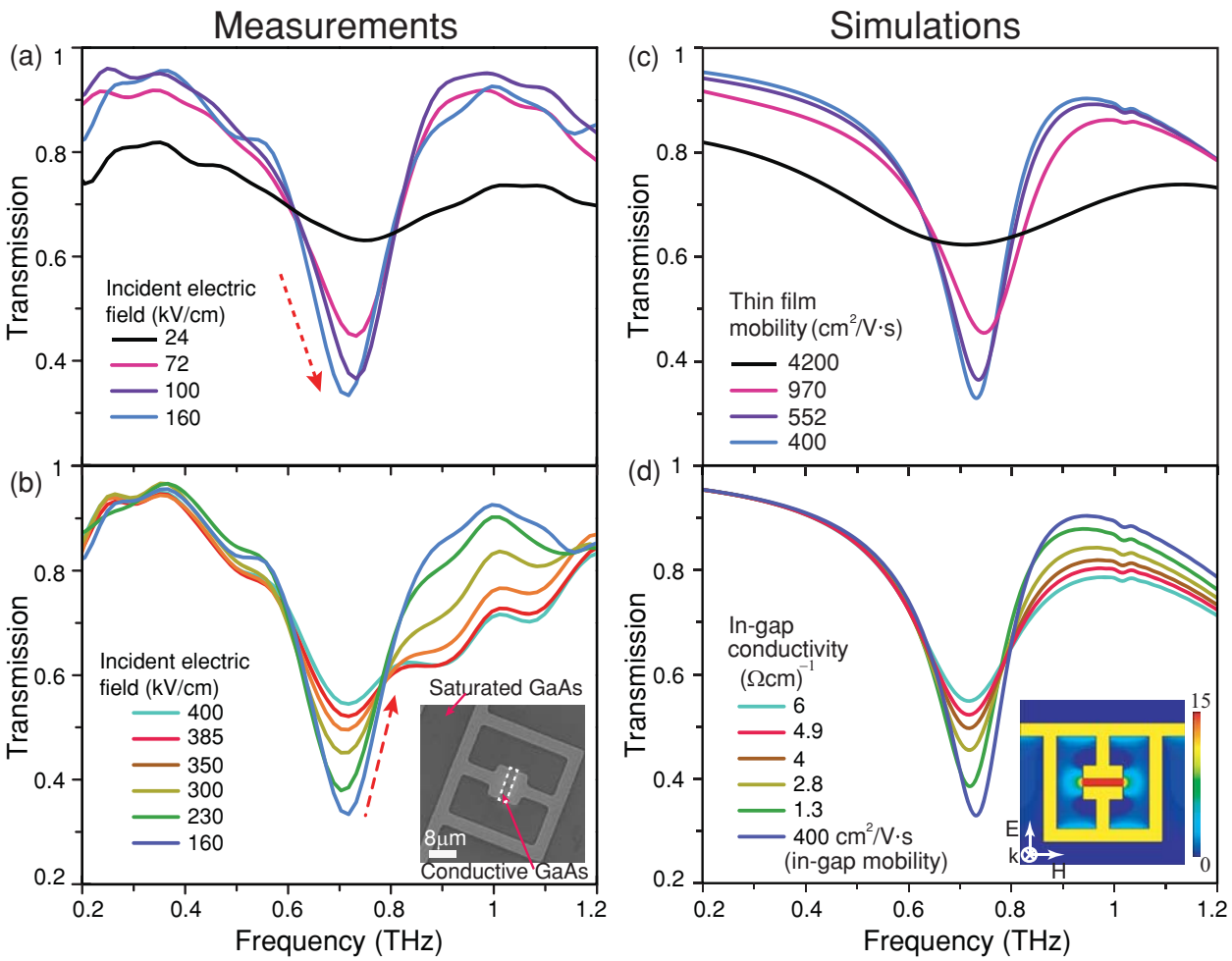

Figure 2. (a) & (b) Experimental electric field transmission of ELCR array as a function of frequency for various incident peak electric fields. **(c)** Simulated transmission of ELCRs on doped GaAs as a function of mobility over the entire thin film. **(d)** Simulated transmission of ELCRs on doped GaAs as a function of conductivity of within the capacitive gaps. The inset in (b) shows a SEM picture of an ELCR after high-field (above 160 kV/cm) irradiation. The dotted white region in the inset indicates the region over which impact ionization produces conductive GaAs. The inset in (d) shows the simulated on-resonance field enhancement of ELCRs at the interface of saturated substrate with gold thin film.

The two distinct nonlinear processes happening at different field levels are the result of two different nonequilibrium carrier transport processes in the n-GaAs film. The first process, occurring between 0 and 160 kV/cm, can be ascribed to the photoinduced transparency in doped substrates [12, 23], or saturable absorption. The THz field excitation drives electrons initially in the lowest-energy valley in the conduction-band (Γ valley), upon which they can

acquire energy on the order of 1 eV, scattering them into satellite valleys (e.g. L valley). Since the mobility in the side valleys can be one order of magnitude smaller than that in the Γ valley, intervalley scattering leads to a less conductive GaAs substrate compared to the low-field situation where the electrons are all in the L valley (as discussed in chapter 5 and [12, 20]). Consequently, the LC resonance builds up gradually as the on-resonance transmission decreases. When the field is above 160 kV/cm, most of the conduction electrons are expected to be scattered into the side valleys. This is consistent with intervalley scattering studied by high field THz experiments on doped GaAs without metamaterials, and the field strength and saturable absorption response are comparable to this demonstration. We note that at the early stages (24 kV/cm) the field enhancement in the SRR gaps is very small because of the highly conducting GaAs surface.

9.1.3 Impact Ionization in n-Type GaAs with Metamaterial-Enhanced THz Fields

With higher THz field impinging on the metamaterials (at incident field strengths of 160 kV/cm to 400 kV/cm), the nonlinear response is attributed primarily to another high-field carrier transport phenomenon—impact ionization. In this field strength regime, there is a large field enhancement in the resonator gaps due to the prominent on resonant response. Therefore, at higher THz fields, with large in-gap THz enhancement (since the substrate is more insulating, the enhancement is much larger), electrons in the conduction band are effectively accelerated by the THz electric field. The energetic electrons collide with valence band electrons generating de-energized conduction band electrons and electron-hole pairs, resulting in a large increase in the carrier density [14].

9.1.4 Modeling the Nonlinear Metamaterial Response in n-Type GaAs

To verify the nonlinear metamaterial responses caused by the two different carrier transport processes, numerical simulations were conducted based on the previous interpretation. For the intervalley scattering-induced resonance enhancement, we modeled the carrier dynamics in the thin film n-type GaAs with the Drude model. In order to simplify the model, several assumptions have been made: 1) the electron-phonon relaxation times in the Γ valley and L valley are the same, 2) the average mobility varies by changing the relative fraction of electrons in the Γ valley and L valley; 3) at 160 kV/cm field strength, all of the conduction electrons are scattered to L valley, and impact ionization in the metamaterial gaps is ignored. Initially (at 24 kV/cm incident THz field strength), the fit to the mobility in the n-type GaAs gave μ = 4200 $cm^2/V{\cdot}s$, which is close to the reported value [24]. When all the conduction electrons are scattered in the L valley (at 160 kV/cm), the fit to the mobility gave μ = 400 $cm^2/V{\cdot}s$, with an effective mass of 0.55 m_0, where m_0 is the mass of an electron at rest. Between these two extremes, the mobility can be fit by averaging the electrons distributed in Γ and L valleys (figure 2c).

At higher field strengths (> 160 kV/cm), as the THz resonance builds up, the in-gap field enhancement also starts to increase. At 160 kV/cm field level, the in-gap electric field is estimated to be enhanced by a factor of 15 at the metamaterial resonance with an overall peak electric field enhancement factor of 4 in the time domain. This is in good agreement with previously reported values [2]. Thus, with an incident field strength of 160 kV/cm, the corresponding in-gap field is estimated to be 0.64 MV/cm, which above the 0.47 MV/cm

threshold for observing impact ionization in GaAs quantum wells [15]. As a simple estimate, we describe the motion of electrons under an external field with a rate equation

$$\frac{d\langle V(t)\rangle}{dt} = \frac{eE(t)}{m_e} - \frac{\langle V(t)\rangle}{\tau(E)} \quad (1)$$

where $\langle V(t)\rangle$ is the average electron velocity, *E(t)* is the THz field, m_e is the electron effective mass, $\tau = \frac{m_e\mu}{e}$ is the relaxation time, and μ is the electron mobility [25]. We assume that impact ionization happens when the kinetic energy of an electron reaches a threshold energy, E_{th} = 2.4 eV (assuming impact ionization happens at the L valley and not at the Γ valley where E_{th} = 1.7 eV) [26]. Assuming the impact ionization time is much shorter than the pulse duration, tens of impact ionization iterations produce numerous carriers. However this may not be the case as discussed later in this chapter. For now, we will use this simplification so that we can estimate carrier densities. Model calculations show that with an initial carrier density of 1 x 10^{16} cm^{-3}, an incident field of 400 kV/cm (2.4 MV/cm in gap field) can increase the carrier density up to 10^{17} cm^{-3} in the capacitive regions. This process leads to an in-gap conductivity of ~6 $(\Omega\cdot cm)^{-1}$. The estimated carrier density (conductivity) is consistent with the experimental and simulation results (figure 2b and d). The energy conversion efficiency is estimated to be about 4.3 x 10^{-4} since only part of the energy is absorbed into the substrate. Importantly, to obtain reasonable agreement with simulations in the highest field, we must assume an average electron mobility of 260 $cm^2/V\cdot s$ in gaps, which is more than one order of magnitude lower than that of a steady state in the Γ valley, while in good agreement with the lower end of the L valley mobility previously reported with optical excitation [27, 28]. Monte Carlo simulations were also performed by the Averitt group to address the number of impact ionization events assuming a 1D electron band structure including the Γ, L and X valleys. The results are quantitatively in

agreement with the rate equation estimation. Full band Monte Carlo simulations would be helpful to further address the carrier transport properties, however, it is beyond the scope of this experimental demonstration.

9.1.5 Impact Ionization in Semi-Insulating GaAs with Metamaterial-Enhanced THz Fields

Taking advantage of the localized enhanced field in the capacitive regions, we also observed a strong nonlinear metamaterial response on a semi-insulating GaAs (SI-GaAs) substrate with initial carrier density of 6×10^7 cm^{-3}. The inset of figure 3 shows the fabricated electric split-ring resonators on SI-GaAs substrate. The size and period of the SRR resonators are the same as those of the ELCRs on the doped GaAs, which keeps the resonance roughly at the same frequency. However, we designed a smaller SRR gap, g = 1.3 μm, to induce a larger field enhancement since it is expected to be much more difficult to observe the impact ionization process in semi-insulating GaAs due to the low initial carrier density.

Figure 3a shows the experimentally measured transmission of the metamaterials as a function of frequency for various incident (peak) electric fields. At the lowest field (100 kV/cm), the response is in the linear regime with a characteristic dip in the transmission at the LC resonance frequency. As the incident field increases, the metamaterial transmission at the resonant frequency gradually increases and broadens, while there is negligible change at lower frequencies. It is worth mentioning that even at the highest incident fields, no nonlinear transmission changes were detected in the bare semi-insulating GaAs substrate. These facts suggest that the observed nonlinearity arises from changes in the capacitive gap regions.

Similar to the nonlinear high field results (> 160 kV/cm) in the n-doped GaAs, the results suggest a large increase in the conductivity in the ESRR gaps, indicating substantial carrier generation in the SRR gaps via impact ionization.

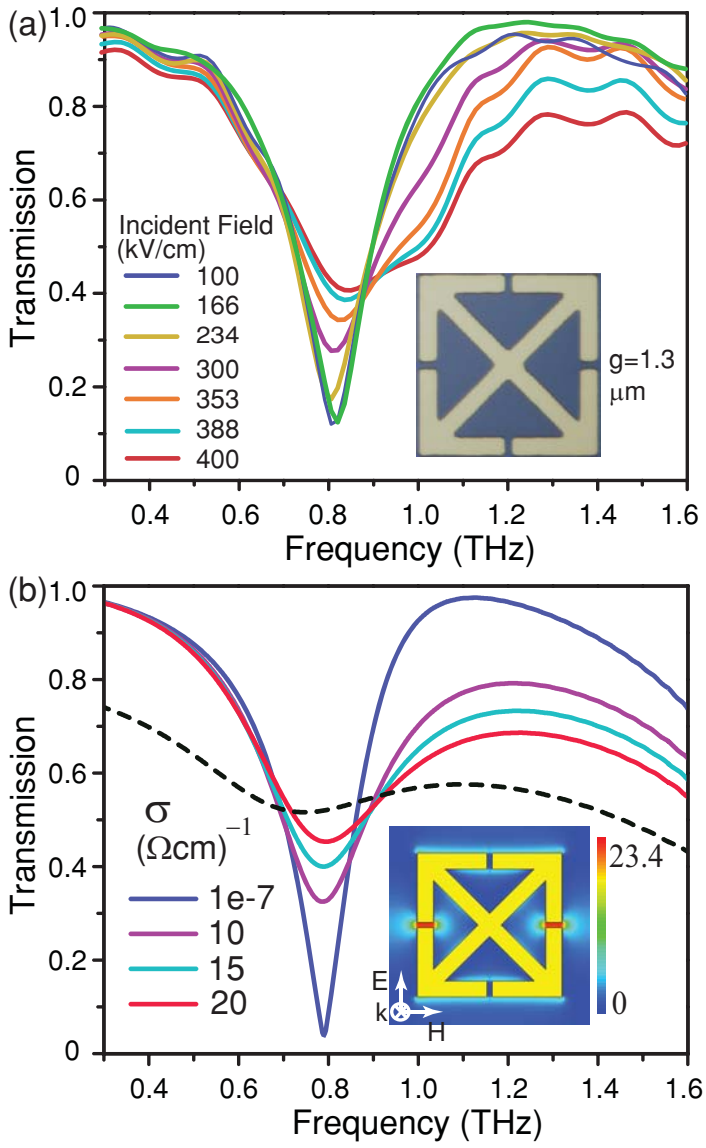

Figure 3. (a) Experimental electric field transmission of ESRR array as a function of frequency for various incident peak electric fields. (b) Simulated transmission of ESRR on SI-GaAs as a function of conductivity within the capacitive gaps. The dashed curve shows the response when the entire surface of GaAs substrate becomes conductive with σ of 20 $(\Omega \cdot cm)^{-1}$.

Simulations were performed by changing the conductivity of the GaAs only in the vertical gaps as shown in the inset of figure 2b. The plot shows the transmission changes upon increasing the in-gap conductivity of GaAs from 10^{-7} $(\Omega\cdot cm)^{-1}$ to 20 $(\Omega\cdot cm)^{-1}$. Clearly, the simulations show a markedly similar trend to the experimental results. The dashed curve in figure 3b indicates the simulated transmission response assuming the conductivity of the entire surface (up to 0.5 μm thick) of GaAs substrate is 20 $(\Omega\cdot cm)^{-1}$. The large deviation from our experimental results suggests that the increase in conductivity is confined to the gap region. The inset of figure 3b shows the field within gaps enhanced by over 20 times on the peak of the metamaterial resonance. The peak electric field in the time domain is enhanced by a factor of about 7. Model calculations show that with an initial carrier density of 6 x 10^7 cm^{-3}, an in-gap field of 3.5 MV/cm (the highest field estimated based on the enhancement) can increase the carrier density by more than ten orders of magnitude up to ~10^{18} cm^{-3}. We note that in order to get quantitative agreement with the experimental results, the average mobility μ should be assumed to be as low as 230. This suggests that in semi-insulating GaAs the electron mobility is suppressed prior to the impact ionization process, even though we could not observe the intervalley scattering process directly from the metamaterial response as in the case of the n-doped GaAs.

9.1.6 Effect of Strong Carrier Generation on the Effective Real Permittivity

It is well known that the effective nonresonant nonlinearities of materials within the gaps of SRRs can be enhanced by orders of magnitude, due to the subwavelength field enhancement in the metamaterials [29]. The present results highlight that this is also the case for resonant

nonlinearities. For our metamaterials, the nonlinearity corresponds to a change of the oscillator strength of the LC resonance. This necessarily leads to changes in the effective permittivity and refractive index at frequencies away from resonance, because of dispersion. This can be understood by considering figures 4a and c, which show the effective real permittivity as a function of the incident field strength for metamaterials on n-type GaAs and SI-GaAs, respectively. These plots were obtained by performing parameter extraction (for a cubic unit cell) using the full wave simulations of figures 2 and 3 and subsequently mapping the in-gap conductivity to the corresponding incident peak electric field required to achieve that conductivity. It is clear that ε_{re} shows a different field strength dependence for ELCRs and ESRRs.

For the ELCRs on n-type GaAs, the off-resonance ε_{re} at 0.82 THz changes from positive to negative value owing to the intervalley scattering in the doped thin film. With fields above 160 kV/cm, ε_{re} increases from negative to positive values. For ESRRs on SI-GaAs substrate, the induced impact ionization of the capacitive gaps increases the ε_{re} monotonically from negative to positive values at 0.85 THz.

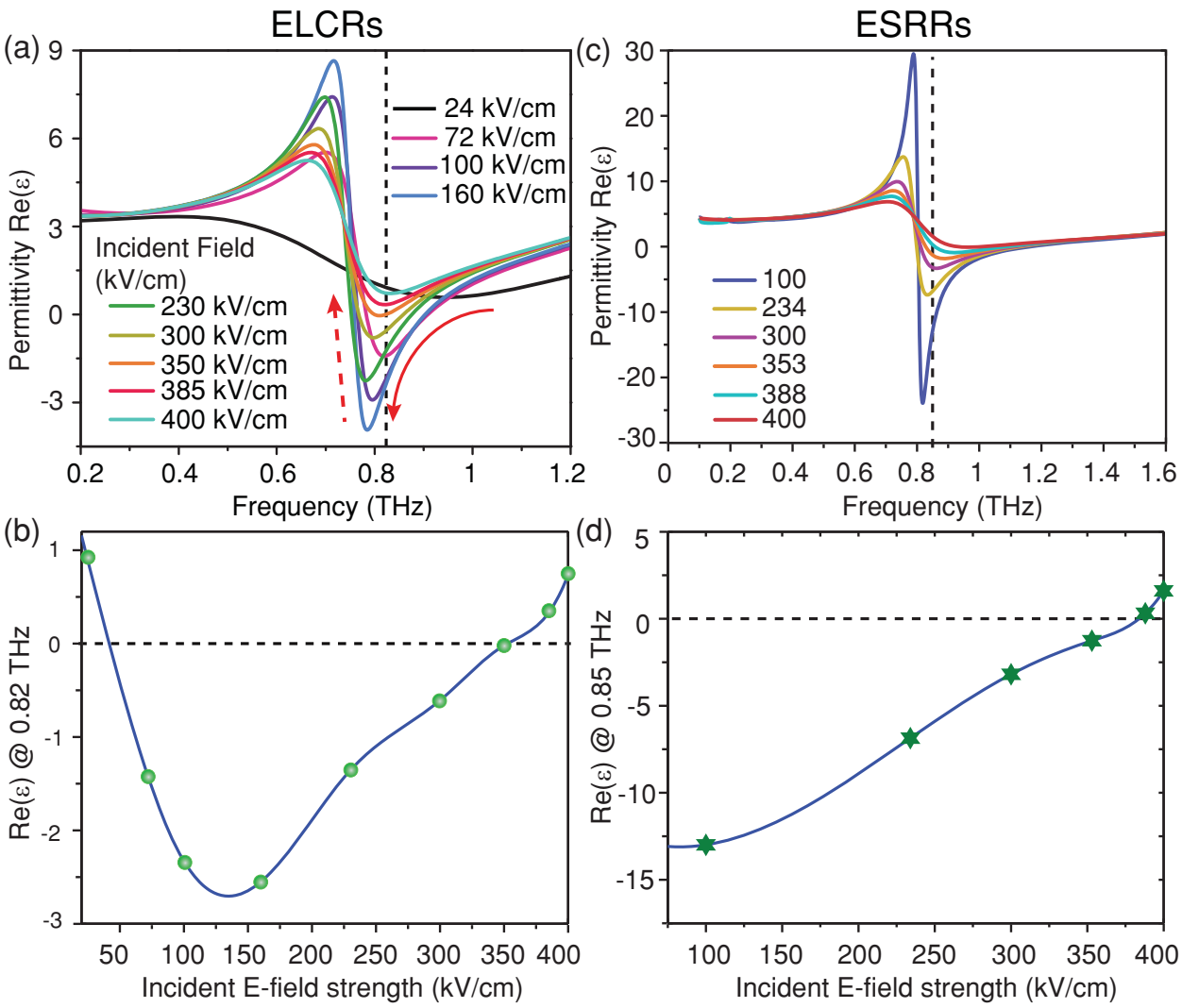

Figure 4. (a) Effective real permittivity $\varepsilon_{re}(\omega)$ of ELCRs on doped GaAs for various incident electric fields. **(b)** ε_{re} as a function of incident peak electric field strength at 0.82 THz for metamaterials on doped GaAs. **(c)** Effective real permittivity $\varepsilon_{re}(\omega)$ of ESRRs on SI-GaAs for various incident electric fields. **(d)** ε_{re} as a function of incident peak electric field strength at 0.85THz for metamaterials on SI-GaAs.

9.1.7 Impact Ionization Dynamics in SI-GaAs

Collinear THz-pump/THz-probe measurements were performed to study the dynamics of the impact ionization process in SI-GaAs. For comparison, optical-pump/THz-probe measurements were performed as well. Figure 5 depicts dynamic measurements under 400 nm optical pump

and THz pump conditions. For the optical pump, carriers are generated instantaneously via direct band-to-band absorption. The metamaterial response was measured as a function of pump-probe delay time. The transmission signal at 0.8 THz is plotted showing a few-picosecond risetime in the response, due to the metamaterial response convoluting the true response time. However, THz-pump/THz-probe measurements reveal much longer dynamics. This suggests that the impact ionization process continues after the THz-pump pulse passes through the sample. This is in contrast to what is assumed in other work, where ballistic electron motion on the order of hundreds of picoseconds [15, 25] is thought to restrict impact ionization to the duration of the THz pulse, before electron-phonon scattering can play a significant role in the energy dissipation of the THz-field accelerated electrons. This result indicates that a more sophisticated model must be used to properly understand impact ionization processes in SI-GaAs.

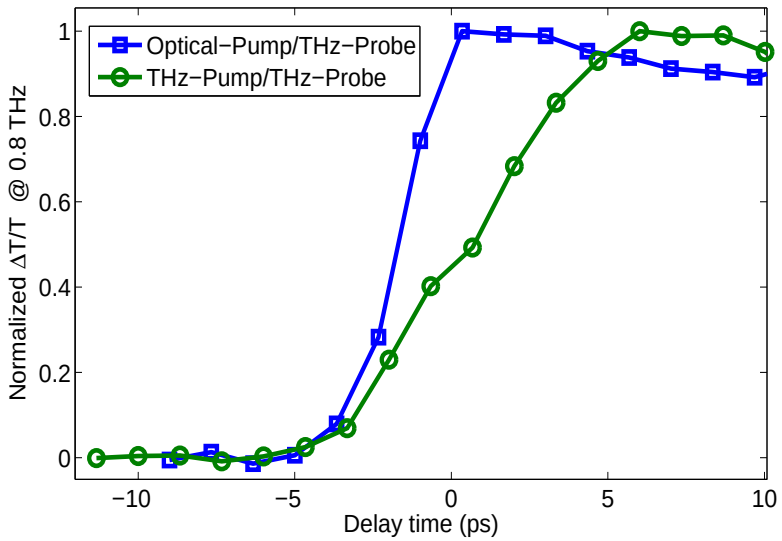

Figure 5. Comparison of optical-pump/THz-probe (OPTP) and THz-pump/THz-probe (TPTP) measurements of carrier generation dynamics in SI-GaAs metamaterials. OPTP (blue) measurements were performed with 400 nm excitation collinear with the THz probe pulse. The carrier generation dynamics with optical pump should be instantaneous with the excitation,

however, the metamaterial response time lengthens the response. TPTP (green) measurements reveal substantially slower generation dynamics, suggesting that the impact ionization process continues long after the THz-pump pulse has passed.

9.1.8 THz-Induced Damage in GaAs

Over the course of the experiments, continuous irradiation of the sample at the highest THz field strength (400 kV/cm) resulted in irreversible changes in the capacitive regions as shown in figure 6. Time dependent damage tests show that the damage does not occur in a single shot but rather is a cumulative effect over a few hours. As shown in figure 6a, damage only occurs in the gaps with side bars parallel to the incident electric field. These results are important as they directly confirm that it is within the capacitive regions that nonlinear effects occur. The cracks and pinholes extending along the direction of the electric field indicate an avalanche breakdown process occurring in the SI-GaAs substrate as shown in the inset of figure 6b. Nevertheless, the effective nonlinear response did not degrade. That is, the field could be repeatedly ramped up to the highest incident electric field of 400 kV/cm with subsequent low field and high field transmission measurements yielding data very similar to that in figure 3a. Figure 6b shows the transmission response measured before and after the damage occurring with low incident fileld. This indicates the damaged area remains insulating instead of conducting in contrast to some permanent dielectric breakdown processes that occur in various dielectric insulators [30]. As a result, the nonlinear electrodynamic response remains unchanged subsequent to damage in the SI-GaAs.

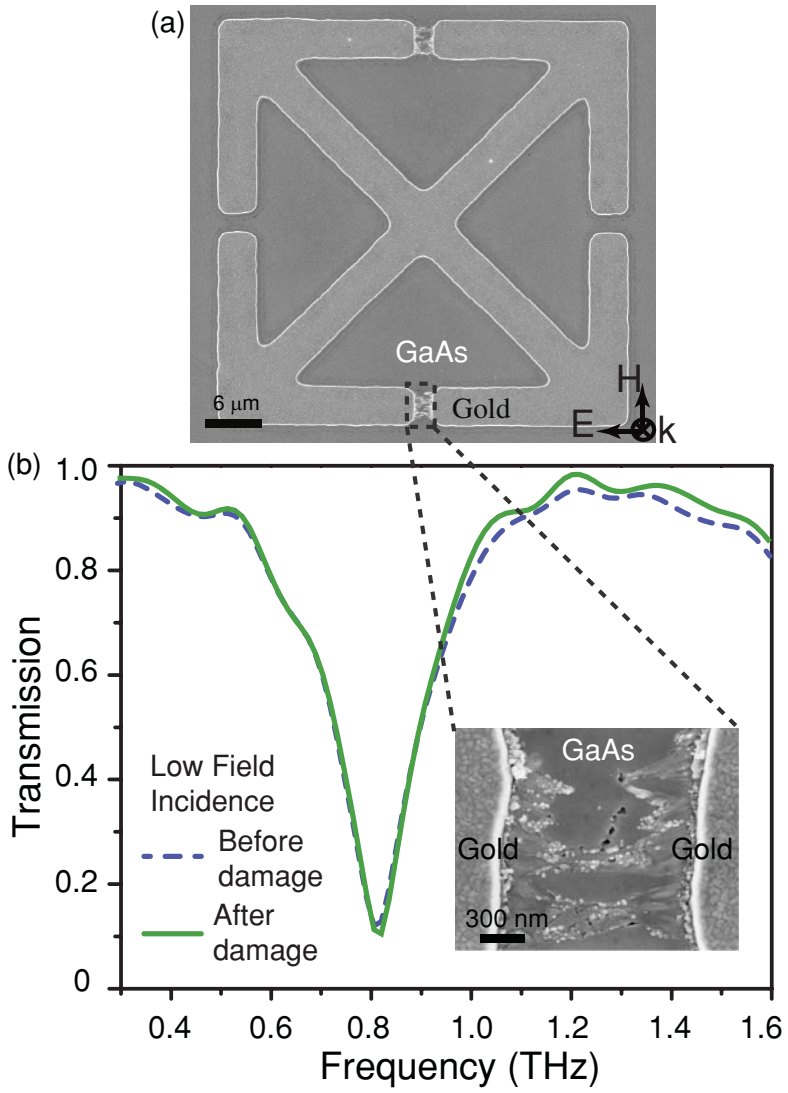

Figure 6. (a) Unit-cell view of the field-induced degradation of the SI-GaAs in the ESRR gaps. **(b)** Measured transmission of ESRR array as a function of frequency with low incident field before and after in-gap damage. Inset shows the damage in the gap of an ESRR close to the center of the THz beam where the electric field is the greatest.

9.1.9 Conclusions

Our results show that metamaterials enable strongly enhanced resonant nonlinearities at terahertz frequencies. With the incorporation of metamaterials with n-type GaAs, incident high-field THz pulses induce multiple nonequilibrium carrier transport phenomena in the

substrate, such as intervalley scattering and impact ionization. The consequent conductivity change results in an enhancement and diminishment of resonant strength, respectively. Therefore, the associated effective permittivity shows a `V' shape variation between positive and negative values. With the incorporation of metamaterials with nominally undoped GaAs, incident fields up to 400 kV/cm lead to a dramatic increase in the impact ionization efficiency in the capacitive regions of the ESRRs. The real part of the effective permittivity presents a monotonic increase from negative to positive values as a function of incident field amplitude. Dynamic experiments suggest that the impact ionization process may take longer to complete than previously thought, and highlight the fact that these separate transport processes are highly dependent on each other, complicating the modeling. Nevertheless, simplifications allow for a rough estimate of the mobility saturation and carrier generation schemes. At the highest field strengths, prolonged exposure to the THz radiation resulted in damage akin to dielectric breakdown. As our proof-of-principle results demonstrate, it will be possible to create a host of nonlinear THz metamaterials which includes, as but one example, nonlinear perfect absorbers for saturable absorber or optical limiting applications.

9.2 THz-Induced Insulator-to-Metal Phase Transition in Vanadium Dioxide

Electron-electron interactions can render an otherwise conducting material insulating [31] with the insulator-metal phase transition in correlated electron materials being the canonical macroscopic manifestation of the competition between charge carrier itinerancy and localization. The transition can arise from underlying microscopic interactions between the charge, lattice, orbital, and spin degrees of freedom, the complexity of which leads to multiple

phase transition pathways. For example, in numerous transition metal oxides, the insulator-metal transition has been achieved with external stimuli including temperature, light, electric or magnetic fields, and mechanical strain [32-37]. Vanadium dioxide is particularly intriguing because both the lattice and on-site coulomb repulsion contribute to the insulator-to-metal transition at 340K [38]. Thus, while the precise microscopic origin of the phase transition remains elusive, vanadium dioxide serves as a testbed for correlated electron phase transition dynamics. We demonstrate a terahertz electric field-induced insulator-metal transition in vanadium dioxide. This is achieved utilizing metamaterial-enhanced picosecond high-field terahertz pulses to reduce the coulomb-induced potential barrier for carrier transport [39]. A nonlinear metamaterial response is observed through the phase transition demonstrating that high-field terahertz pulses provide alternative pathways to induce collective electronic and structural rearrangements. The metamaterial resonators play a dual role, providing subwavelength field enhancement that locally drives the nonlinear response and global sensitivity to the local changes thereby enabling macroscopic observation of the dynamics [2, 9]. This methodology provides a powerful platform to investigate low-energy dynamics in condensed matter and, further demonstrates that integration of metamaterials with complex matter is a viable pathway to realize functional nonlinear electromagnetic composites.

Ultrafast spectroscopic techniques are important for investigating phase transition dynamics with regards to initiating changes and providing sufficient temporal resolution to monitor excited states or metastable order parameters not accessible with time integrated measurements [36, 37, 40, 41]. Indeed, recent ultrafast pump-probe measurements on vanadium dioxide (VO_2) with near-infrared pulses revealed that excitation of electrons across

the insulating Hubbard gap results in percolative metallicity on a picosecond timescale [40, 41]. DC electric fields (~100 kV/cm) also induce the insulator to metal transition but do not permit measurement of the field-induced transition dynamics [39, 42]. From existing DC measurements it is not clear whether ultrafast electric fields could induce the IM transition or what the time scale would be.

9.2.1 Temperature Dependent THz Conductivity in VO_2: Probing Conductivity Changes with THz Time Domain Spectroscopy

Recent developments have enabled generation of ultrafast terahertz (THz) pulses with 0.1-1 MV/cm field levels [20, 43, 44]. Time-resolved THz-pump/THz-probe measurements have revealed dynamic electronic responses initiated by such high fields [11, 20]. THz probe pulses are ideally suited to monitor the insulator-metal transition (IMT) since they provide a direct measure of the conductivity in the GHz-THz frequency range. Figure 7a shows the temperature dependent far infrared conductivity (σ_1) of our 75nm VO_2 film deposited on sapphire substrate [45]. The results were obtained by fitting a Drude response to the transmission from a conventional THz time domain spectroscopy (THz-TDS) measurement using low-field THz pulses [36, 41]. The IMT occurs at 340K, and in the high temperature rutile phase the conductivity of ~5000 $(\Omega\ cm)^{-1}$ is comparable to bulk single crystal VO_2. Hysteresis, associated with the first-order structural transition, is also observed. Below 330 K, the conductivity is below our detection limit with conventional THz-TDS.

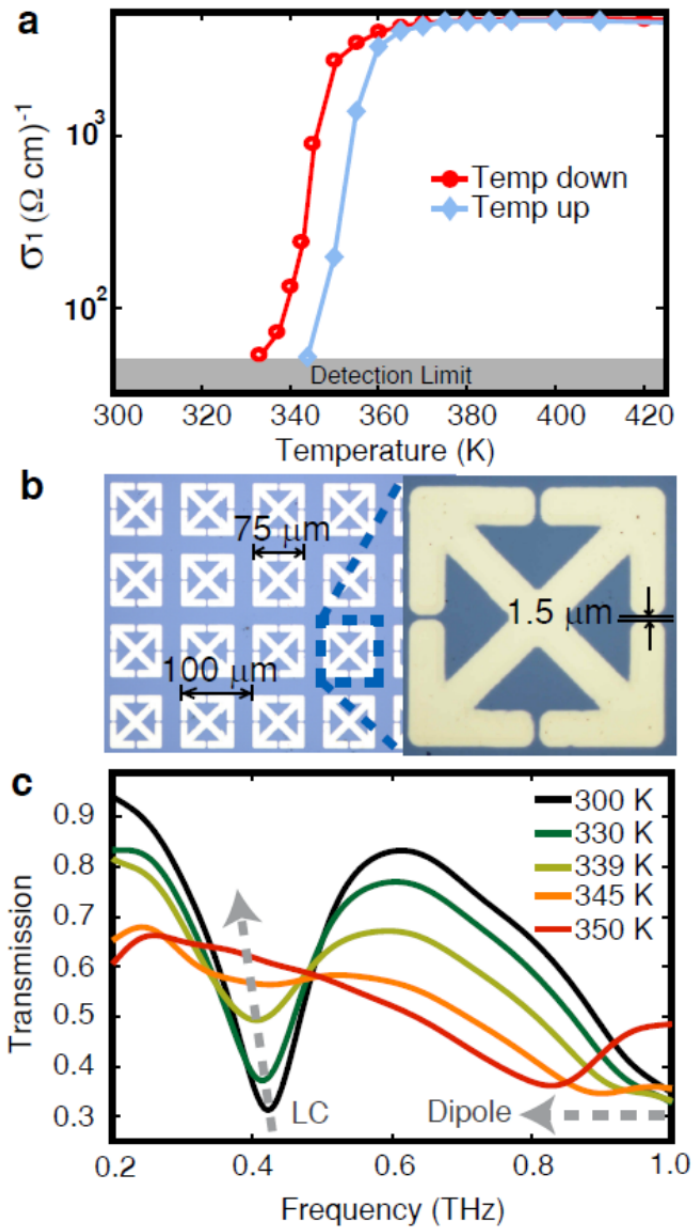

Figure 7: **Low field THz characterization of 75nm VO_2 thin film on sapphire with and without metamaterials. a)** Temperature-dependent far infrared conductivity (σ_1) of VO_2 measured by THz time domain spectroscopy of the bare VO_2 thin film sample. σ_1 was obtained by fitting the THz transmission to a standard Drude response. **b)** Optical image of metamaterial split ring resonators deposited on VO_2/sapphire. The SRR gap is 1.5 μm. **c)** Temperature-dependent THz transmission spectra of SRRs on VO_2.

9.2.2 Metamaterial Arrays as Local Probes of Film Conductivity and THz Field Enhancement in Metamaterial Structures for Driving the Insulator-to-Metal Phase Transition in VO_2

For intense THz excitation, we deposited metamaterial (MM) structures that served as local resonant THz concentrators [1]. Using gold split ring resonators (SRRs), which are essentially subwavelength LC circuits, the THz electric field inside the SRR capacitive gap can be enhanced by more than an order of magnitude.

Figure 7b shows an optical image of the 200 nm thick gold SRRs that we deposited onto a VO_2 film. The SRR lateral dimension is 76 μm with a periodicity of 100 μm. For our experiments, the most important regions are the SRR 1.5 μm capacitive gaps that are oriented horizontally, where enhancement of the vertically polarized THz field occurs. For these SRRs, the LC resonance, shown in Fig. 7c (300 K data) is at 0.4 THz while the pure electric dipole resonance (which would occur in the gap with just the two adjacent vertical gold segments forming a dipole antenna) is around 1 THz. In addition to THz field enhancement in the gaps, the SRR structures provide exquisite sensitivity for THz probing of small changes in the VO_2 thin-film transmission in the vicinity of the phase transition where the conductivity is small. Although only a small fraction of the THz probe radiation directly irradiates the gaps, the resonant behavior of the entire SRR array is affected profoundly by the in-gap VO_2 properties. Figure 7c shows the frequency-dependent SRR/VO_2 response as a function of temperature measured using low-field THz time domain spectroscopy (THz-TDS). The SRR gap is gradually shorted as the VO_2 becomes metallic, leading to a transmission increase at the resonance frequency with increasing temperature. The LC resonance disappears at ~350 K corresponding to a film conductivity of about 200 $(\Omega\ cm)^{-1}$. From 300 K to 340 K, there is a small but

perceptible redshift of the LC resonance due to increasing permittivity of the VO_2 film associated with percolation of the metallic phase. A small hysteresis in the transmission is also observed (not shown), analogous to figure 7a and to previous experiments performed by Driscoll et. al. [46]. In addition, the higher-frequency dipolar resonance redshifts since the effective dipole length is increased as the SRR gaps are shorted. As figure 7c shows, the SRRs provide enhanced conductivity sensitivity to changes in the material properties within the gaps. Thus, in the following nonlinear dynamics measurements, SRRs provide local excitation by field enhancement in the capacitive gaps and global probe sensitivity to the induced changes of the VO_2 within the gaps.

Full-wave electromagnetic simulations reveal the spatiotemporal features of the field enhancement in the SRRs. Figure 8a shows that in the horizontally oriented gaps, there is a 27-fold field enhancement at the LC resonance frequency. Figure 8b shows the simulated time-dependent electric field (red curve) in the middle of the horizontal gaps, with the experimentally measured THz field (blue curve) used as input for the simulation. An incident peak field amplitude of ~300 kV/cm leads to a peak field of 4 MV/cm in the gap. Fourier transformation of the time-domain field profiles in Fig. 8b and calculation of the ratio of the spectral amplitudes yields the field enhancement as a function of frequency as shown in Fig. 8c. The field enhancement is quite broadband as a result of the breadth and close proximity of the LC and electric dipole modes. We note that the magnitude of the calculated field enhancement is consistent with calculated and experimental results recently obtained on simpler antenna structures [1, 16, 47].

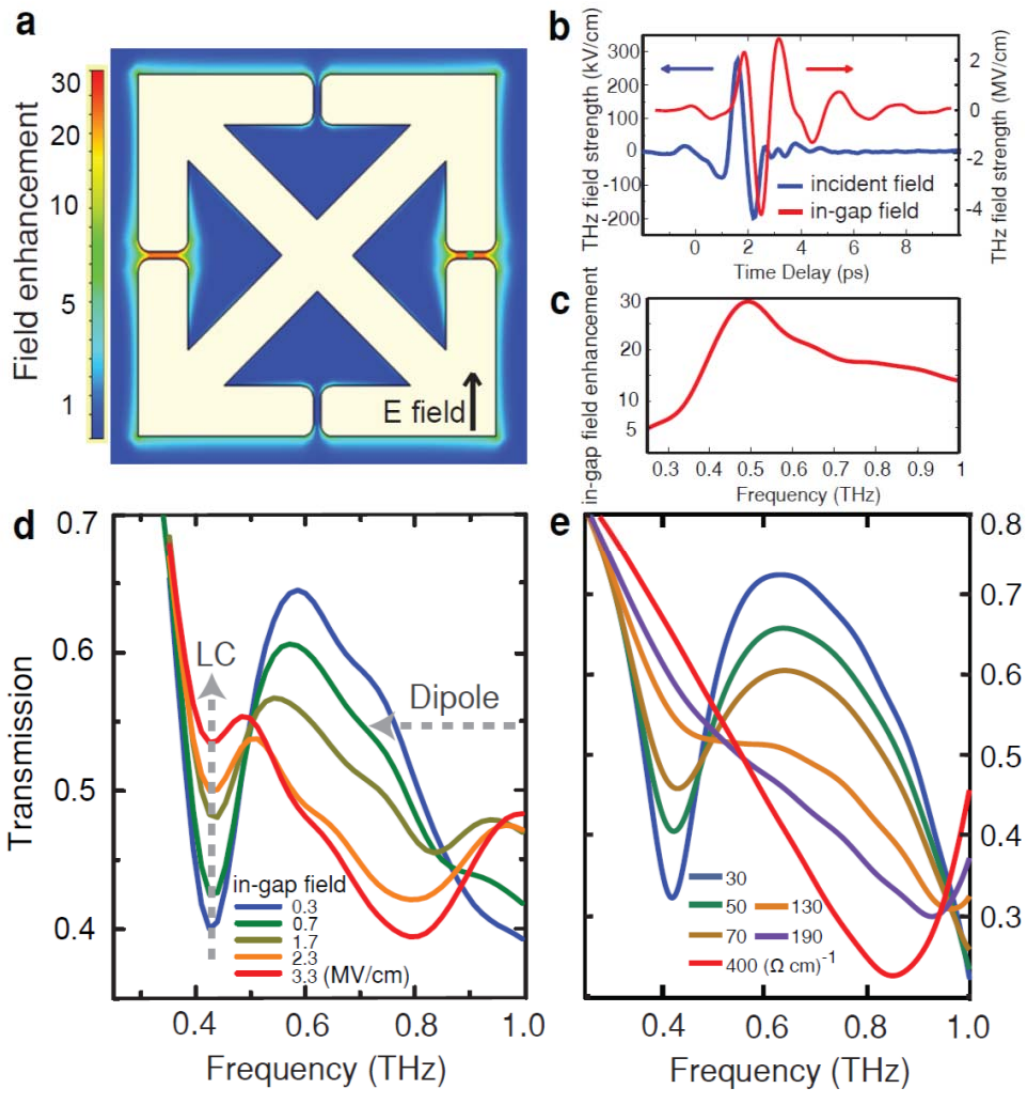

Figure 8: **Full-wave simulations of the electric field enhancement in the SRR and nonlinear THz transmission experiment. a)** Field enhancement as a function of position at the time delay (2.3 ps) of maximum enhancement factor of 27 in the horizontally oriented gaps. **b)** Simulated time-dependent THz field (red) in the horizontal gaps utilizing experimental data (blue) as the input incident field. **c)** Frequency-dependent in-gap field enhancement obtained from the ratio of Fourier amplitudes of the simulated in-gap and measured incident fields in (b). **d)** Experimental data showing field-dependent nonlinear THz transmission spectra of SRRs on VO_2 at 324K. As the field strength is increased, the transmission at the resonant frequency increases and the resonance nearly disappears. The dipole resonance frequency redshifts to below 0.8THz. **e)** Full wave simulations of THz SRR response with different in-gap conductivity (assuming the conductivity of VO_2 only changes in the SRR gaps).

Figure 8d shows the experimentally measured nonlinear response of SRRs on VO_2 that is initially in the insulating state (324 K). These single-beam measurements show that with increasing incident field, the transmission at the LC resonance frequency (0.41 THz) increases. Given the temperature-dependent data in Fig. 7c, this is consistent with an increase in the VO_2 conductivity in the SRR gaps. The higher frequency dipole also redshifts as the in-gap VO_2 conductivity increases (peak at ~0.8 THz for the highest incident fields). At the highest field strength below damage threshold, the average conductivity increase is above 500 $(\Omega\ cm)^{-1}$ as estimated by the dipole frequency shift. Figure 8e shows simulations that assume the conductivity change occurs only within the horizontal gaps. There is good agreement with experiment, though the measured resonance does not completely vanish. This is likely because the Gaussian-like THz beam profile leads to a larger effect in the center of the beam than at the edge where the THz field is weaker, and averaging of the measurement over the beam profile is not accounted for in the simulations.

9.2.3 THz Dynamics of the IMT in VO_2

While the results in Fig. 8 clearly indicate a nonlinear response, further measurements are required to determine the dynamic response which could suggest its probable microscopic origins. Figure 9 shows the time-dependent transmission of a weak-field THz probe pulse that was variably delayed with respect to the high-field THz pump pulse at an in-gap field strength of ~1 MV/cm (below the damage threshold). Figure 9a plots transmission as a function of frequency and pump-probe delay showing the temporal evolution of the THz spectral response. From these data it is clear that the 0.4 THz LC resonance transmission increases while the 1.0

THz dipole resonance exhibits a frequency shift. These changes occur on a picosecond timescale as the VO_2 conductivity increases toward that of the metallic phase. Line scans in Fig. 9b and 9c more clearly reveal the dynamics. The time constants for initial change in transmission at 0.4 THz and 0.8 THz are 7 ps and 9 ps respectively, comparable to what has been observed in optical-pump THz-probe experiments and consistent with a percolative phase transition [36, 37, 41]. The intrinsic conductivity response may be even faster as the THz pump fields in the gaps are time-broadened as shown in Fig. 8b. Nonetheless, it is clear that the THz pump induces a rapid change in the in-gap VO_2 conductivity. The change persists with little or no relaxation during the 100 ps range of our probe-probe time delay.

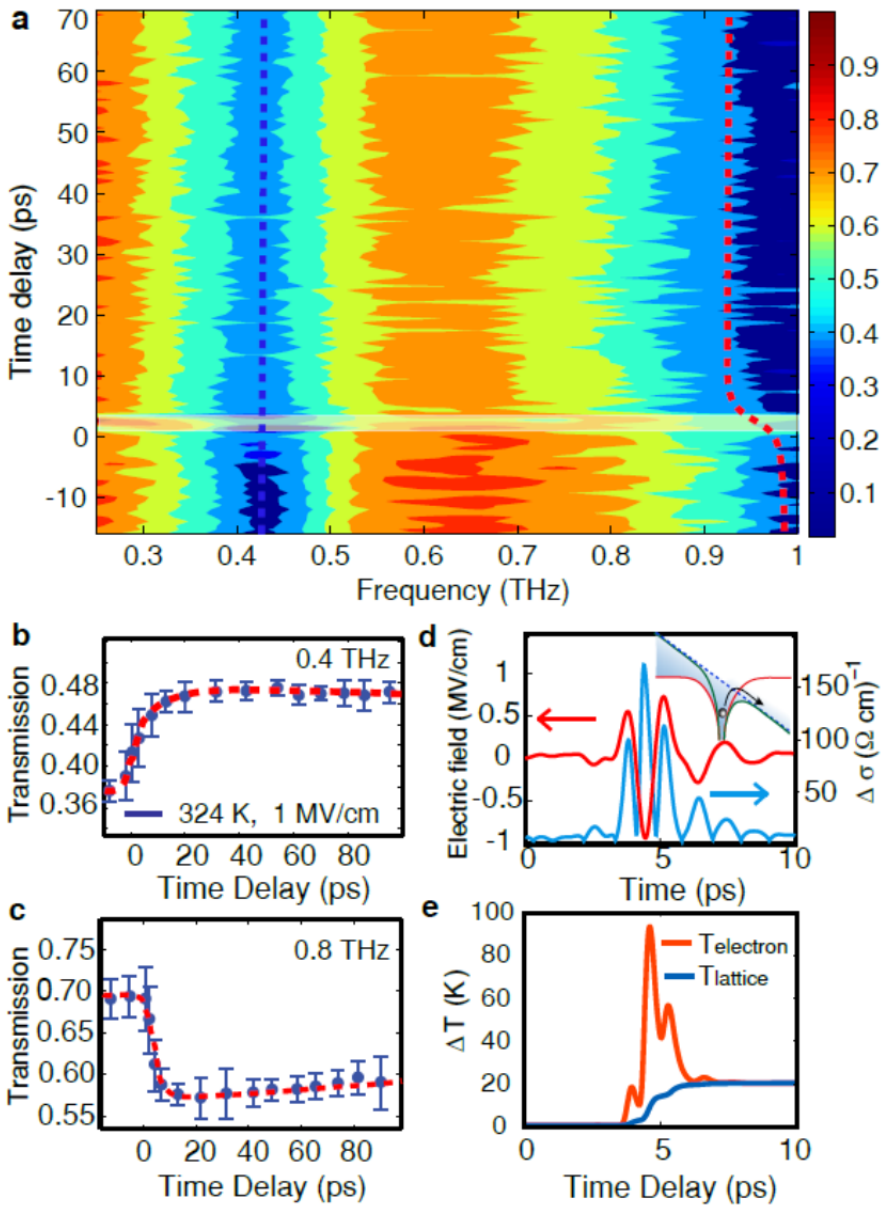

Figure 9: **THz-pump/THz-probe measurement at 1 MV/cm in-gap field strength and model calculation. a)** Two-dimensional experimental terahertz-pump terahertz-probe data. Line-scans as a function of time at **b)** 0.4 THz–the metamaterial LC resonance–and **c)** 0.8 THz–the metamaterial dipole resonance. The blue dots are the data and the red curves are exponential fits. In (b) the data reveal an increase in transmission with a risetime of 7 ps. In (c) there is a decrease in transmission that results from frequency shifting of the electric dipole resonance (9 ps risetime). Error bars show the standard error of mean (n=8). **d)** From the in-gap electric field (red curve), it is possible to calculate the Poole-Frenkel conductivity (green curve) that, as the inset illustrates, results from the electric field-induced lowering of the confining potential for the carriers. **e)** The Poole-Frenkel conductivity releases carriers, leading to an absorbed power density that heats the electrons and subsequently the lattice, driving the VO_2 toward the metallic phase.

9.2.4 Theoretical Analysis: Impact Ionization, the Poole-Frenkel Effect, and Thermal Effects

There are several possible mechanisms which could be responsible for the THz-induced IMT. One possibility is impact ionization whereby carriers accelerated by the electric field acquire sufficient kinetic energy to create additional carriers through collisions. Although impact ionization plays an important role in the high-field THz response of semiconductors, it cannot be the origin of the IMT in our experiment because of the low carrier mobility in the insulating state of VO_2 (~1 $cm^2/V{\cdot}sec$). For impact ionization, the carrier kinetic energy should be larger than the ionization threshold (> 0.67 eV), which requires an accelerated electron speed > $3x10^7$ cm/s. Model calculations based on a simple rate equation approximate the critical field strength to be ~25 MV/cm, which is greater than the highest enhanced field strength in our experiments. The related parameters of VO_2 are listed in table 1 as summarized from previous experimental data [38].

VO_2	**Insulating state (room temperature)**	**Metallic state**
Carrier mobility	**0.1-1 $cm^2/V{\cdot}sec$**	**1-10 $cm^2/V{\cdot}sec$**
Effective mass	**1.6-7**	**1-3**
Electron density	**10^{19}-10^{20} cm^{-3}**	**1-3x10^{21} cm^{-3}**
Energy gap	**0.6-0.7 eV**	**N/A**

Table 1: Electronic properties of VO_2.

Since impact ionization could not have initiated the phase transition, other possibilities must be considered. The THz photon energy (~3 meV) is far lower than the bandgap (0.7 eV) and the lowest-frequency IR active mode [48] (23.4 meV), ruling out direct electron-hole creation or coherent vibrational excitation by the THz pump pulse [37, 40, 41, 49].

The Poole Frenkel (PF) effect and thermal effects are the two obvious choices for an induced conductivity change [50, 51]. Since the initial conductivity at ~320K is quite low (~10 $(\Omega\ cm)^{-1}$), pure thermal heating (σE^2) cannot solely explain the phase transition behavior. An in-gap field of ~1 MV/cm with the initial low conductivity yields a temperature rise less than 1 K in the two-temperature model (equations 3 & 4), which is clearly insufficient to explain the measured change in transmission. Thus, an initial conductivity change must occur before the thermal effects take over. The PF effect lowers the potential barrier arising from on-site coulomb repulsion in VO_2, yielding additional carriers. When the carrier density approaches a critical value, typically ~10^{21} cm^{-3}, a phase transition occurs. With a DC field, this requires a critical field of a few hundred kV/cm [39, 42, 52-55]. Dynamically with ultrafast THz pulses, we found the critical field to be on the order of 1 MV/cm. Accompanied with the initial conductivity rise induced by PF effect, heating described by σE^2 raises the electron temperature, then electron-lattice equilibration through electron-phonon scattering takes place heating the lattice on the picosecond timescale.

Our analysis suggests a two-step process for the THz-induced phase transition. First, the electric field reduces the coulomb-induced activation barrier for carrier motion. This can be modeled by the Poole-Frenkel (PF) effect described as [51, 55]:

$$\sigma = \sigma_0 exp\left(\frac{\beta\sqrt{|E(t)|}}{rk_BT}\right) \qquad (2)$$

where σ is the conductivity, σ_0 is the initial conductivity, *E(t)* is the electric field, *T* is the temperature, and $\beta = \sqrt{e^3/\pi\varepsilon}$ is the PF constant where ε is the dielectric constant and r is a constant that depends on the position of the Fermi level. The PF effect contributes to the early dynamics of the IMT while the THz field is still acting on the sample. The electric field lowers the potential barrier to carrier hopping, increasing the carrier density [51, 54, 55]. A calculation of the transient PF conductivity is shown in Fig. 9d along with a schematic illustration of the field-induced barrier reduction. The peak conductivity change (~150 $(\Omega\ cm)^{-1}$) is consistent with the conductivity required to obtain the experimental transmission changes shown in Fig. 8 and 9. In principle, if the carrier number density reaches the critical value (~10^{21} cm^{-3}) obtained by a modified Mott criterion for VO_2 [54], the PF effect alone would be sufficient to induce the IMT. However, as we now discuss, thermal effects rapidly follow the PF dynamics.

9.2.5 The Two Temperature Model: Poole-Frenkel Electron Emission and Electron-Lattice Equilibration

The PF-induced carrier density increase serves as the initial condition for subsequent electric field-induced carrier acceleration leading to Joule heating through electron-lattice coupling [50]. This results in a temperature increase that drives the VO_2 into the persistent metallic phase. This can be modeled approximately with the well-known two-temperature model describing the temporal evolution of the energy density in the electrons and lattice:

$$C_e\frac{dT_e}{dt} = -G(T_e - T_i) + \sigma(t)E^2(t) \qquad (3)$$

$$C_i \frac{dT_i}{dt} = +G(T_e - T_i) \qquad (4)$$

T_e (C_e) and T_i (C_i) are the temperature (specific heat) of the electrons and lattice, respectively, and G is the electron-phonon coupling coefficient, all of which have been determined experimentally for VO_2. The energy density from the incident electric field is approximated as $\sigma(t)E^2(t)$.

For the numerical calculations, we used a value of 324 K for the initial temperature; 10 for insulating state relative permittivity; 10 $(\Omega\ cm)^{-1}$ for the insulating state conductivity; 60 J/mol·K for the lattice specific heat; 4000 J/mol for latent heat (which can be included in specific heat data as an input term); 1.4×10^{-2} J/mol·K^2 for the electronic specific heat coefficient; 10^{18} W/K·m^3 for the electron-phonon coupling coefficient; and 4.3 g/cm^3 for the density [38, 56-58].

Using the PF conductivity calculated in Fig. 9d and the experimental electric field (peak in-gap field 1 MV/cm), the above equation can be solved for T_e and T_i as a function of time as shown in Fig. 9e. The initial electron heating dynamics that approximately follow the THz intensity profile are followed by equilibration of the lattice and electronic temperatures. The calculations indicate a rise of the VO_2 lattice temperature by ~20 K on a several picosecond timescale, consistent with the measured dynamics. The dynamics are clearly more complex than our simple model since the field enhancement decreases as the conductivity increases within the gaps. Nonetheless, THz-induced carrier release and acceleration followed by Joule heating on a picosecond timescale seems very likely to be the IMT mechanism in our experiments. The large nonlinear transmission shown in Fig. 8 for the THz pump and Fig. 9 for the THz probe is only observed within about 30 K of the transition temperature of 340 K, given the present experimental conditions. We note that a 1 MV/cm in-gap THz field corresponds to

~2 mJ/cm^2 in THz fluence, which is similar to the typical fluence threshold of the optically (800nm) induced IMT [40, 41, 59]. The very different excitation wavelengths act initially on the system in very different ways, driving the initial responses through different mechanisms. The extent of lattice heating that sustains the metallic phase at longer times may be comparable.

9.2.6 THz-Induced Damage

At our highest in-gap electric fields of ~4 MV/cm (~30 mJ/cm^2 fluence), the THz electric field induces irreversible damage to the VO_2 metamaterials. As shown in Fig. 10a, the black dots in the MM side gaps are damage spots to the VO_2 thin film horizontal gaps. Figures 10b-d show close-up images of the VO_2 damage. The damage pattern depends strongly on the field strength, increasing toward the beam center. The unique SRR geometry allows approximate visualization of the THz electric field as the damage pattern follows the equipotential lines of the field (figure 12).

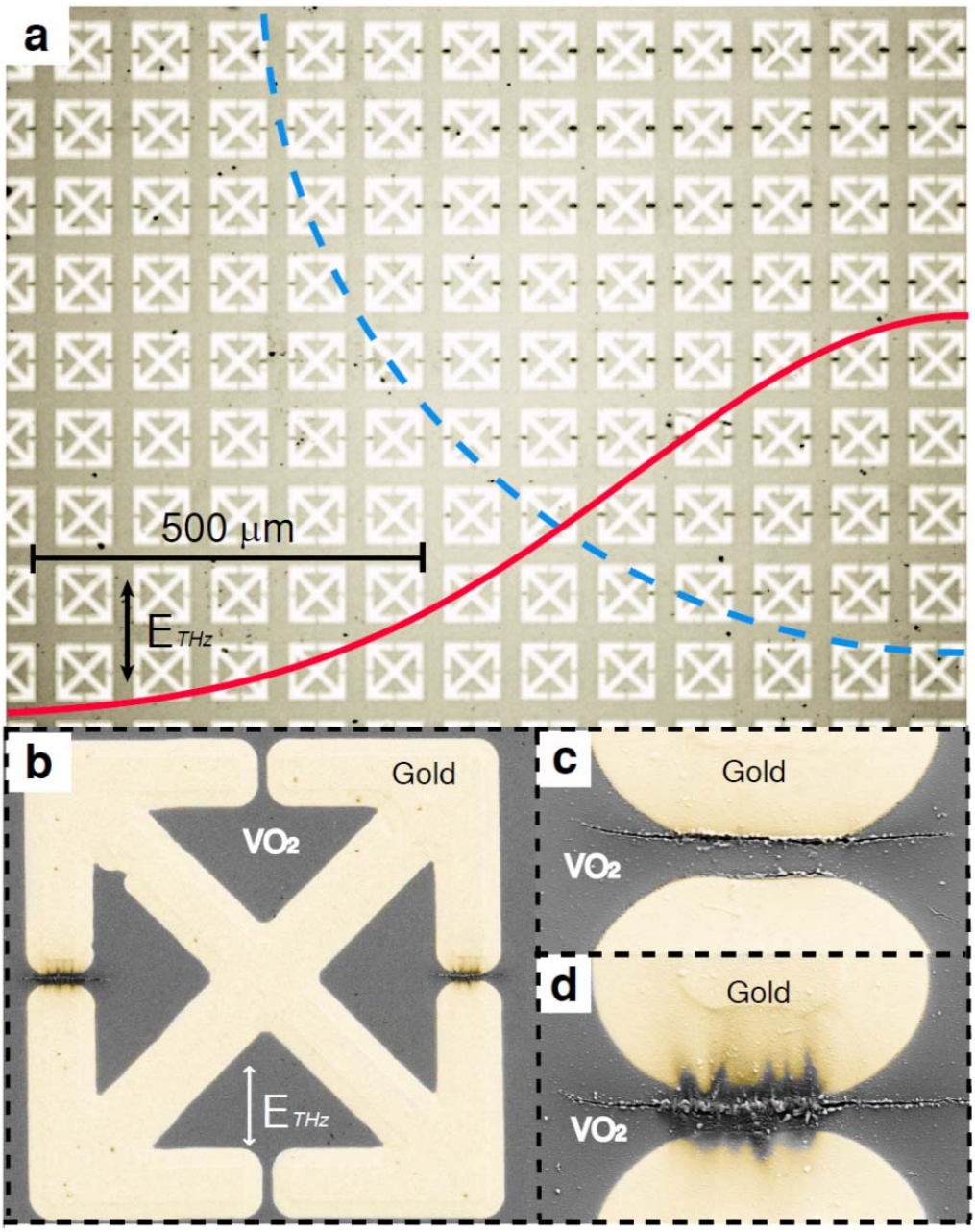

Figure 10: **THz induced damage pattern as revealed by optical and SEM images. a)** mm scale optical image of the THz-induced damage of VO_2 in the SRR gaps. The black dots are damaged VO_2 thin film regions, all in the horizontal gaps. The dashed blue circle approximates the THz beam waist and the red curve approximates the THz intensity profile assuming a Gaussian shape. **b)** SEM image of a single SRR reveals VO_2 is damaged by the vertically polarized THz field. Note that the vertically oriented SRR gaps remain undamaged. **c)** Expanded view of damage to SRR at the edge of the THz beam and **d)** damage to an SRR near the beam center where the THz field is largest. The gold SRRs were post processed with false color.

The THz damage threshold was measured by gradually increasing the THz field strength while monitoring the SRR resonance change at 0.4 THz. Above a certain field strength (Figure 11), the on-resonance THz transmission no longer increases, nor does the transmission resonance fully recover upon decreasing the field. These signatures indicate film damage. The resulting cracking of the film (figure 10 & 12) forms an insulating gap which enhances rather than diminishes the SRR resonance. The second (Down1) and third (Up2) scans with varying pump fluences show that the resulting damage is permanent and that no further damage occurs after the in-gap VO_2 is cracked. At higher temperatures, the damage threshold is smaller due to larger THz absorption in the VO_2 thin film. After the in-gap VO_2 film was permanently damaged, optical microscopy (figure 10) and SEM (figure 10 & 12) were used to characterize the damage patterns at different positions relative to the THz illumination spot. Severe damage was found at the center of the beam and different patterns were found in the vicinity of the THz spot. Figure 10a and 12 indicate that the damage patterns are directly related to the THz intensity. Different SRR structures with different gap sizes fabricated on VO_2 thin films were also investigated and the results were in good accordance with our interpretation. For example, with simple SRRs with larger gaps deposited (4 μm and 10 μm), much smaller nonlinear effects were observed and no damage occurred under the highest field strengths.

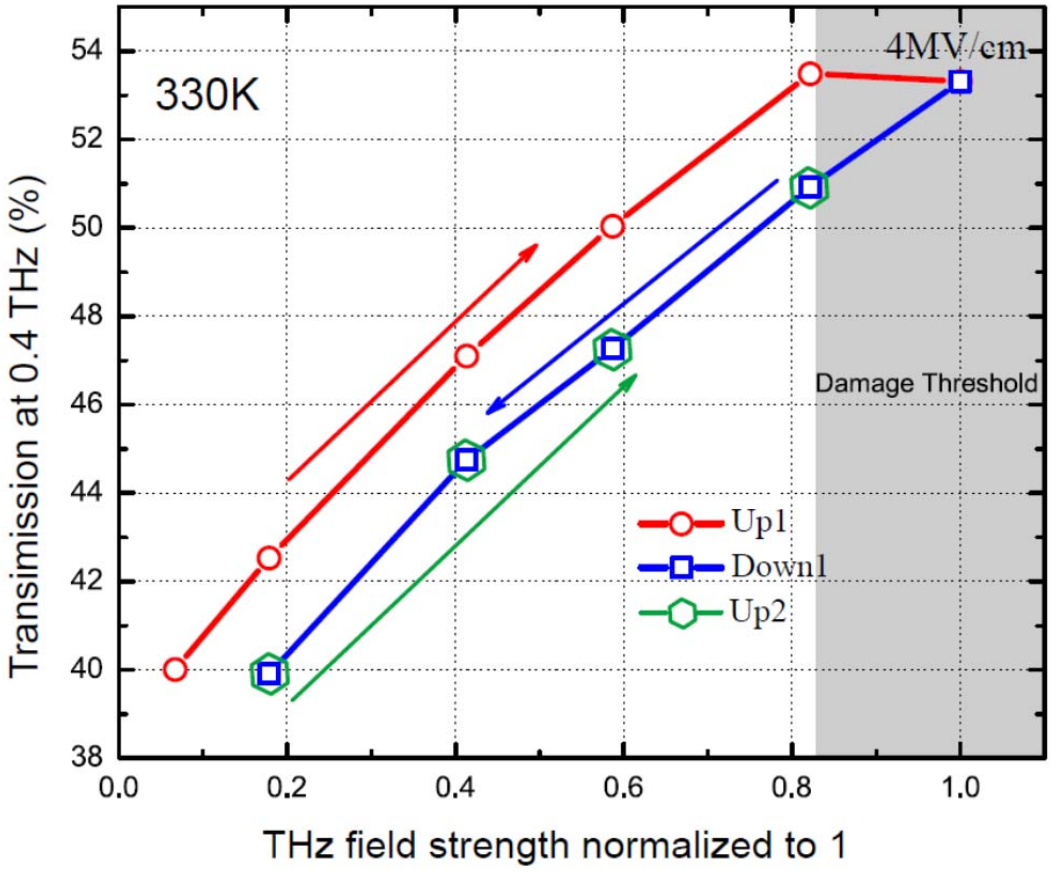

Figure 11: Field strength-dependent THz transmission of VO_2 with metamaterials at 0.4 THz. The arrows indicate the directions in which the field is changed. Down1 and Up2 curves indicate that permanent damage to the film occurred above ~3.5 MV/cm THz field strength.

At the highest THz fluence the temperature rise of the electrons is substantial but the absolute value is hard to estimate due to the extreme nonlinear nature of this process. The mechanism for damage is still unclear at this stage and is worthy of further investigation. It appears that damage process is significantly different from dielectric breakdown since the damage is along the equipotential lines while typical dielectric breakdown is along the direction of the electric field. At room temperature, the transmission change is near the detection limit even when we probe the metamaterials resonance change with enhanced sensitivity provided by the metamaterials and no damage occurs at room temperature. This indicates the

importance of the initial carrier density and electron-phonon coupling in the dynamics, which is consistent with our model calculation.

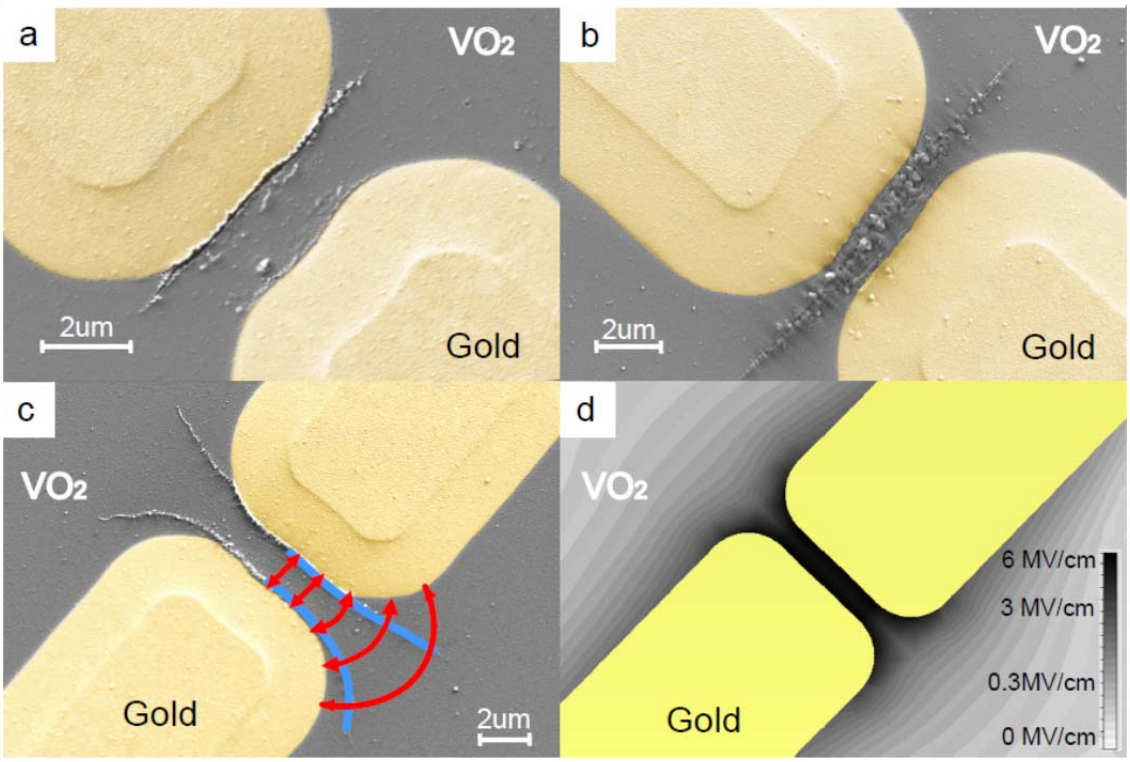

Figure 12: Damage patterns of VO_2 metamaterials. a) THz-induced damage at the edge of the THz pump spot. **b)** THz-induced damage at the center of the THz pump spot. **c)** The damage pattern follows the equal potential lines of the induced high field in the MM gap. **d)** Simulated in-plane THz electric field in the vicinity of the MM SRR gap. The color scale indicates the THz field strength at the resonance frequency.

9.2.7 Conclusions

In summary, we have demonstrated a THz-driven insulator-metal phase transition and shown that in VO_2 it is initiated by Poole-Frenkel electron liberation followed by lattice equilibration on a picosecond timescale. Our work has demonstrated that metamaterial-enhanced high-field THz pulses can be used to study correlated electron materials in a nonperturbative regime. The

technique is extremely versatile and can be used to study THz-induced phase transitions in other correlated materials and transition metal oxides such as high T_c superconductors [56, 60] and THz-induced changes in electronic properties generally. The metamaterial design can be optimized to balance the requirements in any particular measurement for maximum field enhancement, bandwidth, and mode volume. Magnetic field enhancement will be also of considerable interest since SRRs provide temporal and spatial separation of the peak electric and magnetic fields.

9.2.8 Methods Summary

VO_2 thin film fabrication: Highly oriented VO_2 thin films on Al_2O_3 (0001) substrates were deposited by reactive sputtering from a vanadium target through reactive bias target ion beam deposition using an Ar + O_2 gas mixture [45, 61].

Metamaterial fabrication: Metamaterials (MM) on VO_2 films were made by stencil deposition techniques [62]. The shadow masks used as stencils were made from 400nm SiN films with engraved metamaterial patterning. Once the masks were made, no photo-lithography was needed for the MM fabrication onto the VO_2 surface. This prevented chemical contamination, thus ensuring high quality samples.

High field THz generation and measurement: The output of a 1kHz, 6.5W, 100fs Ti:Sapphire amplifier was used to generate nearly single-cycle THz pulses via optical rectification in a $LiNbO_3$ (LN) crystal with the tilted pulse front technique [43]. Our peak THz field strength was

measured to be 300 kV/cm with an estimated spot size of 1.5 mm. A standard electro-optic sampling setup was used to measure time-dependent fields. The THz field and a femtosecond optical pulse were overlapped spatially on a ZnTe (or GaP) electro-optic crystal and the THz-induced optical birefringence was measured as the femtosecond pulse arrival time was varied, yielding the THz field temporal profile as in Fig. 8b (blue curve). Fourier transformation yielded the transmitted THz field in the 0.2-2.5THz frequency range. Measurements with different THz pump-probe time delays [11, 20] yielded the 2D data shown in Fig. 9a. All the experiments were performed in a high vacuum cryostat with temperature control.

Electromagnetic Simulations: The simulations in Figs. 8a-c and 8e and Fig. 12d were conducted using CST Microwave Studio 2011. All simulations were performed with extremely fine mesh cell settings determined by adaptive meshing results (up to 8 million). All the parameters used in the CST simulations were those reported from experimental measurements, e.g., the conductivity in the insulating state at 320K is 10 $(\Omega\ cm)^{-1}$ and the relative permittivity of VO_2 in the insulating state is ~10. The simulations were performed using a time-domain transient solver.

Figures 8b and 8c were created by using the temporal profile of the real pulse as the excitation source, then calculating the temporal profile of an electric field probe defined at the center of the gap in real space. The resulting curves were Fourier transformed and normalized to the excitation signal to calculate field enhancement in the frequency domain.

For Fig. 8e we specified a region within the SRR gap consisting of VO_2 where the conductivity could range over the values obtained through the phase transition, while

maintaining the conductivity in the remaining portions of the VO_2 film at the value for the initial temperature. We obtained those data sets by sweeping the electrical conductivity across the values shown in the Fig. 8.

References

[1] C. A. Werley, K. Fan, A. C. Strikwerda, S. M. Teo, X. Zhang, R. D. Averitt and K. A. Nelson. "Time-resolved imaging of near-fields in THz antennas and direct quantitative measurement of field enhancements." *Opt. Express*, **20**, 8551 (2012).

[2] H. Merbold, A. Bitzer and T. Feurer. "Second harmonic generation based on strong field enhancement in nanostructured THz materials." *Opt. Express*, **19**, 7262 (2011).

[3] A. A. Zharov, I. V. Shadrivov and Y. S. Kivshar. "Nonlinear Properties of Left-Handed Metamaterials." *Physical Review Letters*, **91**, 037401 (2003).

[4] M. W. Klein, M. Wegener, N. Feth and S. Linden. "Experiments on second- and third-harmonic generation from magnetic metamaterials." *Opt. Express*, **15**, 5238 (2007).

[5] B. Wang, J. Zhou, T. Koschny and C. M. Soukoulis. "Nonlinear properties of split-ring resonators." *Opt. Express*, **16**, 16058 (2008).

[6] A. Fang, T. Koschny, M. Wegener and C. M. Soukoulis. "Self-consistent calculation of metamaterials with gain." *Physical Review B*, **79**, 241104 (2009).

[7] E. Poutrina, D. Huang and D. R. Smith. "Analysis of nonlinear electromagnetic metamaterials." *New Journal of Physics*, **12**, 093010 (2010).

[8] A. Rose, D. Huang and D. R. Smith. "Controlling the Second Harmonic in a Phase-Matched Negative-Index Metamaterial." *Physical Review Letters*, **107**, 063902 (2011).

[9] H.-T. Chen, W. J. Padilla, J. M. O. Zide, A. C. Gossard, A. J. Taylor and R. D. Averitt. "Active terahertz metamaterial devices." *Nature*, **444**, 597 (2006).

[10] H. Tao, A. C. Strikwerda, K. Fan, W. J. Padilla, X. Zhang and R. D. Averitt. "Reconfigurable Terahertz Metamaterials." *Physical Review Letters*, **103**, 147401 (2009).

[11] M. C. Hoffmann, J. Hebling, H. Y. Hwang, K.-L. Yeh and K. A. Nelson. "Impact ionization in InSb probed by terahertz pump—terahertz probe spectroscopy." *Physical Review B*, **79**, 161201 (2009).

[12] J. Hebling, M. C. Hoffmann, H. Y. Hwang, K.-L. Yeh and K. A. Nelson. "Observation of nonequilibrium carrier distribution in Ge, Si, and GaAs by terahertz pump–terahertz probe measurements." *Physical Review B*, **81**, 035201 (2010).

[13] I. C. Ho and X. C. Zhang. "Driving intervalley scattering and impact ionization in InAs with intense terahertz pulses." *Applied Physics Letters*, **98**, 241908 (2011).

[14] M. Tanaka, H. Hirori and M. Nagai. "THz Nonlinear Spectroscopy of Solids." *Terahertz Science and Technology, IEEE Transactions on*, **1**, 301 (2011).

[15] H. Hirori, K. Shinokita, M. Shirai, S. Tani, Y. Kadoya and K. Tanaka. "Extraordinary carrier multiplication gated by a picosecond electric field pulse." *Nat Commun*, **2**, 594 (2011).

[16] M. A. Seo, H. R. Park, S. M. Koo, D. J. Park, J. H. Kang, O. K. Suwal, S. S. Choi, P. C. M. Planken, G. S. Park, N. K. Park, Q. H. Park and D. S. Kim. "Terahertz field enhancement by a metallic nano slit operating beyond the skin-depth limit." *Nat Photon*, **3**, 152 (2009).

[17] V. Giannini, A. Berrier, S. A. Maier, J. A. Sánchez-Gil and J. G. Rivas. "Scattering efficiency and near field enhancement of active semiconductor plasmonic antennas at terahertz frequencies." *Opt. Express*, **18**, 2797 (2010).

[18] H. R. Park, Y. M. Park, H. S. Kim, J. S. Kyoung, M. A. Seo, D. J. Park, Y. H. Ahn, K. J. Ahn and D. S. Kim. "Terahertz nanoresonators: Giant field enhancement and ultrabroadband performance." *Applied Physics Letters*, **96**, 121106 (2010).

[19] J. Hebling, Y. Ka-Lo, K. A. Nelson and M. C. Hoffmann. "High-Power THz Generation, THz Nonlinear Optics, and THz Nonlinear Spectroscopy." *Selected Topics in Quantum Electronics, IEEE Journal of*, **14**, 345 (2008).

[20] M. C. Hoffmann, J. Hebling, H. Y. Hwang, K.-L. Yeh and K. A. Nelson. "THz-pump/THz-probe spectroscopy of semiconductors at high field strengths [Invited]." *J. Opt. Soc. Am. B*, **26**, A29 (2009).

[21] T. Driscoll, S. Palit, M. M. Qazilbash, M. Brehm, F. Keilmann, B.-G. Chae, S.-J. Yun, H.-T. Kim, S. Y. Cho, N. M. Jokerst, D. R. Smith and D. N. Basov. "Dynamic tuning of an infrared hybrid-metamaterial resonance using vanadium dioxide." *Applied Physics Letters*, **93**, 024101 (2008).

[22] N.-H. Shen, M. Kafesaki, T. Koschny, L. Zhang, E. N. Economou and C. M. Soukoulis. "Broadband blueshift tunable metamaterials and dual-band switches." *Physical Review B*, **79**, 161102 (2009).

[23] F. H. Su, F. Blanchard, G. Sharma, L. Razzari, A. Ayesheshim, T. L. Cocker, L. V. Titova, T. Ozaki, J. C. Kieffer, R. Morandotti, M. Reid and F. A. Hegmann. "Terahertz pulse induced intervalley scattering in photoexcited GaAs." *Opt. Express*, **17**, 9620 (2009).

[24] N. Katzenellenbogen and D. Grischkowsky. "Electrical characterization to 4 THz of N- and P-type GaAs using THz time-domain spectroscopy." *Applied Physics Letters*, **61**, 840 (1992).

[25] W. Kuehn, P. Gaal, K. Reimann, M. Woerner, T. Elsaesser and R. Hey. "Coherent Ballistic Motion of Electrons in a Periodic Potential." *Physical Review Letters*, **104**, 146602 (2010).

[26] C. L. Anderson and C. R. Crowell. "Threshold Energies for Electron-Hole Pair Production by Impact Ionization in Semiconductors." *Physical Review B*, **5**, 2267 (1972).

[27] J. T. Darrow, X. C. Zhang, D. H. Auston and J. D. Morse. "Saturation properties of large-aperture photoconducting antennas." *Quantum Electronics, IEEE Journal of*, **28**, 1607 (1992).

[28] M. C. Nuss, D. H. Auston and F. Capasso. "Direct Subpicosecond Measurement of Carrier Mobility of Photoexcited Electrons in Gallium Arsenide." *Physical Review Letters*, **58**, 2355 (1987).

[29] A. Rose, S. Larouche and D. R. Smith. "Quantitative study of the enhancement of bulk nonlinearities in metamaterials." *Physical Review A*, **84**, 053805 (2011).

[30] J. F. Verweij and J. H. Klootwijk. "Dielectric breakdown I: A review of oxide breakdown." *Microelectronics Journal*, **27**, 611 (1996).

[31] F. J. Morin. "Oxides Which Show a Metal-to-Insulator Transition at the Neel Temperature." *Physical Review Letters*, **3**, 34 (1959).

[32] P. Limelette, A. Georges, D. JÃ©rome, P. Wzietek, P. Metcalf and J. M. Honig. "Universality and Critical Behavior at the Mott Transition." *Science*, **302**, 89 (2003).

[33] A. Asamitsu, Y. Tomioka, H. Kuwahara and Y. Tokura. "Current switching of resistive states in magnetoresistive manganites." *Nature*, **388**, 50 (1997).

[34] J. Wang, J. B. Neaton, H. Zheng, V. Nagarajan, S. B. Ogale, B. Liu, D. Viehland, V. Vaithyanathan, D. G. Schlom, U. V. Waghmare, N. A. Spaldin, K. M. Rabe, M. Wuttig and R. Ramesh. "Epitaxial $BiFeO_3$ Multiferroic Thin Film Heterostructures." *Science*, **299**, 1719 (2003).

[35] J. Cao, E. Ertekin, V. Srinivasan, W. Fan, S. Huang, H. Zheng, J. W. L. Yim, D. R. Khanal, D. F. Ogletree, J. C. Grossman and J. Wu. "Strain engineering and one-dimensional organization of metal-insulator domains in single-crystal vanadium dioxide beams." *Nat Nano*, **4**, 732 (2009).

[36] M. K. Liu, B. Pardo, J. Zhang, M. M. Qazilbash, S. J. Yun, Z. Fei, J.-H. Shin, H.-T. Kim, D. N. Basov and R. D. Averitt. "Photoinduced Phase Transitions by Time-Resolved Far-Infrared Spectroscopy in V_2O_3." *Physical Review Letters*, **107**, 066403 (2011).

[37] A. Cavalleri, C. Tóth, C. W. Siders, J. A. Squier, F. Ráksi, P. Forget and J. C. Kieffer. "Femtosecond Structural Dynamics in VO_2 during an Ultrafast Solid-Solid Phase Transition." *Physical Review Letters*, **87**, 237401 (2001).

[38] C. N. Berglund and H. J. Guggenheim. "Electronic Properties of VO_2 near the Semiconductor-Metal Transition." *Physical Review*, **185**, 1022 (1969).

[39] G. Stefanovich, A. Pergament and D. Stefanovich. "Electrical switching and Mott transition in VO_2." *Journal of Physics: Condensed Matter*, **12**, 8837 (2000).

[40] C. Kübler, H. Ehrke, R. Huber, R. Lopez, A. Halabica, R. F. Haglund, Jr. and A. Leitenstorfer. "Coherent Structural Dynamics and Electronic Correlations during an Ultrafast Insulator-to-Metal Phase Transition in VO_2." *Physical Review Letters*, **99**, 116401 (2007).

[41] D. J. Hilton, R. P. Prasankumar, S. Fourmaux, A. Cavalleri, D. Brassard, M. A. El Khakani, J. C. Kieffer, A. J. Taylor and R. D. Averitt. "Enhanced Photosusceptibility near T_c for the

Light-Induced Insulator-to-Metal Phase Transition in Vanadium Dioxide." *Physical Review Letters*, **99**, 226401 (2007).

[42] H.-T. Kim, B.-G. Chae, D.-H. Youn, S.-L. Maeng, G. Kim, K.-Y. Kang and Y.-S. Lim. "Mechanism and observation of Mott transition in VO_2-based two- and three-terminal devices." *New Journal of Physics*, **6**, 52 (2004).

[43] K. L. Yeh, M. C. Hoffmann, J. Hebling and K. A. Nelson. "Generation of 10 μJ ultrashort terahertz pulses by optical rectification." *Applied Physics Letters*, **90**, 171121 (2007).

[44] H. Hirori, A. Doi, F. Blanchard and K. Tanaka. "Single-cycle terahertz pulses with amplitudes exceeding 1 MV/cm generated by optical rectification in $LiNbO_3$." *Applied Physics Letters*, **98**, 091106 (2011).

[45] K. G. West, J. Lu, J. Yu, D. Kirkwood, W. Chen, Y. Pei, J. Claassen and S. A. Wolf. "Growth and characterization of vanadium dioxide thin films prepared by reactive-based target ion beam deposition." *J. Vac. Sci. Technol. A*, **26**, 133 (2008).

[46] T. Driscoll, H.-T. Kim, B.-G. Chae, B.-J. Kim, Y.-W. Lee, N. M. Jokerst, S. Palit, D. R. Smith, M. Di Ventra and D. N. Basov. "Memory Metamaterials." *Science*, **325**, 1518 (2009).

[47] M. Shalaby, H. Merbold, M. Peccianti, L. Razzari, G. Sharma, T. Ozaki, R. Morandotti, T. Feurer, A. Weber, L. Heyderman, B. Patterson and H. Sigg. "Concurrent field enhancement and high transmission of THz radiation in nanoslit arrays." *Applied Physics Letters*, **99**, 041110 (2011).

[48] A. Heinrich, E. I. Terukov, W. Reichelt, H. Wagner and H. Oppermann. "IR-Absorption in Doped and Undoped VO_2." *physica status solidi (a)*, **72**, K61 (1982).

[49] M. Rini, Z. Hao, R. W. Schoenlein, C. Giannetti, F. Parmigiani, S. Fourmaux, J. C. Kieffer, A. Fujimori, M. Onoda, S. Wall and A. Cavalleri. "Optical switching in VO_2 films by below-gap excitation." *Applied Physics Letters*, **92**, 181904 (2008).

[50] R. H. M. Groeneveld, R. Sprik and A. Lagendijk. "Femtosecond spectroscopy of electron-electron and electron-phonon energy relaxation in Ag and Au." *Physical Review B*, **51**, 11433 (1995).

[51] J. R. Yeargan and H. L. Taylor. "The Poole-Frenkel Effect with Compensation Present." *Journal of Applied Physics*, **39**, 5600 (1968).

[52] H.-T. Kim, Y. W. Lee, B.-J. Kim, B.-G. Chae, S. J. Yun, K.-Y. Kang, K.-J. Han, K.-J. Yee and Y.-S. Lim. "Monoclinic and Correlated Metal Phase in VO_2 as Evidence of the Mott Transition: Coherent Phonon Analysis." *Physical Review Letters*, **97**, 266401 (2006).

[53] A. Pergament, E. Kazakova and A. Morak. "The photoinduced Mott transition from metal to insulator: the problem of critical concentration." *Journal of Physics: Condensed Matter*, **17**, 1151 (2005).

[54] A. L. Pergament, P. P. Boriskov, A. A. Velichko and N. A. Kuldin. "Switching effect and the metal–insulator transition in electric field." *Journal of Physics and Chemistry of Solids*, **71**, 874 (2010).

[55] J. G. Simmons. "Poole-Frenkel Effect and Schottky Effect in Metal-Insulator-Metal Systems." *Physical Review*, **155**, 657 (1967).

[56] M. M. Qazilbash, M. Brehm, B.-G. Chae, P.-C. Ho, G. O. Andreev, B.-J. Kim, S. J. Yun, A. V. Balatsky, M. B. Maple, F. Keilmann, H.-T. Kim and D. N. Basov. "Mott Transition in VO_2 Revealed by Infrared Spectroscopy and Nano-Imaging." *Science*, **318**, 1750 (2007).

[57] V. Surikov, S. V. Danilov, V. I. Surikov, Y. A. Vereshchagin and I. I. Piratinskaya. "Specific heat and magnetic susceptibility of vanadium dioxide." *Sov. Phys. Solid State*, **29**, 351 (1987).

[58] V. Surikov, S. V. Danilov and V. I. Surikov. "Influence of deviation from stoichiometry on thermophysical properties of vanadium dioxide." *Sov. Phys. Solid State*, **28**, 892 (1986).

[59] A. Pashkin, C. Kübler, H. Ehrke, R. Lopez, A. Halabica, R. F. Haglund, Jr., R. Huber and A. Leitenstorfer. "Ultrafast insulator-metal phase transition in VO_2 studied by multiterahertz spectroscopy." *Physical Review B*, **83**, 195120 (2011).

[60] D. N. Basov, R. D. Averitt, D. van der Marel, M. Dressel and K. Haule. "Electrodynamics of correlated electron materials." *Reviews of Modern Physics*, **83**, 471 (2011).

[61] K. G. West. "Exploration and development of novel rutile oxide materials for next generation spin torque transfer heterostructures." (*PhD Thesis*) Department of Materials Science and Engineering, University of Virginia: Charlottesville, VA (2009).

[62] H. Tao, L. R. Chieffo, M. A. Brenckle, S. M. Siebert, M. Liu, A. C. Strikwerda, K. Fan, D. L. Kaplan, X. Zhang, R. D. Averitt and F. G. Omenetto. "Metamaterials on Paper as a Sensing Platform." *Advanced Materials*, **23**, 3197 (2011).

Chapter 10

Conclusions and Future Directions

Though still in its infancy, nonlinear THz spectroscopy has proven to be of both fundamental and technological importance in a variety of systems. In this work, we have demonstrated the ability of high-field tabletop THz sources to drive nonlinear responses in several condensed matter systems and we have described their implementation into different nonlinear THz spectroscopic techniques.

We have observed nonlinear free-carrier effects including free-carrier mobility saturation through direct carrier heating by a THz pulse and the subsequent cooling dynamics, impact ionization and the timescales of carrier generation, and hole-driven THz saturable absorption in graphene.

In simple liquids, we have been able to couple the THz electric field to the polarizablity of a molecule and influence it's orientation in solution. We also observed that the nonlinear

coefficients agreed well with similar measurements performed in the optical range (optical Kerr effect measurements).

In ferroelectric crystals, we have shown that we can drive nonlinear lattice responses with a THz electric field. This has implications for controlling the ferroelectric polarization with THz pulses. We saw second order nonlinearities in the driving THz field suggesting the observation of vibrational population relaxation.

Finally, we have demonstrated metamaterial-enhanced nonlinear THz spectroscopy in gallium arsenide (GaAs) and vanadium dioxide (VO_2). Here we used the inherent field enhancement in metamaterial antenna structures to drive nonlinear responses in a localized volume. In GaAs, we have observed nonlinear metamaterial effects stemming from free-carrier mobility saturation and impact ionization. The free-carrier mobility saturation was similar to the same effect observed in chapter 5, however, in this case, we used the free-carrier mobility saturation to control the metamaterial response. With a THz-induced conductivity decrease in the GaAs, the strength of the metamaterial response increased. Impact ionization in GaAs was particularly interesting since we could damage the sample from the avalanche carrier generation process, and because we demonstrated carrier multiplication by a factor of about 10^9 over a 1.5 eV bandgap with 4 meV photons. Finally, we were able to use our strong THz fields to induce an insulator-to-metal phase transition in VO_2. We have seen that the phase transition occurs on a picosecond timescale, and that we could also damage the VO_2 film. The difference in damage pattern in the GaAs and VO_2 were indicative of different mechanisms. In particular, the VO_2 damage pattern indicated localized heating with respect to the THz electric

field strength, which is consistent with the dominant carrier generation mechanism at short timescales via the Poole-Frenkel effect.

These demonstrations show that nonlinear THz spectroscopy can be used to study several interesting physical phenomena. Now that the general approach has been developed, we can now study several interesting phenomena in other systems. In the rest of this chapter, I will discuss some new preliminary results, and offer some new research directions made possible by the advances in nonlinear THz spectroscopy in this work and others.

10.1 Nonlinear Vibrational Responses in Molecular Crystals

Nonlinear vibrational spectroscopy has proven to be a useful tool in studying anharmonicity, mode coupling, coherent and incoherent energy transfer, and chemical reaction dynamics [1-6]. The mode couplings of localized vibrations in the mid-infrared (mid-IR) are mediated by the interaction of the system with a bath of modes [7, 8]. The bath modes consist of low energy states, some of which lie in the THz range. As a result, it is important to understand how energy transfer and coupling occur in the THz range, since the low energy modes can influence the movement of energy in higher-energy degrees of freedom. In addition, the low-energy modes have great importance in their own right as they mediate intermolecular interactions including collisions and chemical reactions. However, technological complications have thus far limited the advancement of nonlinear vibrational THz spectroscopy. The development of high-intensity THz radiation and its incorporation into nonlinear spectroscopies have enabled the study of nonlinear vibrational effects in the THz range. Recent measurements have suggested THz ladder climbing in amino acid crystals with nonlinear THz transmission spectroscopy [9]. Other

nonlinear measurements of THz electronic transitions in quantum well structures have demonstrated time-domain techniques to study dynamics with THz pulses [10-12]. In this chapter, I will discuss time-resolved THz-pump/THz-probe measurements on THz vibrations in a molecular crystal, tartaric acid, and some of the implications these measurements have on the understanding of coupling in condensed matter systems.

10.1.1 Experimental Setup

The experimental setup is shown in Figure 1. 7.5 mJ, 100 fs pulses at a 1kHz repetition rate were used to generate two separate THz beams that were noncollinearly recombined with a large parabolic mirror. The pump arm used 90% of the optical pulse to generate THz pulses by tilted pulse front generation yielding ~6 μJ THz pulses at the output face of the lithium niobate generation crystal, and about 3 μJ at the sample focus. 10% of the optical pulse was used to generate the THz probe by collinear optical rectification in zinc telluride. About 1% of the optical beam was split off as a probe for electro-optic detection of the THz pulses. The sample was a 10% wt 1.3 mm thick pellet of L-tartaric acid in a high-density polyethylene powder matrix. For peak-scan measurements where the electro-optic sampling delay was set to the peak of the THz probe field and the pump-probe delay was scanned, we only chopped the probe arm of the measurement. For full frequency-resolved pump-probe measurements, we also chopped only the probe field, since this offered better signal-to-noise than differential chopping for the same acquisition times. This results because a small amount of pump light leaked into the probe direction, and because differential chopping with a lock-in amplifier requires that we lock-in at f/12 (1 kHz/12 = 83.3 Hz) making the data acquisition longer for the

same signal-to-noise ratio compared to chopping at f/2 (1 kHz/2 = 500 Hz). Both methods showed excellent suppression of the THz pump. All experiments were performed at room temperature.

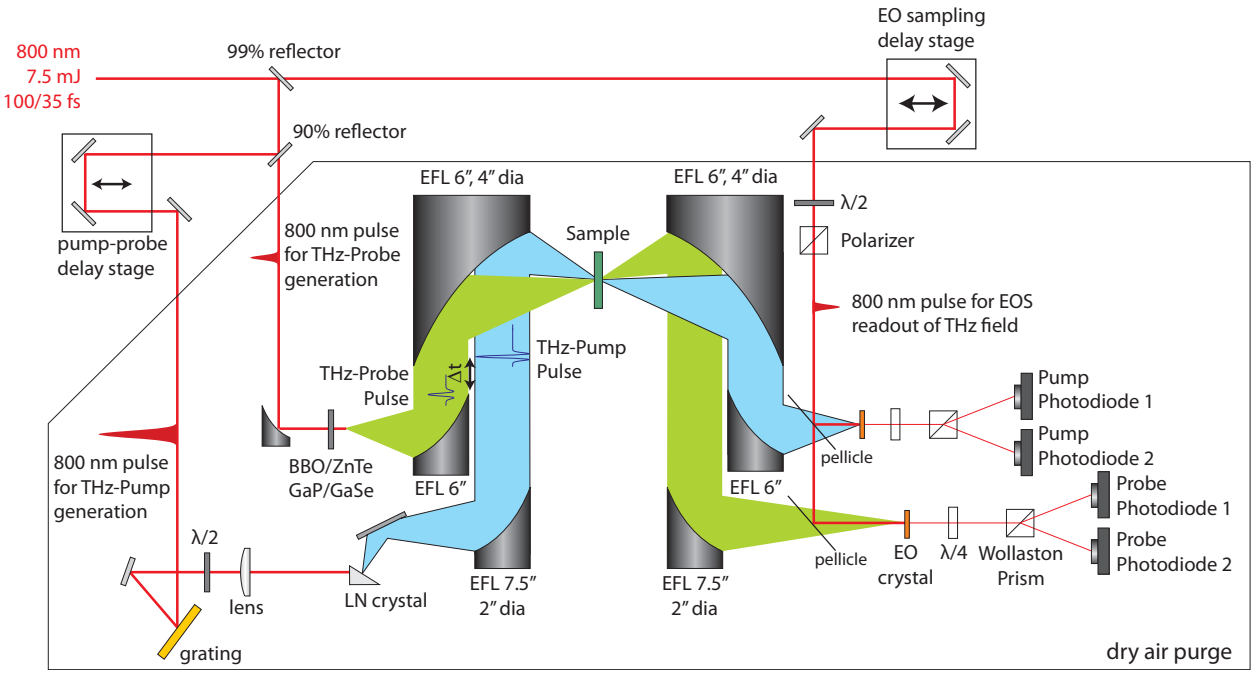

Figure 1: Noncollinear THz-pump/THz-probe setup. An 800 nm amplified optical pulse is split into three arms. Two arms are used for the generation of the THz pump and THz probe pulses. The third arm is used for electro-optic sampling of the THz electric fields. The THz-pump pulse is generated by tilted pulse front excitation in lithium niobate, and directed onto a sample with a pair of off-axis parabolic mirrors. The THz probe arm is generated by optical rectification in ZnTe. The THz probe arm is directed onto the sample with a pair of off-axis parabolic mirrors. The THz pump and THz probe arms are separated spatially since different generation schemes are used. However, they are focused to the same spot on the sample since both beams hit a common large diameter off-axis parabolic mirror immediately before the sample (any parallel beams hitting a parabola will focus to the same spot). For clarity, the THz pump and THz probe arms are shown horizontally displaced. They are vertically displaced in the actual setup. The electric field of either the THz pump or THz probe pulse is measured independently with electro-optic sampling.

10.1.2 THz-Pump/THz-Probe Spectroscopy on Tartaric Acid

Figure 2 is the linear THz transmission of a tartaric acid pellet showing absorption features at 1.1 and 1.8 THz. These resonances can be pumped within the bandwidth of the THz pump pulse in nonlinear pump-probe measurements.

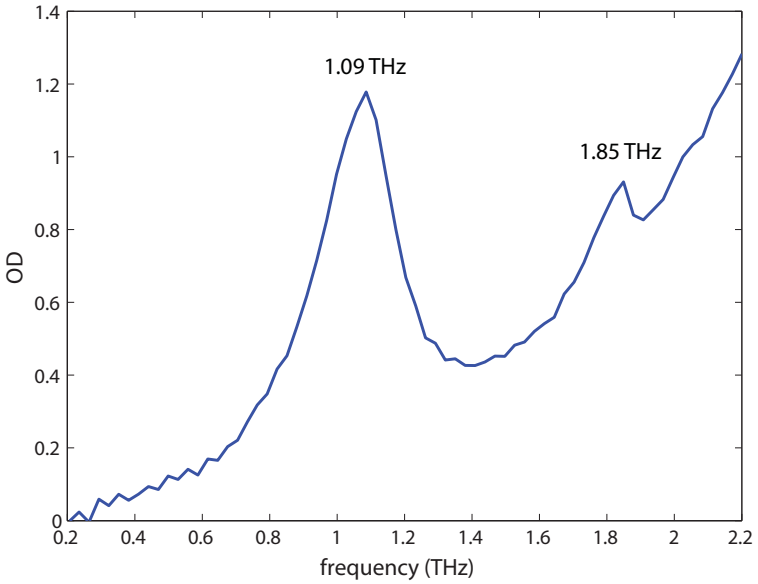

Figure 2: Linear THz optical density of a tartaric acid pellet. There are resonances near 1.1 and 1.8 THz.

Figure 3 illustrates results from a pump-probe peak scan measurement, where the electro-optic sampling delay was set to the peak of the probe THz pulse and the pump-probe delay was scanned. There are clear oscillations near the arrival of the THz pump pulse at 0 ps on the plot. The Fourier transform of the signal reveals weak features at 1.1 and 0.7 THz. Full frequency-resolved THz-pump/THz-probe measurements were performed where a full electro-optic sampling trace of the transmitted THz probe pulse was measured as a function of pump-probe delay. The results are shown in figure 4.

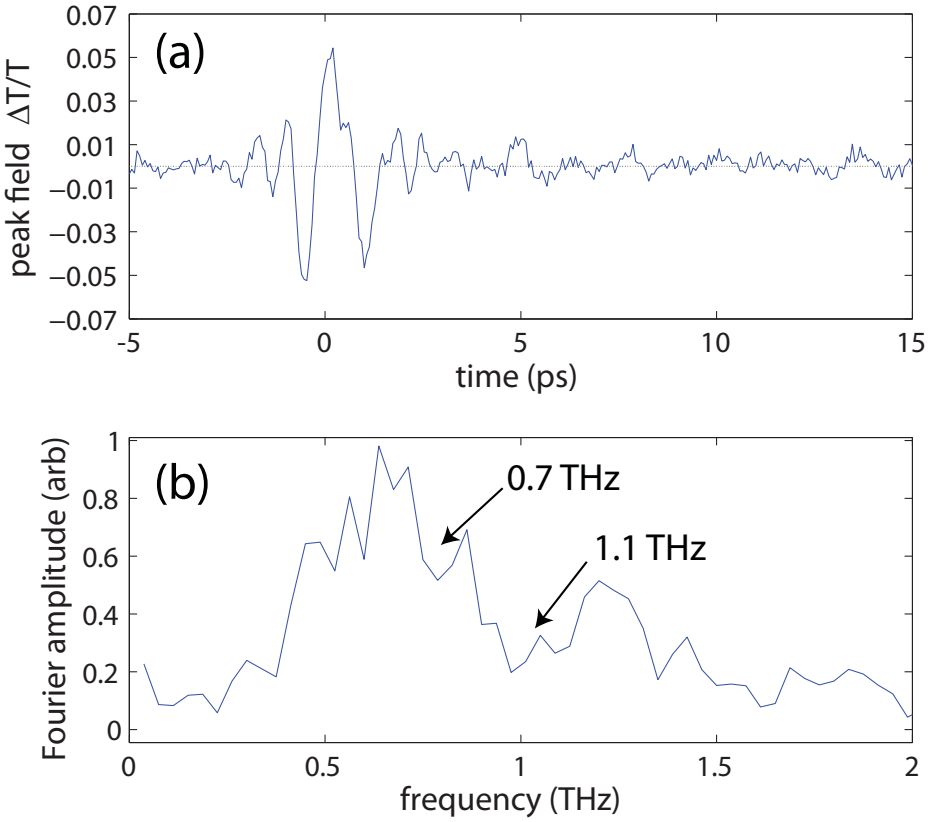

Figure 3: THz-pump/THz-probe peakscan of a tartaric acid pellet. There are clear oscillations occurring after the overlap time. The Fourier transform of the data shows poor signal-to-noise. However, there may be dips in the spectrum at 1.1 and 0.7 THz, corresponding to the 1.1 THz mode in tartaric acid and the difference frequency between the 1.1 and 1.8 THz mode.

Frequency-resolved pump-probe measurements were performed in a noncollinear geometry to have a clear view of time-zero dynamics that are typically obscured in collinear pump-probe measurements. The probe was chopped and compared to a reference of air. The transmission was calculated from the electro-optic sampling traces of the reference and sample and the pre-time zero contribution was subtracted from each pump-probe delay transmission trace. The

results are plotted in figure 4a. There is a beating of the differential transmission as a function of pump-probe delay time centered at 0.7 and 1.1 THz, just as in the peak scan from figure 3. A Fourier transform along the pump-probe delay axis reveals diagonal components to the signal at 0.7 and 1.1 THz (figure 4b). There may be a weak cross peak above the diagonal between the two diagonal features.

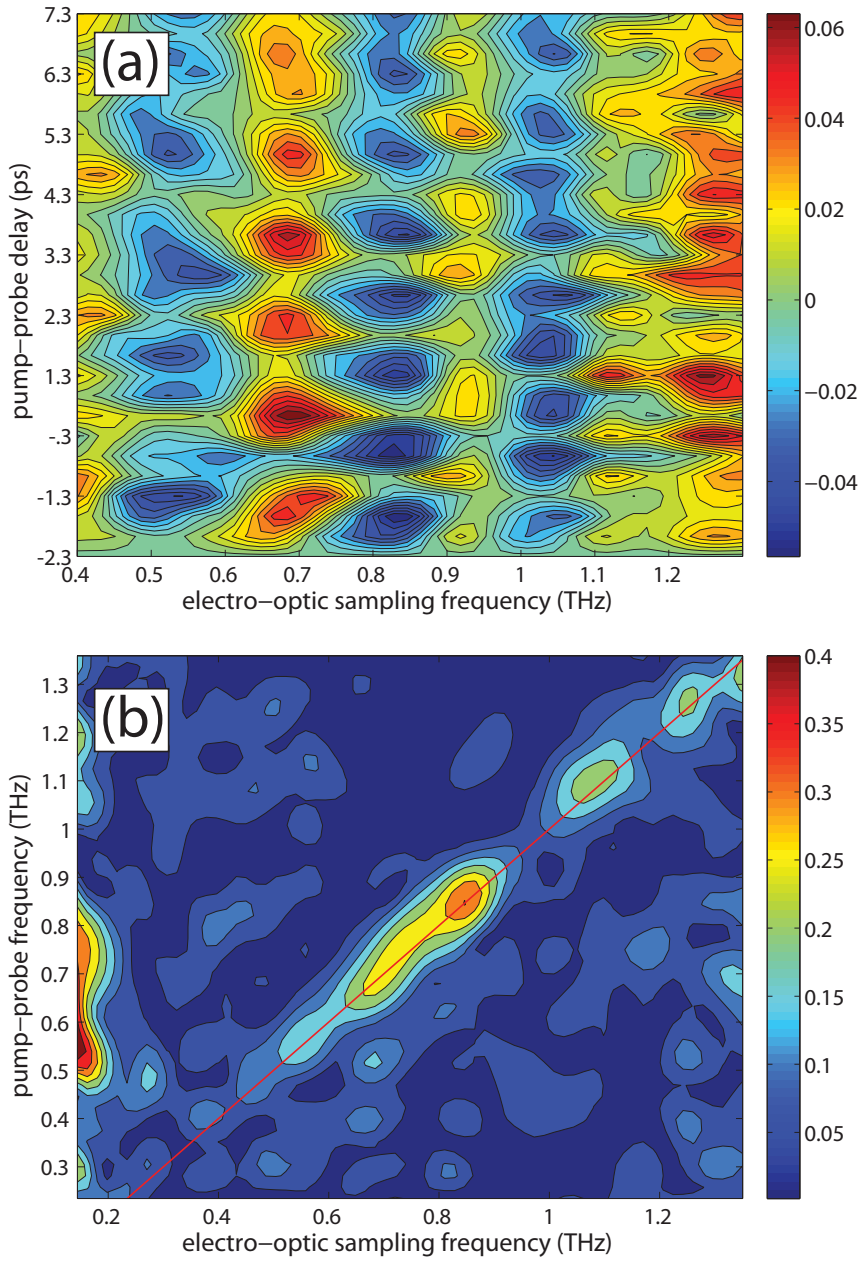

Figure 4: Noncollinear THz-pump/THz-probe spectroscopy of a tartaric acid pellet. **(a)** Time-frequency plot of the THz-pump/THz-probe measurement with the pre-time zero transmission subtracted from the experimental transmission at each pump-probe delay. This eliminates the linear response of tartaric acid from the THz probe pulse. The horizontal axis is the Fourier transformed electro-optic sampling axis. The vertical axis is the pump-probe delay time. The out-of-plane axis is the differential transmission—the transmission of the probe with the linear response from the pre-time zero signal subtracted out. There is a clear beating of the difference spectrum at 0.7 THz and 1.1 THz. **(b)** Fourier transform amplitude of the pump-probe delay axis. The 2D transform shows a peak at the difference frequency on the diagonal (0.7 THz) and a weaker feature at the 1.1 THz diagonal.

The 0.7 THz feature on the diagonal is atypical of a nonlinear spectroscopic measurement, since there is no apparent Feynman diagram that can lead to such an effect. However, we explain the response by modeling the third order response from a coupled pair of anharmonic oscillators.

10.1.3 Modeling the Nonlinear THz Response

Most of the discussion in this section has been taken from [5, 6][13], unless otherwise cited. We may model perturbative nonlinear spectroscopies using a density matrix formalism assuming a static system Hamiltonian and a time-dependent perturbation describing the light-matter interaction

$$H = H_0 + V(t) = H_0 + \mu \cdot E(t) \qquad (1)$$

The nonlinear polarization may be expressed as a perturbative expansion

$$P = P^{(0)} + P^{(1)} + \cdots + P^{(n)} \qquad (2)$$

The polarization is the average dipole moment per unit volume, so we can describe the polarization *P* as the expectation value of the quantum mechanical dipole operator normalized by the number density *N* of oscillators in the system, where each order of the polarization

expansion is related to a different order of the density matrix. The expectation value of an operator is simply the trace of the operator multiplied by the density matrix ρ

$$P = N\langle\mu\rangle = N\,Tr(\mu\rho) = N\left[Tr\left(\mu\rho^{(0)}\right) + Tr\left(\mu\rho^{(1)}\right) + \cdots + Tr\left(\mu\rho^{(n)}\right)\right] \qquad (3)$$

where higher orders of the density matrix occur through multiple light-matter interactions accounted for by $\mu \cdot E(t)$. The linear response function is given by

$$R^{(1)}(\tau) = \left(\frac{i}{\hbar}\right)\theta(\tau)Tr\{[\mu(\tau), \mu(0)]\rho_0\} \qquad (4)$$

In our pump-probe experiment, we are interested in the third order polarization, since it is the lowest order nonlinearity allowed in the far field. Since tartaric acid is non-centrosymmetric, there exist even orders of the polarization. However, since we are using a polycrystalline sample where the crystal sizes are smaller than the interaction volume of our THz pulses, the even orders of the polarization spatially cancel out, leaving only odd orders of the polarization to be observed in the far-field. The third order response function is given by

$$R^{(3)}(\tau_1, \tau_2, \tau_3) = \left(\frac{i}{\hbar}\right)^3 \theta(\tau_3)\theta(\tau_2)\theta(\tau_1)Tr\left\{\left[\left[\left[\mu(\tau_1 + \tau_2 + \tau_3), \mu(\tau_1 + \tau_2)\right], \mu(\tau_1)\right], \mu(0)\right]\rho_0\right\} \quad (5)$$

Using the formalism outlined above, we can model third order nonlinear perturbative spectroscopies assuming a two-dimensional anharmonic oscillator model with bilinear coupling starting with two separate harmonic oscillators [1]

$$H(Q_m, Q_n) = \frac{1}{2}m_m\omega_{m,0}^2Q_m^2 + \frac{1}{2}m_n\omega_{n,0}^2Q_n^2 + V_{mn}Q_mQ_n + \frac{1}{6}(g_{mmm}Q_m^3 + g_{nnn}Q_n^3) + \frac{P_m^2}{2m_m} + \frac{P_n^2}{2m_n} \quad (6)$$

In this case, we choose modes *m* and *n* to correspond to the 1.1 and 1.8 THz modes in tartaric acid, and we add in phenomenological bilinear coupling and anharmonicity constants, V_{mn} and $g_{mmm/nnn}$ respectively. For simplicity, we assume the dipole operator is proportional to displacement *Q* [1, 14]

$$M(Q_m, Q_n) = \mu_m^{(1)} Q_m + \mu_n^{(1)} Q_n \qquad (7)$$

The assumptions of bilinear coupling and a linear dipole in the displacement have been made for simplicity in the calculation. The important features of this calculation are the anharmonicity in the modes and the coupling between them. The correspondence to the experimental results discussed below would result from other considerations of the anharmonicity of the modes and their coupling.

10.1.4 Combination Bands and Difference Frequency Effects

The above model was used to calculate the third-order response function of a coupled pair of anharmonic oscillators with a common ground state. The potentials were populated thermally with a Boltzmann distribution yielding the initial diagonal populations of the density matrix.

$$\rho_0^{i,i} = \frac{e^{-E_i/k_B T}}{\sum_n e^{-E_n/k_B T}} \qquad (8)$$

where $\rho_0^{i,i}$ is a diagonal element of the density matrix, E_i is the energy of mode *i*, k_B is Boltzmann's constant, and *T* is temperature. Since the states involved in the calculation scale approximately as n^2 in the expansion of the two-oscillator basis to a combination band basis, it was not computationally practical to consider room temperature calculations. However, temperature-dependent effects up to 100 K demonstrate the same properties we are interested in.

The calculated linear response (equation 4) of the Hamiltonian given by equation 6 is plotted as a function of frequency and temperature in figure 5a. In the simulation, 15 basis states were used for each oscillator, giving a total of 136 combination states, with ω_m = 1.2 THz,

ω_n = 1.9 THz, V_{mn} = 0.2 THz, g_{111} = 0.12, g_{222} = 0.095, and unity linear dipoles $\mu_m^{(1)}, \mu_n^{(1)}$. As expected for an anharmonic oscillator that is softer than a harmonic potential, both modes redshift as they are thermally populated, and the overall strength of the response goes down. Figure 5b illustrates the equilibrium population in the lowest energy modes in the combination band basis (up to 6 THz). At higher temperatures (100 K) the distribution is flatter, such that higher energy populations contribute more significantly to the calculated polarization.

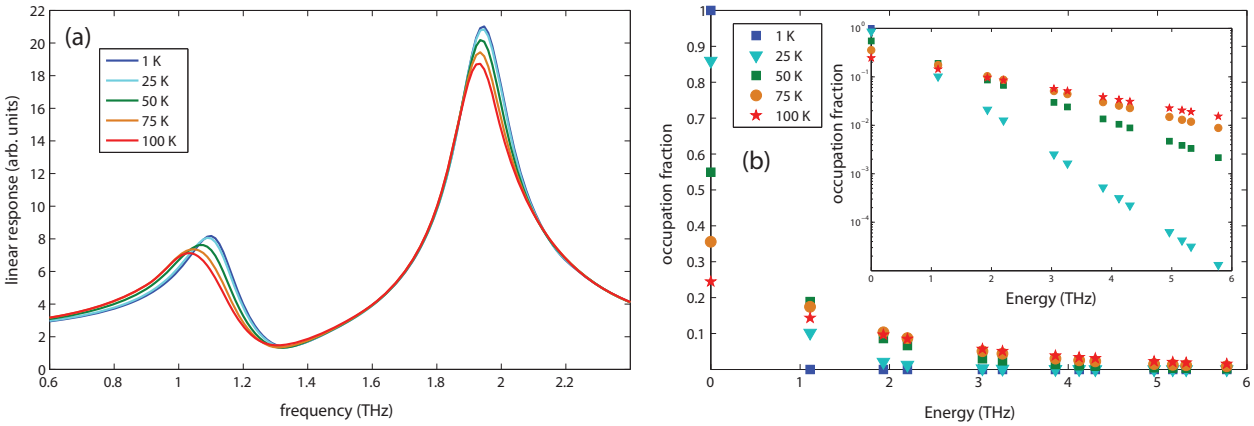

Figure 5: (a) Calculated linear response of two coupled anharmonic oscillators. The response in each mode shifts to lower frequency and the response decreases in magnitude as a function of increasing temperature. (b) The occupation in each of the energy states calculated in the combination basis. The inset shows the occupation fraction on a log scale. As temperature is increased, the distribution flattens out, making populations lying at higher energies contribute more to the polarization.

A third order calculation where two light-matter interactions occur with a first pulse, and one light-matter interaction occurs with a second pulse was performed on the system at several temperatures. This is different from a two-pulse echo calculation where one interaction occurs with a first pulse and two interactions occur with a second pulse. The second scenario is minimized in our experimental setup since the pump pulse is over an order of magnitude higher

in energy than the probe pulse. Figure 6 illustrates the results of the third order calculation. At zero frequency in the pump-probe axis (vertical), there are features at 1.2 and 1.9 THz corresponding to the population relaxation component of the signal. There are also weaker features at 1.9 and 1.9 THz on the diagonal possibly corresponding to 2 quantum transitions in the pump field interaction, with weak evidence of cross-peaks resulting from inter-mode coupling.

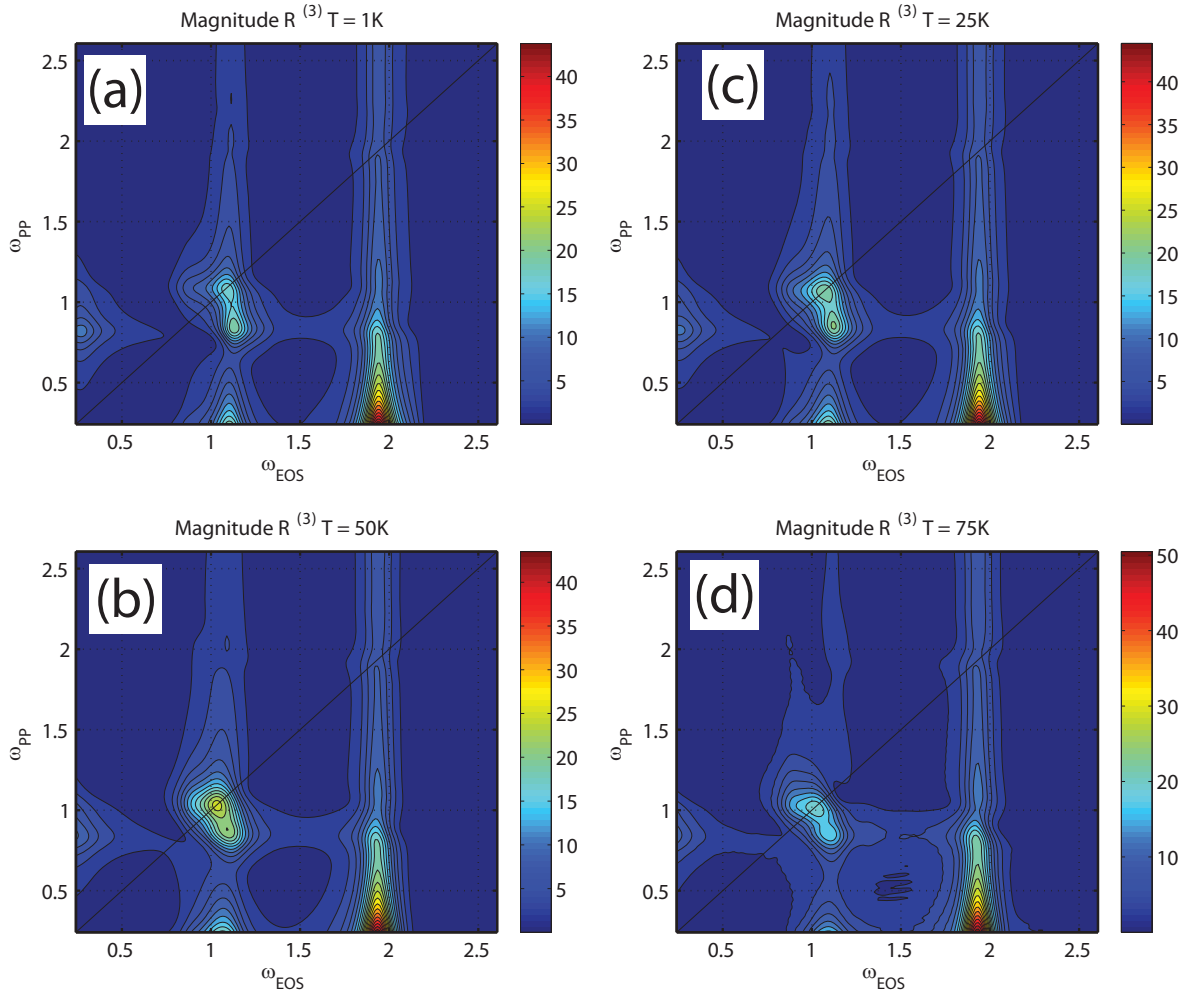

Figure 6: Third order nonlinear response calculation results. (a) T = 1 K. (b) T = 25 K. (c) T = 50 K. (d) T = 75 K. There is a weak temperature-dependence in the 2D pump probe spectra, however the qualitative features remain the same.

If we look closer within the spectral range of our measurement, we can see temperature dependent effects that form a feature at the difference frequency of 1.9 – 1.2 THz = 0.7 THz on the diagonal of the 2D spectrum (figure 7). This feature only grows in at higher temperatures. Even at 50 K, the feature is not present. As a result, the calculations suggest that the prominent diagonal feature at the difference frequency of the two modes in our pumping bandwidth (1.1 and 1.8 THz) arises from populating combination states where allowed transitions of the dipole matrix given by equation 7 allow for absorption and emission at the difference frequency.

Phase-matching considerations were not accounted for in these calculations. The full third-order response is calculated at once. If the specific interactions leading to the diagonal feature are found to be poorly wavevector matched, then this would imply that phasematching considerations in noncollinear THz experiments are greatly relaxed. However, more study is required to confirm both the diagonal difference frequency feature and phase matching considerations. In particular, higher-temperature scaling of the difference frequency diagonal feature would be useful to further elucidate the origin of the effect. This would require time-intensive simulations with a larger basis set of states to do properly since it takes a considerable number of basis states from each oscillator for the dipole matrix to converge at higher thermal populations of the density matrix.

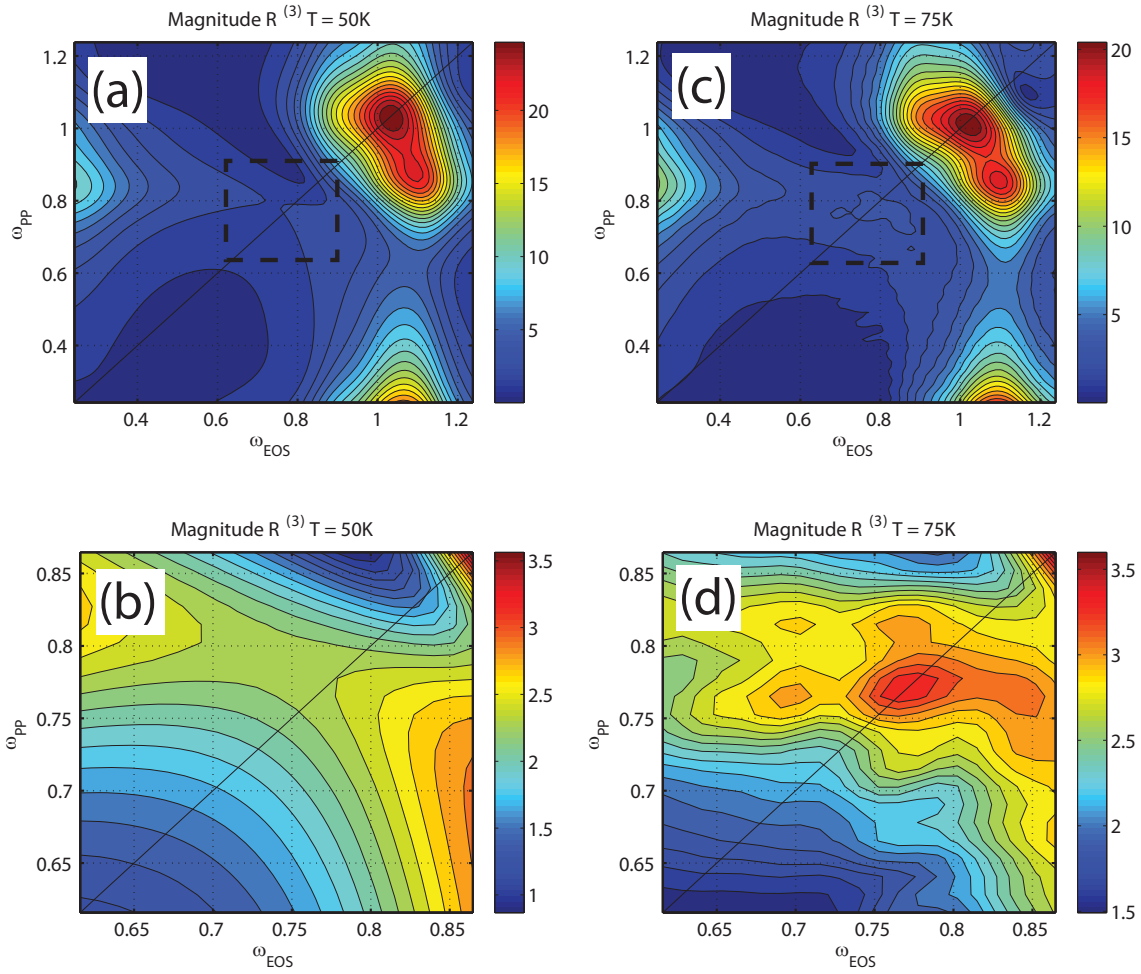

Figure 7: (a) & (b) Calculated third-order pump-probe response at T = 50 K. The boxed out portion of (a) is shown in (b). (c) & (d) Calculated third-order pump-probe response at T = 75 K. The boxed out portion of (c) is shown in (d). Of note at T = 75 K is the prominent feature at ~0.75 THz on the diagonal.

10.1.5 Nonlinear Vibrational Responses in Tartaric Acid: Conclusions

We have started to observe what may be third order nonlinear vibrational effects in the molecular crystal, tartaric acid. We observe a prominent difference frequency peak at 0.7 THz on the diagonal of our 2D spectrum corresponding to the difference between the 1.1 and 1.8 THz modes in tartaric acid. This feature arises as a result of thermally populating coupled anharmonic oscillators, where the combinations of populations are taken into consideration.

Further temperature dependent experiments to confirm the correspondence with our model are still needed. The results may also indicate that phase-matching constraints in the THz range are largely relaxed.

The results in this section are an important starting point for realizing two-dimensional THz vibrational spectroscopy. This is particularly important, since modes in the THz range coincide with the bath modes of a system, which mediate energy transfer and coupling to higher energy degrees of freedom. Also, it is particularly relevant in high-energy materials like RDX, whose detonation is initiated by energy transfer from lower energy degrees of freedom (acoustic phonon modes) to localized vibrations along the reaction coordinate (N-N vibrations).

We can make further steps to realizing 2D THz vibrational spectroscopy by performing two-pulse echo experiments in a collinear geometry. Here, since the two-pulse echo should give a signal at time delays longer than the THz pulse itself, we can easily resolve echo effects in the time-domain without the limitations of the nonlinear effects that occur at the overlap time of the pump and probe optical generation pulses in the collinear geometry.

10.2 Impulsive Stimulated Raman Scattering as a Probe

We can also find new ways to probe nonlinear responses initiated by strong THz fields. One way is to use impulsive stimulated Raman scattering (ISRS) [15-17] to probe changes in Raman active vibrational modes within the optical pulse bandwidth. This would be a powerful way to track changes in systems that undergo structural changes upon excitation—whether it is from ferroelectric domain switching, or going from an insulating to a metallic state. For the latter case, VO_2 itself would be an ideal system. We can use metamaterial enhancement to initiate

the IMT in VO_2 and then use an optical probe, which can fit into the SRR gaps, to watch how the structural changes correlate with the electronic phase transition.

10.3 THz-Driven Ferroelectric Switching

Other ways to use metamaterial enhancements to induce nonlinear effects with THz pulses would be to try and switch ferroelectric domains in BFO, or PMT-PT. Here, metamaterial enhancement would be used to switch the ferroelectric domain direction of an in-plane poled sample, and an above-bandgap probe would be used to generate photo-carriers that would move in the ferroelectric field—similar to a recent study at LCLS [18]. Depending on the orientation of the domain, the initiated photocurrent response would change. Furthermore, the lattice response could be probed with ISRS, where the distortion of the lattice potential by the strong THz field will change crystal symmetries, bringing Raman-active vibrational modes in and out of the ISRS spectrum depending on the state of the sample.

10.4 Ultrafast Magnetoresistance

Another interesting route to follow would be to look at ultrafast magnetoresistance in PCMO and EuO. PCMO undergoes an ultrafast change in resistivity upon optical or infrared excitation [19]. Recent studies have also shown that thin films of EuO undergo changes in resistivity by over an order of magnitude [20]. We can use metamaterial structures that enhance the magnetic field component of a THz pulse to induce magnetoresistive responses that can be probed with an optical pulse. This would be a first look at ultrafast magnetoresistive dynamics.

10.5 Other Nonlinear THz Responses in Graphene

In CVD-graphene, recent advances have made it possible to have near intrinsically doped, >100 μm single domain size samples. With these samples, we can try to induce strongly nonlinear currents in graphene with THz pulses, generating high-order THz harmonics. We can also try and use the magnetic field component of the THz pulse to initiate nonlinear magnetic effects related to ultrafast modulation of the Hall effect in graphene.

10.6 Superconductivity Dynamics

We have also begun to study nonlinear THz effects in the high critical temperature superconductor, YBCO ($YBa_2Cu_3O_{7-d}$, d ~ 0.05). We observe THz induced transparency in nonlinear THz transmission measurements (figure 8). The THz pulse decreases the conductivity of a YBCO thin film at high THz intensities, increasing the THz transmission.

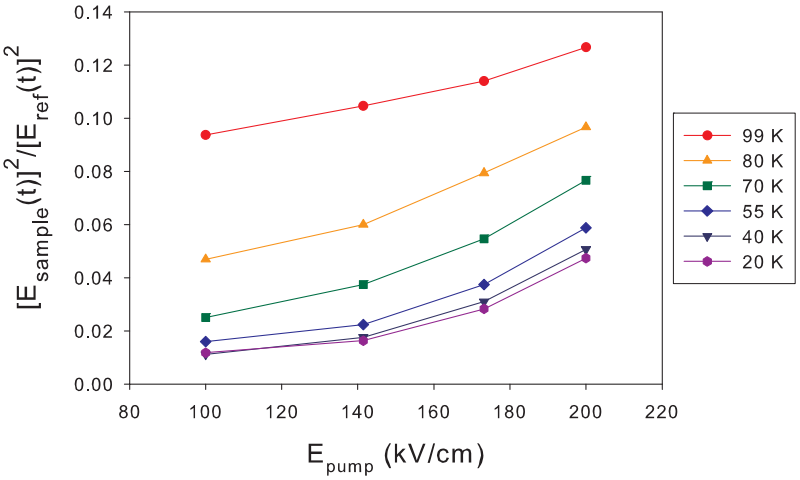

Figure 8: Nonlinear THz transmission measurements on a YBCO thin film as a function of temperature. The average intensity transmission is plotted as a function of incident THz field

strength. The relative change increases as the temperature is decreased. Above T_c, the effect is the smallest.

Time-resolved collinear THz-pump/THz-probe measurements demonstrate that the conductivity change persists for several picoseconds (figure 9). The temperature dependence of the pump-probe signal indicates that the effect depends on the presence of superconductivity. Above T_c = 90 K, the effect is much smaller. The THz-pump pulse transiently breaks superconductivity and the weak THz-probe pulse probes the conductivity change as a function of time. This opens up a large variety of experiments to observe magnetic and lattice effects with ISRS (magnons, phonons, polarons) upon THz excitation, which may provide clues to unveil the coupling boson involved in high T_c superconductivity.

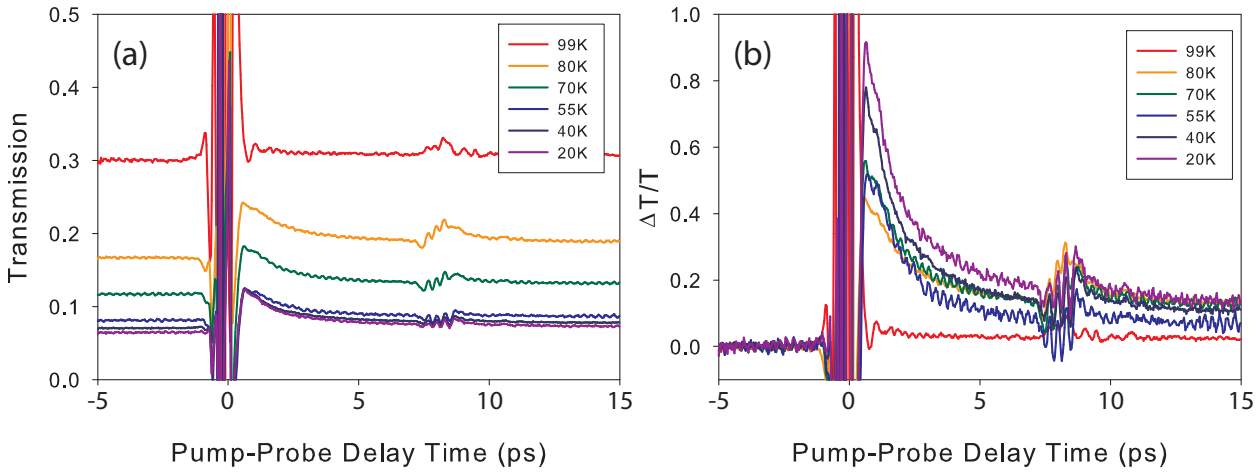

Figure 9: Collinear THz-pump/THz-probe spectroscopy of a YBCO thin film. (a) The transmission of the peak of the THz probe field as a function of temperature. Above T_c = 90 K, the dynamic change disappears. As the temperature is decreased deeper into the superconducting state, the absolute transmission decreases, and (b) the relative transmission increases. The dynamics also seem to change as a function of temperature.

10.7 THz-Induced Chemistry

Finally, we have begun measurements to demonstrate that we can initiate chemical reactions with THz pulses. We have used metamaterial split ring resonators (SRRs) to achieve strong enhancement of the THz electric field, which in turn drives chemical decomposition of material deposited in the gaps (figure 10). Gold metamaterial SRRs were deposited on a 400 nm thick SiN_x membrane. The SRR gaps were etched away, leaving just air in the gaps. Earlier nonlinear measurements have shown that SiN_x exhibits nonlinear THz electronic responses as well. Etching away the gaps minimizes the nonlinear effects in the enhanced gap regions.

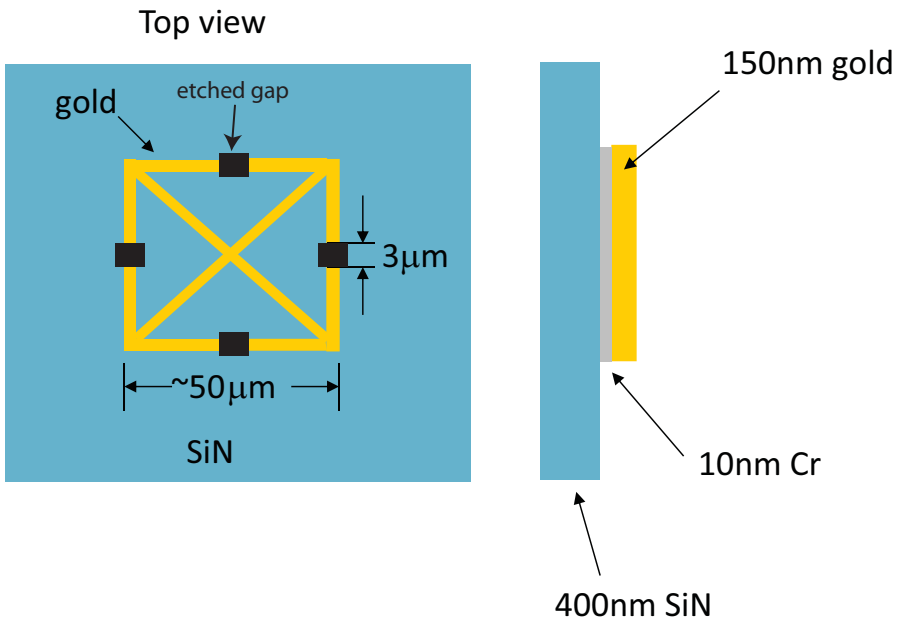

Figure 10: Schematic of metamaterial split ring resonators on a silicon nitride (SiN_x) membrane. The gaps are etched away such that a material can be deposited within, and to minimize nonlinear conductivity effects in the SiN_x.

Trinitrotoluene (TNT) was deposited in the gaps of the SRRs by slow evaporation of TNT in toluene solution, where the solution was dropped onto the back side of the sample (figure 11).

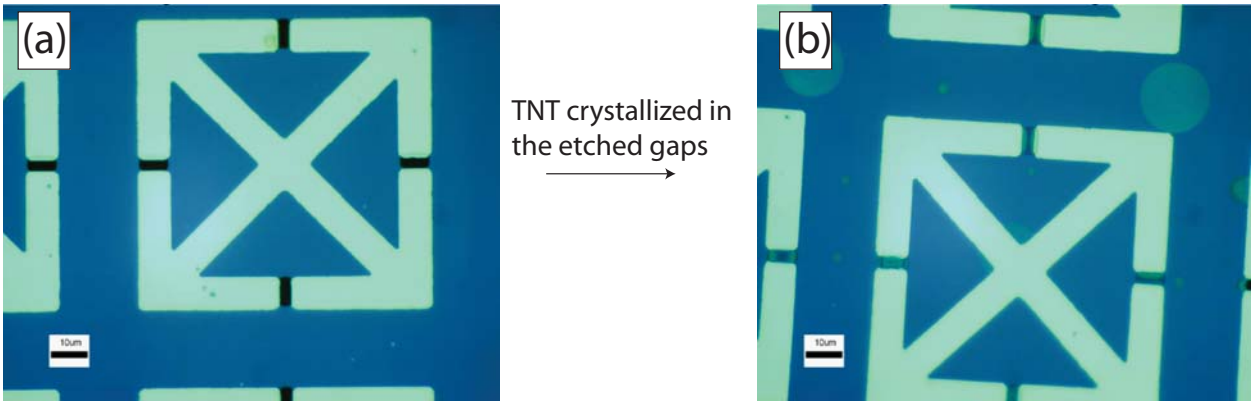

Figure 11: Optical microscope images of SRRs on a SiN_x membrane. (a) The membrane prior to crystallizing trinitrotoluene (TNT) in the gaps by slow evaporation of a concentrated TNT/toluene solution. The black areas indicate empty SRR gaps. (b) After depositing TNT into the 3 µm SRR gaps, small translucent crystals are seen in the gaps.

After exposure to strong THz radiation from tilted pulse front excitation for one hour, there is optical evidence of decomposition (figure 12). Further studies are currently underway to analyze the decomposition products by gas chromatography/mass spectrometry.

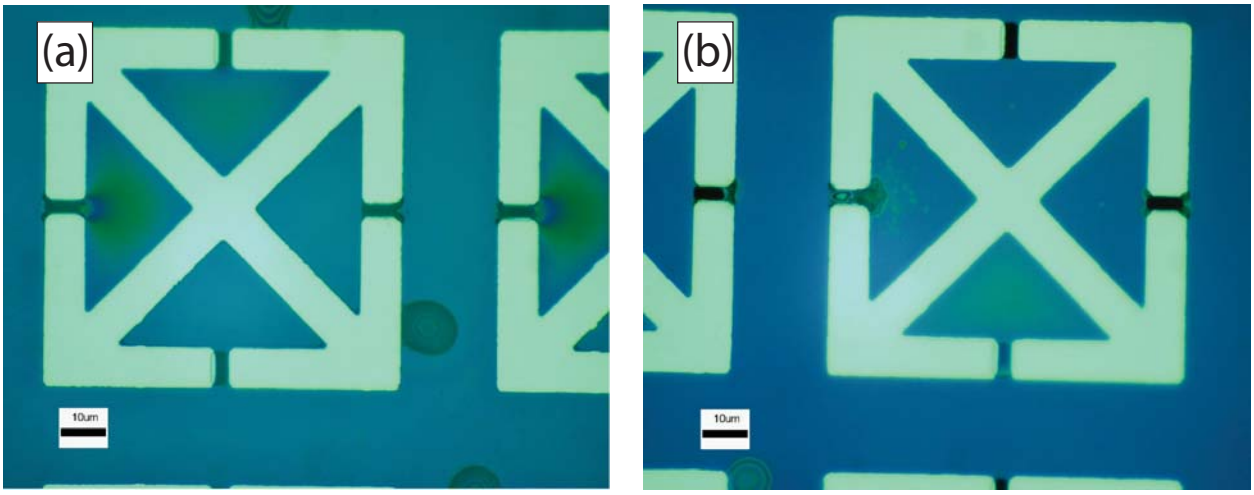

Figure 12: Optical microscope image of SiN_x membrane with TNT deposited in the gaps after one hour of intense THz illumination. (a) Small plumes of discoloration are seen in the gaps,

indicating some decomposition of the TNT in the gaps. (b) More dramatic evidence is seen with a speckle pattern indicating heavier damage. Notice the vertical gaps are minimally affected, while the horizontally oriented gaps (along the incident THz polarization) have the most dramatic changes.

10.8 Concluding Remarks

I have discussed the importance of nonlinear THz spectroscopy in advancing our understanding of several phenomena in condensed matter systems. These demonstrations are only a start to some of the capabilities granted by our advances in tabletop THz generation. Further study and spectroscopic development will aid in maturing the field for use as a more routine general methodology in condensed matter spectroscopy.

References

[1] M. Khalil, N. Demirdöven and A. Tokmakoff. "Coherent 2D IR Spectroscopy: Molecular Structure and Dynamics in Solution." *The Journal of Physical Chemistry A*, **107**, 5258 (2003).

[2] M. Khalil, N. Demirdoven and A. Tokmakoff. "Vibrational coherence transfer characterized with Fourier-transform 2D IR spectroscopy." *The Journal of Chemical Physics*, **121**, 362 (2004).

[3] C. J. Fecko, J. D. Eaves, J. J. Loparo, A. Tokmakoff and P. L. Geissler. "Ultrafast Hydrogen-Bond Dynamics in the Infrared Spectroscopy of Water." *Science*, **301**, 1698 (2003).

[4] J. Zheng, K. Kwak, J. Asbury, X. Chen, I. R. Piletic and M. D. Fayer. "Ultrafast Dynamics of Solute-Solvent Complexation Observed at Thermal Equilibrium in Real Time." *Science*, **309**, 1338 (2005).

[5] S. Mukamel. **Principles of nonlinear optical spectroscopy**. (New York: Oxford University Press) (1995).

[6] M. Cho. **Two-dimensional optical spectroscopy**. (Boca Raton: CRC Press) (2009).

[7] J. Sung and R. J. Silbey. "Four wave mixing spectroscopy for a multilevel system." *The Journal of Chemical Physics*, **115**, 9266 (2001).

[8] J. Sung, R. J. Silbey and M. Cho. "Effects of temperature on the nonlinear response function for two-dimensional vibrational spectroscopy." *The Journal of Chemical Physics*, **115**, 1422 (2001).

[9] M. Jewariya, M. Nagai and K. Tanaka. "Ladder Climbing on the Anharmonic Intermolecular Potential in an Amino Acid Microcrystal via an Intense Monocycle Terahertz Pulse." *Physical Review Letters*, **105**, 203003 (2010).

[10] W. Kuehn, K. Reimann, M. Woerner and T. Elsaesser. "Phase-resolved two-dimensional spectroscopy based on collinear n-wave mixing in the ultrafast time domain." *The Journal of Chemical Physics*, **130**, 164503 (2009).

[11] W. Kuehn, K. Reimann, M. Woerner, T. Elsaesser and R. Hey. "Two-Dimensional Terahertz Correlation Spectra of Electronic Excitations in Semiconductor Quantum Wells." *The Journal of Physical Chemistry B*, **115**, 5448 (2010).

[12] W. Kuehn, K. Reimann, M. Woerner, T. Elsaesser, R. Hey and U. Schade. "Strong Correlation of Electronic and Lattice Excitations in GaAs/AlGaAs Semiconductor Quantum Wells Revealed by Two-Dimensional Terahertz Spectroscopy." *Physical Review Letters*, **107**, 067401 (2011).

[13] Andrei Tokmakoff, 5.74 Introductory Quantum Mechanics II, Spring 2009. (Massachusetts Institute of Technology: MIT OpenCourseWare), http://ocw.mit.edu (Accessed May 2, 2012). License: Creative Commons BY-NC-SA

[14] O. Golonzka, M. Khalil, N. Demirdoven and A. Tokmakoff. "Coupling and orientation between anharmonic vibrations characterized with two-dimensional infrared vibrational echo spectroscopy." *The Journal of Chemical Physics*, **115**, 10814 (2001).

[15] Y.-X. Yan and K. A. Nelson. "Impulsive stimulated light scattering. I. General theory." *The Journal of Chemical Physics*, **87**, 6240 (1987).

[16] Y.-X. Yan and K. A. Nelson. "Impulsive stimulated light scattering. II. Comparison to frequency-domain light-scattering spectroscopy." *The Journal of Chemical Physics*, **87**, 6257 (1987).

[17] S. Ruhman, A. G. Joly and K. A. Nelson. "Time-resolved observations of coherent molecular vibrational motion and the general occurrence of impulsive stimulated scattering." *The Journal of Chemical Physics*, **86**, 6563 (1987).

[18] D. Daranciang, M. J. Highland, H. Wen, S. M. Young, N. C. Brandt, H. Y. Hwang, M. Vattilana, M. Nicoul, F. Quirin, J. Goodfellow, T. Qi, I. Grinberg, D. M. Fritz, M. Cammarata, D. Zhu, H. T. Lemke, D. A. Walko, E. M. Dufresne, Y. Li, J. Larsson, D. A. Reis, K. Sokolowski-Tinten, K. A. Nelson, A. M. Rappe, P. H. Fuoss, G. B. Stephenson and A. M. Lindenberg. "Ultrafast Photovoltaic Response in Ferroelectric Nanolayers." *Physical Review Letters*, **108**, 087601 (2012).

[19] M. Rini, R. a. Tobey, N. Dean, J. Itatani, Y. Tomioka, Y. Tokura, R. W. Schoenlein and A. Cavalleri. "Control of the electronic phase of a manganite by mode-selective vibrational excitation." *Nature*, **449**, 72 (2007).

[20] T. Mairoser, A. Schmehl, A. Melville, T. Heeg, L. Canella, P. Böni, W. Zander, J. Schubert, D. E. Shai, E. J. Monkman, K. M. Shen, D. G. Schlom and J. Mannhart. "Is There an Intrinsic Limit to the Charge-Carrier-Induced Increase of the Curie Temperature of EuO?" *Physical Review Letters*, **105**, 257206 (2010).